

Abstract

Title of Dissertation: An Analysis of the Environment and
Gas Content of Luminous Infrared Galaxies

Bevin Ashley Zauderer, Doctor of Philosophy, 2010

Dissertation directed by: Professor Stuart N. Vogel
Department of Astronomy

Luminous and ultraluminous infrared galaxies (U/LIRGs) represent a population among the most extreme in our universe, emitting an extraordinary amount of energy at infrared wavelengths from dust heated by prolific star formation and/or an active galactic nucleus (AGN). We present three investigations of U/LIRGs to better understand their global environment, their interstellar medium properties, and their nuclear region where molecular gas feeds a starburst or AGN. To study the global environment, we compute the spatial cluster-galaxy amplitude, B_{gc} , for 76 $z < 0.3$ ULIRGs. We find the environment of ULIRGs is similar to galaxies in the field. Comparing our results with other galactic populations, we conclude that ULIRGs might be a phase in the lives of AGNs and QSOs, but not all moderate-luminosity QSOs necessarily pass through a ULIRG phase. To study the interstellar medium properties, we observe H I and other spectral lines in 77 U/LIRGs with the Arecibo telescope. We detect H I in emission or absorption in 61 of 77 galaxies, 52 being new detections. We compute the implied gas mass for galaxies with emission, and optical depths and column densities for the seven sources with absorption detections. To study the molecular gas in the nuclear region of LIRG Arp 193, sub-arcsecond scale angular resolution is required and a method of atmospheric phase correction imperative. We present results of a large experiment observing bright quasars to test the limitations of the Combined Array for Research in Millimeter Astronomy's

Paired Antenna Calibration System (C-PACS) for atmospheric phase correction. We conclude that C-PACS improves imaging capabilities when the atmospheric calibrator is nearby ($\leq 6^\circ$), bright (> 1 Jy), and at moderately high elevation ($> 45^\circ$). We map Arp 193 in $^{12}\text{CO}(2-1)$ with CARMA, achieving $0.18'' \times 0.12''$ (~ 65 pc) resolution, and demonstrating an improvement with C-PACS. We compute a molecular gas mass of $2 \times 10^9 M_\odot$ and find $\sim 20\%$ of the total mass is in the form of molecular gas out to a radius of 750 pc. In the inner 150 pc of the nucleus, $N(\text{H}_2) > 10^{25} \text{ cm}^{-2}$.

An Analysis of the Environment and Gas Content of Luminous Infrared Galaxies

by

Bevin Ashley Zauderer

Dissertation submitted to the Faculty of the Graduate School of the
University of Maryland at College Park in partial fulfillment
of the requirements for the degree of
Doctor of Philosophy
2010

Advisory Committee:

Professor Stuart N. Vogel, chair
Professor Alberto D. Bolatto
Dr. Emmanuel Momjian
Professor Rachel T. Pinker
Professor Sylvain Veilleux

© Bevin Ashley Zauderer 2010

Preface

This thesis was written under the joint supervision of University of Maryland professors Stuart Vogel, Sylvain Veilleux and Alberto Bolatto. It is divided into five chapters and four appendices.

Chapter 2, “The Environment of Local Ultraluminous Infrared Galaxies,” was previously published in its entirety as Zauderer et al. (2007). Followup work completed since publication, under the additional guidance of Professor Sukyoung Yi of Yonsei University in Seoul, Korea, is summarized in Appendix C. Results based on Chapter 2 were presented at the First Korea-Japan Workshop on Galaxy Evolution and at the University of Maryland Graduate Research Interaction Day (GRID), both in 2008.

Chapter 3 was written under the additional guidance of Dr. Emmanuel Momjian of the National Radio Astronomy Observatory (NRAO), Dr. Chris Salter and Dr. Tapasi Ghosh of the National Astronomy and Ionosphere Center (NAIC) at the Arecibo Observatory, and is a continuation of the radio spectral line survey of luminous infrared galaxies (LIRGs), published by Fernandez et al. (2010). The majority of Chapter 3 will be published as Part II of this survey (Zauderer et al., in preparation), with the survey completion (Part III) and sample analysis forthcoming. Early results based on Chapter 3 were presented at the American Astronomical Society (AAS) January 2010 meeting (Zauderer et al. 2010).

Chapter 4 will be submitted in its entirety for publication in the near future, with a number of co-authors listed in the Acknowledgements. Results based on Chapter 4 were presented in 2009 at the Combined Array for Research in Millimeter Astronomy (CARMA) Science Symposium, at the Fourth North American ALMA Science Center Conference (Assembly, Gas Content and Star Formation History of Galaxies), and at the Siemens Competition in Math, Science and Technology by high school student summer interns Roger G. Curley and Dalton C. Wu. Data presented in Clemens and Alexander (2004) were obtained via private communication and used for comparative analysis (i.e., Figures 4.15 and 4.16) with the author's permission.

Appendices A and B were submitted to the CARMA Memoranda series on September 2, 2008 and June 16, 2009 as Memorandum 49 and 51, respectively. The CARMA Memoranda series is available electronically to the community at <http://www.mmarray.org/memos/>. Appendix A, "Single-Dish Aperture Efficiency Measurements at CARMA," was guided by and written with Dr. Stephen M. White (Space Vehicles Directorate, Air Force Research Laboratory). Appendix B, "Shadowing in the CARMA E-Array," was guided by and written with Dr. Peter J. Teuben (University of Maryland).

Permission to reproduce copyrighted portions of *Nature* articles was obtained by the author on October 15, 2010 and includes license number 2530020309008 for article "The New Observatory at Vienna" (Nature 1876) and license number 2530020550757 for article "Another Monster Refractor" (Nature 1875).

Figures that are taken from the published literature or online resources include: Figure 1.1 generated using the photometric data plotting tool from the NASA/IPAC Extragalactic Database, Figure 1.2 from NASA, ESA, the Hubble Heritage Team-ESA/Hubble Collaboration and A. Evans, Figure 1.3 compiled from a digitization of Herschel (1858) by the Armagh Observatory (www.arm.ac.uk), Figure 1.4 from the

European Southern Observatory (www.spacetelescope.org), Figure 1.5 courtesy of the NAIC-Arecibo Observatory, a facility of the National Science Foundation, Figure 1.6c courtesy of the CARMA observatory (www.mmarray.org), Figure 1.7 generated by Nicola Schneider via private communication with the author, Figure 1.8 from Fernandez et al. (2010), Figure 1.9 first published as Figure 7 by Zwicky (1956), and Figure 1.10 from Veilleux et al. (1995). Online resources utilized include the NASA/IPAC Extragalactic Database (NED), NASA's Astrophysics Data System (ADS) Abstract Service, the Sloan Digital Sky Survey (SDSS), the HyperLeda database (<http://leda.univ-lyon1.fr>), the Historic IC Catalog from Dr. W. Steinicke's archive (www.klima-luft.de/steinicke), and Google Book Search <http://books.google.com/>.

כְּבֹד אֱלֹהִים הַסֵּתֵר דְּבָר וּכְבֹד מְלָכִים חֲקֹר דְּבָר:
משלי כ"ה ב'

Acknowledgements

There are a number of people and institutions which have supported the work presented in this thesis, which I would like to formally acknowledge.

Chapter 2 For the research presented in Chapter 2, I would like to thank Sylvain Veilleux for hiring me as a second-year graduate student to begin work on this project, and introducing me to the subject matter that would become the focus for my studies throughout graduate school. I also thank Howard Yee for hosting me at the University of Toronto for several weeks and for his patience as I was learning methods of photometry analysis. Sylvain, Howard and I thank D.C. Kim for his help in organizing the data set we used. Partial support for the research in Chapter 2 was funded by a National Science Foundation (NSF) CAREER grant AST 98-74973 and NASA grant 1263752 issued by the Jet Propulsion Laboratory, California Institute of Technology.

For the followup research, summarized in Appendix C, I would like to thank Professor Sukyoung Yi and his Galaxy Evolution Meeting (GEM)

research group for hosting me during the summer of 2008 at Yonsei University in Seoul, Korea. I thank Joo Heon Yoon for helping me analyze a subset of my galaxies with his spectro-photometric environment analysis tools. Financial support for this research was provided by the National Science Foundation through the East Asia and Pacific Summer Institute (EAPSI) under Grant No. 0813179 and co-sponsored by the National Research Foundation of Korea (formerly, the Korean Science Foundation).

Chapter 3 For the research presented in Chapter 3, I would like to first thank and acknowledge David Rupke for sharing with me his idea of doing an H I survey of LIRGs. I thank my collaborators, Tapasi Ghosh, Chris Salter and Emmanuel Momjian for giving me the opportunity to pick up the survey where it was left off by former REU summer student, Ximena Fernández. Support for this research was provided by the National Science Foundation (NSF) under Grant No. AST 0808075. I also acknowledge and thank the Arecibo Observatory scientists, engineers and staff, especially Phil Perillat for the large amount of code he maintains for data reduction. The Arecibo Observatory is part of the National Astronomy and Ionosphere Center (NAIC), which is operated by Cornell University under a cooperative agreement with the National Science Foundation.

Chapter 4 The work presented in Chapter 4 will be published with a large number of co-authors including advisors Stuart Vogel and Alberto Bolatto, Laura Pérez, John Carpenter, John Carlstrom, Tom Culverhouse, James Lamb, Erik Leitch, Dick Plambeck, Marc Pound, Dan

Marrone, Lee Mundy, Peter Teuben, Dave Woody and Melvyn Wright. I thank them each for helpful discussions, suggestions and support. I especially thank Lee Mundy for giving me the opportunity to take a lead role in this project and Alberto Bolatto for his guidance and daily support navigating the challenges associated with the project. I thank John Carpenter for patiently sharing his advice and expertise in every step of this project, from designing the experiment to analyzing the results. Laura Pérez, a graduate student at Caltech, did a large amount of work identifying atmospheric calibrators, writing MIRIAD programs for C-PACS data analysis, and debugging. Her enthusiasm is contagious.

The nuts and bolts of the PACS commissioning effort to integrate the SZA into the CARMA array relied heavily on the work of John Carlstrom's group at the University of Chicago. On behalf of all who contributed to the SZA array and this transition, I acknowledge and thank the efforts of a few people I interacted with during observing trips: Tom Culverhouse deriving baseline solutions, Dan Marrone troubleshooting and diagnosing obscure system errors, and Erik Leitch supporting our efforts, even from the South Pole.

Stephen White and I thank Andy Harris, James Lamb, Lee Mundy and Dave Woody for valuable discussions and suggestions to the Single Dish Aperture Efficiency CARMA Technical Memo (Appendix A). I also acknowledge useful discussions with Dick Plambeck and Juergen Ott in the early stages of this commissioning project, especially related to the calculation of zenith opacity.

Commissioning a telescope (or new capabilities) requires the joint ef-

fort of a very large team. I would like to acknowledge and thank the entire Owens Valley Radio Observatory Staff (OVRO) including those currently employed and those who have moved on to new positions. The observatory would not function and my research would not have been possible without the work of Andy Beard, Steve Scott, Rick Hobbs, Ron Lawrence, Russ Keeney, Dave Hawkins, Michael Cooper, Curt Giovanine, Stan Hudson, Michael Laxen, Cecil Patrick, Terry Sepsey, Nikoluas Volgenau, Douglas Bock, Tony Beasley, Dave Hawkins, Brad Wiitala, Paul Rasmussen, Steve Miller, Mark Hodges, Nick Scoville, Anneila Sargent, Mary Daniel, Debbie Juliff, and Paul Daniel, to name a few. In honor of all those whose ideas, creativity, and effort literally built the observatory, I acknowledge Chick Lackore.

Support for CARMA construction was derived from the states of California, Illinois, and Maryland, the James S. McDonnell Foundation, the Gordon and Betty Moore Foundation, the Kenneth T. and Eileen L. Norris Foundation, the University of Chicago, the Associates of the California Institute of Technology, and the National Science Foundation. Ongoing CARMA development and operations are supported by the National Science Foundation under a cooperative agreement, and by the CARMA partner universities.

General Research in all three chapters has made use of the NASA/IPAC Extragalactic Database (NED), which is operated by the Jet Propulsion Laboratory, California Institute of Technology, under contract with the National Aeronautics and Space Administration (NASA). I acknowledge financial support from the University of Maryland's Department of As-

tronomy and the State of Maryland throughout my tenure in graduate school.

On a personal note, I conclude by publicly acknowledging and thanking those who have encouraged me in this pursuit. Sometimes the guidance or support was large in quantity and at other times it was small in quantity, but timely, and the person who gave it may not even realize just how meaningful their words or actions were to me. I thank my teachers, friends and family for their love and support.

Contents

List of Tables	xiv
List of Figures	xvi
1 Introduction	1
1.1 Galaxies in A Historical Perspective	4
1.1.1 Island Universes	4
1.1.2 Global Environmental Studies	8
1.1.3 Galaxy–galaxy Interactions	9
1.1.4 Radio Observations of Galaxies	12
1.2 Luminous & Ultraluminous Infrared Galaxies	17
1.3 Organization of Thesis	19
2 The Environment of Local Ultraluminous Infrared Galaxies	21
2.1 Abstract	21
2.2 Introduction	22
2.3 Sample	24
2.4 Analysis	28
2.4.1 Object Identification and Classification	29
2.4.2 Environment Richness Parameter	30
2.5 Results	33
2.6 Comparison with AGN Samples	41
2.6.1 Local Seyferts	41
2.6.2 Local QSOs	45
2.6.3 Intermediate-Redshift QSOs	49
2.7 Conclusions	51
3 Interstellar Medium Properties of IR Galaxies	53
3.1 Abstract	53
3.2 Introduction	54
3.3 The Sample	57
3.4 Observations and Data Reduction	64

3.5	Results	66
3.6	Analysis and Discussion	71
3.6.1	H I Emission	72
3.6.2	H I Absorption	84
3.7	Notes on Individual Objects	87
3.8	Conclusions	91
3.8.1	Summary of Results	91
3.8.2	Future Work	91
4	Sub-Arcsecond Molecular Gas Imaging and Phase Correction	94
4.1	Abstract	94
4.2	Introduction	95
4.2.1	The Problem	95
4.2.2	Description of Paired Antenna Phase Correction	99
4.3	Experiment Setup	101
4.4	Data Reduction	106
4.5	Results	108
4.5.1	Successful C-PACS Correction	109
4.5.2	Systematic Effects	111
4.5.3	Environmental Influences	116
4.6	Analysis	122
4.6.1	Interpolation	122
4.6.2	Time Scale for Phase Variations	124
4.6.3	Structure Function of the Atmosphere	126
4.7	Science Application - Arp 193	129
4.7.1	Motivation: IR Galaxies and Arp 193	130
4.7.2	Observations and Data Reduction	132
4.7.3	Results: Application of C-PACS	133
4.7.4	Results: Arp 193	135
4.8	Conclusions	146
5	Concluding Remarks	150
5.1	Summary	150
5.2	Future Work	152
A	Single-Dish Aperture Efficiency Measurements at CARMA	153
A.1	Abstract	153
A.2	Introduction	153
A.3	Single-Dish Aperture Efficiency Measurements: Theory	155
A.4	Planet Temperature Contributions	160
A.5	Measurements on Jupiter	163

A.6	Filled–Aperture Measurements on the Moon	167
A.7	Aperture Efficiency Memo Appendices	169
A.7.1	Telescope Calibration	169
A.7.2	Opacities from Weather Data	171
A.7.3	Sky Dips	172
A.7.4	Primary Beam Sizes	177
A.7.5	The ApertureEfficiencySD Script	179
B	Antenna Shadowing in E array	183
B.1	Abstract	183
B.2	Simulating E Array Data: Model Parameters	184
B.3	Shadowing Math	185
B.4	Flagged Visibilities	186
B.5	Results and Example Script	186
C	SDSS Follow up to Environmental Study of ULIRGs	195
C.1	Summary of Work	195
	Glossary	199
	Bibliography	199

List of Tables

2.1	Galaxies Properties	26
2.1	Galaxies Properties	27
2.1	Galaxies Properties	28
2.2	Comparisons with AGN and QSO Environmental Studies	39
2.2	Comparisons with AGN and QSO Environmental Studies	40
3.1	Sample Properties	59
3.1	Sample Properties	60
3.1	Sample Properties	61
3.1	Sample Properties	62
3.1	Sample Properties	63
3.2	Parameters of Galaxies with H I Emission	76
3.2	Parameters of Galaxies with H I Emission	77
3.2	Parameters of Galaxies with H I Emission	78
3.2	Parameters of Galaxies with H I Emission	79
3.2	Parameters of Galaxies with H I Emission	80
3.3	H I Mass for Different L_{IR} Ranges	81
3.4	Parameters of Galaxies with H I Absorption	85
3.5	Statistical Summary	86
4.1	Observed QSOs	105
4.1	Observed QSOs	106
4.2	Science Observations of Arp 193	132
4.3	Molecular Gas in Arp 193	145
A.1	Single-dish aperture efficiency measurements on Jupiter at 95 GHz	163
A.2	Single-dish aperture efficiency measurements at 1 mm	166
A.3	Single-dish Forward-scattering Efficiency Measurements on the Moon	168
A.4	Sky-dip Measurements of τ and T_{Rx}	175
A.5	Theoretical Primary Beam Sizes at 100 GHz	178
A.6	Measured Primary Beam Sizes at 100 GHz	178
B.1	Flagged Visibilities as a Function of Declination	188

B.1	Flagged Visibilities as a Function of Declination	189
B.1	Flagged Visibilities as a Function of Declination	190
B.1	Flagged Visibilities as a Function of Declination	191
B.1	Flagged Visibilities as a Function of Declination	192
B.2	E Array Configuration File	193

List of Figures

1.1	Spectral Energy Distribution of Arp 193	2
1.2	Hubble Space Telescope Image of Arp 193	3
1.3	Resolved Spiral Structure in M51	5
1.4	Hubble Tuning Fork Diagram for Galaxy Classification	7
1.5	Zwicky’s Sketch of Interacting Galaxies	10
1.6	Arecibo 305-m Radio Telescope	14
1.7	Combined Array for Research in Millimeter Astronomy	15
1.8	Atmospheric Transmission at CARMA	16
1.9	OH Megamaser Emission from Luminous Infrared Galaxy	18
1.10	Spectral Identification of U/LIRGs versus IR Luminosity	19
2.1	Environment Richness vs. IR Luminosity	35
2.2	Environment Richness vs. Redshift	37
2.3	Environment Richness vs. 25-to-60 μm flux ratio	38
2.4	Comparison with Environment of Seyfert Galaxies	42
2.5	Environment Richness Distributions for Different Samples	43
2.6	Pie-chart Diagrams Comparing Sample Distributions	44
2.7	Comparison with PG QSOs	47
2.8	Comparison with Radio-Quiet and Radio-Loud QSOs	48
2.9	Comparison with Different QSO Samples	50
3.1	Radio–FIR and Radio–IR Correlations	56
3.2	Spectra of H I 21 cm Emission Detections	67
3.3	Spurious Detections of Galaxies	71
3.4	Spectra of H I 21 cm Absorption Detections	71
3.5	q parameter vs. L_{FIR}	73
3.6	H I mass versus L_{FIR}	82
3.7	H I mass vs. $L_{1.4\text{GHz}}$	83
3.8	Optical image of IRAS 08507+3520	90
3.9	H I mass/ H_2 mass vs. f_{25}/f_{60}	92
4.1	Paired Antenna Phase Correction Geometry	100

4.2	2010 A & B Array Antenna Configuration	103
4.3	Example C-PACS Correction	108
4.4	Improvement in Coherence versus Angular Separation	112
4.5	Change in Coherence for Basic Parameters	114
4.6	Change in Coherence with Atmospheric Parameters	118
4.7	Opacity versus Atmospheric Delay	119
4.8	Interpolation for Non-Paired Antennas	125
4.9	Root Phase Structure Function	128
4.10	Improvement in Coherence for Phase Calibrator 1310+323	134
4.11	A Array Map of Arp 193	136
4.12	Arp 193 Integrated Intensity Map	137
4.13	Arp 193 Position Velocity Diagram	139
4.14	Arp 193 Rotation Curve	139
4.15	High Resolution CO Emission and H I Absorption Comparison	140
4.16	Arp 193 Position Velocity Diagram Comparison for CO and H I	141
4.17	Ratio of Molecular Gas Mass to Dynamical Mass	143
A.1	Single-dish Aperture Efficiency Measurements at 3 mm using Jupiter	164
A.2	Single-Dish Aperture Efficiency Measurements at 1 mm using Jupiter	165
A.3	Apparent Brightness Temperature of Center of Moon	166
A.4	Y-factor versus Air Mass	173
A.5	Comparison of Predictions and Measurements for τ_o from Sky Dips	176
B.1	CARMA Antenna Shadowing in E Array	194
C.1	Overlap of 1-Jy ULIRGs with SDSS Sky Coverage	196
C.2	Sample SDSS Results	197

Chapter 1

Introduction

In this thesis, we study a population of galaxies that have long enticed and puzzled astronomers. These galaxies are among the most extreme known in our universe and are identified by a single criterion: their prolific energy emission at infrared (IR) wavelengths (see Fig. 1.1). Luminous infrared galaxies (LIRGs), ultraluminous infrared galaxies (ULIRGs), and hyperluminous infrared galaxies (HLIRGs or HyLIRGs) are defined¹ to have IR luminosity (L_{IR}) greater than or equal to $10^{11} L_{\odot}$, $10^{12} L_{\odot}$, and $10^{13} L_{\odot}$ respectively. The IR energy is emitted from dust within the galaxy that has been heated by an energetic source, thought to be either an episode of prolific star formation (starburst) and/or the presence of an active galactic nucleus (AGN). Once thought to be oddities and relatively rare, these types of systems have been discovered to be increasingly common at earlier cosmological time. This fact, in combination with the observation that a large fraction of these IR luminous galaxies are not a single galaxy, but a system of interacting or merging galaxies

¹We will use these acronyms if referring to a specific population per these energy cutoff definitions. U/LIRGs means we are referring to either LIRGs or ULIRGs. More generally, we will use the term “luminous infrared” or “infrared luminous” interchangeably to refer to any galaxy with $L_{\text{IR}} > 10^{11} L_{\odot}$.

(see Fig. 1.2), means they are useful as laboratories to study galaxy evolution and properties of more distant cousins, for which we do not yet have the technological capabilities to study in detail.

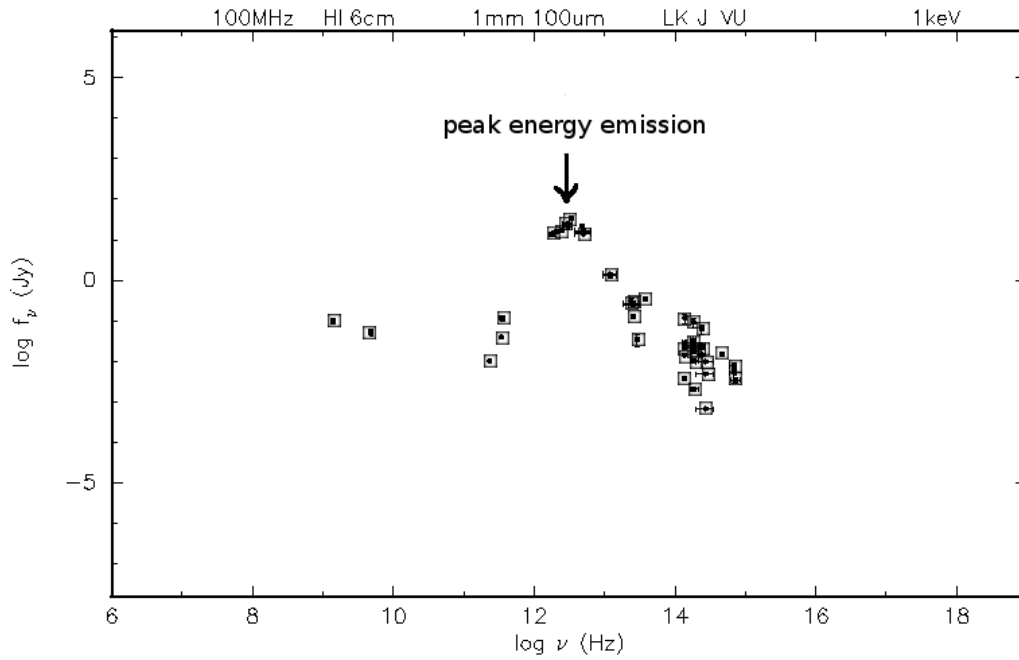


Figure 1.1: Spectral energy distribution for the LIRG Arp 193. This is a representative example of the spectrum for all luminous infrared galaxies, with a peak in energy emission at infrared wavelengths. Plot generated using the NASA/IPAC Extragalactic Database (NED).

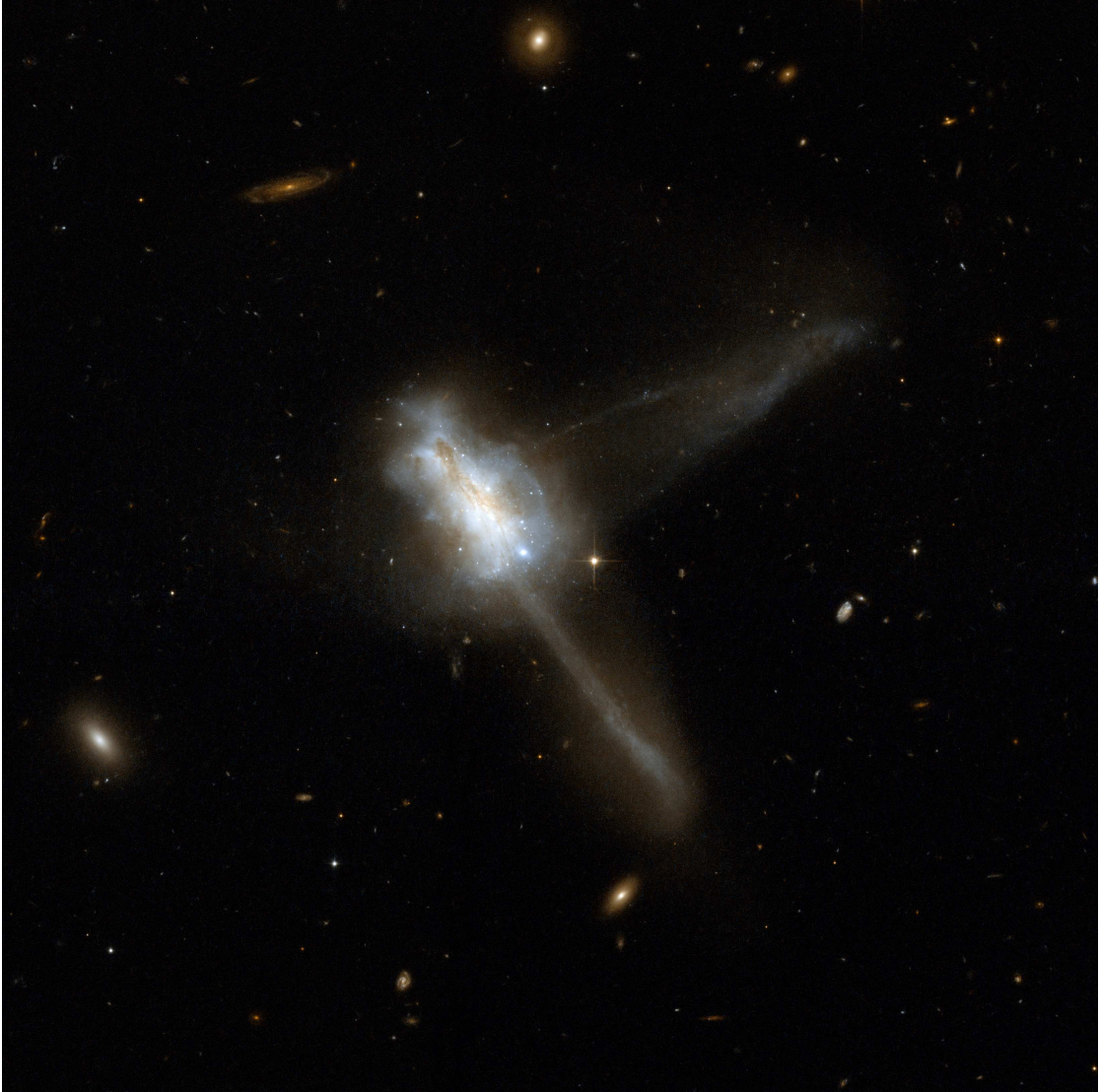


Figure 1.2: Optical image of Arp 193 with the Hubble Space Telescope. The two extended tidal tails are clear evidence of an interacting/merging system, especially typical of ULIRGs and HyLIRGs. Image Credit: NASA, ESA, the Hubble Heritage Team (STScI/AURA)-ESA/Hubble Collaboration and A. Evans (University of Virginia, Charlottesville/NRAO/Stony Brook University)

Here, we aim to put the work of this thesis in context, both with respect to the larger body of scientific knowledge and with respect to our topics of inquiry. In the remainder of the introduction, we present a brief summary of our understanding of galaxies in historical perspective, including their discovery as entities outside the Milky Way (§1.1.1), global environmental studies (§1.1.2), galaxy–galaxy interactions (§1.1.3), and the study of galaxies with radio telescopes (§1.1.4). A brief summary of what is known about luminous infrared galaxies is presented in §1.2. We conclude our introduction in §1.3 with an overview of the organization of this thesis.

1.1 Galaxies in A Historical Perspective

1.1.1 Island Universes

Since the suggestion by Immanuel Kant in the mid-18th century that nebulae might be “island universes,” there has been an explosion of knowledge about galaxies and numerous divisions in the classification of these fuzzy objects. Advancements in technology, the key to discovery, included methods of spectroscopy, engineering to build larger telescopes, and photography. When nebulae were first identified, only different from stars qualitatively in their fuzzy instead of point-like appearance, William Huggins pioneered studies to unambiguously quantify differences by comparing spectra. “Huggins found that while the stellar and resolvable nebulae gave spectra resembling the spectra of the fixed stars, the planetary and irresolvable nebulae gave spectra consisting of bright lines, thus showing that in these bodies we have masses of incandescent gas (Watts 1904).” Huggins was also the first to measure the velocity of stars using the Doppler effect, finding Sirius to be approaching and Arcturus to be receding from Earth. Upon building a new 72” telescope, Lord Rosse

was first able to spatially resolve a nebulae in 1845, making a famous drawing of the spiral structure in M51, the Whirlpool Galaxy, discovered almost three-quarters of a century before by Charles Messier (see Fig. 1.3). The late 19th century was

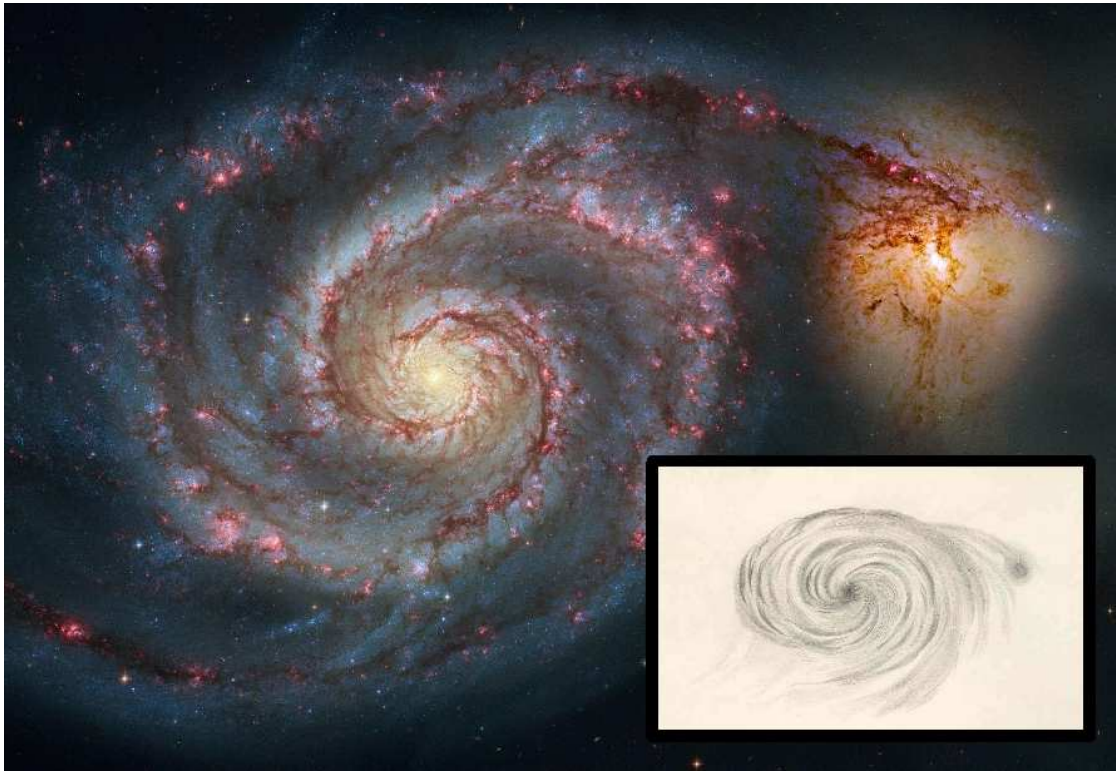


Figure 1.3: Comparison of a sketch of M51 by Lord Rosse (Herschel 1858) to an image by the Hubble Space Telescope (HST). This is the object where spiral structure was first resolved. Optical Image Credit: NASA, Hubble Heritage Team, (STScI/AURA), ESA, S. Beckwith (STScI) with additional processing by Robert Gendler.

a time of intense competition among observatories around the world to discover new objects. In an article about a new elaborate observatory being constructed in Vienna to house “Another Monster Refractor (Nature 1875)”, British astronomer, Warren De la Rue, is quoted addressing the Royal Astronomical Society, “Grand preparations are now being made at several Continental State-observatories to grapple with the important truths which can only be revealed by adequate instrumental appliances (Nature 1876).” The discovery of Arp 193 was made by Rudolf Spitaler

at this Vienna Observatory in 1891 with the 27” Grubb Refractor, the largest of its day. As we summarize in §1.3, the bulk of our research in Chapter 4 is related to pushing the modern-day instruments to understand the nature of Arp 193, a luminous infrared galaxy.

The Vienna Observatory was just one of the major observatories where much research was done in applying photography to astronomical research (see Spitaler 1887). As advances were made in photographic techniques, long exposures allowed astronomers to “see” fainter objects that are invisible to the naked eye. Furthermore, photographic plates recorded information on many objects simultaneously, leading to many large scale optical surveys. The first comprehensive catalogs² were published by Dreyer (1888, 1908). Edwin Hubble did extensive work classifying the varying types of galaxies (e.g. Hubble 1922, 1926), and found the vast majority could be identified and placed in a classification sequence, comprised of ellipticals and spirals in three sections: early, intermediate and late (see Fig. 1.4). It is now thought that galaxies evolve in precisely the opposite direction³, with spirals merging to eventually form the “early type” ellipticals. This is ironic considering Hubble’s warning, “The nomenclature, it is emphasized, refers to position in the sequence, and temporal connotations are made at one’s peril. The entire classification is purely empirical and without prejudice to theories of evolution... the classification was devised primarily for statistical studies (Hubble 1927).”

Another important contribution by Hubble was his observational work identifying Cepheid variable stars in spiral galaxies, whose period-luminosity relationship

²The New General Catalog (NGC) contained all types of extragalactic objects. The Index Catalogue (IC) supplemented the NGC and contained star clusters, nebulae and galaxies, exclusively.

³Very recent work by Wei et al. (2010) among others, has demonstrated that evolution of galaxies might occur in both directions.

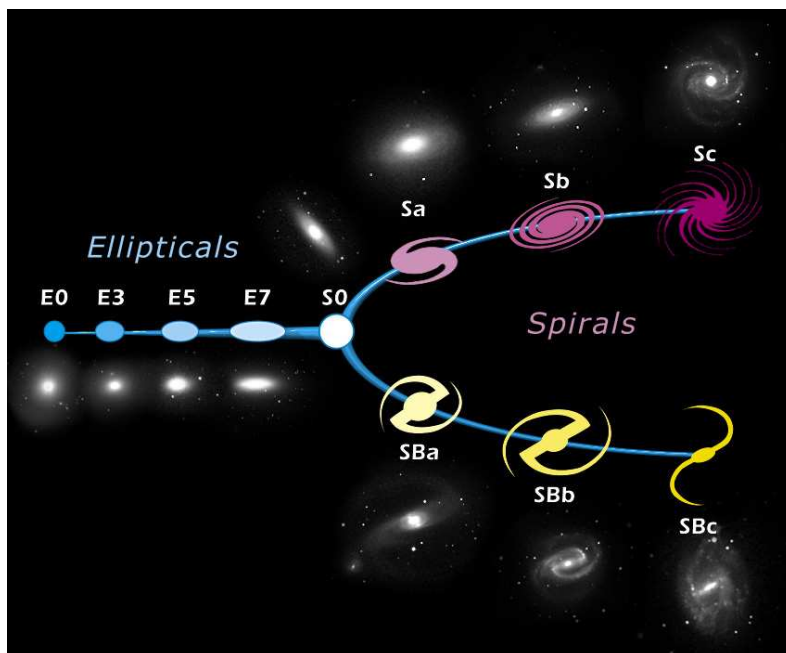


Figure 1.4: Figure of Edwin Hubble’s classification scheme for galaxies. Image Credit: European Southern Observatory (ESO).

(discovered by Henrietta Leavitt: Leavitt and Pickering 1912) makes them excellent standard candles for distance determination. Hubble was thus able to confirm that galaxies are indeed far away (and receding) from our own Milky Way, and are “island universes” unto themselves (Hubble 1936)⁴.

In addition to having allowed long exposures to study fainter objects than are visible with the naked eye, photographic plates recorded information on many objects simultaneously and images could then be compared with each other. It was found that the majority of galaxies are not isolated, but are found in pairs, groups or clusters. Hence, the application of photographic techniques to astronomy allowed

⁴Hubble’s discovery that the velocity of recession is proportional to the galaxy’s distance is now known as Hubble’s law and can be written as $v=H_0 \times D$, where v is the velocity of recession and D is the distance to the galaxy. The distance to a galaxy depends on the value assumed for Hubble’s constant (H_0), which is currently thought to be 73 ± 2 (random) ± 4 (systematic) $\text{km s}^{-1} \text{Mpc}^{-1}$ (see Freedman and Madore 2010, for an excellent review).

a new field to flourish: the study of large-scale structure and galactic environments.

1.1.2 Global Environmental Studies

Zwicky studied the distribution of clusters of galaxies in different regions of the sky beginning in 1938 and he continued for several decades (e.g. Zwicky 1938; Zwicky and Kowal 1968; Zwicky 1942). Scott, Shane and Swanson determined galaxy counts on photographic plates, and compared them with statistical information on synthetic plates to determine the extent to which galaxies can be found in clusters. They concluded that clusters of galaxies might be the fundamental building block of matter in the Universe (Scott et al. 1954). A few years later, the first systematic study of the richness of individual galactic clusters was conducted by Abell (1958). Abell found 1682 statistically significant rich clusters in the Palomar Sky Survey. He established a set of criteria to determine the “richness” of the cluster, i.e. there had to be at least 50 objects no more than two magnitudes fainter than the 3rd brightest object in the cluster, and the cluster had to be compact (members must be within 830 Mpc from the central object).

Analysis schemes were revised later to obtain more accurate and quantitative measurements of the Abell richness parameter (e.g. Bahcall 1981 and Abell et al. 1989). Longair and Seldner (1979) introduced the cluster-galaxy correlation function, B_{gc} , studying the clustering of galaxies about extragalactic radio sources (see §1.1.4 for a discussion of radio astronomy). The B_{gc} parameter offers a quantitative way to measure the richness of galactic clusters, converting a two-dimensional count of galaxies into a volumetric count.

There are a variety of problems with the past schemes used to measure the “richness” of a galaxy’s environment. Even with the quantitative method outlined by Longair and Seldner (1979), B_{gc} is still difficult to quantify because of inac-

curate estimates in photometry, poor star-galaxy classification in the image field, contamination from galaxies in the background, and uncertainties in redshift (hence, uncertainties in distance). Since a large area is required for counting galaxies, the likelihood for contamination is large. The calculated richness parameter is only useful if it is robust enough to apply to different cluster samples at different redshifts. In the past, many studies used a single luminosity function for galaxies. Yee and Green (1987) used a luminosity function that evolves with time in their study of quasar environments. For the global environmental study in Chapter 2, we use the same method of analysis that Howard Yee developed and that has been shown to be robust.

In addition to these global environmental studies of the richness of galactic clusters, intense study began on the peculiar galactic systems that were dubbed “irregulars” for their failure to conform to the standard types defined in the Hubble sequence. These irregular galaxies appeared to be comprised of two or more interacting galaxies, with intergalactic bridges and sweeping tidal tails. Interactions were thus proposed as the process by which galaxies evolve between Hubble types. These interactions are the topic of the next section.

1.1.3 Galaxy–galaxy Interactions

A discussion of the environment of galaxies is impossible without considering galaxy–galaxy interactions. Indeed, in his 1956 review, “Multiple Galaxies,” Zwicky begins with a discussion of some of the close groupings of extragalactic nebulae that have been known for a long time: Andromeda and its two companions (NGC 205 and NGC 221), and M51 (see noticeable companion in Fig. 1.3). A large number of double nebulae systems were observed with the 60” telescope at Mt. Wilson by F. G. Pease (published in papers in 1917 and 1920). Lundmark (e.g. 1920, 1926, 1928)

and Holmberg (1937) did a substantial amount of work identifying over 1000 double and multiple systems of galaxies between them. However, as Zwicky remarks, the study of double systems and multiple galaxies was “severely neglected for a long time (1956).” Zwicky made the study of interacting systems a primary focus of much of his research, exploring the effect that gravity would have on the individual stars within a galaxy during a close encounter with another galaxy (see Fig. 1.5).

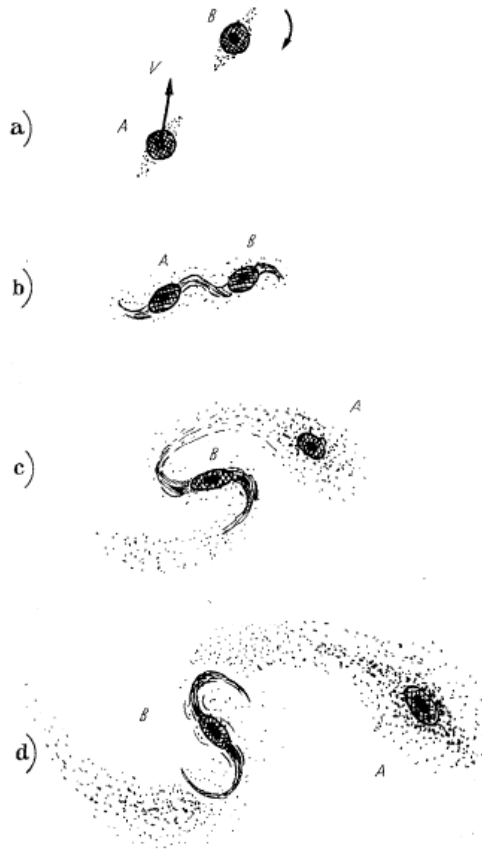


Figure 1.5: Sketch of possible interaction between galaxies resulting in an intergalactic “bridge,” as published by Zwicky (1956, Figure 7). These sketches look like snapshots of modern N-body simulations made of galactic interactions (e.g., Barnes and Hernquist 1992).

In the 1950s a Russian astronomer, Vorontsov-Velyaminov, took a special interest in those galaxies which were disturbed in nature and showed signs of interaction. His catalog of ~ 2000 objects was published in 1959. Halton Arp published his

“Atlas of Peculiar Galaxies” in 1966, drawing many objects for his sample from the work by Vorontsov-Velyaminov⁵. What is particularly useful and relevant about these catalogs is that, since their publication, a large number of luminous infrared galaxies have been found to be in merging/interacting systems.

Toomre & Toomre (1972) demonstrated that starbursts and nuclear activity can be triggered by interactions (see Barnes and Hernquist 1992; Toomre 1974, for good summaries of dynamical effects on galaxy interactions). An important gravitational effect in the merging process of galaxies is dynamical friction, “a systematic tendency to be decelerated in the direction of motion (Chandrasekhar 1943).” Theorized by Chandrasekhar, it took decades for numerical computing power to progress and N-body simulations to be proposed and performed (e.g. Ahmad and Cohen 1974; Ahmed 1979; Lecar 1975). First studied in the context of stellar orbits in a galaxy, the same physics affect a galaxy’s motion in a cluster or each individual star in a galaxy-galaxy merger. Smaller and less massive objects are gravitationally drawn to a more massive object passing nearby, which results in drag force, a loss of angular momentum and ultimately mass segregation and an inward spiralling behavior for the orbiting satellite. Furthermore, it is a process thought to aid in the transfer of angular momentum between a galactic bar and the galaxy halo (Weinberg 1985) and to be associated with the funneling of molecular gas to the central nuclear region. In recent years, more advanced simulations have confirmed the importance of major mergers to the triggering of starburst activity (e.g. Mihos and Hernquist 1994, 1996) and the funneling of molecular gas to the nuclear regions to fuel black holes (e.g. Barnes and Hernquist 1991; Hopkins and Quataert 2010).

At optical wavelengths, the nuclear region of luminous infrared galaxies is ob-

⁵Arp organized the objects in his catalog by similar properties. Arp 193 is simply the 193rd object in the catalog.

scured by dust extinction. However, the dust is transparent at radio wavelengths, allowing investigation of previously hidden physical processes inside the nuclear region of luminous infrared galaxies. We discuss the history and application of radio astronomy to the study of galaxies in the next section.

1.1.4 Radio Observations of Galaxies

A new window to study the Universe was serendipitously opened by Karl Jansky of Bell Laboratories in 1932 when he discovered a strange source of noise in his radio receiver (Jansky 1933) was non-terrestrial in origin. In this section, we explore how radio astronomy is useful in the study of galaxies.

Dust grains scatter and absorb photons at optical wavelengths ($\lambda \sim 400\text{-}800$ nm), but are too small to affect the much longer radio waves ($\lambda \sim 1$ mm – 1 km). Hence, astronomers can probe deeper into dust-enshrouded objects, seeing what was once hidden. Radio continuum emission from galaxies arises primarily from two processes: free-free emission (thermal bremsstrahlung) or synchrotron radiation from relativistic electrons spiraling around magnetic fields (Condon 1992). Both of these processes require very massive stars ($\sim 8 M_{\odot}$). As massive stars have shorter lives, radio continuum emission probes young stellar populations and recent star formation. See Condon (1992) for a review. Hence, for normal galaxies (without energy contribution from an AGN), radio continuum is a good proxy for star formation.

The first spectral line discovered at radio wavelengths was the 21 cm neutral hydrogen (H I) line (Ewen and Purcell 1951; Muller and Oort 1951). The discovery of this spectral line via its “spin-flip” transition was predicted by Dutch astronomer Van de Hulst (Verschuur and Kellermann 1988). Based on the quantum mechanical interpretation of electromagnetic radiation having both wave properties and being

quantized in “packets” of energy, Planck’s law gives

$$E_{excited} - E_{ground} = h\nu = hc/\lambda. \quad (1.1)$$

H I is in its ground state if the electron and proton have opposite spin ($F = 1/2 - 1/2 = 0$), and in an excited state if they have the same spin ($F = 1/2 + 1/2 = 1$). The transition from $F=1$ to $F=0$ results in energy emission at a wavelength of 21 cm (Dyson and Williams 1997). Spectral line emission gives specific information about the atom or molecule which it probes. For example, $\lambda=21$ cm emission gives information about the abundance, spatial location, and motion (via the Doppler effect) of H I.

Since radio wavelengths are very large relative to visible wavelengths, and the resolution of a telescope is proportional to λ/D , where D is the diameter of the telescope, radio telescopes must be much larger than optical telescopes to achieve comparable angular resolution. Ground-based optical telescopes are limited to a resolution of about 1” due to atmospheric turbulence, unless a sophisticated method like adaptive optics is employed to correct for scintillation real time. To achieve a resolution of 1” observing the H I line, one would need a telescope that is 43 km in diameter. It is structurally difficult (currently impossible) to build a single structure that large. The largest single-dish radio telescope in existence is the 305-m spherical reflector at the Arecibo Observatory located in Puerto Rico (see Fig. 1.6). Arecibo is built into a natural valley and is immobile, so it can only observe astronomical objects as they transit, in a limited declination range. The largest single-dish steerable radio telescope is the 100-m Green Bank Telescope located in West Virginia.

To achieve higher resolution, arrays of multiple radio telescopes are linked together. This technique, referred to as radio interferometry, gives the same angular resolution of a telescope with a diameter equivalent to the maximum separation



Figure 1.6: Aerial view of the Arecibo 305-m radio telescope in Arecibo, Puerto Rico. Its construction was a technical feat in its day (Kavanagh and Tung 1965). We use this telescope for spectroscopic observations of H I and other lines for 78 U/LIRGs, presented in Chapter 3. Image courtesy of the NAIC - Arecibo Observatory, a facility of the NSF.

between individual antennas (see Fig. 1.7). The interference patterns measured by antennas on each baseline are Fourier transforms of the actual sky brightness (Taylor et al. 1999). Hence, performing an inverse Fourier transform allows correlated signals to be processed and the original emitting source to be recovered. The major developments in radio interferometry include the first astronomical observations with a two-element array in 1946, solar arrays to observe 21 cm emission of the solar disk in the 1950s, arrays of antennas which would track sources as they moved across the sky (instead of being fixed in a stationary position) in the 1960s, the use of Earth-rotation synthesis and spectral line capabilities in 1962, very long baseline interferometry (VLBI) in 1967, advanced image processing techniques in the mid 1970s, and since the 1980s, millimeter and submillimeter interferometry, and space-based VLBI (Thompson et al. 2001). Radiation at different wavelengths

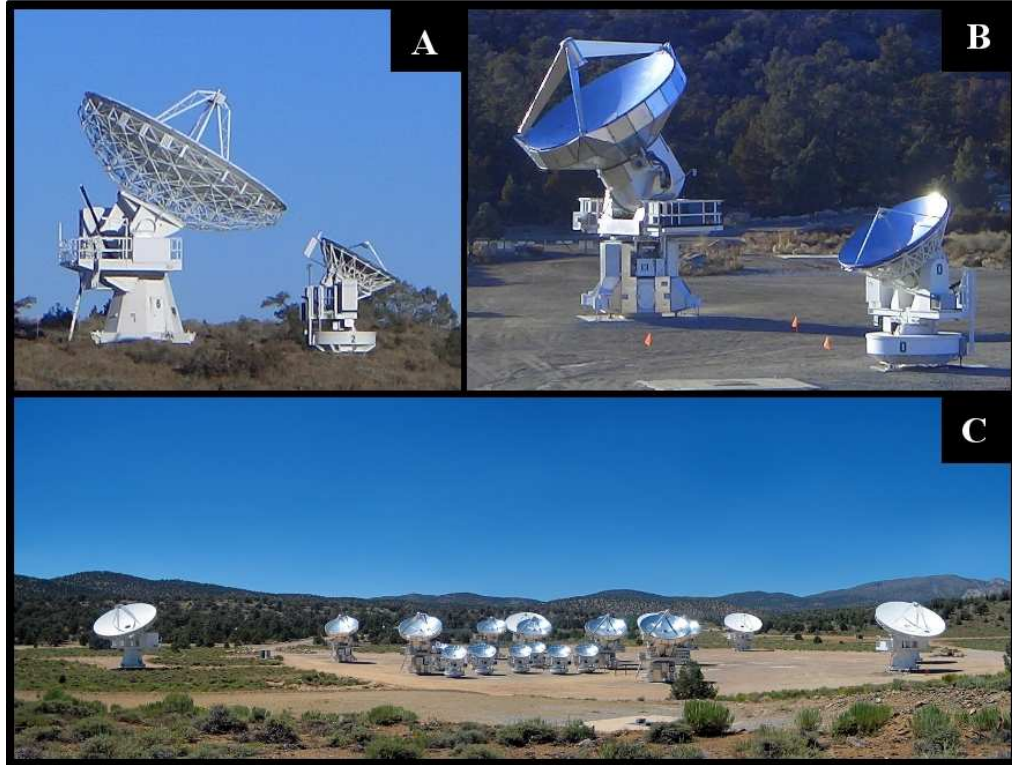


Figure 1.7: Three views of antennas in the Combined Array for Research in Millimeter Astronomy (CARMA). The top two photos (A & B) show the setup for the paired antenna calibration method for phase correction that we discuss in Chapter 4. A 3.5-m telescope is paired with a 10.4-m and 6.1-m, respectively. The bottom photo shows all 23 antennas in the CARMA array. Correlating the signal between every baseline pair allows the synthesis of an image as if one had a telescope with a diameter equal to the longest baseline. Top images taken by the author. Bottom image credit: www.mmarray.org

gives unique information, so it is only through a multi-wavelength approach that a full understanding of physical processes can be pieced together.

There are two points about the millimeter radio regime that make it very rich scientifically and pertinent to our research: some of the most abundant molecules have their fundamental lines in the millimeter domain and there are large windows of transparency in the atmosphere (see Fig. 1.8) making observations of these lines convenient. Molecular transitions in the 3 mm regime include SiO (86.847 GHz), HCN (88.632 GHz), HCO⁺ (89.189 GHz), ¹²CO(1-0) and isotopes C¹⁸O and ¹³CO

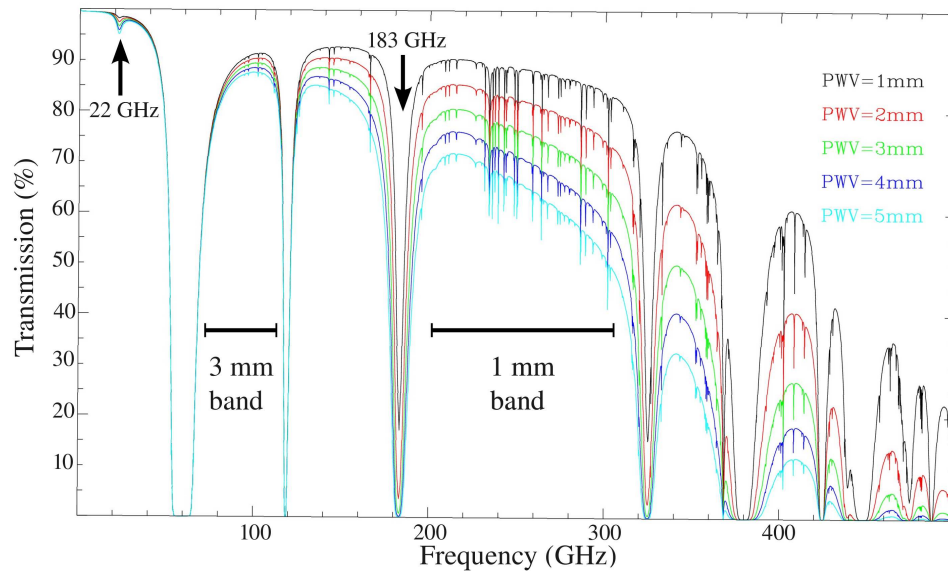


Figure 1.8: Atmospheric transmission at CARMA in the millimeter regime. The two primary millimeter observing bands are labeled. Atmospheric transmission decreases as the precipitable water vapor in the atmosphere increases, making it important for millimeter observatories to be located in high, dry locations. The 22 and 183 GHz atmospheric water emission lines are useful for atmospheric phase correction (see Chapter 4). These curves were determined based on the MOLIERE forward inversion atmospheric model by J. Urban and D. Lamarre (Urban et al. 2004) and was kindly provided by Nicola Schneider for the CARMA observing site at 2200 m in Cedar Flat, CA.

(at 115.271, 109.782 and 110.201 GHz, respectively), just to name a few. In the 1 mm regime, higher order transitions of these molecules can be observed, most notably $^{12}\text{CO}(2-1)$ at 225 GHz. These rotational transitions of CO are useful as tracers of molecular hydrogen (H_2) (Solomon and Barrett 1991). Molecular gas is the fuel for star formation and AGN, pertinent to this thesis because the dust in luminous infrared galaxies is heated by the energy from starbursts and/or AGN.

1.2 Luminous & Ultraluminous Infrared Galaxies

U/LIRGs were discovered in large number by the Infrared Astronomical Satellite (IRAS) in 1983. This spacecraft engaged in the first comprehensive, all-sky survey at IR wavelengths and discovered tens of thousands of IR bright galaxies. Prior to this, only a handful of IR bright objects were known (Neugebauer et al. 1971; Rieke and Lebofsky 1979). Sanders and Mirabel (1996) summarize important properties of luminous infrared galaxies:

- Most luminous infrared galaxies formed from strong interactions or mergers of gas-rich spirals. This can be inferred by observations of resolved double nuclei, disturbed morphologies (both visually and spectroscopically), and beautiful tidal tails extending far beyond the nuclear region in the manner predicted by galaxy merger simulations.
- Starbursts are the energy source for a large fraction of the infrared luminosity emission in these systems. Theoretical models have demonstrated that it is feasible to build up large quantities of molecular gas in the nuclear regions, and millimeter observations have measured as much as $10^{10} M_{\odot}$ in the central 0.5 kpc.
- 18 cm OH Megamasers occur in objects with the largest $L_{\text{FIR}}/M(\text{H}_2)$ ratio, and they originate in the nuclear regions of high-density molecular gas typical of U/LIRGs. See Fig. 1.9.
- Starbursts may lead to superwinds, enhancing metallicity of the intergalactic medium.
- Luminous infrared galaxies are likely a link between starburst galaxies and the energetic populations of quasars and radio-loud galaxies. Furthermore,

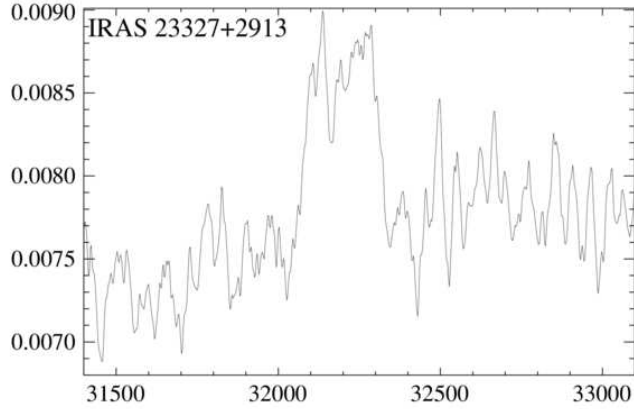


Figure 1.9: New OH 18 cm megamaser detection by Fernandez et al. (2010) in the ULIRG IRAS 23327+2913. Flux density (Jy) is plotted versus heliocentric velocity (km s^{-1}). The galaxies in Fernandez’s sample with OH emission have $L_{\text{IR}} \geq 10^{11.5} L_{\odot}$, while those with absorption are less IR luminous. Our survey of U/LIRGs in Chapter 3 is a continuation of this work.

they may be transition objects between merging gas-rich spirals and gas-poor ellipticals.

- The percentage of luminous infrared galaxies with evidence for an AGN increases with increasing IR luminosity (see Fig. 1.10).

Research in the last decade has led to the discovery that ULIRGs were more numerous at earlier cosmological times (higher redshift), increasing the importance of studying the few ULIRGs in the nearby Universe. Many large-scale surveys have been conducted at optical and radio wavelengths, allowing statistics of the population to be built up and compared with other types of galaxies (see review by Lonsdale et al. 2006). Large-scale galactic winds have been discovered to emanate from galaxies with starbursts and AGN, including many U/LIRGs, enriching the intergalactic medium with metals (Veilleux et al. 2005). This and other work will be discussed in more detail in the introductory sections of each chapter, as relevant to the investigation of that chapter. In the next section, we outline the organization of

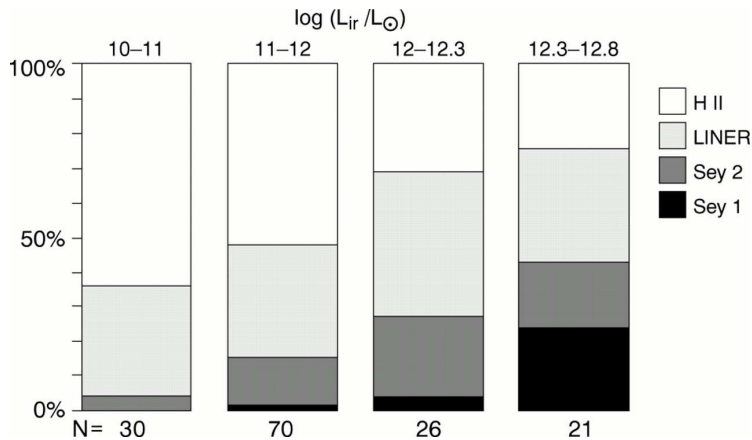


Figure 1.10: Spectral identification of luminous infrared galaxies versus L_{IR} . IR bright galaxies are dominated by starbursts (H II). LIRGs have a larger fraction of their population showing optical spectral signatures of LINERs or Seyfert 2 galaxies, but still are dominated by starbursts. In contrast, the majority of ULIRGs and HyLIRGs show optical signatures of an AGN (Veilleux et al. 1995).

this thesis and the specific outstanding questions about luminous infrared galaxies we address.

1.3 Organization of Thesis

We have undertaken distinct studies, presented in the following three chapters, in order to better understand (1) why luminous infrared galaxies exist and have such prolific IR emission, (2) what physical properties are different from and in common with other types of galaxies, and (3) how much variation exists within this population.

In Chapter 2, we examine the global environment of 76 ULIRGs using deep R-band optical images. We consider the spatial density of the “neighborhood” in which each ULIRG resides, whether it is similar to other populations of galaxies thought to be related to ULIRGs in an evolutionary sense (i.e. quasars), and whether any significant variations in environmental richness within the population can be

detected⁶. In Chapter 3, we consider the local environment of 78 U/LIRGs, studying properties of the interstellar medium (ISM) from spectroscopic observations of H I, OH, HCN and HCO⁺. We compare properties of galaxies in our sample for which we detect H I in emission to those for which we detect H I in absorption. In Chapter 4, we narrow our focus to a study of the molecular gas content in the nuclear region of U/LIRGs. We initially set out to study five of the closest and brightest U/LIRGs (Arp 220, Arp 193, Mrk 273, Mrk 231 and II Zw 31) with the intention of imaging CO and several other dense molecular gas tracers (HCN, HNC, CS and HCO⁺) to probe different physical parameters. However, in order to use the CARMA interferometer (see Fig. 1.7) in its longest (1-2 km) baseline configurations, and obtain the highest resolution maps to-date, a method of atmospheric phase correction is necessary. Hence, we conducted an in-depth study of the newly implemented paired antenna calibration system (PACS) for phase correction, which we discuss at great length in Chapter 4. We only present science observations of the LIRG Arp 193 as it was the most suitable source for observations using the technically challenging PACS method. Each of these chapters can be read and understood independently from the others, as each chapter has been published or will be submitted for publication in the near future. We summarize our conclusions and outline future work in Chapter 5.

⁶We conducted a short followup investigation using the Sloan Digital Sky Survey, summarized in Appendix C.

Chapter 2

The Environment of Local Ultraluminous Infrared Galaxies

2.1 Abstract

The spatial cluster-galaxy correlation amplitude, B_{gc} , is computed for a set of 76 $z < 0.3$ ultraluminous infrared galaxies (ULIRGs) from the 1-Jy sample. The B_{gc} parameter is used to quantify the richness of the environment within 0.5 Mpc of each ULIRG. We find that the environment of local ULIRGs is similar to that of the field with the possible exceptions of a few objects with environmental densities typical of clusters with Abell richness classes 0 and 1. No obvious trends are seen with redshift, optical spectral type, infrared luminosity, or infrared color (f_{25}/f_{60}). We compare these results with those of local AGNs and QSOs at various redshifts. The 1-Jy ULIRGs show a broader range of environments than local Seyferts, which are exclusively found in the field. The distribution of ULIRG B_{gc} -values overlaps considerably with that of local QSOs, consistent with the scenario where some QSOs go through a ultraluminous infrared phase. However, a rigorous statistical analysis

of the data indicates that these two samples are not drawn from the same parent population. The B_{gc} distribution of QSOs shows a distinct tail at high B_{gc} -values which is not apparent among the ULIRGs. This difference is consistent with the fact that some of the QSOs used for this comparison have bigger and more luminous hosts than the 1-Jy ULIRGs.

2.2 Introduction

Ultraluminous Infrared Galaxies (ULIRGs) are defined as galaxies with $L_{\text{IR}} = L(8 - 1000 \mu\text{m}) \geq 10^{12} L_{\odot}$ (see reviews by Sanders & Mirabel 1996; Lonsdale, Farrah, & Smith 2006). This luminosity limit is roughly equivalent to the minimum bolometric luminosity of QSOs. At luminosities above $10^{12}L_{\odot}$, the space density of ULIRGs in the local universe is greater than that of optically selected quasars with similar bolometric luminosities by a factor of ~ 1.5 . Thus local ULIRGs represent the most common type of ultraluminous galaxy. Systematic optical and near-infrared imaging surveys have revealed that local ULIRGs are almost always undergoing major mergers (e.g., Surace & Sanders 1999; Surace, Sanders, & Evans 2001; Scoville et al. 2000; Veilleux et al. 2002, 2006). Most of the gas and star formation (and AGN) activity in these systems are concentrated well within the central kpc (e.g., Downes & Solomon 1998; Soifer et al. 2000, 2001). Ground-based optical and near-infrared spectroscopic studies of these objects have shown that at least 25% – 30% of them show genuine signs of AGN activity (e.g., Kim, Veilleux, & Sanders 1998; Veilleux, Kim, & Sanders 1997, 1999; Veilleux, Sanders, & Kim 1999). This fraction increases to $\sim 50\%$ among the objects with $\log[L_{\text{IR}}/L_{\odot}] \gtrsim 12.3$. These results are compatible with those from mid-infrared spectroscopic surveys (e.g., Genzel et al. 1998; Lutz et al. 1998; Lutz, Veilleux, & Genzel 1999; Rigopoulou et al. 1999; Tran

et al 2001).

ULIRGs are relevant to a wide range of astronomical issues, including the role played by galactic mergers in forming some or all elliptical galaxies (Genzel et al. 2001; Veilleux et al. 2002), the efficiency of transport of gas into the central regions of such mergers and the subsequent triggering of circumnuclear star formation (e.g., Mihos & Hernquist 1996; Barnes 2004), the resulting heating and metal enrichment of the IGM by galactic winds (e.g. Rupke, Veilleux, & Sanders 2002, 2005ab; Veilleux, Cecil, & Bland-Hawthorn 2005; Martin 2005), the potential growth and fueling of supermassive black holes and the possible origin of quasars (Sanders et al. 1988). The discovery of $z = 1 - 4$ submm sources with SCUBA (e.g., Smail et al. 1997; Hughes et al. 1998) suggests that ULIRGs are also relevant to the dominant source of radiant energy in the universe today. Indeed, integration of the light from the SCUBA population shows that it may account for most of the submm/far-infrared background, as a result of the strong cosmological evolution of these sources (e.g., Chapman et al. 2005). Thus, while the present-day ULIRGs provide a relatively small contribution to the total present background, their cousins at high z are fundamentally important in this regard.

If ULIRGs are the predecessors of QSOs, one would expect ULIRGs and QSOs to live in similar environments. Surprisingly little has been published on the environments of local ULIRGs, in stark contrast to the abundant literature on the small- and large-scale environments of AGNs and QSOs (e.g., Yee, Green, & Stockman 1986; Yee & Green 1987; Ellingson et al. 1991; Hill & Lilly 1991; de Robertis et al. 1998; McLure & Dunlop 2001; Wold et al. 2000, 2001; Barr et al. 2003; Miller et al. 2003; Kauffmann et al. 2004; Söchting et al. 2004; Wake et al. 2004; Croom et al. 2005; Waskett et al. 2005; Serber, Bahcall, & Richards 2006) and the growing literature on the environments of $z \gtrsim 1$ ULIRGs (e.g., Blain et al. 2004; Farrah et

al. 2004, 2006). To our knowledge, Tacconi et al. (2002) is the only published study that has attempted to quantify the environments of local ULIRGs. They correlated the positions of local ULIRGs with the catalogs of galaxy clusters and groups available in NED and found that none of them are located within a galaxy cluster. The lack of comprehensive imaging database at the time prevented them from carrying out a more quantitative clustering analysis of these objects.

The present paper remedies the situation by using the large imaging database of Veilleux et al. (2002) to quantify the environment of local ($\langle z \rangle \sim 0.15$) ULIRGs from the 1-Jy sample. We note that the spectroscopy portion of the Sloan Digital Sky Survey (SDSS) provides redshift information for only the bright tail of the galaxy luminosity function at $z \sim 0.15$, so a method that relies solely on the photometric measurements of the galaxies in the field surrounding the ULIRG must be used for the present analysis. The properties of the 1-Jy sample and imaging dataset are reviewed in §2.2. In §2.3, the procedure for deriving the environmental richness, B_{ge} , is outlined. Results for our sample are presented in §2.4. The findings of environmental studies for quasars and Seyferts are compared with our results in §2.5. Our conclusions are summarized in §2.6. We use $H_0 = 50 \text{ km s}^{-1} \text{ Mpc}^{-1}$, $\Omega_m = 1$, and $\Omega_\lambda = 0$ throughout this paper. These values were selected to match those of previous studies and facilitate comparisons; they have no effect on our conclusions.

2.3 Sample

The *IRAS* 1-Jy sample of 118 ULIRGs identified by Kim & Sanders (1998) is the starting point of our investigation. The 1-Jy ULIRGs were selected to have high galactic latitude ($|b| \geq 30^\circ$), 60- μm flux greater than 1 Jy, 60- μm flux greater than

their 12- μm flux (to exclude infrared-bright stars), and ratios of 60- μm flux to 100- μm flux above $10^{-0.3}$ (to favor the detection of high-luminosity objects).

All 1-Jy ULIRGs were imaged at optical (R) and near-infrared (K') wavelengths using the U. of Hawaii 2.2-meter telescope. The present study uses only the R-band images since they have a larger field of view (FOV) and are deeper than the K'-band images. The R filter at 6400 Å was a Kron-Cousins filter. Details of the observations and data reduction can be found in Kim, Veilleux, & Sanders (2002). The analysis of these data is presented in Veilleux et al. (2002). These data are part of comprehensive imaging and spectroscopic surveys which also include a large set of optical and near-infrared spectra of the nuclear sources (Veilleux et al. 1999ab and references therein), a growing set of spatially-resolved near-infrared spectra to study the gas and stellar kinematics of the hosts (Genzel et al. 2001; Tacconi et al. 2002; Dasyra et al. 2006a, 2006b), and mid-infrared spectra from the Infrared Space Observatory (ISO) and the *Spitzer* Space Telescope (SST; e.g., Genzel et al. 1998; Veilleux et al. 2006b, in prep.). This effort is called *QUEST*: Quasar / ULIRG Evolutionary Study.

Since the set of data presented in Kim et al. (2002) was compiled from observations made over the course of 14 years, a variety of CCDs were used and therefore the FOV sizes and spatial resolutions are not uniform. For consistency, we limit the set of data in this paper to the images of the 76 objects taken under good photometric conditions with the TEK 2048 \times 2048 CCD. Of these images, 32 (42%) were irrecoverably cropped during an earlier stage of data reduction and have a significantly reduced FOV size. The effects of the cropping on the results of our analysis are discussed in §2.4. Table 2.1 lists the objects in our sample along with the FOV size and several other properties of the sources.

Table 2.1. Galaxies Properties

Name	l	b	z	$\log(\frac{L_{\text{IR}}}{L_{\odot}})$	ST	$\log(\frac{f_{25}}{f_{60}})$	B_{gc}	$1-\sigma$	Field
(1)	(2)	(3)	(4)	(5)	(6)	(7)	(8)	(9)	(10)
F00091-0738	95.6	-68.1	0.118	12.19	HII	-1.08	-80	97	1240
F00188-0856	100.5	-70.2	0.128	12.33	L	-0.85	-26	103	1330
F00397-1312	113.9	-75.6	0.261	12.90	HII	-0.74	25	137	2220
F00456-2904	326.4	-88.2	0.110	12.12	HII	-1.27	-34	94	1220
F00482-2721	49.4	-89.8	0.129	12.00	L	-0.80	45	111	1390
F01004-2237	152.1	-84.6	0.118	12.24	HII	-0.54	34	103	1290
F01166-0844	143.6	-70.2	0.118	12.03	HII	-1.01	70	109	1240
F01199-2307	183.3	-81.8	0.156	12.26	HII	-1.00	-26	112	1550
F01298-0744	151.1	-68.1	0.136	12.27	HII	-1.11	34	112	1390
F01355-1814	174.9	-75.9	0.192	12.39	HII	-1.07	-61	121	720
F01494-1845	184.3	-73.6	0.158	12.23	-	-0.93	-99	113	1620
F01569-2939	225.6	-74.9	0.141	12.15	HII	-1.09	-118	108	1430
F02411+0353	168.2	-48.6	0.144	12.19	-	-0.79	24	113	1450
F02480-3745	243.1	-63.0	0.165	12.23	-	-1.06	-70	114	1680
F03209-0806	192.0	-49.3	0.166	12.19	HII	-0.89	-71	115	1620
F03250+1606	168.7	-32.4	0.129	12.06	L	-0.96	-137	103	1330
Z03521+0028	188.4	-38.0	0.152	12.45	L	-1.10	-203	111	1520
F04074-2801	225.9	-46.4	0.153	12.14	L	-1.28	121	130	1520
F04103-2838	226.9	-45.9	0.118	12.15	L	-0.53	31	103	1240
F04313-1649	213.6	-37.8	0.268	12.55	-	-1.16	-17	135	2260
F05020-2941	231.5	-35.1	0.154	12.28	L	-1.29	301	153	1530
F05024-1941	220.1	-32.0	0.192	12.43	S2	-0.88	-25	121	1800
F05156-3024	233.2	-32.4	0.171	12.20	S2	-1.06	-3	116	1660
F08201+2801	195.3	+31.3	0.168	12.23	HII	-0.89	-173	123	650
F08474+1813	208.7	+34.1	0.145	12.13	-	-0.83	-36	181	580
F08591+5248	165.4	+41.0	0.158	12.14	-	-0.80	65	143	620
F09039+0503	225.0	+32.1	0.125	12.07	L	-1.09	-96	120	520
F09539+0857	228.5	+44.8	0.129	12.03	L	-0.98	-100	121	530
F10035+2740	202.7	+53.5	0.165	12.22	-	-0.83	414	198	650
F10091+4704	169.9	+53.2	0.246	12.67	L	-1.17	678	319	860
F10190+1322	227.2	+52.4	0.077	12.00	HII	-0.94	277	140	860
F10485-1447	264.6	+38.7	0.133	12.17	L	-0.84	-45	119	550
F10594+3818	180.5	+64.7	0.158	12.24	HII	-0.93	-11	125	620
F11028+3130	196.5	+66.6	0.199	12.32	L	-1.05	2	131	740
F11180+1623	235.9	+66.3	0.166	12.24	L	-0.80	119	156	650

Table 2.1 (cont'd)

Name	l	b	z	$\log(\frac{L_{\text{IR}}}{L_{\odot}})$	ST	$\log(\frac{f_{25}}{f_{60}})$	B_{gc}	$1-\sigma$	Field
(1)	(2)	(3)	(4)	(5)	(6)	(7)	(8)	(9)	(10)
F11223-1244	272.6	+44.7	0.199	12.59	S2	-0.98	35	136	740
F11387+4116	164.6	+70.0	0.149	12.18	HII	-0.86	180	160	600
Z11598-0112	278.6	+59.0	0.151	12.43	S1	-0.80	-21	111	1510
F12032+1707	254.8	+75.3	0.217	12.57	L	-0.74	-194	127	1970
F12127-1412	283.4	+62.0	0.133	12.10	L	-0.81	-121	117	550
F12265+0219	290.8	+62.4	0.159	12.73	S1	-0.36	-6	149	1570
F12359-0725	295.7	+63.4	0.138	12.11	L	-0.95	192	163	560
F12447+3721	127.9	+80.0	0.158	12.06	HII	-1.02	-103	122	620
F13106-0922	311.9	+52.9	0.174	12.32	L	-1.32	102	131	1680
F13218+0552	324.4	+67.1	0.205	12.63	S1	-0.47	92	148	760
F13305-1739	316.8	+43.8	0.148	12.21	S2	-0.47	-140	122	590
F13335-2612	315.3	+35.3	0.125	12.06	L	-1.00	-58	101	1300
F13342+3932	88.2	+74.6	0.179	12.37	S1	-0.61	140	159	690
F13443+0802	339.6	+66.6	0.135	12.15	S2	-1.13	-1	106	1380
F13454-2956	317.3	+31.1	0.129	12.21	S2	-1.49	118	122	1330
F13469+5833	109.1	+57.2	0.158	12.15	HII	-1.50	-134	128	620
F13509+0442	338.8	+62.9	0.136	12.27	HII	-0.83	162	159	560
F14053-1958	326.4	+39.1	0.161	12.12	S2	-0.86	-42	123	630
F14060+2919	44.0	+73.0	0.117	12.03	HII	-1.06	-84	115	490
F14121-0126	341.1	+54.9	0.151	12.23	L	-1.10	-85	122	600
F14197+0813	355.5	+61.2	0.131	12.00	-	-0.76	-139	104	1350
F14202+2615	35.1	+69.6	0.159	12.39	HII	-1.00	6	130	630
F14252-1550	334.3	+40.9	0.149	12.15	L	-0.70	80	144	600
F15043+5754	94.7	+51.4	0.151	12.05	HII	-1.16	251	179	600
F15206+3342	53.5	+56.9	0.125	12.18	HII	-0.70	45	123	660
F15225+2350	35.9	+55.3	0.139	12.10	HII	-0.86	-64	120	570
F15327+2340	36.6	+53.0	0.018	12.17	L	-1.12	-8	103	90
F17044+6720	98.0	+35.1	0.135	12.13	L	-0.55	-73	106	1440
F17068+4027	64.7	+36.1	0.179	12.30	HII	-1.04	1192	240	870
F17179+5444	82.5	+35.0	0.147	12.20	S2	-0.83	-161	110	1540
F21208-0519	47.3	-35.9	0.130	12.01	HII	-0.89	153	127	1340
F21477+0502	62.5	-35.6	0.171	12.24	L	-0.85	-76	116	1660
F22491-1808	45.2	-61.0	0.076	12.09	HII	-1.00	46	119	440
F22541+0833	81.2	-44.6	0.166	12.23	S2	-0.82	73	126	1620
F23060+0505	81.7	-49.1	0.173	12.44	S2	-0.43	-221	116	1670

Table 2.1 (cont'd)

Name	l	b	z	$\log(\frac{L_{\text{IR}}}{L_{\odot}})$	ST	$\log(\frac{f_{25}}{f_{60}})$	B_{gc}	$1-\sigma$	Field
(1)	(2)	(3)	(4)	(5)	(6)	(7)	(8)	(9)	(10)
F23129+2548	97.4	-32.0	0.179	12.38	L	-1.35	133	137	1710
F23233+2817	101.1	-30.6	0.114	12.00	S2	-0.65	-2	96	1250
F23234+0946	90.9	-47.4	0.128	12.05	L	-1.29	46	111	1330
F23327+2913	103.7	-30.5	0.107	12.06	L	-0.98	78	108	1150
F23389+0300	91.2	-55.2	0.145	12.09	S2	-0.55	167	134	1460
F23498+2423	106.3	-36.3	0.212	12.40	S2	-0.93	278	161	1930

Col (1): Name from the *IRAS* Faint Source Database. The prefix Z indicates the two objects not in the Faint Source Catalog.

Col. (2): Galactic longitude.

Col. (3): Galactic latitude.

Col. (4): Redshift from Kim & Sanders (1998).

Col. (5): Logarithm of the infrared (8–1000 μm) luminosity in units of solar luminosity computed using the flux in all four *IRAS* bands following the prescription of Kim & Sanders (1998).

Col. (6): Optical spectral type from Veilleux et al. (1999a).

Col. (7): *IRAS* 25-to-60 μm flux ratio.

Col. (8): Environment richness parameter computed using PPP program, as described in §2.3 of this paper, in $\text{Mpc}^{1.77}$.

Col. (9): One-sigma uncertainty on B_{gc} in $\text{Mpc}^{1.77}$.

Col. (10): Field size in kpc.

2.4 Analysis

In this section we explain the methods that we used to quantify the environment richness around each ULIRG. First, we describe the algorithms used to find objects in the field and identify them as stars or galaxies. Next, we discuss the formalism applied to calculate the environment richness parameter, B_{gc} . The techniques used for our analysis have already been described in detail in Yee (1991), Ellingson et al. (1991), Yee & Lopez-Cruz (1999), and Gladders & Yee (2005); here we highlight the main steps.

2.4.1 Object Identification and Classification

Object identification was accomplished using the Picture Processing Package (PPP) developed by Yee (1991). This program systematically examines each pixel in the image and determines whether it has the potential to be part of an object: a star, a galaxy, a cosmic ray, or an artifact of the CCD. After running through a series of tests, the PPP object finding program identifies and catalogs the location and peak brightness of objects in the image. The algorithms used here are modified versions of that used by Kron (1980), which depend on searching for local maxima. They have been shown to be robust for object identification in sparse to moderately crowded fields (Yee 1991). The 1-Jy sample selection criterion $|b| \geq 30^\circ$ avoids extremely crowded fields (and reduces the effects of dust extinction on the galaxy counts), which could lead to object misclassification and erroneous environment richness measurements. We therefore find that this object finding routine is perfectly adequate for all ULIRGs in our sample

To address the problem of bad pixels or cosmic rays, objects were thrown out automatically if a given pixel was five times brighter than those immediately surrounding it. This did not always work well because bright bad pixels are sometimes surrounded by other bad pixels. So, some misidentified objects were also identified by eye and removed by hand.

The next step was to run an aperture photometry algorithm on the identified objects in each image to determine whether these objects are stars or galaxies. For each object, a growth curve was calculated using a series of circular apertures centered on the intensity centroid of the object. A reference-star growth curve was created for each quadrant of the CCD frame by averaging the growth curves of bright, isolated, and unsaturated stars within each quadrant. The growth curves of

the other objects were then compared with the reference-star growth curve using the classification parameter C_2 defined by Yee (1991). In essence, C_2 computes the average difference per aperture between the growth curves of the objects and the growth curve of the reference star after they have been scaled to match at the center and effectively compares the ratio between the fluxes in the center and the outer part of an object with that of the reference star. This method has been thoroughly tested by Yee (1991); readers interested in knowing more about this classification scheme should refer to this paper for detail.

2.4.2 Environment Richness Parameter

We use the parameter B_{gc} to quantify the richness of the environment of ULIRGs. B_{gc} is the amplitude of the galaxy-galaxy correlation function calculated for each object of interest individually. It was first used by Longair & Seldner (1979) to measure the environment of radio galaxies using galaxy counts, and subsequently adopted in most studies of the environments of quasars and other active galaxies (e.g., Yee & Green 1984; Ellingson et al. 1991; de Robertis et al. 1998; McLure & Dunlop 2001; Wold et al. 2000, 2001; Barr et al. 2003; Waskett et al. 2005), and also used as a quantitative measurement of galaxy cluster richness (e.g., Andersen & Owen, 1994; Yee & López-Cruz 1999). Yee & Lopez-Cruz (1999) have demonstrated the robustness of the B_{gc} parameter when galaxies are counted to different radii and to different depth. Furthermore, measurements of the environmental richness based on the photometrically-derived B_{gc} -values have been shown to be entirely consistent with measurements based on spectroscopic data. This was demonstrated by Yee & Ellingson (2003), who used the data from the Canadian Network for Observational Cosmology Cluster Redshift Survey (CNOC1) to compare B_{gc} -values derived from (1) photometric data with background subtraction, and (2) from properly weighted

spectroscopy data to account for incompleteness. We describe briefly the procedure for deriving B_{gc} below.

In order to determine the richness of the environment around a ULIRG, we need to count the number of galaxies within a spherical volume with radius, r , from the ULIRG of interest. However, we necessarily must begin with a two-dimensional image, which is a projection of this volume onto the sky plane. The number of galaxies in a solid angle $d\Omega$, at an angular distance θ from the object of interest is given by (Seldner & Peebles 1978)

$$N(\theta)d\Omega = N_g[1 + w(\theta)]d\Omega, \quad (2.1)$$

where N_g is the average surface density of galaxies and $w(\theta)$, the angular correlation function, can be expressed approximately as a power law,

$$w(\theta) = A_{gc}\theta^{1-\gamma}. \quad (2.2)$$

A_{gc} is a measure of the average enhancement of galaxies in angular area, and $\gamma \approx 1.77$ empirically. Integrating equation (2.2) within a circle with radius θ yields

$$A_{gc} = \frac{N_{tot} - N_{bgc}}{N_{bgc}} \frac{(3 - \gamma)}{2} \theta^{\gamma-1}, \quad (2.3)$$

where N_{tot} and N_{bgc} are the the total numbers of galaxies and background galaxies, respectively, within an angular radius of θ .

Next, the two-dimensional parameters must be translated into three dimensions. The angular correlation function $w(\theta)$ is translated into the spatial correlation function, $\xi(r)$, which describes the number of galaxies in volume element dV at distance r from the object of interest. It can be shown that $\xi(r) = B_{gc}r^{-\gamma}$, where γ has the same value as in equation (2.3) and B_{gc} is the spatial correlation amplitude, a measure of the richness of the environment around the galaxy. Longair & Seldner (1979) have shown that

$$B_{gc} = \frac{A_{gc}n_{bg}(m)D^{\gamma-3}}{L_\gamma\Psi(m, z)}. \quad (2.4)$$

The constant I_γ is an integration constant which depends on γ (Groth & Peebles 1977). $n_{bg}(m)$ is the expected count per unit angular area of background galaxies brighter than apparent magnitude m , $\Psi(m, z)$ is the normalized integrated luminosity function of galaxies to apparent magnitude m , at redshift z of the cluster, and D is the angular diameter distance to the ULIRG at redshift z . For our calculations, we used $\gamma = 1.77$, $I_\gamma = 3.78$, and the cosmological parameters $H_0 = 50 \text{ km s}^{-1}\text{Mpc}^{-1}$, $\Omega_m = 1$, and $\Omega_\lambda = 0$ to match those of previous papers. For Ψ and $n_{bg}(m)$, we use the luminosity function and background counts derived from the Red-Sequence Cluster Survey (RCS; e.g., Gladders & Yee 2005).

The uncertainty on B_{gc} is computed using the formula

$$\frac{\Delta B_{gc}}{B_{gc}} = \frac{(N_{net} + 1.3^2 N_{bg})^{\frac{1}{2}}}{N_{net}} \quad (2.5)$$

where N_{net} is the net counts of galaxies over the background counts, N_{bg} . This is a conservatively large error estimate as it includes the expected counting statistics in N_{net} and the expected dispersion in background counts. The factor 1.3^2 is included to account approximately for the additional fluctuation from the clustered (and hence non-Poissonian) nature of the background counts (discussed in detail in Yee, Green, & Stockman 1986). We follow the prescription of Yee & López-Cruz (1999) and integrate the luminosity function from approximately $M_R = -25$ to $M_R^* + 2$ (where $M_R^* \approx -22.3$ for our cosmology) to calculate the galaxy counts. This corresponds roughly to $R = 15 - 20$ for the galaxies in our sample ($\langle z \rangle \approx 0.15$). This range of integration was found by Yee & López-Cruz (1999) to reduce the sensitivity to small intrinsic variation of M^* and variations in the faint-end slopes of the cluster luminosity function. The B_{gc} parameter is computed over a radius $r = 500 \text{ kpc}$, either directly from the data when $\text{FOV} \geq 1 \text{ Mpc}$ or extrapolated to this radius when $\text{FOV} < 1 \text{ Mpc}$. This radius is selected to match that of previous studies. The B_{gc} parameter is not sensitive to this radius (Yee & Lopez-Cruz 1999;

see also §2.4).

2.5 Results

The spatial correlation amplitude parameter, B_{gc} , was computed for each of the 76 ULIRGs in our sample. The B_{gc} -values and associated $1-\sigma$ uncertainties are listed for each object in Table 2.1. The average (median) value of B_{gc} and $1-\sigma$ scatter around the mean for our sample of 76 ULIRGs is $\langle B_{gc} \rangle = 35 \pm 198 \text{ Mpc}^{1.77}$ ($-3 \text{ Mpc}^{1.77}$). For comparison, the B_{gc} -values of field galaxies and clusters of Abell richness class (ARC) 0-4 are ~ 67.5 , 600 ± 200 , 1000 ± 200 , 1400 ± 200 , 1800 ± 200 , and $2200 \pm 200 \text{ Mpc}^{1.77}$, respectively (the field B_{gc} -value is from Davis & Peebles 1983; the values for ARC 0-4 are from Yee & López-Cruz 1999). The average clustering around the local ULIRGs therefore corresponds to an environment similar to the field. A large scatter is seen in our data: although most objects are consistent with no galaxy enhancement, a few objects apparently lie in clusters of Abell classes 0 and 1.

Before discussing the results any further, it is important to verify that our analysis of the cropped (FOV $< 1 \text{ Mpc}$) images does not introduce any bias when compared with the results from the uncropped (FOV $\geq 1 \text{ Mpc}$) images. The average (median) B_{gc} -value for the 44 objects with uncropped images is $4 \pm 121 \text{ Mpc}^{1.77}$ ($-5 \text{ Mpc}^{1.77}$); *i.e.* slightly smaller than the values found for the entire sample. Statistical tests give mixed results regarding the significance of this discrepancy (Table 2.2). The results from a two-sided K-S (Kolmogorow-Smirnov) test, a Wilcoxon matched-pairs signed-ranks test, and a Student's t-test on the means of the distributions suggest that the distribution of B_{gc} -values for the uncropped images is not significantly different from the distribution of B_{gc} -values as a whole, while the results

from a F-test on the standard deviations of the distributions suggest a significant difference.

We have examined the distributions of B_{gc} -values for cropped and uncropped images as a function of Galactic latitudes and longitudes. Assuming that the B_{gc} -values are unaffected by stellar contaminants from our Galaxy, there should be no trend with Galactic latitude or longitude. Indeed, the distributions of B_{gc} -values with latitude and longitude are consistent with being random. Our data therefore confirm the results of Yee & López-Cruz (1999), who found that changing the counting radius by a factor of two, both increasing to 1 Mpc and decreasing to 0.25 Mpc, did not alter the B_{gc} -values significantly. However, given the mixed results from the statistical tests, we track the cropped and uncropped data using different symbols in the various figures of this paper. We have verified that none of the results discussed below are affected if the counting radius is chosen to be 0.25 Mpc or 1 Mpc rather than 0.50 Mpc, although quantization errors becomes noticeable when the counting radius is 0.25 Mpc due to poorer number statistics. A counting radius of 0.5 Mpc is adopted in the rest of this paper to match that of previous studies.

Next, we explore the possibility of a dependence of the environment richness on ULIRG properties. The first parameter we examine is the infrared luminosity (Fig. 2.1). Statistical tests indicate that no trend is present between B_{gc} and L_{IR} . This is true for both the uncropped data and the entire sample. The same result is found when we examine the environment richness as a function of redshift (Fig. 2.2). Here, however, the redshift range covered by our ULIRGs is very narrow ($z = 0.1 - 0.22$, if we exclude four objects in the sample), so this statement is not statistically very significant. Comparisons with the results of Blain et al. (2004) and Farrah et al. (2004, 2006) suggest that the environment of high- z ULIRGs is richer than that of local ULIRGs. We return to this point in §2.5.

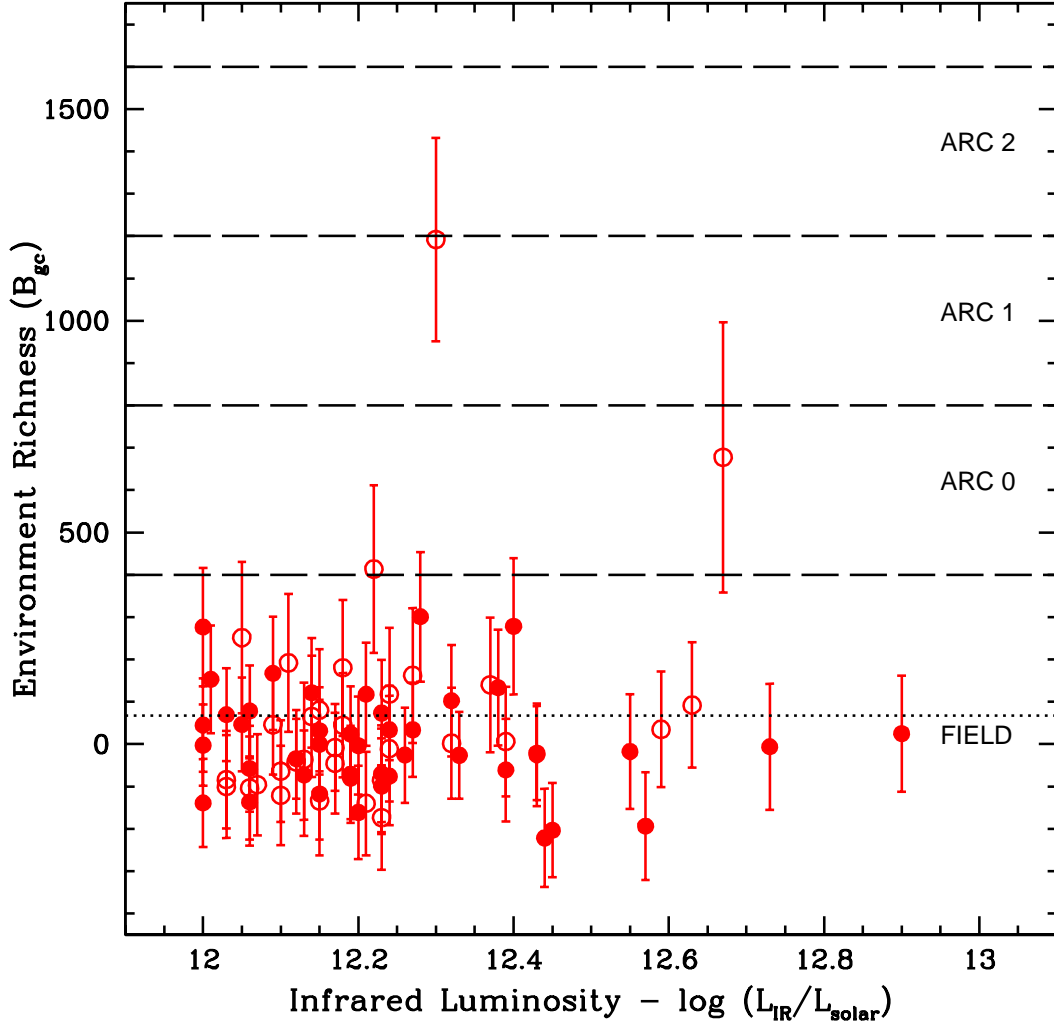


Figure 2.1: The environment richness parameter versus the infrared luminosity for local ULIRGs. Images which were cropped smaller than $1 \text{ Mpc} \times 1 \text{ Mpc}$ are noted by open circles, while the non-cropped images are shown as filled circles. The horizontal dashed line at $B_{gc} = 67.5 \text{ Mpc}^{1.77}$ indicates the average value for typical field galaxies. The range of environment richness parameters for the Abell richness classes are marked, following the definitions of Yee & López-Cruz (1999). No systematic trend is visible between environment richness and infrared luminosity.

In Figure 2.2, we also distinguish between optical spectral types. We separate our sample into Seyfert 1s, Seyfert 2s, LINERs, and HII region-like galaxies based on the optical classification of Veilleux et al. (1999a). No obvious trends are observed with spectral type, but the subdivision of our sample into four subsets necessarily leads to poorer statistics. In Figure 2.3, we plot B_{gc} as a function of $\log(f_{25}/f_{60})$, another clear indicator of AGN activity [objects with $\log(f_{25}/f_{60}) > -0.7$ have “warm”, AGN-like *IRAS* colors]. The lack of trends in this figure and Figure 2.2 indicates that the nature of the dominant energy source in local ULIRGs (starburst or AGN) is not influenced by the environment. This result is consistent with the ULIRG – QSO evolutionary scenario of Sanders et al. (1988), where the nature of the dominant energy source varies with merger phase (starburst in early phases and QSO in late phases) but is independent of the environment (as long as the dispersion in velocity of the galaxies within the cluster is not too large to prevent mergers altogether).

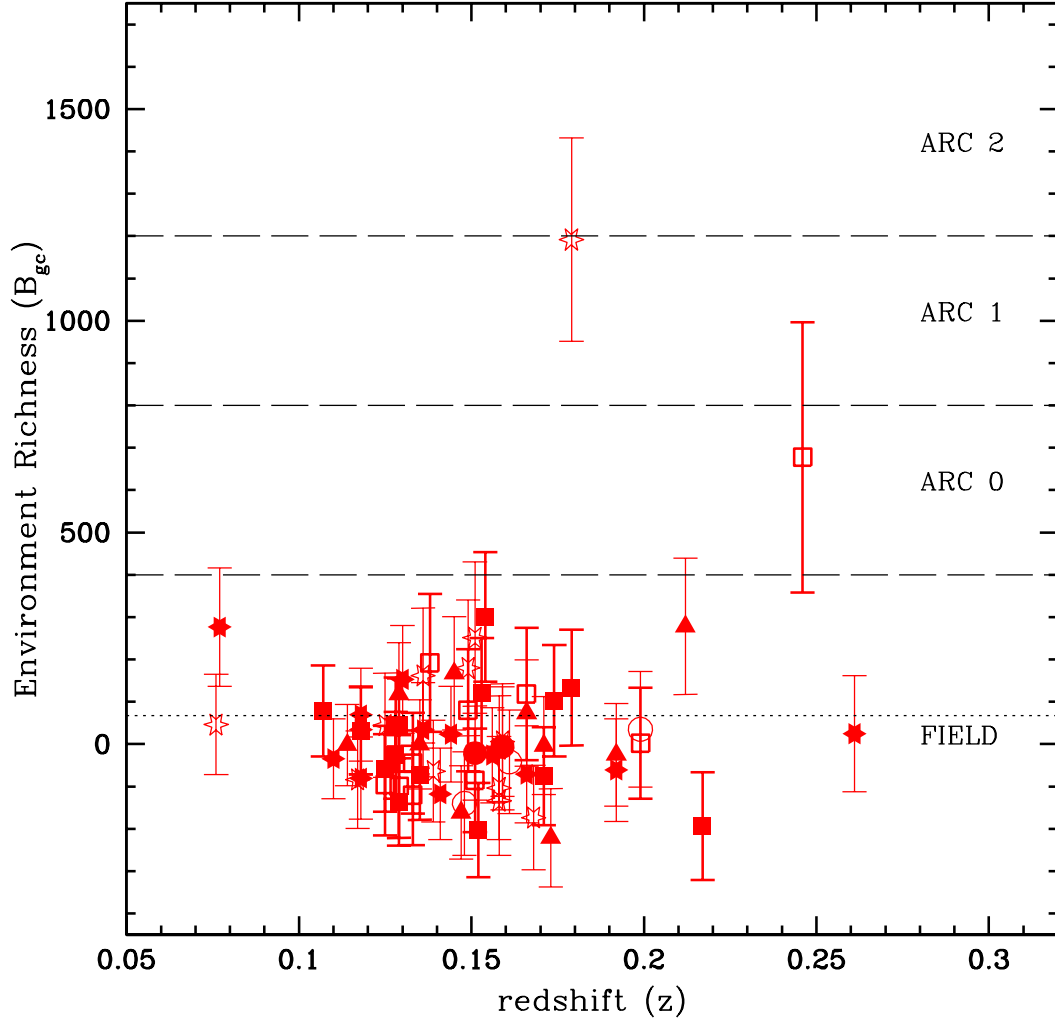


Figure 2.2: The environment richness parameter versus the redshift for local ULIRGs. The symbols reflect the optical spectral types of the ULIRGs, as listed in Veilleux et al. (1999a): circles are Seyfert 1 galaxies, triangles are Seyfert 2 galaxies, squares are LINERs, and stars are HII region-like galaxies. Open and filled symbols stand for cropped and uncropped images, respectively. The meaning of the horizontal lines is the same as that in Fig. 2.1. There are no statistically significant trends between environment richness and redshift or optical spectral type.

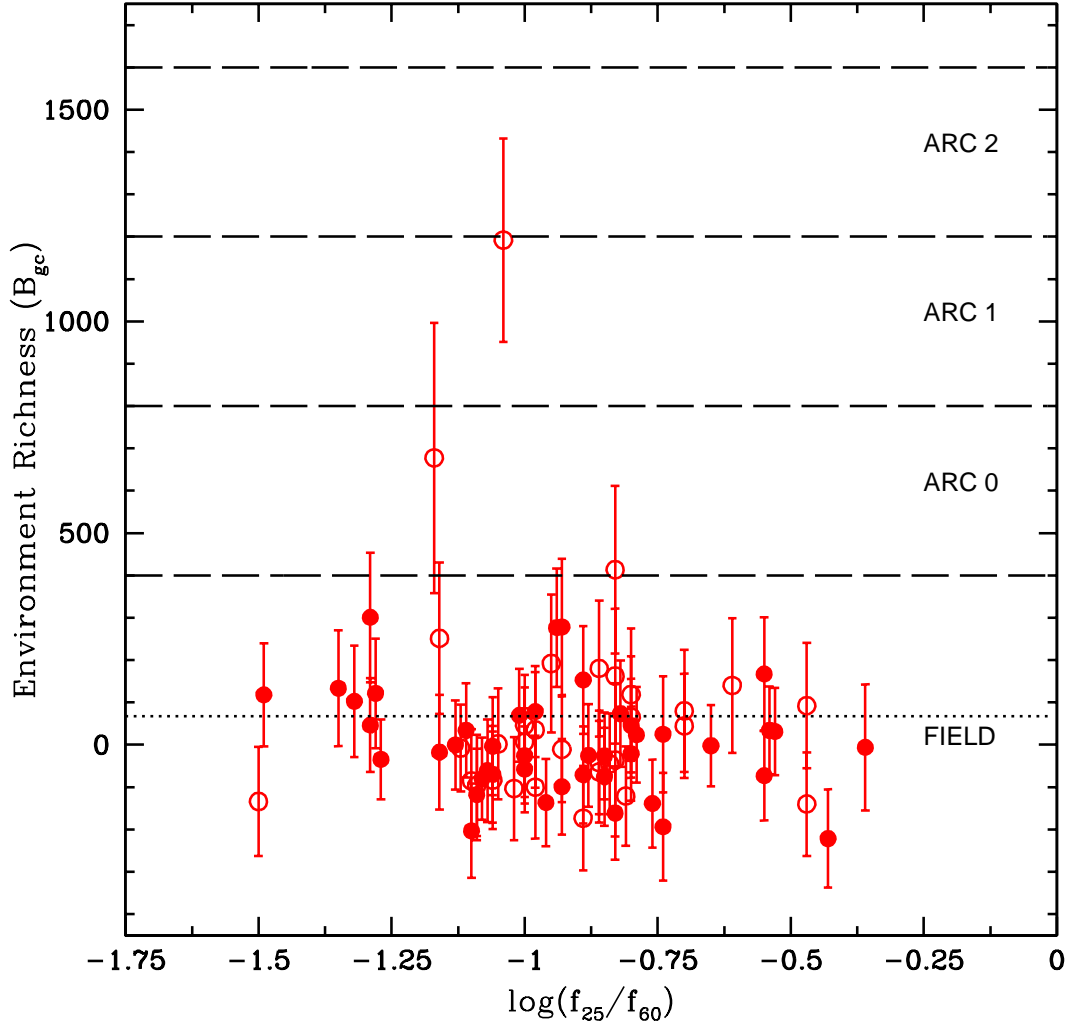


Figure 2.3: The environment richness parameter versus the logarithm of the *IRAS* 25-to-60 μm flux ratio, $\log(f_{25}/f_{60})$, for local ULIRGs. ULIRGs with $\log(f_{25}/f_{60}) > -0.7$ are “warm” AGN-like systems. The meaning of the horizontal lines and symbols is the same as that in Fig. 2.1. No systematic trend is visible between environment richness and the 25-to-60 μm flux ratio.

Table 2.2. Comparisons with AGN and QSO Environmental Studies

Sample Set (1)	N (2)	$\langle z \rangle$ (3)	$\langle B_{gc} \rangle$ (4)	Error (5)	Median (6)	KS-test		Wilcoxon		t-test		F-test	
						P_{large} (7)	P_{all} (8)	P_{large} (9)	P_{all} (10)	P_{large} (11)	P_{all} (12)	P_{large} (13)	P_{all} (14)
1 Jy ULIRGs (large FOV only) ^a	44	0.152	4±121	±18	-5	1.000	1.000	1.000	0.717	1.000	0.356	1.000	<0.001
1 Jy ULIRGs (all) ^b	76	0.151	35±198	±15	-3	1.000	1.000	0.717	1.000	0.356	1.000	<0.001	1.000
de Robertis et al. (1998)	27	0.022	40±64	±13	27	0.031	0.020	0.067	0.113	0.166	0.901	<0.001	<0.001
Yee & Green (1984), PG QSOs	34	0.155	157±208	±28	134	0.001	0.001	0.459	0.001	0.001	0.004	<0.001	0.024
McLure & Dunlop (2001), Entire Sample	44	0.194	365±409	±56	241	<0.001	<0.001	<0.001	<0.001	<0.001	<0.001	<0.001	0.001
McLure & Dunlop (2001), Radio-Quiet & Radio-Loud QSOs	34	0.192	304±355	±61	218	<0.001	<0.001	0.797	<0.001	<0.001	<0.001	<0.001	0.216
McLure & Dunlop (2001), Radio-Quiet QSOs	21	0.174	326±432	±79	209	<0.001	<0.001	0.006	0.007	<0.001	<0.001	<0.001	0.455
Ellingson et al. (1991)	63	0.435	121±341	±25	74	0.017	0.018	0.150	0.210	0.032	0.065	<0.001	<0.001
Wold et al. (2001), Model #1	20	0.676	336±343	±42	203	<0.001	<0.001	<0.001	<0.001	<0.001	<0.001	<0.001	0.512
Wold et al. (2001), Model #2	20	0.676	212±332	±43	146	0.001	0.001	0.011	0.019	0.001	0.003	<0.001	0.410
Wold et al. (2001), Model #3	20	0.676	210±365	±43	129	0.012	0.021	0.055	0.079	0.001	0.005	<0.001	0.740
Barr et al. (2003)	20	0.823	463±677	±143	347	<0.001	<0.001	0.001	0.002	<0.001	<0.001	<0.001	0.001

Table 2.2 (cont'd)

Sample Set	N	$\langle z \rangle$	$\langle B_{gc} \rangle$	Error	Median	KS-test		Wilcoxon		t-test		F-test	
						P_{large}	P_{all}	P_{large}	P_{all}	P_{large}	P_{all}	P_{large}	P_{all}
(1)	(2)	(3)	(4)	(5)	(6)	(7)	(8)	(9)	(10)	(11)	(12)	(13)	(14)

Col. (1): Sample set used for statistical comparison.

Col. (2): Number of objects in the sample.

Col. (3): Mean redshift of sample.

Col. (4): Mean B_{gc} -value and $1\text{-}\sigma$ scatter around the mean of sample in $\text{Mpc}^{1.77}$.

Col. (5): Root-mean square uncertainty on the mean of the B_{gc} -values in $\text{Mpc}^{1.77}$.

Col. (6): Median B_{gc} -value of sample in $\text{Mpc}^{1.77}$.

Cols. (7) and (8): Results from two-sided Kolmogorow-Smirnov test. Entries in col. (7) refer to comparison with the set of 44 ULIRGS that have an image size greater than $1 \text{ Mpc} \times 1 \text{ Mpc}$, while the entries in col. (8) refer to comparison with the entire set of 76 ULIRG images, regardless of field size.

Cols. (9) and (10): Results from Wilcoxon matched-pairs signed-ranks test. Entries in col. (9) refer to comparison with the set of 44 ULIRGS that have an image size greater than $1 \text{ Mpc} \times 1 \text{ Mpc}$, while the entries in col. (10) refer to comparison with the entire set of 76 ULIRG images, regardless of field size.

Cols. (11) and (12): Results from Student's t-test on the means of the distributions. Entries in col. (11) refer to comparison with the set of 44 ULIRGS that have an image size greater than $1 \text{ Mpc} \times 1 \text{ Mpc}$, while the entries in col. (12) refer to comparison with the entire set of 76 ULIRG images, regardless of field size.

Cols. (13) and (14): Results from F-test on the standard deviations of the distributions. Entries in col. (13) refer to comparison with the set of 44 ULIRGS that have an image size greater than $1 \text{ Mpc} \times 1 \text{ Mpc}$, while the entries in col. (14) refer to comparison with the entire set of 76 ULIRG images, regardless of field size.

^aThese entries refer to the 44 ULIRGS that have an image size greater than $1 \text{ Mpc} \times 1 \text{ Mpc}$.

^bThese entries refer to the entire set of 76 ULIRG images, regardless of field size.

2.6 Comparison with AGN Samples

In this section we compare our results with those from published environmental studies of AGNs and QSOs. Table 2.2 summarizes the statistical results of these comparisons and Figures 2.4 – 2.9 display the B_{gc} -values from the various samples. Unless otherwise noted in the text below, all data sets use the same cosmology.

2.6.1 Local Seyferts

First, we compare our results with those derived on nearby AGNs. De Robertis et al. (1998) studied the environments of nearby ($z < 0.05$) Seyfert galaxies using the exact same procedure as the one we use here, so we can directly compare their results with ours. For the 27 galaxies with $z > 0.0045$, de Robertis et al. (1998) find $\langle B_{gc} \rangle = 40 \pm 63 \text{ Mpc}^{1.77}$ (median of $27 \text{ Mpc}^{1.77}$), consistent with the environment of field galaxies. Recent studies based on the SDSS database confirm this result (e.g., Miller et al. 2003; Wake et al. 2004). The average environment of local ULIRGs is therefore not dissimilar to that of local Seyferts. However, as indicated in Table 2.2, virtually all statistical tests except perhaps the t-test on the means indicate that the two B_{gc} distributions are not drawn from the same parent population. Figures 2.4 and 2.5 show why that is the case: The distribution of B_{gc} -values among ULIRGs is distinctly broader than that of the Seyferts. This slight difference is also seen in Figure 2.6, where we display the distribution of local Seyferts and local ULIRGs as a function of Abell richness classes.

As discussed in §2.4, Seyfert-like ULIRGs do not reside in distinctly poorer or richer environments than non-Seyfert ULIRGs, so the broader scatter in ULIRG environments cannot be attributed to the broad range of AGN activity level within the ULIRG population. We note that typical error bars for the de Robertis et al.

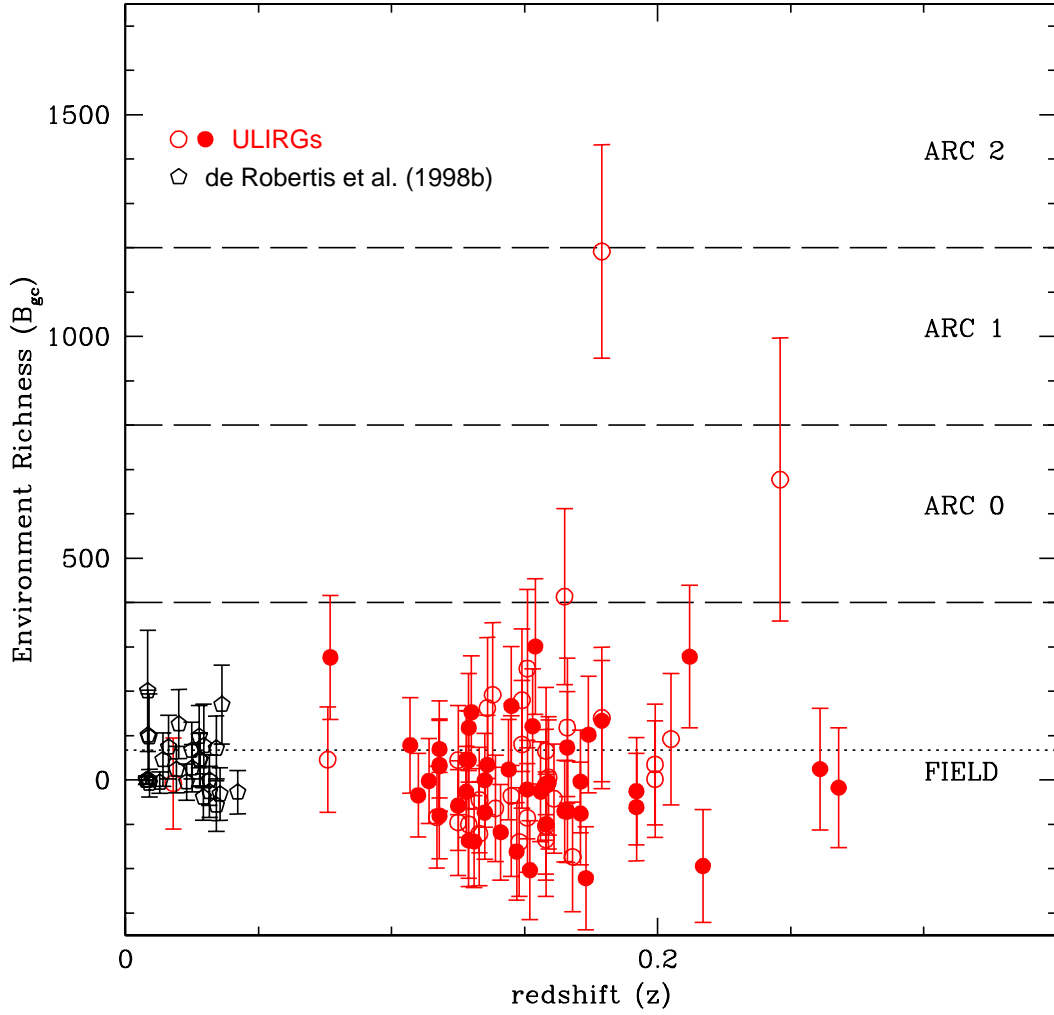


Figure 2.4: Comparison of the environment richness parameters for the local ULIRGs with those of $z < 0.05$ Seyfert galaxies from de Robertis et al. (1998). The meaning of the horizontal lines and filled and open circles is the same as that in Fig. 2.1. Pentagons are the data from de Robertis et al. The B_{gc} distribution of local ULIRGs is distinctly broader than that of nearby Seyferts.

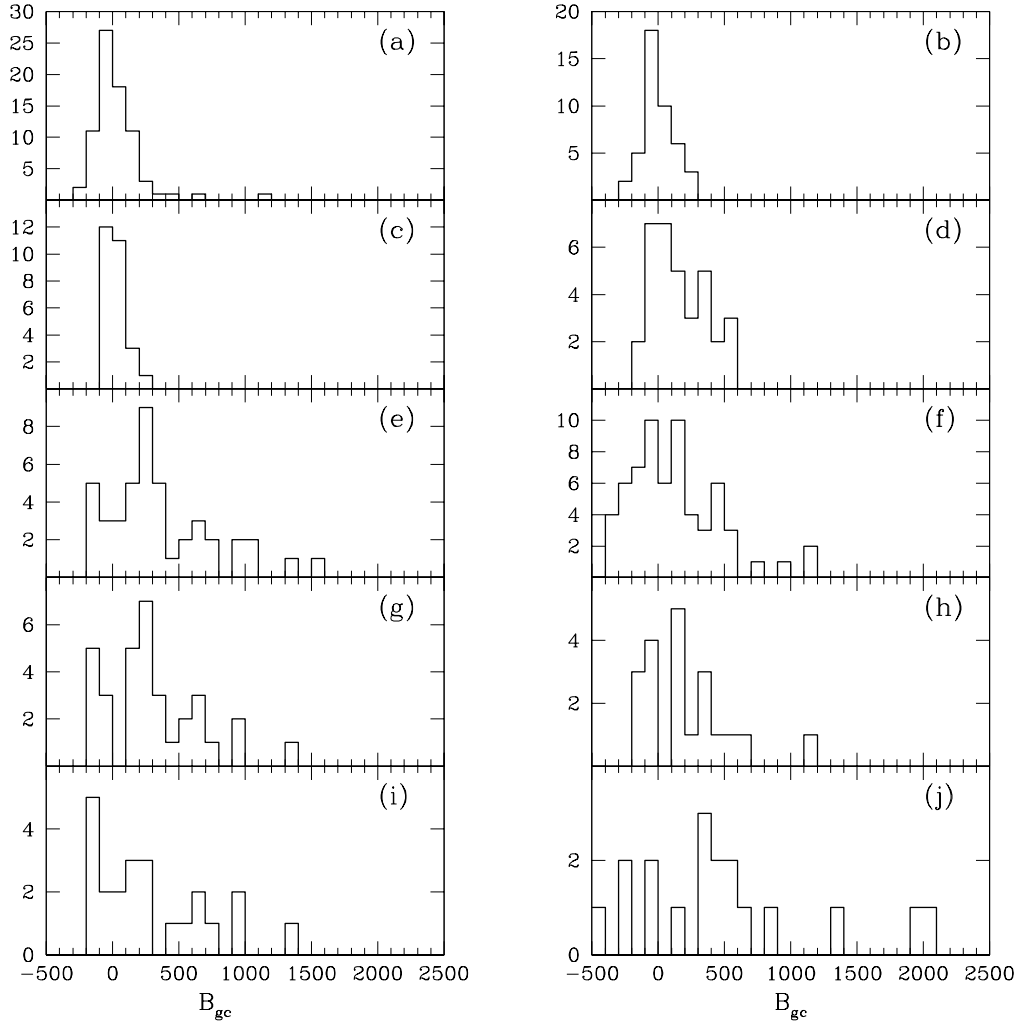


Figure 2.5: Histograms showing the distributions of environment richness parameters for: (a) local ULIRGs from this paper (entire sample); (b) local ULIRGs from this paper (uncropped data only); (c) $z < 0.05$ Seyfert galaxies from de Robertis et al. (1998); (d) $z \approx 0.2$ PG QSOs from Yee & Green (1984); (e) $z \approx 0.2$ QSOs and radio galaxies from Dunlop & McLure (2001); (f) $z \approx 0.2$ QSOs from Dunlop & McLure (2001); (g) $z \approx 0.2$ radio-quiet QSOs from Dunlop & McLure (2001); (h) $0.3 < z < 0.6$ radio-loud and radio-quiet QSOs from Ellingson et al. (1991); (i) $0.5 \leq z \leq 0.8$ radio-quiet QSOs from Wold et al. (2001; model #2 of the background galaxies); and (j) $0.6 < z < 1.1$ radio-loud QSOs from Barr et al. (2003). The results of statistical comparisons between these various data sets are listed in Table 2.2. None of these data sets appears to be drawn from the same parent population as the local ULIRGs, although considerable overlap in the values of the environmental richness parameters is seen between the various samples, particularly the local ULIRGs (this paper), local Seyferts (de Robertis et al. 1998) and PG QSOs (Yee & Green 1984).

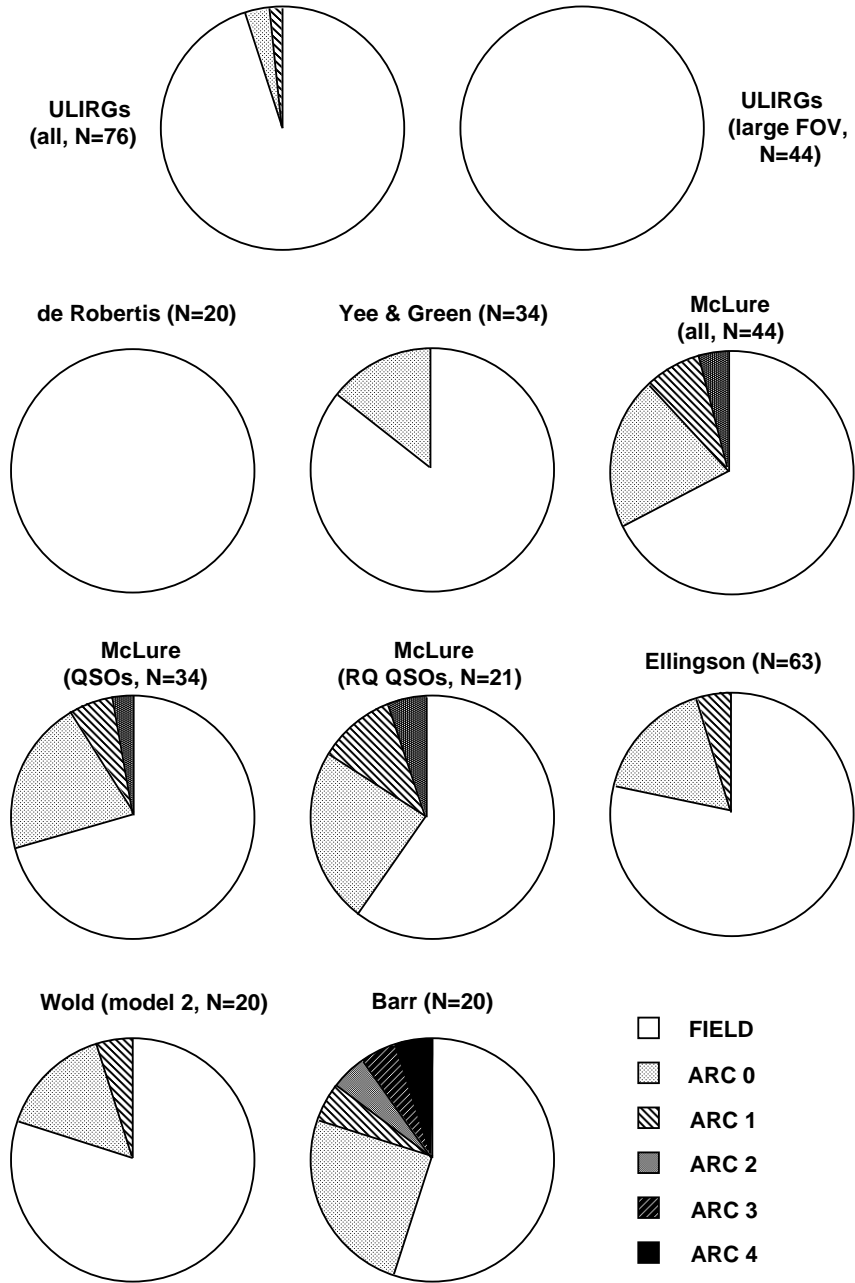


Figure 2.6: Pie-chart diagrams showing the distributions of environment richness parameters typical of field galaxies and clusters of Abell richness classes 0-4 for the eleven different samples considered in this paper. See caption to Fig. 2.5 for a description of these samples. The results of statistical comparisons between these various data sets are listed in Table 2.2. None of these data sets appears to be drawn from the same parent population as the local ULIRGs, although considerable overlap in the values of the environmental richness parameters is seen between the various samples, particularly the local ULIRGs (this paper), local Seyferts (de Robertis et al. 1998) and PG QSOs (Yee & Green 1984).

(1998) sample is $\sim 100 \text{ Mpc}^{1.77}$, while it is $\sim 150 \text{ Mpc}^{1.77}$ for the ULIRG sample. (The difference is due to the redshift difference between the samples – the ULIRG data requires counting to a fainter magnitude, which introduces larger uncertainties from background counts.) But the full ULIRG sample distribution is about 3 times broader than the Seyfert distribution – so, the broader distribution of the ULIRG sample cannot be fully explained by the larger error bars.

2.6.2 Local QSOs

Next, we compare our results with those derived on the nearby ($z \approx 0.2$) QSOs by Yee & Green (1984) and McLure & Dunlop (2001). The measurements of Yee & Green (1984) can be directly compared with our ULIRG results since their results were derived using the same method and parameters as that of the present study. McLure & Dunlop also apply the same formalism to calculate B_{gc} . However, they use a different analysis package to identify and classify the objects in the field and carry out the photometry. Their use of *HST* WFPC2 data also limits their survey area to only $\sim 200 \text{ kpc}$ around the QSOs, smaller than even our cropped data. These possible caveats should be kept in mind when comparing their results with ours.

Yee & Green (1984) get $\langle B_{gc} \rangle = 157 \pm 208$ and a median of $134 \text{ Mpc}^{1.77}$ for 34 QSOs from the Palomar-Green sample (Schmidt & Green 1983), while McLure & Dunlop (2001) derive an average (median) B_{gc} of $365 \pm 404 \text{ Mpc}^{1.77}$ ($241 \text{ Mpc}^{1.77}$) for a set of 44 radio-quiet and radio-loud QSOs and radio galaxies. If we limit our discussion to the QSOs in McLure & Dunlop sample (21 radio-quiet QSOs and 13 radio-loud QSOs), the average (median) B_{gc} becomes $304 \pm 350 \text{ Mpc}^{1.77}$ ($218 \text{ Mpc}^{1.77}$). The average environment of the QSOs in both studies is therefore slightly richer than that of local ULIRGs. The B_{gc} distributions of the two sets of local

QSOs (particularly that of the McLure & Dunlop sample; see Fig. 2.5) show a distinct tail at high B_{gc} -values which is not apparent in the ULIRG distribution.

A quantitative analysis generally confirms that the B_{gc} distributions of Yee & Green and B_{gc} distributions for the radio-quiet and radio-loud QSOs from McLure & Dunlop are statistically different from that of the local ULIRGs (Table 2.2). However, note that the Wilcoxon test suggests that the difference is barely significant. Indeed, Figures 2.5, 2.7, and 2.8 show that there is considerable overlap between the B_{gc} distributions of 1-Jy ULIRGs and low- z QSOs, particularly the PG QSOs. This result is consistent with the idea that some, but perhaps not all, of these QSOs may have formed through a IR-luminous phase like that observed at low redshift in the 1-Jy ULIRGs. A more physically meaningful test of this scenario would be to compare the environment of local QSOs with the environment of $z \gtrsim 0.5$ ULIRGs to take into account the finite duration of the ULIRG – QSO evolutionary sequence. The recent environmental studies of distant ULIRGs by Blain et al. (2004) and Farrah et al. (2004, 2006) indeed point to slightly richer environments, which more strongly resemble the environments of the QSOs from McLure & Dunlop.

A posteriori, the distinct high- B_{gc} tail in the distribution of the QSOs of McLure & Dunlop (2001) is not unexpected given the host properties of these particular QSOs: ~ 4 -5 times larger host sizes and luminosities relative to the 1-Jy ULIRGs (Dunlop et al. 2003; Veilleux et al. 2002, 2006). More luminous hosts live in richer environments on average than hosts of lower luminosity. As pointed out by Veilleux et al. (2006) and Dasyra et al. (2006c), the hosts of the QSOs from the Palomar-Green sample (these QSOs are less radio and X-ray luminous than the QSOs of McLure & Dunlop 2001) are a better match in host size and luminosity to the local ULIRGs. This may explain the generally better (although not perfect) agreement between the environments of PG QSOs and 1-Jy ULIRGs.

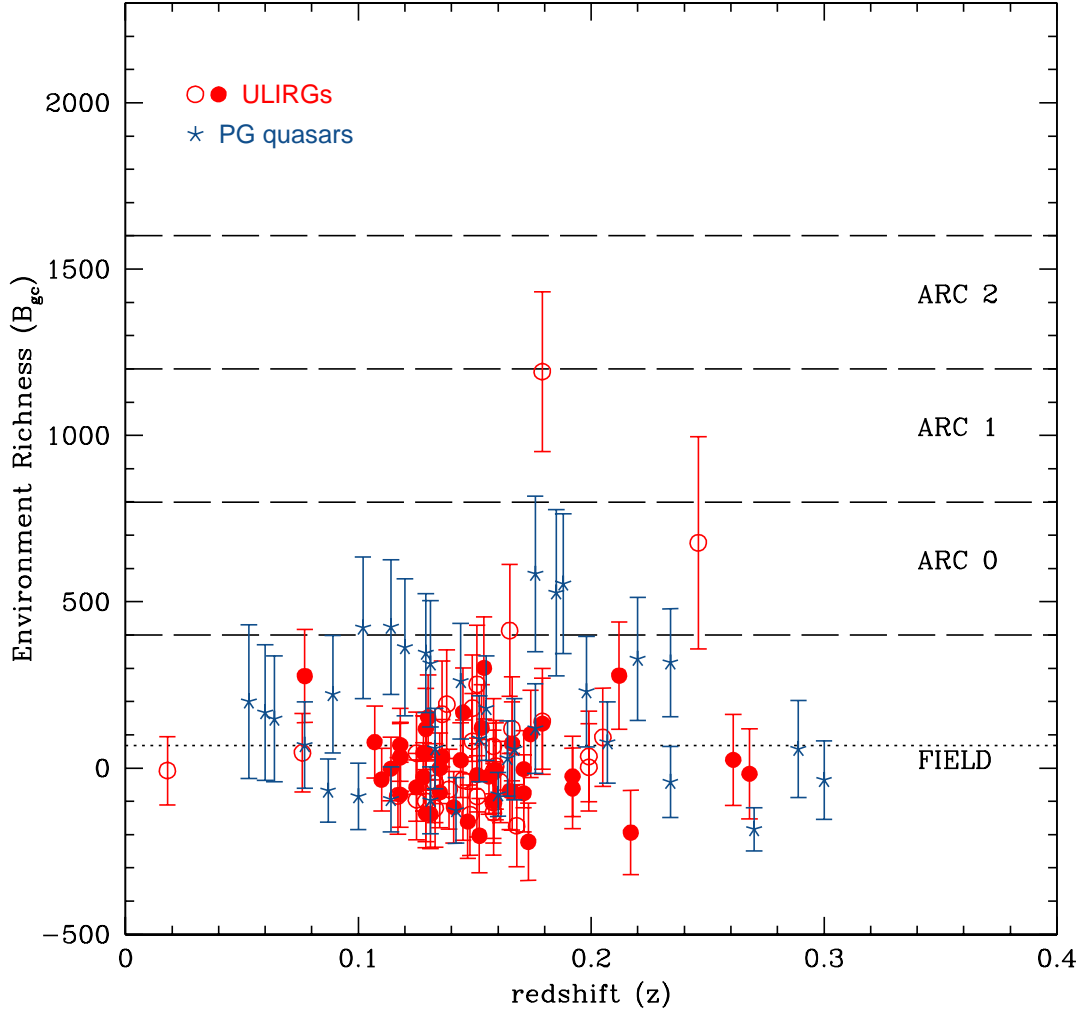


Figure 2.7: Comparison of the environment richness parameter for the local ULIRGs with the $z \approx 0.2$ PG QSOs of Yee & Green (1984). The meaning of the horizontal lines and open and filled circles is the same as that in Fig. 2.1. There is considerable overlap in the B_{gc} distributions of local ULIRGs and PG QSOs, although a statistical analysis between these two sets of objects generally indicates that they are not drawn from the same parent population.

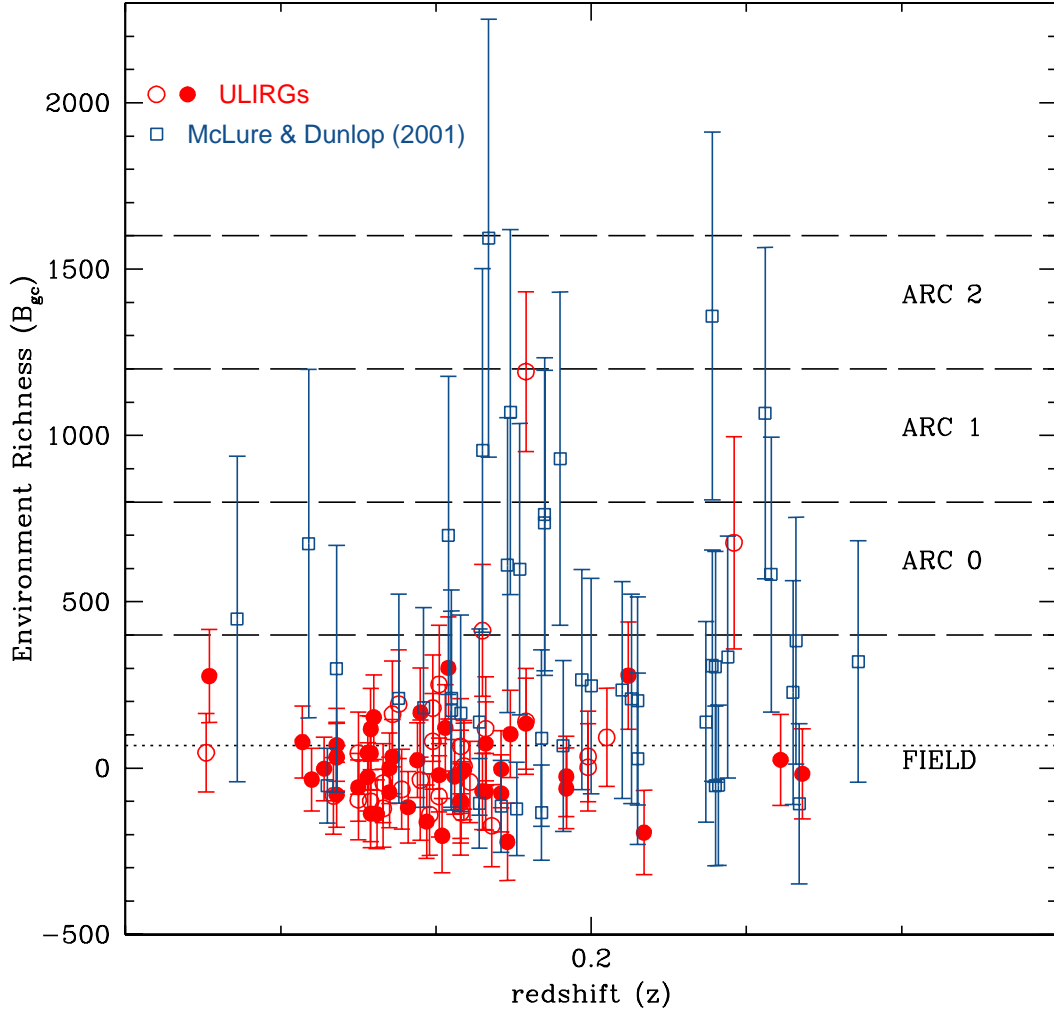


Figure 2.8: Comparison of the environment richness parameter for the local ULIRGs with the $z \approx 0.2$ radio-quiet and radio-loud QSOs of McLure & Dunlop (2001; the radio galaxies are not shown). The meaning of the horizontal lines and open and filled circles is the same as that in Fig. 2.1. The environment of these QSOs is distinctly richer on average to that of the local ULIRGs, as confirmed in general by a more rigorous statistical analysis.

2.6.3 Intermediate-Redshift QSOs

For the sake of completeness, we display in Figures 2.5, 2.6, and 2.9 the results from our study of local ULIRGs alongside the results presented by Ellingson et al. (1991), Wold et al. (2001), and Barr et al. (2003) for 63 radio-quiet and radio-loud QSOs at $0.3 < z < 0.6$, 20 radio-quiet QSOs at $0.5 \leq z \leq 0.8$, and 20 radio-loud QSOs at $0.6 < z < 1.1$, respectively. All three groups use the same basic method outlined in §2.3 to calculate the spatial correlation amplitude, and all groups assume the same value for H_0 . However, Ellingson et al. (1991) assume $q_0 = 0.02$ instead of 0.5 ($\Omega_m = 0.04$ instead of 1, if $\Omega_\lambda = 0$). There is no simple way to scale the B_{gc} -values for different cosmological models (other than H_0) since its computation is rather complicated (§2.3), so Figures 2.5, 2.6, and 2.9 show the B_{gc} -values corrected for the different H_0 but not the different Ω_m . Once again, we see considerable overlap between the various distributions, but the statistical analysis formally rules out that they come from the same parent population (Table 2.2). The amount of overlap in B_{gc} -values is quite remarkable given the difference in redshifts between the various samples. These results further support a connection between ULIRGs and some QSOs.

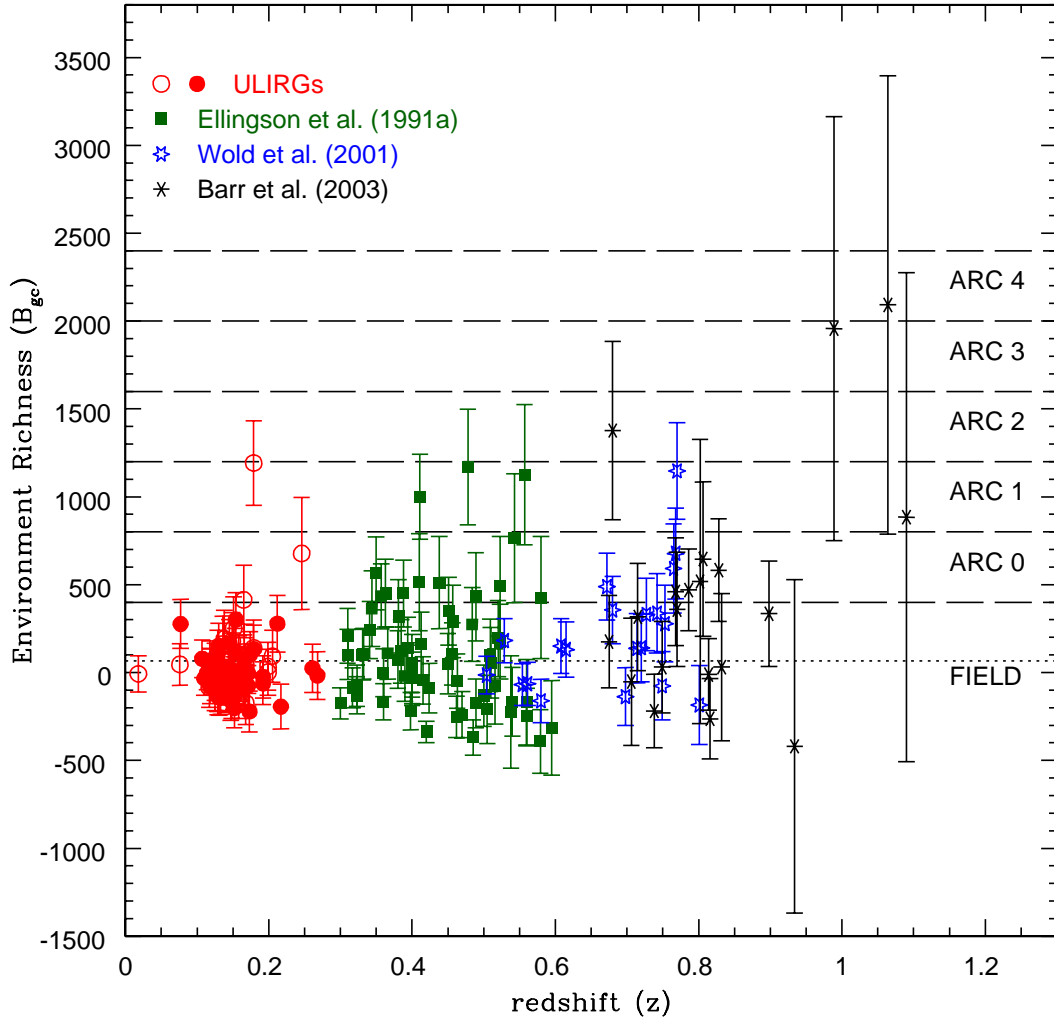


Figure 2.9: Comparison of the environment richness parameter for the local ULIRGs with the $0.3 < z < 0.6$ radio-loud and radio-quiet QSOs of Ellingson et al. (1991), the $0.5 \leq z \leq 0.8$ radio-quiet QSOs of Wold et al. (2001), and the $0.6 < z < 1.1$ radio-loud QSOs of Barr et al. (2003). The meaning of the horizontal lines and open and filled circles is the same as that in Fig. 2.1. The B_{gc} distributions of these QSOs overlap considerably with that of the local ULIRGs, despite the significant difference in redshifts.

2.7 Conclusions

We have derived the spatial cluster-galaxy correlation amplitude, B_{gc} , for 76 $z < 0.3$ ULIRGs from the 1-Jy sample and compared our results with those in the literature on $z < 0.05$ AGNs, $z \approx 0.2$ QSOs, and $0.3 \lesssim z \lesssim 1$ QSOs. The main results are as follows:

1. Local ULIRGs live in environments which are similar on average to that of field galaxies. However, there are a few exceptions: some objects apparently lie in clusters of Abell classes 0 and 1.

2. The infrared luminosity, optical spectral type, and *IRAS* 25-to-60 μm flux ratios of ULIRGs show no dependence with environment.

3. The ULIRG environment does not vary systematically over the redshift range covered by our sample (mostly $0.1 < z < 0.22$).

4. There is a lot of overlap between the B_{gc} distribution of local ULIRGs and those of local Seyferts, local QSOs, and intermediate- z QSOs. However, quantitative statistical comparisons show that the various B_{gc} distributions are not drawn from the same parent population. The average environment of ULIRGs appears to be intermediate between that of local Seyferts and local QSOs. Local ULIRGs show a broader range of environments than local Seyferts, which are exclusively found in the field. The B_{gc} distribution of QSOs show a distinct tail at high values which is not seen among local ULIRGs. This slight environmental discrepancy between local QSOs and ULIRGs is not unexpected: recent morphological studies have found that some of the more radio and X-ray luminous local QSOs used in this comparison have more luminous and massive hosts than local ULIRGs. A better match in host and environmental properties is seen when the comparison is made with the PG QSOs.

5. Overall, the results of this study suggest that ULIRGs can be a phase in the

lives of all types of AGNs and QSOs, but not all moderate-luminosity QSOs may have gone through a ULIRG phase. Published studies of the environments of more distant ULIRGs, perhaps the actual predecessors of the local QSOs we see today, provide further support for an evolutionary connection between ULIRGs and QSOs.

Chapter 3

Interstellar Medium Properties of IR Galaxies

3.1 Abstract

We present single dish radio spectral line observations of 77 infrared bright galaxies ($L_{\text{FIR}} > 10^9 L_{\odot}$). The data were obtained with the Arecibo 305 m telescope. Our sample is extracted from the 2 Jy IRAS-NVSS sample in the R.A. (B1950) range $02^{\text{h}}-10^{\text{h}}$. We simultaneously searched for the H I 21 cm, OH 18 cm main and satellite, ^{18}OH , HCN, and HCO^+ lines. We present our spectra for 61 H I 21 cm line detections, with 52 new detections. In seven of these galaxies, we detect H I in absorption. We made no detections of the other spectral lines. We derive H I mass for galaxies with H I emission from the line profiles and integrated flux density. For galaxies with absorption, we compute the optical depth and column density. We compare the population of galaxies with and without absorption, and present a statistical summary of our sample.

3.2 Introduction

Infrared (IR) bright galaxies emit the bulk of their bolometric luminosity at IR wavelengths. Tens of thousands of IR bright galaxies were detected by the Infrared Astronomical Satellite (IRAS). These galaxies contain large amounts of dust, heated by the absorption of higher energy photons emitted from massive stars in starbursting regions or produced by material accreting onto a central black hole (AGN) (see review articles by Lonsdale et al. 2006; Sanders and Mirabel 1996). Neither energetic process is possible without a substantial reservoir of gas. Studies of atomic (H I) and molecular gas in the interstellar medium (ISM) of IR galaxies provide important constraints on gas mass, density and temperature. Spectral line observations can also provide insight into the morphology, and in the case of isolated spirals, the H I 21 cm line can tightly constrain the rotation velocity and dynamical mass. Furthermore, ISM gas properties are germane to the study of IR galaxies as it has become increasingly clear that it is not the global environment (e.g. Zauderer et al. 2007), but the local, immediate environment and internal conditions triggered by interactions, that prime a galaxy to become a prolific energy producer.

Due to the high sensitivity from its large collecting area, the 305 m Arecibo Radio Telescope has been used for a large number of H I and spectral line studies of IR bright galaxies (e.g., Mirabel 1982, Heckman et al. 1983, Mirabel and Wilson 1984, Garwood, Helou and Dickey 1987). Other less sensitive telescopes have also been used, but as Bottinelli, Gouguenheim, and Paturel (1982) emphasize, a complete and homogeneous set of high-sensitivity data is important for statistical studies to survey global trends. Mirabel and Sanders (1988) conducted a survey of H I in 92 local ($z \leq 0.1$) luminous IR galaxies ($L_{\text{FIR}} > 2 \times 10^{10} L_{\odot}$) with the Arecibo Radio Telescope. A major result of their study was the detection of H I in absorption or emission in

88 of these sources, with an increasing probability of detecting H I in absorption with increasing far-infrared luminosity. They report the chance of detecting H I in absorption increases from $\sim 20\%$ for galaxies with $L_{\text{FIR}} > 2 \times 10^{10} L_{\odot}$ to $\sim 40\%$ for LIRGs and is ubiquitous for ULIRGs.

Yun et al. (2001) established a large sample of 1809 galaxies with IRAS 60 μm flux ≥ 2 Jy and with 1.4 GHz radio counterparts found in the NRAO VLA Sky Survey (hereafter, the 2-Jy IRAS-NVSS sample). Based on the results by Mirabel and Sanders (1988), Fernandez et al. (2010, hereafter, Part I) observed 85 IR galaxies with the Arecibo Radio Telescope in the right ascension range $20^{\text{h}}\text{--}00^{\text{h}}$ from the 2-Jy IRAS-NVSS sample. The H I 21 cm line was detected in emission or absorption in 82 of 85 galaxies, with 18 new detections. Furthermore, the OH 18 cm line was detected in seven galaxies, with four new detections. IRAS 23327+2913, the only bona fide ULIRG in the sample ($L_{\text{IR}} = 12.14 \pm 0.19 L_{\odot}$), had both H I and OH emission lines.

A very tight correlation between the 1.4 GHz radio continuum emission and IR luminosity exists for the NVSS sample (Condon 1992), known as the radio–FIR correlation. The star formation can hence be traced by either the IR emission from dust heated by stars, or synchrotron emission from relativistic particles accelerated in supernova events (Helou et al. 1985; Wunderlich and Klein 1988). In Part I, the correlation coefficient for this relation was 88% and 89% for radio–FIR and radio–IR, respectively. This relation is important to keep in mind as deviations (IR excess or radio excess) indicate probable significant AGN contribution. The correlation for our sample is shown in Figure 3.1.

Helou et al. (1985) gives an expression to quantify the slope of the radio-FIR correlation, known as the q parameter:

$$q = \log \frac{F_{\text{FIR}} / (3.75 \times 10^{12} \text{Hz})}{F_{1.4\text{GHz}}} \quad (3.1)$$

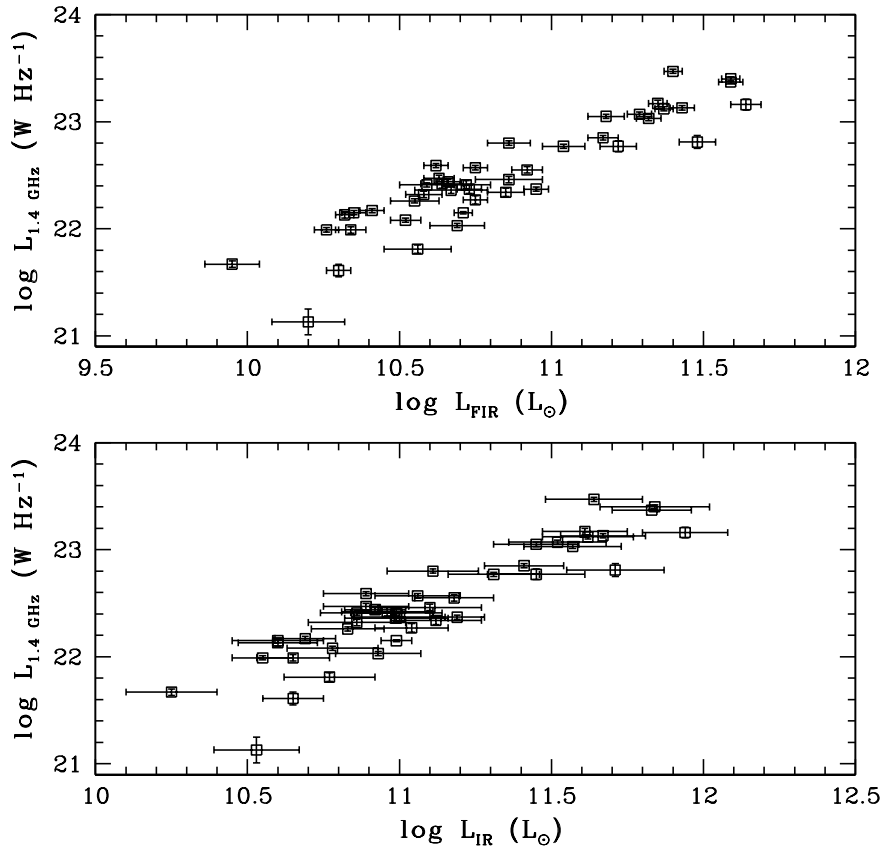


Figure 3.1: Radio–FIR (*top*) and radio–IR (*bottom*) correlation for the 77 galaxies in our observed sample. The computed correlation coefficient for each is $\sim 91\%$.

Here, F_{FIR} is the FIR flux [W m^{-2}] and $F_{1.4\text{GHz}}$ is the 1.4 GHz radio flux density [$\text{W m}^{-2} \text{Hz}^{-1}$] as published in the NVSS by Condon et al. (1998). Helou et al. (1985) lists correlation statistics for the radio–FIR for disk galaxies and starburst galaxies. They find a mean q of 2.21 for starburst galaxies and 2.14 for field galaxies. Within the errors (~ 0.15), these values are indistinguishable.

Based on the high rate of new detections, we continue the work presented in Part I with the goal of a complete H I and OH survey of IR galaxies from the 2-Jy IRAS-NVSS sample. Here, we report on the results for 77 IR galaxies in the R.A. (B1950) range $02^{\text{h}}\text{--}10^{\text{h}}$ (Part II). The final portion of the survey ($00^{\text{h}} < \text{R.A.} < 02^{\text{h}}$ and $10^{\text{h}} < \text{R.A.} < 20^{\text{h}}$) is currently underway, and will be reported in a third paper.

A statistical analysis of the entire sample, including observations in the literature, will be forthcoming upon completion of all observations.

In this paper, we adopt $H_0 = 71 \text{ km s}^{-1} \text{ Mpc}^{-1}$, $\Omega_M = 0.27$, and $\Omega_\Lambda = 0.73$ for consistency with Part I. We summarize details of our sample selection in §3.3. Observations and data reduction are discussed in §3.4. Our results are presented in §3.5. While a full statistical analysis is not in the scope of this paper, we present a brief analysis in §3.6, focusing on the H I emission results in §3.6.1 and the H I absorption results in §3.6.2. Notes on individual galaxies or systems of interest are presented in §3.7 and we conclude in §3.8.

3.3 The Sample

Our sample of 77 galaxies is selected using the same criteria established in Part I from the 2-Jy IRAS-NVSS sample of 1809 galaxies. Galaxies in our sample must lie within the “Arecibo sky” ($-1^\circ < \text{declination} < 38^\circ$), be infrared bright sources ($L_{\text{FIR}} \geq 7 \times 10^9 L_\odot$), and be nearby such that the spectral lines will fall within the observing band (heliocentric velocities between 0 and 50,000 km s^{-1}). These criteria reduce the total sample size from 1809 to 582 galaxies. Based on the high rate of new H I 21 cm and OH 18 cm detections in Part I, we focused our observations on galaxies in the right ascension range of $02^{\text{h}}\text{--}10^{\text{h}}$ (B1950) without prior H I detections listed in the NASA/IPAC Extragalactic Database (NED). Ten of the galaxies did have detections in the blind redshift survey of the Zone of Avoidance by Lu and Freudling (1995), but we chose to include these galaxies in our sample as a consistency check, and for completeness as the 22-cm line feed was upgraded after their study. This resulted in a sample of 77 galaxies that were observed for Part II.

We report basic properties of our sample in Table 3.1. Throughout this paper,

we refer to galaxies by the IRAS names (Column 1). Other common designations for galaxies are listed in Column 2. The right ascension and declination of our sources are given in J2000 coordinates (Columns 3 and 4). In Column 5, we note the optical redshifts from NED. We retrieved 12, 25, 60 and 100 μm flux densities for most galaxies from the IRAS Faint Source Catalog (FSC), and a few from the IRAS Point Source Catalog (PSC). The average flux density uncertainty for these measurements is $\sim 10\%$ (individual uncertainties range from 0% to 30%). The 60 μm flux density is listed in Column 6. We do not list the flux density at other wavelengths in this table, but use them and the uncertainties to calculate IR and FIR luminosities (see Table 3.2). The continuum radio flux density at 1.4 GHz is listed in Column 7, extracted from the NVSS survey (Condon et al. 1998). If a morphology for the galaxy is identified in NED or the Hyperleda database (Paturel et al. 2003), we note the designation in Column 8.

Table 3.1. Sample Properties

IRAS Name	Other Names	R. A. (J2000)	Decl. (J2000)	z	$S_{60\mu m}$ (Jy)	$S_{1.4GHz}$ (mJy)	Morphology
(1)	(2)	(3)	(4)	(5)	(6)	(7)	(8)
02080+3103	–	02 10 58.48	+31 17 40.8	0.0169	2.44	21.9±0.06	-
02150+2201	VZw 214	02 17 50.92	+22 15 16.7	0.0446	2.35	13.0±0.08	-
02153+2636	–	02 18 15.65	+26 49 59.0	0.0500	2.87	22.2±0.06	-
02280+2209	–	02 30 52.94	+22 22 56.7	0.0321	2.14	27.1±0.05	-
02290+2533 ^P	–	02 31 54.31	+25 46 13.8	0.0518	2.66	33.4±0.05	-
02304+0012	UGC 02024	02 33 01.03	+00 25 15.6	0.0224	2.49	6.6±0.18	Sab;Sy2
02433+1544	–	02 46 10.37	+15 57 08.0	0.0252	3.09	12.4±0.19	S0-a
02526–0023	NGC 1142, Arp 118, Mrk 9012/1504, UGC 02389	02 55 12.15	–00 10 58.7	0.0288	5.30	154.6±0.03	E;Sy2
02568+3637	UGC 02456, Mrk 1066	02 59 58.59	+36 49 13.6	0.0121	10.98	100.4±0.04	S0-a;Sy2
03017+0724	–	03 04 27.59	+07 36 13.3	0.0260	2.37	14.7±0.07	-
03020+2336	–	03 04 58.61	+23 48 00.5	0.0528	2.26	9.3±0.11	-
03079+0018	–	03 10 34.09	+00 29 36.8	0.0472	2.74	11.8±0.08	-
03119+1448	–	03 14 46.51	+15 00 01.1	0.0765	2.14	6.5±0.17	-
03144+0104	UGC 02638	03 17 02.10	+01 15 18.5	0.0237	2.67	27.1±0.05	Sab
03207+3734	UGC 02710	03 23 58.49	+37 45 19.2	0.0185	3.15	21.1±0.07	S0
03222+1617	–	03 25 05.11	+16 28 05.7	0.0403	3.52	31.5±0.04	-
03231+3721	–	03 26 22.05	+37 32 08.0	0.0265	2.03	16.8±0.08	-
03275+1535	–	03 30 23.74	+15 46 04.3	0.0249	1.95	13.9±0.08	-

Table 3.1 (cont'd)

IRAS Name	Other Names	R. A. (J2000)	Decl. (J2000)	z	$S_{60\mu m}$ (Jy)	$S_{1.4GHz}$ (mJy)	Morphology
(1)	(2)	(3)	(4)	(5)	(6)	(7)	(8)
03288+0108	–	03 31 24.08	+01 18 24.9	0.0310	2.31	11.9±0.09	-
03315+0055	–	03 34 06.11	+01 05 39.8	0.0479	1.93	20.8±0.06	-
03359+1523	–	03 38 47.00	+15 32 52.9	0.0354	6.20	19.4±0.06	-
03371+1046	–	03 39 56.92	+10 56 34.1	0.0357	2.47	9.7±0.10	-
03521+0028 ^P	–	03 54 41.92	+00 37 04.3	0.1504	2.64	6.1±0.21	-
04012+2159	VV 777	04 04 10.01	+22 07 49.8	0.0210	2.41	25.3±0.06	-
04139+2737 ^P	–	04 17 00.66	+27 44 49.9	0.0176	2.63	18.3±0.07	-
04149+0125	–	04 17 35.00	+01 32 23.3	0.0164	3.46	10.8±0.09	-
04150+3528 ^P	–	04 18 21.97	+35 35 32.0	0.0506	2.07	13.8±0.10	-
04154+1755	–	04 18 21.90	+18 02 41.5	0.0555	3.82	68.6±0.03	Sy2
04232+1436 ^P	–	04 26 04.78	+14 43 37.2	0.0797	3.45	29.4±0.04	LIN
04296+2923	–	04 32 48.60	+29 29 57.9	0.0069	38.18	130.5±0.04	Scd
04298+2714 ^P	–	04 32 59.60	+27 21 12.8	0.0301	3.02	13.0±0.11	Sbc
04332+0209	UGC 03097	04 35 48.33	+02 15 34.7	0.0119	3.38	3.9±0.32	S0
04359+1844	UGC 03115	04 38 54.56	+18 50 19.0	0.0110	2.32	16.0±0.07	S0
04470+0314	MRK 1087, UGC 03179	04 49 37.92	+03 19 30.4	0.0280	3.03	12.1±0.09	S0;HII
04489+1029 ^P	–	04 51 43.40	+10 34 18.4	0.0281	1.05	4.2±0.39	-
04513+0104	–	04 53 55.77	+01 09 16.5	0.0331	2.19	12.9±0.08	-

Table 3.1 (cont'd)

IRAS Name	Other Names	R. A. (J2000)	Decl. (J2000)	z	$S_{60\mu m}$ (Jy)	$S_{1.4GHz}$ (mJy)	Morphology
(1)	(2)	(3)	(4)	(5)	(6)	(7)	(8)
04572-0013	—	04 59 46.37	-00 09 30.1	0.0236	2.33	21.1±0.10	Sab
05029+2135	—	05 05 53.67	+21 39 37.5	0.0173	2.51	18.1±0.06	Sbc
05054+1718	—	05 08 20.72	+17 22 01.9	0.0182	10.21	32.4±0.05	Sa;Sy2
05066+0844	—	05 09 24.04	+08 48 19.0	0.0361	3.46	23.0±0.05	-
05085+2036	—	05 11 32.88	+20 40 12.3	0.0316	3.57	10.5±0.11	Sbc
05135+1534	—	05 16 24.44	+15 37 55.0	0.0203	2.96	27.0±0.05	Sa
05181+0848 ^P	—	05 20 52.22	+08 51 51.4	0.0157	2.44	33.8±0.04	-
05246+0103	—	05 27 16.13	+01 05 59.2	0.0964	2.47	16.3±0.07	-
05405+0035	—	05 43 05.49	+00 37 13.0	0.0143	6.24	22.2±0.05	Sab
06375+3338 ^P	UGC 03508	06 40 47.82	+33 35 53.5	0.0171	3.38	15.9±0.08	-
06443+2925	—	06 47 32.50	+29 22 12.2	0.0174	1.97	19.5±0.07	Sbc
06478+3335 ^P	NGC 2294	06 51 11.36	+33 31 37.3	0.0170	2.06	12.6±0.10	E
06488+2731 ^P	—	06 52 02.51	+27 27 39.0	0.0409	2.49	157.0±0.03	Sbc
06533+2801 ^P	—	06 56 30.06	+27 56 56.9	0.0145	2.29	4.1±0.41	Sbc
06542+2030	UGC 03611	06 57 11.65	+20 26 13.2	0.0170	2.80	15.6±0.07	S0-a
07120+1428	—	07 14 51.84	+14 22 54.2	0.0277	1.86	13.4±0.09	Sbc
07125+2615 ^P	—	07 15 36.45	+26 09 41.6	0.0305	2.54	34.6±0.04	-
07224+3003	—	07 25 37.26	+29 57 14.3	0.0191	3.01	146.3±0.04	-

Table 3.1 (cont'd)

IRAS Name	Other Names	R. A. (J2000)	Decl. (J2000)	z	$S_{60\mu m}$ (Jy)	$S_{1.4GHz}$ (mJy)	Morphology
(1)	(2)	(3)	(4)	(5)	(6)	(7)	(8)
07340+0300 ^P	–	07 36 38.11	+02 53 20.7	0.0171	2.22	18.3±0.06	Sbc
07565–0030	NGC 2494, IC 0487, UGC 04141	07 59 07.07	–00 38 18.0	0.0119	2.84	20.3±0.06	S0-a
07567+3557 ^P	–	07 59 56.79	+35 48 56.1	0.0175	2.57	9.2±0.15	–
08071+0509	–	08 09 47.22	+05 01 08.9	0.0521	4.50	35.8±0.04	–
08072+1847	–	08 10 07.16	+18 38 17.7	0.0161	2.76	6.8±0.15	–
08169+0448	NGC 2561, UGC 04336	08 19 36.91	+04 39 27.7	0.0136	2.58	16.7±0.07	Sc
08300+3714	–	08 33 19.18	+37 04 39.9	0.0426	2.25	4.10±0.57	–
08323+3003	–	08 35 23.44	+29 53 09.2	0.0596	2.90	7.50±0.15	–
08327+2855	–	08 35 47.94	+28 45 11.1	0.0254	2.22	12.70±0.09	S0
08340+1550 ^P	–	08 36 53.71	+15 40 17.2	0.0779	2.08	9.40±0.11	–
08507+3520	ARP 195, UGC 04653, VV 243	08 53 54.38	+35 08 56.4	0.0558	2.18	38.0±0.05	Sbb
08579+3447	–	09 01 05.78	+34 35 28.4	0.0654	2.68	24.4±0.06	–
09014+0139	–	09 04 01.03	+01 27 29.1	0.0536	3.06	19.4±0.06	–
09018+1447	MRK 1224, IC 2431, UGC 04756, VV 645	09 04 34.83	+14 35 38.8	0.0495	4.12	104.10±0.03	Irr
09047+1838 ^P	NGC 2761	09 07 30.89	+18 26 04.7	0.0291	3.97	28.0±0.05	–
09070+0722	NGC 2773, UGC 04815	09 09 44.14	+07 10 25.5	0.0180	2.79	22.6±0.05	–
09143+0939	–	09 16 59.85	+09 26 47.7	0.0475	3.49	20.3±0.06	–
09192+2124	–	09 22 05.93	+21 11 16.4	0.0773	2.52	9.30±0.11	–

Table 3.1 (cont'd)

IRAS Name	Other Names	R. A. (J2000)	Decl. (J2000)	z	$S_{60\mu m}$ (Jy)	$S_{1.4\text{GHz}}$ (mJy)	Morphology
(1)	(2)	(3)	(4)	(5)	(6)	(7)	(8)
09253+1724	UGC 05046	09 28 06.52	+17 11 46.8	0.0141	3.06	22.10±0.05	-
09341+1158	—	09 36 49.98	+11 45 04.6	0.0287	2.44	19.6±0.06	S0-a
09351+0259	NGC 2936, ARP 142, UGC 05130, VV 316	09 37 44.01	+02 45 33.4	0.0233	2.00	29.20±0.06	-
09406+1018	—	09 43 21.59	+10 05 07.4	0.0537	2.42	20.0±0.07	-
09432+1910 ^P	—	09 46 04.52	+18 56 40.4	0.0535	3.71	16.5±0.06	-

^PThe 60 μm values for these specified galaxies are from the IRAS Point Source Catalog (PSC). The majority of 60 μm values are from the IRAS Faint Source Catalog (FSC).

3.4 Observations and Data Reduction

All observations were taken with the 305 m Arecibo Radio Telescope using the L-band wide receiver. The frequency range of this receiver is 1.12-1.73 GHz, which is ample coverage for our sample of galaxies with heliocentric velocities no greater than 50,000 km s⁻¹. We observed eight spectral lines in two polarizations using the dual-board mode of the Wide-band Arecibo Pulsar Processor (WAPP) spectrometer. This gave simultaneous coverage of the following redshifted transitions and frequency ranges: the H I 21 cm line (1420.40575 MHz), both of the OH 18 cm main lines (1665.4018 and 1667.359 MHz), the two OH 18 cm satellite lines at 1612.231 and 1720.530 MHz, HCN (1346.758 MHz), HCO⁺ (1270.3668 MHz), and the ¹⁸OH equivalents of the ¹⁶OH mainlines (1637.564 and 1639.503 MHz). Each board was centered at the frequency of the redshifted transition, except for the ¹⁸OH lines, which we centered at 1638.50 MHz. The bandwidth of each board was 12.5 MHz. We observed in dual polarization mode with 2048 spectral channels per polarization for each of the eight boards. Using the WAPP spectrometer, instead of the 50 MHz Arecibo Interim correlator used in Part I, enabled us to add a search for HCN and HCO⁺ without losing resolution or sensitivity in the observations of our main lines of interest, H I and OH. All observations were obtained between January 2008 and August 2009.

For the majority of sources in our sample, we used simple total-power position switching with a five minute integration on source followed by a five minute integration offset from the source in azimuth. In three cases (IRAS 02526-0023, IRAS 02568+3637, IRAS 06488+2731), we used the Double Position Switching (DPS) observing technique to minimize baseline ripples. This technique includes the observation of a bandpass calibrator in addition to the simple total power measurement

in the “OFF” or sky position, which is usually simply subtracted from the source total power measurement (see Ghosh and Salter 2002, for more details of the DPS observing technique).

Data reduction was performed with standard Arecibo Observatory IDL routines for spectral line processing. We used the noise-diode calibration and standard gain curves for the Arecibo telescope to convert measured antenna temperatures to units of flux density for all of our sources observed in the standard ON-OFF mode. For the galaxies observed in DPS mode, the bandpass calibrators were used to set the flux density scale of their respective target sources. We Hanning smoothed and averaged the two polarizations, except in a handful of cases where one polarization was severely affected by radio frequency interference (RFI). We applied a 9-channel box-car smoothing to improve the signal-to-noise of our spectra and match the 112 kHz spectral resolution of Part I. Prior to spectral line measurements (e.g., velocity width, velocity center, integrated intensity), we fit the baselines with polynomials. In most cases, we used low-order polynomials ($n < 3$), but in a few cases with more extreme ripples, we fit the baseline with a higher order polynomial.

Primary RFI affecting our observations included local military radar (1245 and 1247 MHz), the San Juan airport radar (1330 and 1350 MHz), satellite bands (1525-1600 MHz) including the Russian GPS satellite at 1603 MHz. Other frequencies of RFI that affected our observations included radar at 1275 and 1291 MHz. A full list of sources of RFI and observed frequencies for L-band birdies are maintained at the Arecibo Observatory (<http://www.naic.edu/~phil/rfi>).

3.5 Results

We detected H I 21 cm emission and/or absorption in 61 of the 77 galaxies; nine of which had been previously reported by Lu and Freudling (1995). The remaining 52 detections we report are new, without prior citation in the literature. There are seven sources with absorption features in their spectra, six with pure absorption, and one with emission and an absorption component. Ten of our observed sources were non-detections, seven of which were also reported as non-detections by Lu and Freudling (1995).

Spectra for the 55 galaxies with an H I detection in emission or emission and absorption (03315+0055) are shown in Figure 3.2. These spectra are presented prior to baseline fitting in order to show the quality of the raw baselines. Cases with strong continuum emission are clearly evident. In three cases, a galaxy other than the IRAS galaxy of interest was detected in H I (see Fig. 3.3). We remark on each of these cases as well as galaxies with distorted spectra or interesting features in §3.7. Spectra for the six galaxies with pure absorption are presented in Figure 3.4.

The WAPP spectrometer gave us the ability to simultaneously observe eight different bands. We observed the H I line in one band, and used three others to search for the OH 18 cm main line, and the OH 18 cm satellite lines at 1612 and 1720 MHz. In Part I, OH 18 cm main lines were detected in seven galaxies. Three of these were detected in emission (OHMs) and four in absorption. One OHM and three of the OH absorbers were new detections. For this reason, we included OH main and satellite lines in our observations. However, we did not make any detections (see §3.8 for discussion about future work). We also did not make any detections of HCN or HCO⁺. Most of these boards were ruined by RFI.

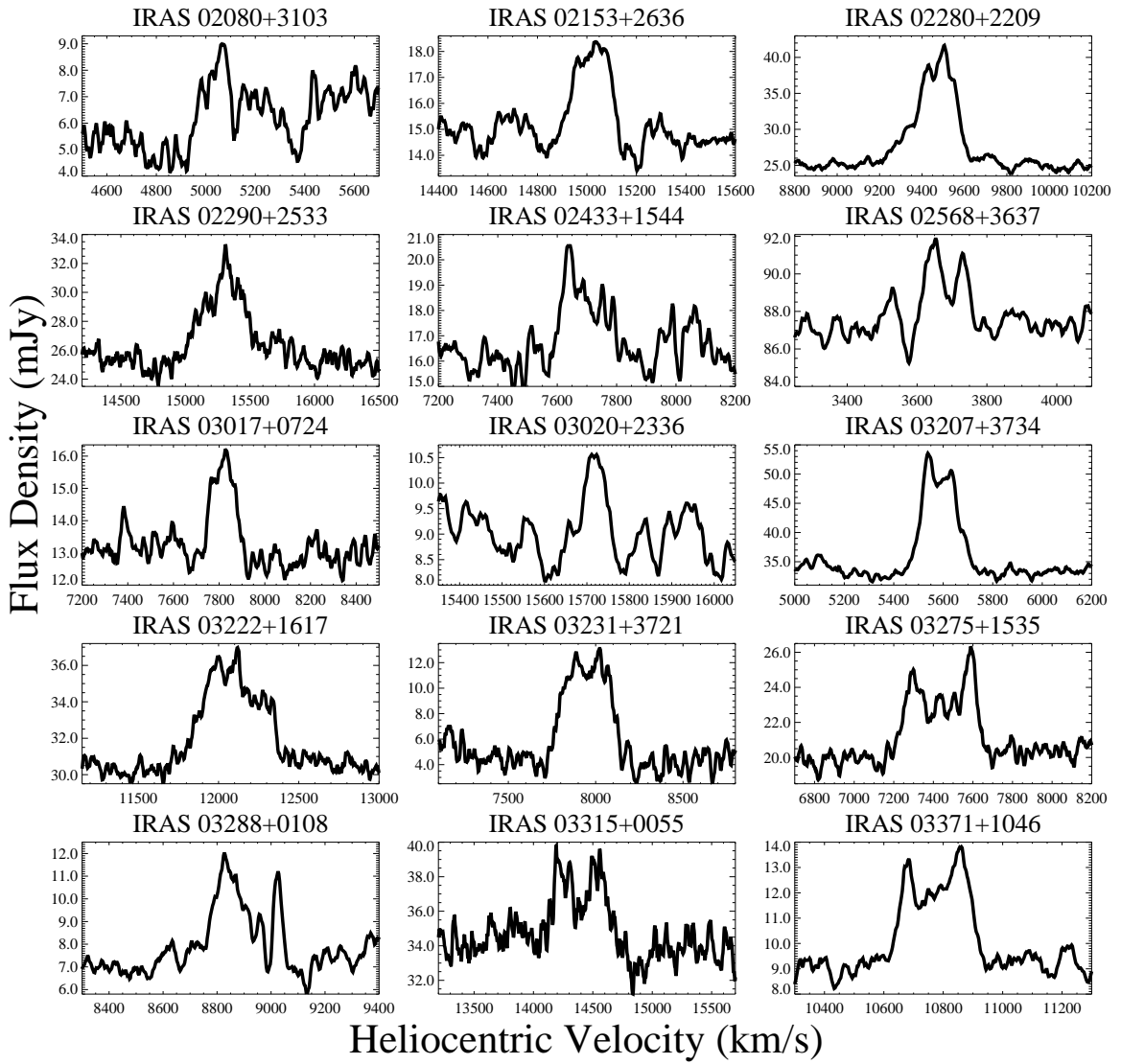


Figure 3.2: Spectra of H I 21 cm emission detections. See Table 3.2 for measured and derived parameters.

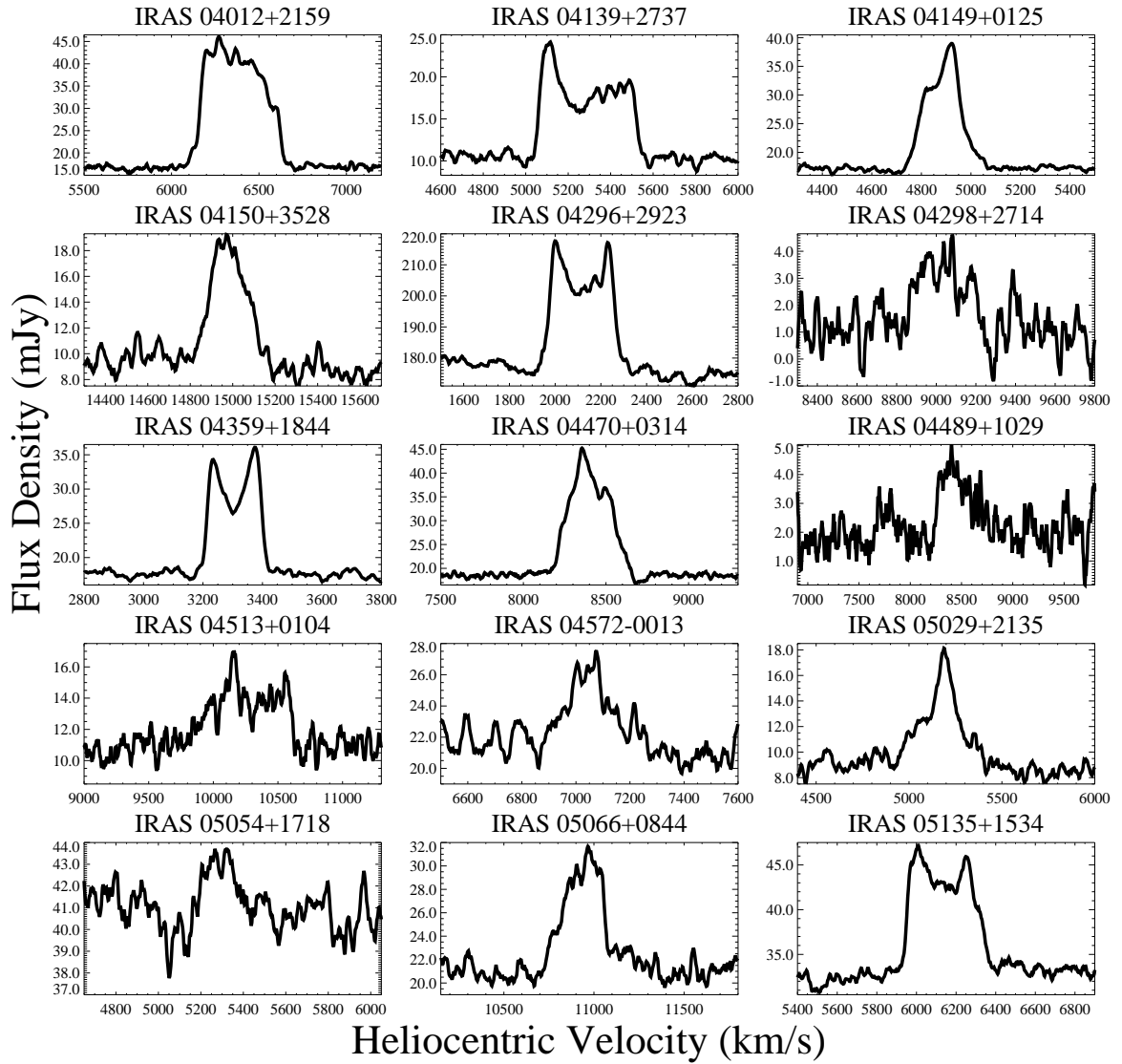


Figure 3.2 (continued)

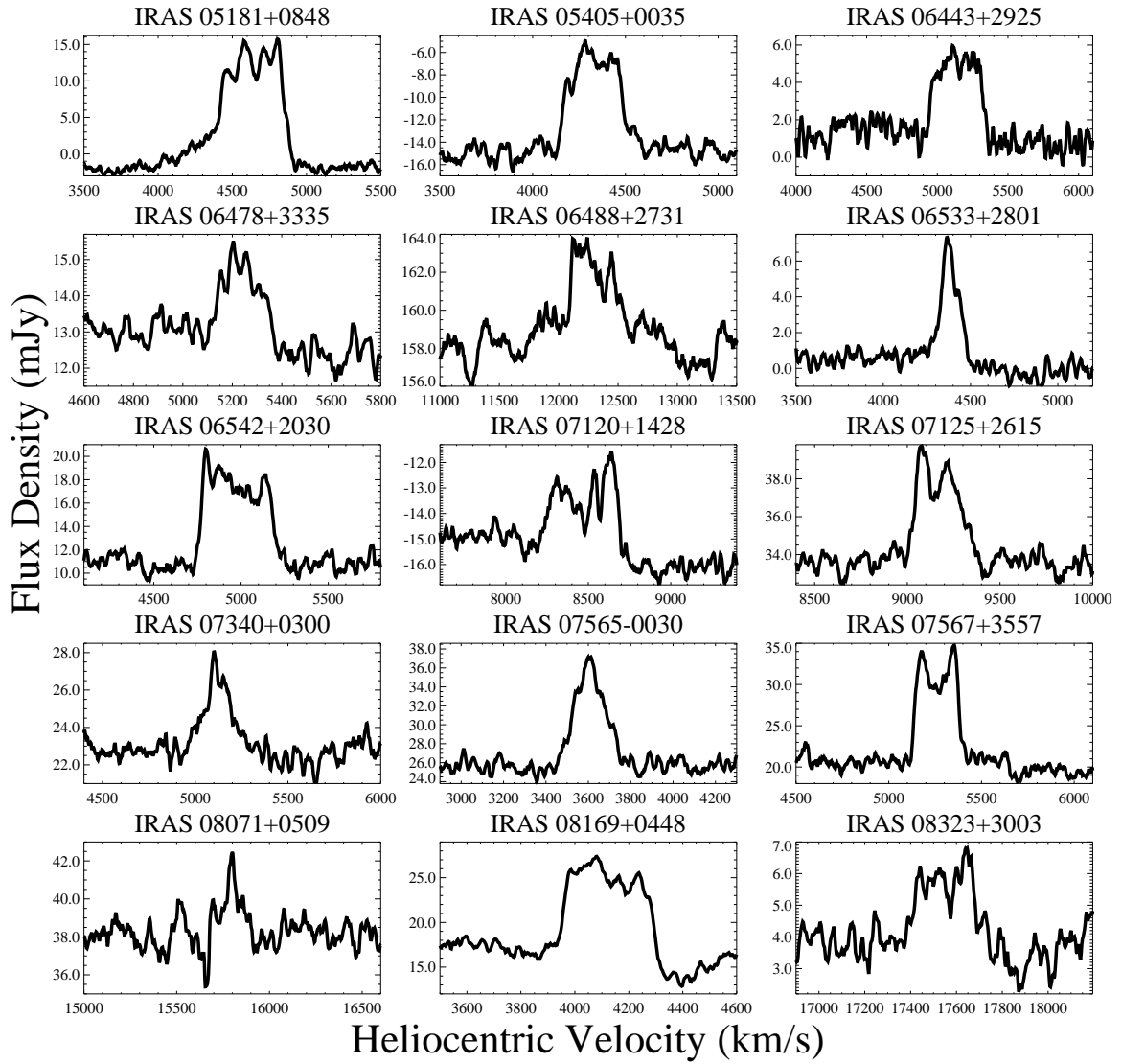


Figure 3.2 (continued)

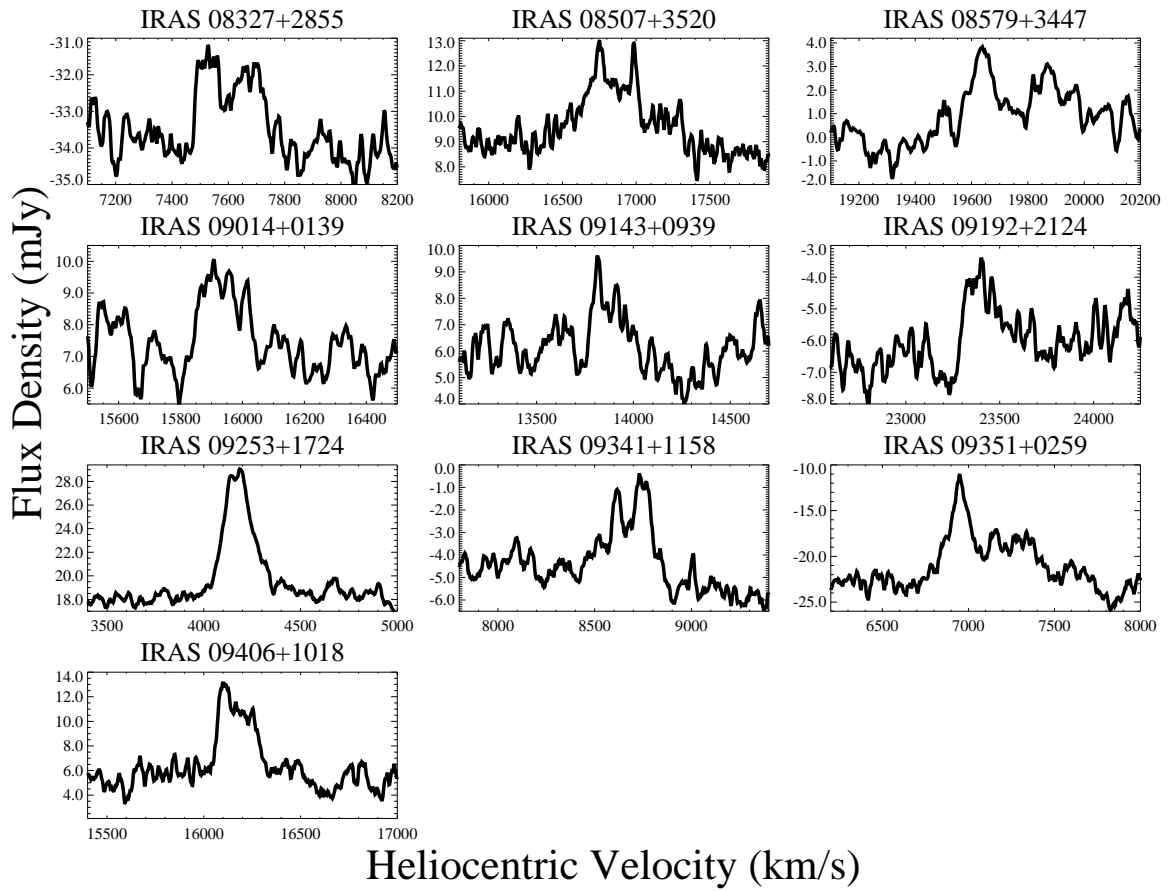


Figure 3.2 (continued)

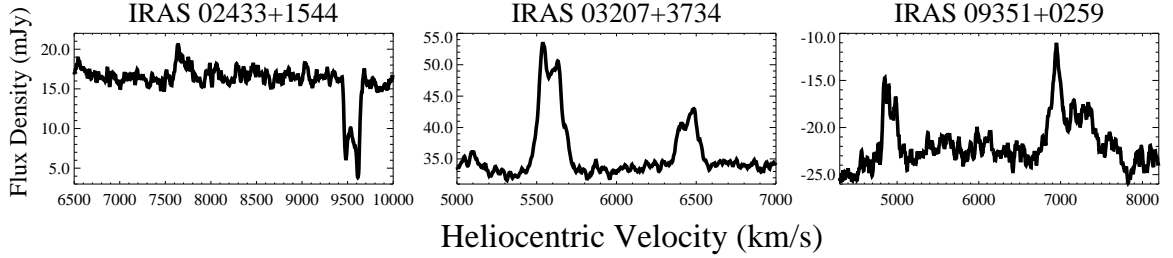


Figure 3.3: Spectra of H I 21 cm emission detections for our IRAS galaxies and another galaxy. For IRAS 02433+1544, the absorption is emission from a galaxy at 9500 km s^{-1} in the off position scan. The other two detections are galaxies in the field of view.

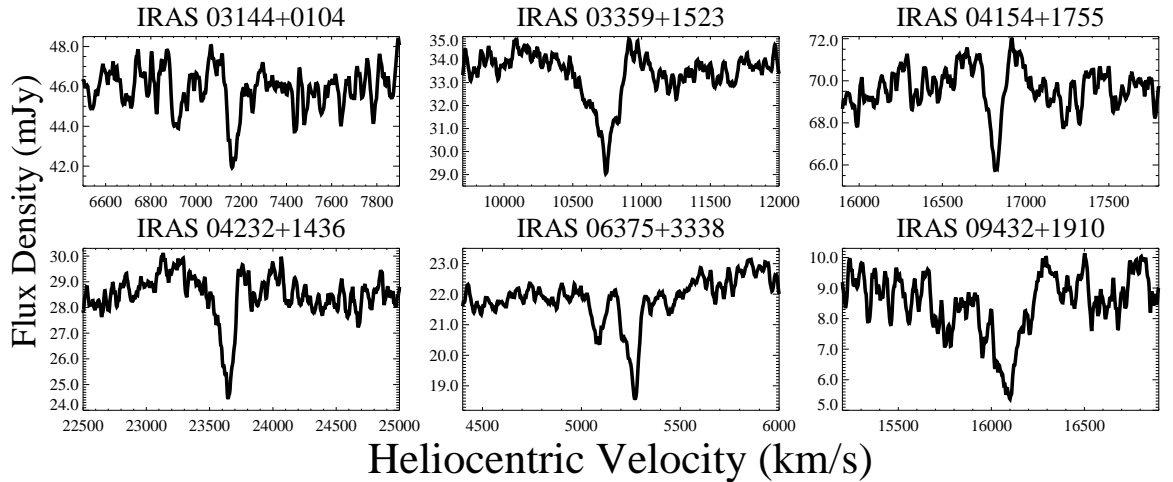


Figure 3.4: Spectra of H I 21 cm absorption detections. We detect absorption in six galaxies. See also the absorption component at $\sim 14,800 \text{ km s}^{-1}$ in the source IRAS 03315+0055, shown in Fig. 3.2.

3.6 Analysis and Discussion

Here we report preliminary statistical analysis for the observed sample. More detailed analysis and conclusions will be presented after completion of the full survey with all 582 galaxies, from our observations and the literature. Measured and derived properties for galaxies with H I emission and absorption spectra are presented in Tables 3.2 and 3.4, respectively. Measurements were performed on baseline corrected

spectra, after we subtracted fitted polynomials. For the one source we indicate to contain emission and absorption (03315+0055), we present measured and derived values for each component in the appropriate table. We explore properties of galaxies with H I emission in §3.6.1 and properties of galaxies with H I absorption in §3.6.2.

In Figure 3.5, we plot the q parameter for our entire sample as a function of FIR luminosity. The mean value of q for starburst galaxies in the IRAS-NVSS sample of 1809 galaxies of 2.34 is overlaid, with dotted lines showing the region above which objects have an IR excess and below which objects have a radio excess (e.g. IRAS 06488+2731) (Yun et al. 2001). Consistent with Part I and the IRAS-NVSS 2 Jy sample at large, our selected sub-sample is overwhelmingly comprised of galaxies which follow the radio–FIR correlation.

3.6.1 H I Emission

We present measured and derived properties based on H I emission in Table 3.2. IRAS names are listed in Column 1, corresponding to Table 3.1. We note the on-source integration time in Column 2. Five minutes was standard, but we re-observed sources for which we did not have a high signal-to-noise when possible. We measured the RMS for each spectrum offset from the emission component, and this value is listed in Column 3. Column 4 gives the heliocentric velocity at which the H I emission line is centered. For the sources that are non-detections, we compute upper limits using their optical velocities. In addition to not having enough integration time on source, it is possible that the reason for the non-detection might be an incorrect optical velocity. The velocity full width at half maximum (FWHM) is given for each spectrum in Column 5 and the integrated flux density ($\int S dv$) in Column 6. The flux density integral is computed for non-detections by assuming $\Delta V_{50} = 400 \text{ km s}^{-1}$.

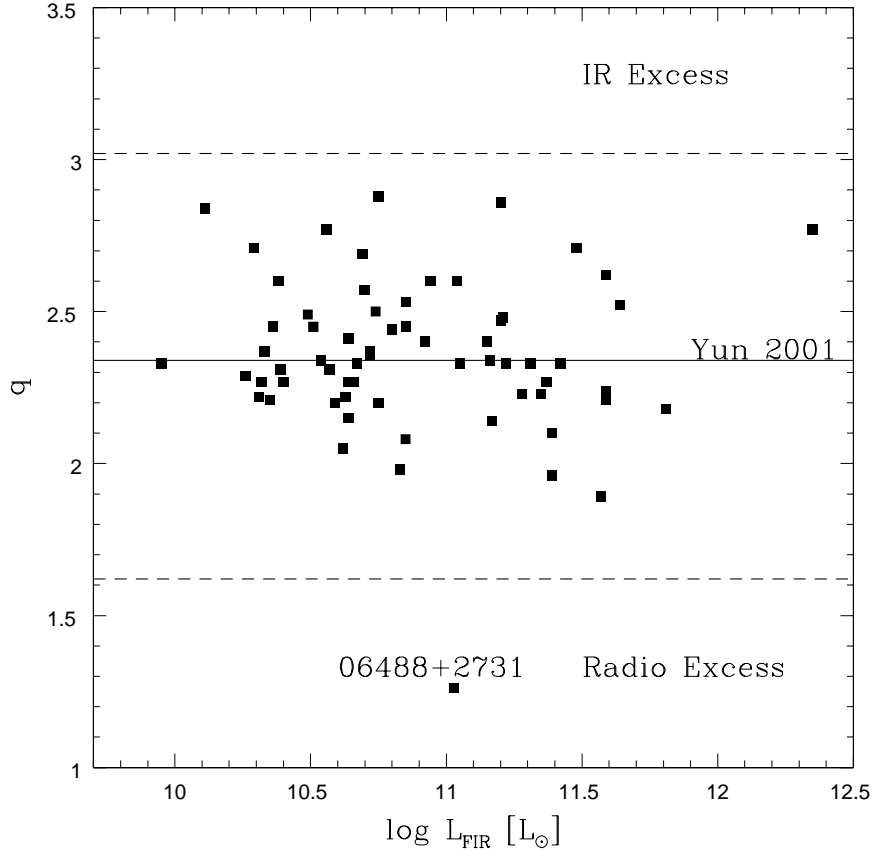


Figure 3.5: Radio–FIR correlation is quantified via the q parameter vs. FIR luminosity for the galaxies in our sample. Regions of IR or radio excess are denoted with the dashed lines (Yun et al. 2001). The only outlier, 06488+2731 has a 1.4 GHz flux of 157 mJy, the highest of all galaxies in our sample.

The luminosity distance (D_L) of each galaxy, listed in Column 7, is derived using the measured H I velocity (Column 4), or the optical velocity for non-detections.

We calculate the FIR and IR luminosities using the IRAS measurements and standard determined relations (e.g. Sanders and Mirabel 1996). The FIR flux is determined by

$$F_{\text{FIR}} [\text{Wm}^{-2}] = 1.26 \times 10^{-14} (2.58f_{60} + f_{100}), \quad (3.2)$$

where f_{60} and f_{100} are the 25 and 60 μm observed flux densities in Jy by the IRAS

satellite. Relating the flux to luminosity,

$$L_{\text{FIR}} [L_{\odot}] = 4\pi D_{\text{L}}^2 C F_{\text{FIR}}, \quad (3.3)$$

where D_{L} is in units of meters, F_{FIR} is from equation 3.2 and C is a scaling factor (usually ~ 1.4 – 1.6) for extrapolated flux beyond $100 \mu\text{m}$. Hence, the FIR luminosity is

$$L_{\text{FIR}}(L_{\odot}) = 3.96 \times 10^5 D_{\text{L}}^2 (2.58f_{60} + f_{100}), \quad (3.4)$$

where D_{L} is in Mpc. We list $\log(L_{\text{FIR}})$ in Column 8. Similar relationships hold in the determination of IR flux and luminosity. Sanders and Mirabel (1996) give the expression for this relationship:

$$L_{\text{IR}} [L_{\odot}] = 5.67 \times 10^5 D_{\text{L}}^2 (13.48f_{12} + 5.16f_{25} + 2.58f_{60} + f_{100}). \quad (3.5)$$

We list $\log(L_{\text{IR}})$ in Column 9.

IR and FIR luminosities have been derived before for the objects in our sample. However, we recompute them using our chosen cosmology and the determined distance (D_{L}) from our measured velocities. We then calculate the total neutral hydrogen mass for each galaxy system with H I emission using this expression, as given by Roberts (1975):

$$M_{\text{HI}} [M_{\odot}] = 2.36 \times 10^5 D_{\text{L}}^2 \int S dv \quad (3.6)$$

where $\int S dv$ is the flux density integral in Jy km s^{-1} . We list $\log(M_{\text{HI}})$ in Column 10. For non-detections, the mass is an upper limit. In five of our non-detections, we only obtained a single 5-minute integration on source. The galaxies for which we did not make a detection tended to be more distant (the average luminosity distance for non-detected galaxies was 241 Mpc compared to 150 Mpc for detected galaxies). Hence, more integration time is needed on these sources. We do not include the mass limits in our statistical analysis, since we have not been able to rule out an

incorrect redshift measurement for these sources. We do not compute dynamical masses as many systems are interacting, merging, or have unknown inclinations.

Table 3.2. Parameters of Galaxies with H I Emission

IRAS Name	Δt (min)	RMS (mJy)	V_{HI} (km s ⁻¹)	ΔV_{50} (km s ⁻¹)	$\int S dv$ (Jy km s ⁻¹)	D_L (Mpc)	$\log \frac{L_{\text{FIR}}}{L_{\odot}}$	$\log \frac{L_{\text{IR}}}{L_{\odot}}$	$\log \frac{M_{\text{HI}}}{M_{\odot}}$
(1)	(2)	(3)	(4)	(5)	(6)	(7)	(8)	(9)	(10)
02080+3103	10	0.53	5110.4±1.7	290.2±3.3	0.1±0.0	72.9±0.0	10.35±0.04	10.60±0.15	8.19±0.10
02150+2201*	15	0.56	13396.0±40 ^a	400.0	0.5	195.3±0.6	11.17±0.05	11.42±0.15	<9.65
02153+2636	10	0.49	15013.4±2.2	212.0±4.5	0.6±0.0	219.5±0.0	11.37±0.03	11.62±0.15	9.85±0.03
02280+2209	14	0.51	9447.3±1.0	305.3±2.0	3.2±0.0	136.3±0.0	10.86±0.07	11.11±0.15	10.15±0.01
02290+2533	5	0.50	15289.0±2.4	515.7±4.8	2.2±0.1	223.6±0.0	11.39±0.06	11.70±0.16	10.40±0.01
02304+0012*	5	0.88	6698.0±17 ^b	400.0	0.5	96.0±0.3	10.51±0.04	10.94±0.07	<9.04
02433+1544	14	0.62	7643.1±1.9	309.5±3.8	0.7±0.0	109.8±0.0	10.75±0.04	11.04±0.12	9.27±0.03
02526−0023 ^{◇*}	5	1.14	8648.0±14 ^c	400.0	0.5	124.6±0.2	11.19±0.03	11.45±0.06	<9.82
02568+3637 [◇]	5	0.48	3680±3.5	128.1±7.0	0.4±0.0	52.3±0.1	10.64±0.03	10.96±0.05	8.41±0.03
03017+0724	15	0.44	7820.0±2.1	145.1±4.2	0.3±0.0	112.4±0.0	10.67±0.12	10.99±0.17	8.94±0.04
03020+2336	19	0.41	15341.1±6.0	61.6±12.0	0.0±0.0	224.5±0.1	11.22±0.06	11.45±0.16	8.72±0.18
03079+0018*	5	0.70	14236.0±20 ^d	400.0	0.5	208.3±0.3	11.25±0.07	11.50±0.15	<9.71
03119+1448*	5	0.81	23006.0±57 ^e	400.0	0.5	343.4±0.9	11.58±0.08	11.83±0.17	<10.14
03207+3734	10	0.61	5592.2±0.6	209.7±1.2	2.9±0.0	79.9±0.0	10.55±0.08	10.83±0.12	9.64±0.01
03222+1617	10	0.41	12098.5±1.7	520.3±3.4	2.3±0.1	175.7±0.0	11.29±0.04	11.52±0.16	10.22±0.01

Table 3.2 (cont'd)

IRAS Name	Δt	RMS	V_{HI}	ΔV_{50}	$\int S dv$	D_L	$\log \frac{L_{\text{FIR}}}{L_{\odot}}$	$\log \frac{L_{\text{IR}}}{L_{\odot}}$	$\log \frac{M_{\text{HI}}}{M_{\odot}}$
	(min)	(mJy)	(km s ⁻¹)	(km s ⁻¹)	(Jy km s ⁻¹)	(Mpc)			
(1)	(2)	(3)	(4)	(5)	(6)	(7)	(8)	(9)	(10)
03231+3721	5	0.76	7951.6±1.7	353.1±3.3	2.3±0.1	114.3±0.0	10.86±0.11	11.10±0.17	9.86±0.02
03275+1535	10	0.38	7438.7±1.3	410.6±2.7	1.3±0.0	106.8±0.0	10.58±0.06	10.86±0.16	9.55±0.01
03288+0108	10	0.48	8833.0±3.1	86.7±6.3	0.0±0.0	127.2±0.0	10.72±0.08	10.99±0.15	8.26±0.16
03315+0055 ^{abs}	5	0.73	14404.7±2.0	473.4±4.0	1.6±0.1	210.3±0.0	11.18±0.06	11.45±0.14	10.23±0.02
03371+1046	15	0.32	10776.8±1.4	279.4±2.8	0.9±0.0	156.0±0.0	11.04±0.07	11.31±0.15	9.74±0.01
03521+0028 ^{RFI}									
04012+2159	12	0.44	6389.7±0.4	467.9±0.8	9.8±0.1	91.5±0.0	10.66±0.04	10.92±0.10	10.29±0.00
04139+2737	10	0.42	5293.6±0.6	471.8±1.2	3.5±0.0	75.6±0.0	10.40±0.06	10.72±0.10	9.67±0.01
04149+0125	15	0.41	4887.7±0.5	225.8±1.0	3.1±0.0	69.7±0.0	10.56±0.11	10.77±0.15	9.54±0.00
04150+3528	10	0.57	14986.3±1.4	248.4±2.9	1.8±0.1	219.1±0.0	11.23±0.06	11.59±0.06	10.32±0.01
04296+2923 [◊]	12	1.33	2120.2±0.7	312.7±1.5	7.9±0.1	30.0±0.0	10.71±0.03	10.99±0.05	9.23±0.01
04298+2714	13	0.38	8545.8±0.2	299.5±0.5	8.4±0.0	123.0±0.0	10.80±0.06	11.13±0.08	10.48±0.00
04332+0209 ^{RFI}									
04359+1844	10	0.44	3306.7±0.4	196.9±0.7	2.4±0.0	47.0±0.0	9.95±0.09	10.25±0.15	9.09±0.01
04470+0314	10	0.42	8402.1±0.4	377.7±0.9	6.9±0.0	120.9±0.0	10.85±0.06	11.12±0.15	10.38±0.00

Table 3.2 (cont'd)

IRAS Name	Δt	RMS	V_{HI}	ΔV_{50}	$\int S dv$	D_L	$\log \frac{L_{\text{FIR}}}{L_{\odot}}$	$\log \frac{L_{\text{IR}}}{L_{\odot}}$	$\log \frac{M_{\text{HI}}}{M_{\odot}}$
	(min)	(mJy)	(km s ⁻¹)	(km s ⁻¹)	(Jy km s ⁻¹)	(Mpc)			
(1)	(2)	(3)	(4)	(5)	(6)	(7)	(8)	(9)	(10)
04489+1029	5	0.56	8508.1±2.8	500.2±5.5	0.7±0.1	122.5±0.0	11.08±0.06	9.39±0.04	9.39±0.04
04513+0104	5	0.51	10226.7±2.2	770.6±4.3	2.2±0.1	147.8±0.0	10.92±0.05	11.18±0.13	10.05±0.01
04572-0013	5	0.68	7093.6±1.5	242.5±3.0	0.7±0.0	101.8±0.0	10.63±0.05	10.89±0.14	9.22±0.02
05029+2135	14	0.38	5188.7±1.1	408.6±2.3	1.6±0.0	74.1±0.0	10.52±0.05	10.78±0.15	9.31±0.01
05054+1718	25	0.62	5345.9±2.6	362.3±5.1	0.6±0.1	76.4±0.0	10.95±0.04	11.19±0.09	8.88±0.04
05066+0844	5	0.57	10913.9±1.8	313.2±3.7	2.2±0.1	158.0±0.0	11.17±0.05	11.41±0.13	10.11±0.01
05085+2036*	20	0.54	9490.0±0.0 ^e	400.0	0.5	137.0±0.0	11.23±0.12	11.44±0.18	<9.35
05135+1534	8	0.57	6144.1±0.8	398.2±1.7	4.0±0.1	87.9±0.0	10.59±0.09	10.86±0.12	9.86±0.01
05181+0848	15	0.36	4642.5±0.7	470.9±1.4	6.7±0.0	66.2±0.0	10.88±0.08	9.84±0.00	9.84±0.00
05246+0103*	2	0.86	29105.0±22 ^f	400.0	0.5	440.7±0.3	11.83±0.11	12.19±0.13	<10.36
05405+0035	8	0.50	4327.3±1.9	342.7±3.7	2.7±0.1	61.6±0.0	10.69±0.09	10.93±0.14	9.38±0.01
06443+2925	5	0.55	5136.7±2.3	378.3±4.5	1.3±0.1	73.3±0.0	10.32±0.03	10.60±0.13	9.21±0.02
06478+3335	21.5	0.32	5229.5±1.3	248.6±2.6	0.4±0.0	74.7±0.0	10.69±0.08	8.68±0.03	8.68±0.03
06488+2731 [◊]	15	0.61	12349.0±3.5	1050.4±6.9	2.7±0.1	179.4±0.0	11.50±0.07	10.31±0.01	10.31±0.01
06533+2801	10	0.49	4377.0±1.5	203.9±2.9	0.9±0.0	62.4±0.0	10.47±0.05	8.91±0.02	8.91±0.02
06542+2030	10	0.70	4979.9±2.2	427.5±4.4	2.9±0.1	71.1±0.0	10.34±0.05	10.65±0.12	9.53±0.01

Table 3.2 (cont'd)

IRAS Name	Δt	RMS	V_{HI}	ΔV_{50}	$\int S dv$	D_L	$\log \frac{L_{\text{FIR}}}{L_{\odot}}$	$\log \frac{L_{\text{IR}}}{L_{\odot}}$	$\log \frac{M_{\text{HI}}}{M_{\odot}}$
	(min)	(mJy)	(km s ⁻¹)	(km s ⁻¹)	(Jy km s ⁻¹)	(Mpc)			
(1)	(2)	(3)	(4)	(5)	(6)	(7)	(8)	(9)	(10)
07120+1428	15	0.33	8468.0±1.6	454.9±3.3	1.0±0.0	121.9±0.0	10.64±0.07	10.96±0.15	9.56±0.01
07125+2615	10	0.39	9181.8±1.2	330.5±2.3	1.3±0.0	132.4±0.0	11.20±0.09	9.74±0.01	9.74±0.01
07224+3003 ^{RFI}									
07340+0300	8	0.51	5108.1±2.6	247.3±5.2	0.5±0.0	72.9±0.0	10.33±0.06	10.67±0.06	8.81±0.03
07565-0030	5	0.53	3627.9±1.4	160.0±2.9	1.8±0.0	51.6±0.0	10.15±0.04	10.45±0.08	9.06±0.01
07567+3557	5	0.75	5261.5±1.1	253.3±2.2	2.9±0.1	75.1±0.0	10.70±0.10	9.59±0.01	9.59±0.01
08071+0509	5	0.56	15792.0±1.3	218.2±2.5	0.4±0.0	231.3±0.0	11.59±0.04	11.83±0.13	9.69±0.04
08072+1847 ^{RFI}									
08169+0448	5	0.50	4097.1±0.8	327.9±1.5	3.3±0.1	58.3±0.0	10.21±0.03	10.47±0.11	9.42±0.01
08300+3714*	5	0.57	12516.0±29 ^g	400.0	0.5	182.1±0.4	11.03±0.04	11.33±0.14	<9.59
08323+3003	5	0.53	17561.9±2.5	345.0±4.9	0.7±0.0	258.2±0.0	11.48±0.06	11.71±0.16	10.02±0.03
08327+2855	5	0.53	8550.8±0.8	237.3±1.6	2.1±0.0	123.1±0.0	10.73±0.04	11.00±0.15	9.88±0.01
08340+1550*	5	0.77	23413.0±8 ^h	400.0	0.5	349.8±0.1	11.60±0.06	11.96±0.06	<10.16
08507+3520	10	0.39	16815.7±5.2	366.4±10.4	1.2±0.0	246.8±0.1	11.4±0.03	11.64±0.16	10.25±0.02
08579+3447	10	0.64	19632.3±3.6	110.8±7.1	0.1±0.0	290.0±0.0	11.59±0.03	11.84±0.18	9.46±0.11
09014+0139	5	0.73	15941.6±3.3	182.5±6.6	0.4±0.1	233.5±0.0	11.43±0.04	11.67±0.14	9.67±0.06

Table 3.2 (cont'd)

IRAS Name	Δt	RMS	V_{HI}	ΔV_{50}	$\int S dv$	D_L	$\log \frac{L_{\text{FIR}}}{L_{\odot}}$	$\log \frac{L_{\text{IR}}}{L_{\odot}}$	$\log \frac{M_{\text{HI}}}{M_{\odot}}$
(1)	(min)	(mJy)	(km s ⁻¹)	(km s ⁻¹)	(Jy km s ⁻¹)	(Mpc)	(8)	(9)	(10)
09018+1447*	5	0.88	14591.0±36 ⁱ	400.0	0.5	218.8±0.6	11.52±0.03	11.79±0.09	<9.75
09047+1838 ^{RFI}									
09070+0722 ^{RFI}									
09143+0939	10	0.63	13873.1±2.0	197.6±4.1	0.3±0.0	202.3±0.0	11.32±0.04	11.57±0.16	9.53±0.03
09192+2124	9	0.55	23405.9±2.7	205.7±5.4	0.3±0.0	348.6±0.0	11.64±0.05	11.94±0.14	9.95±0.06
09253+1724	18	0.41	4197.1±0.9	260.0±1.7	2.0±0.0	59.8±0.0	10.26±0.04	10.55±0.10	9.22±0.01
09341+1158	24	0.38	8659.2±0.5	374.4±1.1	1.0±0.0	124.7±0.0	10.75±0.04	11.06±0.14	9.56±0.02
09351+0259	5	0.83	7220.0±3.4	787.5±6.8	3.1±0.1	103.6±0.0	10.62±0.04	10.89±0.14	9.90±0.01
09406+1018	5	0.73	16192.6±2.3	271.1±4.5	1.5±0.0	237.3±0.0	11.35±0.03	11.61±0.14	10.30±0.01

[◊]Sources observed in DPS mode.

^{abs}The spectrum for this source has a possible absorption component in addition to the HI emission.

^{RFI}The spectra for these sources were contaminated by radio frequency interference. Therefore, no HI parameters are given or derived.

*Non-detections. We use optical redshifts obtained from NED: ^a(CFA redshift catalog, Huchra et al. 1992), ^b(Mahdavi and Geller 2004), ^c(Keel 1996), ^d(Lu and Freudling 1995), ^e(Strauss et al. 1992), ^f(Murphy et al. 2001), ^g(Sloan Digital Sky Survey 2004), ^h(Sloan Digital Sky Survey 2007), ⁱ(RC3 catalog, de Vaucouleurs et al. 1991). To derive 3σ upper limits on HI mass, we assume a velocity width of 400 km s⁻¹ and a flux density integral of 0.5 Jy km s⁻¹.

Table 3.3. H I Mass for Different L_{IR} Ranges

IR Luminosity (L_{\odot})	$L_{\text{IR}} < 10^{10.5}$	$10^{10.5} \leq L_{\text{IR}} < 10^{11.0}$	$10^{11.0} \leq L_{\text{IR}} < 10^{11.5}$	$L_{\text{IR}} \geq 10^{11.5}$
No. (emission)	10	20	13	12
Mean HI mass [M_{\odot}]	$10^{9.24 \pm 0.02}$	$10^{8.69 \pm 0.08}$	$10^{9.15 \pm 0.10}$	$10^{9.77 \pm 0.06}$
Median HI mass [M_{\odot}]	$10^{9.41}$	$10^{9.35}$	$10^{9.88}$	$10^{9.99}$

We plot the derived H I mass versus FIR and IR luminosity for the galaxies in our sample with H I emission in Figure 3.6 and versus 1.4 GHz radio continuum emission in Fig. 3.7. There are weak trends, but no strong correlation, similar to Part I. Relating the H I mass to either FIR or IR luminosity, the correlation coefficient is less than 44%. The H I mass versus 1.4 GHz radio continuum emission correlation is not much better, with a correlation coefficient of 45.2%. Statistics for derived H I mass as a function of IR luminosity are summarized in Table 3.3, where we bin our sample into four IR luminosity ranges. There is a broad global trend of increasing H I mass with increasing luminosity, but large variations between individual sources.

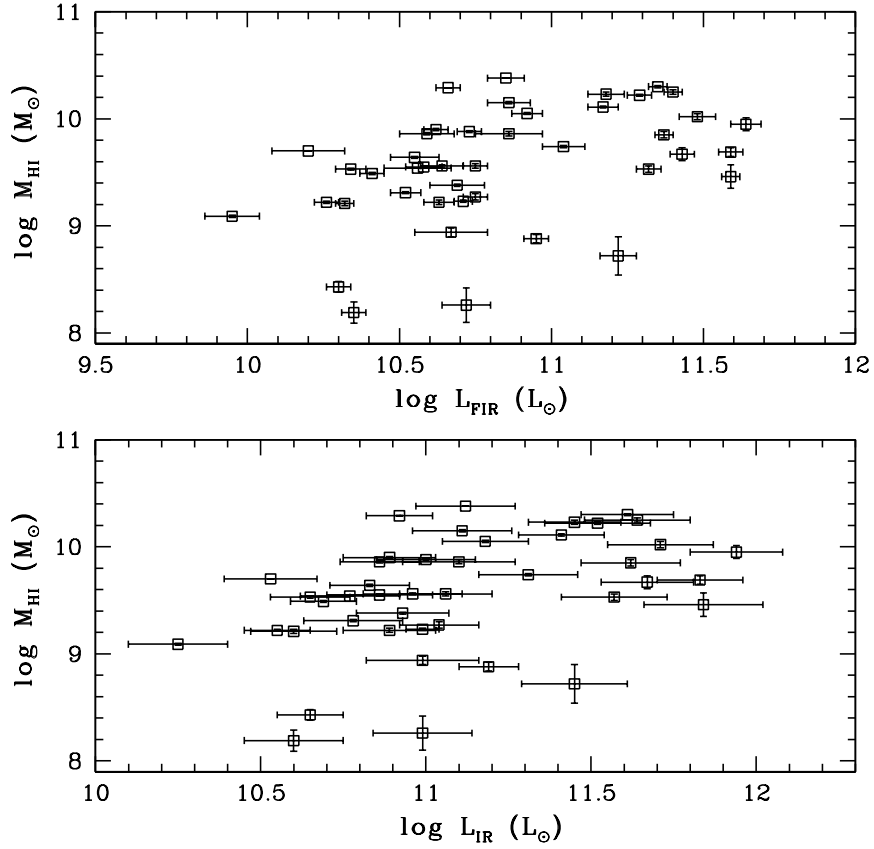


Figure 3.6: Logarithmic plots of the H I mass vs. FIR luminosity (*top*) and total IR luminosity (*bottom*) of the galaxies in our observed sample. The correlation coefficients are 43.3% and 43.6% for the *top* and *bottom* plots, respectively.

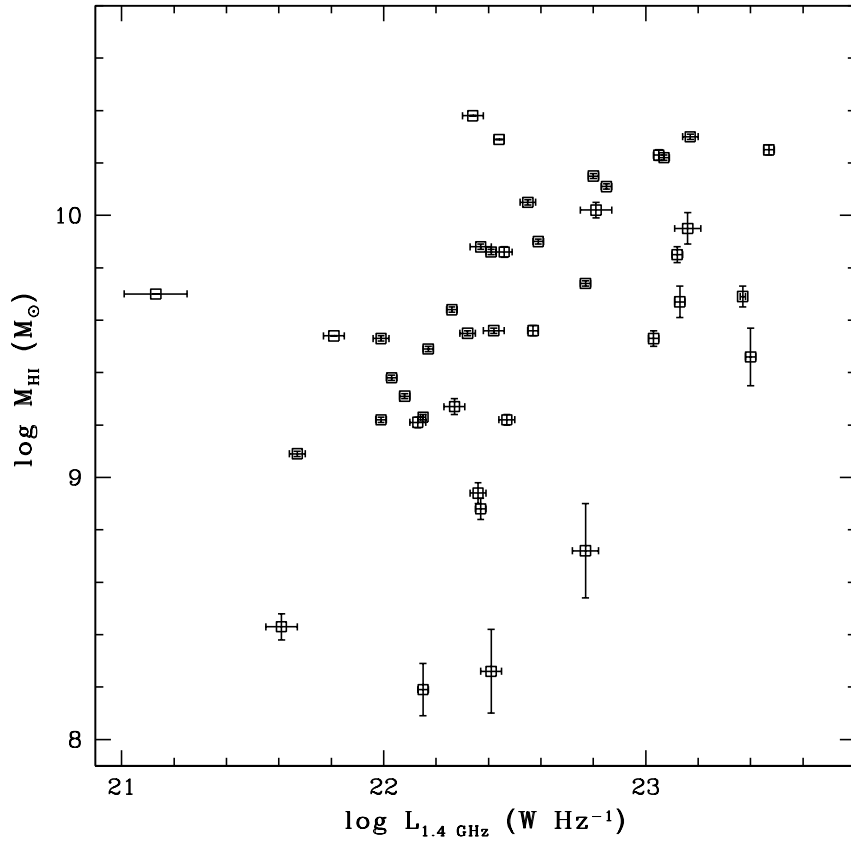


Figure 3.7: Logarithmic plot of the H I mass vs. the 1.4 GHz radio luminosity of the galaxies in our observed sample. The correlation coefficient in this plot is 45.2%.

3.6.2 H I Absorption

For the galaxies with H I absorption, we list measured and derived properties in Table 3.4. The IRAS name is given in Column 1. We calculate the luminosity distance (Column 2) from the measured velocity of peak optical depth (Column 8), except in the case of 03315+0055, for which we use the velocity of the H I emission peak. The FIR and IR luminosities are given in Columns 3 and 4, calculated as described in the section above. The integration time on source is listed in Column 5, with the measured RMS noise in each spectrum noted in Column 6. For easy comparison, we note the optical heliocentric velocity in Column 7. The FWHM velocity width is given in Column 9. Column 10 lists the peak optical depth, and Column 11 lists the derived H I column densities divided by the spin temperature (Rohlfs 1986):

$$N(\text{HI})/T_{\text{S}}(\text{cm}^{-2} \text{ K}^{-1}) = 1.823 \times 10^{18} \int \tau d\nu \quad (3.7)$$

Binning the sample in four L_{IR} ranges, we find that a larger fraction of galaxies with H I absorption come from the highest IR luminosity bin (Table 3.5). We do not find as strong a trend in the 1.4 GHz continuum flux levels as noted in Part I. In five of the galaxies with absorption, the peak velocity of H I absorption is greater than the optical heliocentric velocity, suggestive of inflow. We note, however, that the optical velocities are uncertain. High resolution imaging of the H I gas is needed to pin down the actual dynamics of the gas (see Momjian et al. 2003).

Table 3.4. Parameters of Galaxies with H I Absorption

IRAS Name	D_L^a (Mpc)	$\log \frac{L_{\text{FIR}}}{L_\odot}$	$\log \frac{L_{\text{IR}}}{L_\odot}$	Δt (min)	RMS (mJy)	V_{Helio} (km s $^{-1}$)	$V_{\text{HI-Peak}}$ (km s $^{-1}$)	ΔV_{50} (km s $^{-1}$)	$\tau_{\text{max}} \times 10^{-2}$	$N_{\text{HI}}/T_s \times 10^{18}$ (cm $^{-2}$ K $^{-1}$)
(1)	(2)	(3)	(4)	(5)	(6)	(7)	(8)	(9)	(10)	(11)
03144+0104	102.7 ± 0.3	10.65 ± 0.05	10.91 ± 0.15	4	0.79	7098	7159 ± 16	43 ± 23	7.0 ± 1.0	7.0 ± 0.4
03315+0055 [†]	210.3 ± 0.0	11.18 ± 0.06	11.45 ± 0.14	5	0.73	14235	14838 ± 97	118 ± 126	9.0 ± 2.0	16.4 ± 0.9
03359+1523	155.4 ± 0.2	11.33 ± 0.04	11.57 ± 0.13	15	0.30	10613	10739 ± 11	141 ± 82	15.0 ± 1.0	42.8 ± 0.6
04154+1755	246.8 ± 0.3	11.58 ± 0.08	11.88 ± 0.10	5	0.54	16659	16815 ± 17	78 ± 8	6.0 ± 0.8	9.3 ± 0.3
04232+1436	352.3 ± 0.2	11.82 ± 0.06	12.12 ± 0.06	10	0.44	23972	23646 ± 15	78 ± 13	17.0 ± 1.0	38.9 ± 0.7
06375+3338	75.3 ± 0.1	10.49 ± 0.06	10.77 ± 0.06	5	0.52	5137	5273 ± 5	53 ± 7	17.0 ± 1.0	23.0 ± 0.7
–	–	–	–	–	–	–	5092 ± 3	65 ± 32	7.0 ± 1.0	7.3 ± 0.4
09432+1910	235.0 ± 1.0	11.49 ± 0.06	11.78 ± 0.06	2	0.82	16048	16035 ± 69	163 ± 182	50.0 ± 6.0	66.9 ± 2.9

[†]03315+0055 exhibits both emission and absorption features. Values in this table are for the absorption portion only.

^a D_L derived using the velocity of peak H I absorption except in the case of 03315+0055 where we use the H I emission peak velocity.

Table 3.5. Statistical Summary

IR Luminosity (L_{\odot})	$L_{\text{IR}} < 10^{10.5}$	$10^{10.5} \leq L_{\text{IR}} < 10^{11.0}$	$10^{11.0} \leq L_{\text{IR}} < 10^{11.5}$	$L_{\text{IR}} \geq 10^{11.5}$
HI 21 cm Absorption for Different L_{IR} Ranges				
No. (abs. or abs.+emis.)	0	2	1	4
Total No. of galaxies	10	22	13	16
% with Absorption	0%	9.1%	7.7%	25.0%
1.4 GHz Flux Density Distribution				
Total Sample (N=61)				
Median NVSS Flux (mJy)	16.4	20.3	13.0	21.3
Mean NVSS Flux (mJy)	12.4±0.3	23.9±0.1	15.4±0.1	20.9±0.1
Galaxies with Absorption (N=7)				
Mean NVSS Flux (mJy)	–	20.2±0.1	20.8±0.1	28.36±0.1

3.7 Notes on Individual Objects

- **IRAS 02433+1544:** The absorption at 9500 km s^{-1} (see Fig. 3.3) is from H I emission of a galaxy in the off position scan. A probable source is 2MASX J02574457+1539218, $168'$ from IRAS 02433+1544. It has a measured H I line strength of 1.1 Jy km s^{-1} (Springob et al. 2005) and a redshift of 0.032 (corresponding to a heliocentric velocity of 9518 km s^{-1}).
- **IRAS 03207+3734:** The H I spectrum of this source shows two emission lines (see Fig. 3.3). The H I emission at 5592 km s^{-1} is associated with IRAS 03207+3734. The source of the other emission at $\sim 6500 \text{ km s}^{-1}$ is questionable. This IRAS source is also referred to as UGC 02710, known to be in a galaxy group. However, the offset in velocity between the two emission peaks of $\sim 1000 \text{ km s}^{-1}$ makes it unlikely to be coming from the cluster. We measured a flux of 1.1 Jy km s^{-1} . The emission at $\sim 6500 \text{ km s}^{-1}$ could be from a number of galaxies within the field of view. One potential source is NVSS J032402+374348, $1.67'$ away. It has a measured 1.4 GHz continuum flux of $\sim 103 \text{ mJy}$, but no redshift information listed in NED. B2 0320+37A is another candidate, at a separation of $2.7'$. Its measured 1.4 GHz flux is 8.7 mJy (Condon et al. 1998). It is also possible that the seeming source of emission is from absorption in the off position. This is the most likely source, as there is a galaxy at the right redshift for which the H I line has been detected in absorption. UGC 02714 is $16.5'$ from our IRAS source and has a redshift of 0.021 (6422 km s^{-1}) (Springob et al. 2005).
- **IRAS 03288+0108:** The optical velocity for this source is reported to be $9295 \pm 51 \text{ km s}^{-1}$. We detect the H I line at $\sim 8800 \text{ km s}^{-1}$.

- **IRAS 03315+0055:** Emission and a possible absorption component are detected in the spectrum for this source. The absorption component is at a velocity 400 km s^{-1} greater than the emission, consistent with inflow.
- **IRAS 04489+1029:** The baseline in this spectrum is very ripply. The component that appears to be a low signal-to-noise H I emission detection at 7700 km s^{-1} is not real. The behavior is different in each polarization, which is characteristic of RFI. We attempted to measure the H I line emission at 8500 km s^{-1} , but note that it might also be suspect due to the RFI.
- **IRAS 05054+1718:** The baseline for this spectrum is very ripply and it is doubtful that the possible absorption detection at 5050 km s^{-1} is real. For this reason, this source has been excluded from our formal absorption analysis. If we fit a 5th order polynomial to the baseline, we find this component has a depth of 2 mJy , slightly above the 3σ level. The peak optical depth is 0.078 ± 0.02 . The velocity of peak optical depth is $5051 \pm 8 \text{ km s}^{-1}$ and the FWHM is $85 \pm 90 \text{ km s}^{-1}$. $\int \tau d\nu$ is 4.7 ± 0.4 , which corresponds to a column density of $8.7 \pm 0.7 \text{ cm}^{-1} \text{ K}^{-1}$.
- **IRAS 06375+3338:** H I is detected in absorption at two different velocities: 5273 km s^{-1} and 5092 km s^{-1} . The measured parameters for both lines are presented in Table 3.4.
- **IRAS 08071+0509:** The dip in the spectrum at $15,700 \text{ km s}^{-1}$ is not absorption, but due to RFI at a rest frequency of 1350 MHz . The source of this RFI is the San Juan Airport radar.
- **IRAS 08072+1847:** The broad dip in the spectrum between 4000 and 4500 km s^{-1} is not absorption, but due to a very ripply baseline.

- **IRAS 08169+0448:** The steep dropoff in the spectrum at 4500 km s^{-1} is due to RFI at the edge of the H I emission. This RFI only occurs in one polarization and affects frequencies between 1394 and 1398 MHz. No regular known sources of RFI occur at these frequencies, but there are some harmonics of cameras and beepers noted in the L-band birdie RFI reference page (<http://www.naic.edu/~phil/rfi/rfiflist.html#lband%20birdies>).
- **IRAS 08507+3520:** There is a flat component to the H I emission between $17,000$ and $17,300 \text{ km s}^{-1}$. IRAS 08507+3520 is a complicated source that is clearly merging/interacting resulting in an odd-shaped spectrum (see Fig. 3.8).
- **IRAS 09192+2124:** The two dips in the spectrum at $22,800$ and $23,300 \text{ km s}^{-1}$ are not quite 2σ . The RMS noise in this spectrum is 0.55 mJy . This spectrum is very noisy because the first scan was ruined by a large RFI signal at 1330 MHz from the San Juan Airport radar, affecting the entire band. The spectrum we present is from the second observation, only a four minute integration.
- **IRAS 09351+0259:** H I emission is detected at 5000 km s^{-1} in addition to the emission at $\sim 6981 \text{ km s}^{-1}$ from IRAS 09351+0259. The optical field for this IRAS source shows two galaxies. A likely candidate for the 5000 km s^{-1} line is NGC 2960, which is $65'$ from the target source. It is too far away at $65.2'$ to be within the field of view during the target observations, but as it has been detected in H I absorption at 4932 km s^{-1} , the apparent emission at this velocity is really absorption in the off position. This also explains the negative continuum level (Springob et al. 2005). The H I emission of the IRAS source is much broader than many other sources. As the field is rich with galaxies

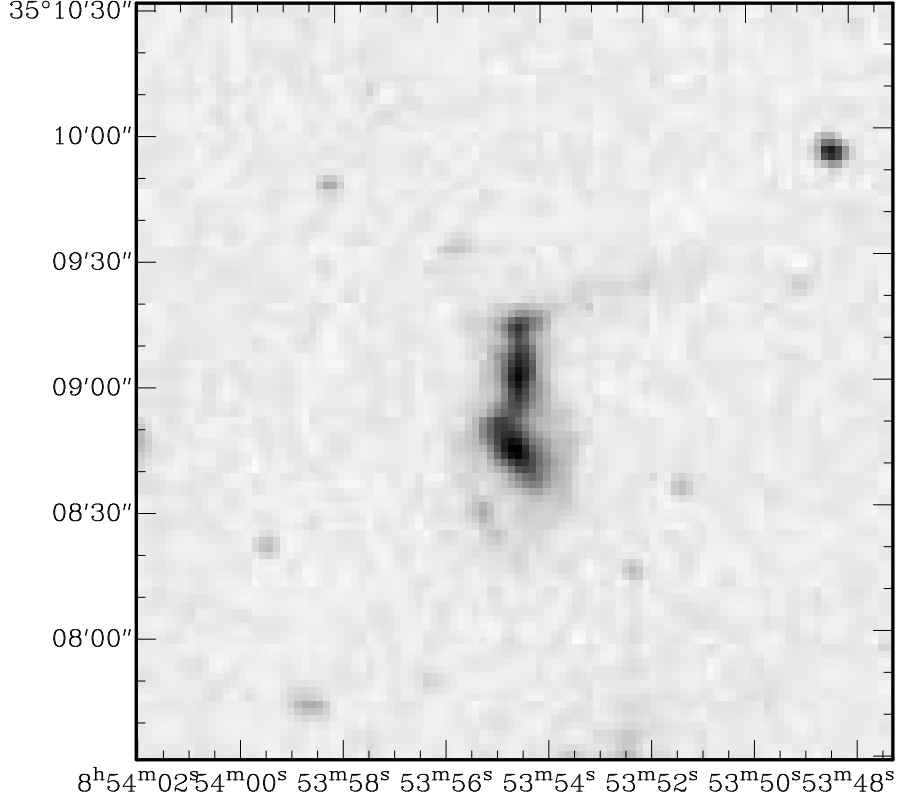


Figure 3.8: Optical image of IRAS 08507+3520 from the Palomar 48 inch telescope. Image is $3' \times 3'$, digitized in 1994 by the Space Telescope Science Institute (ST ScI).

at similar velocities, it is quite possible that not all of the H I emission is coming from IRAS 09351+0259. Nearby sources include an SDSS galaxy $0.21'$ away (6981 km s^{-1}), NGC 2936 $0.29'$ away (6989 km s^{-1}) and another SDSS galaxy $0.52'$ away (7161 km s^{-1}). These galaxies are all well within the $\sim 3.5'$ primary beam of the Arecibo telescope at L-band. None of these galaxies have H I measurements noted in the literature.

- **IRAS 09406+1018:** RFI at a rest frequency of 1340 MHz is most likely the source of the dip in the spectrum at $16,800 \text{ km s}^{-1}$.

3.8 Conclusions

3.8.1 Summary of Results

We observed 77 galaxies from the IRAS-NVSS 2 Jy sample in the range $2^{\text{h}} < \text{R.A.} < 10^{\text{h}}$ with the Arecibo Radio Telescope. We used the L-band wide receiver and the eight-board WAPP spectrometer to search for emission and/or absorption in H I, OH 18 cm main and satellite lines, HCN and HCO⁺. We detected H I in emission or absorption in 61 galaxies, with 52 being new detections. Six sources revealed strong absorption and one source had emission and weak absorption. We did not detect any other lines, the majority of these bands being ruined by RFI.

3.8.2 Future Work

We have begun the final portion of this survey (Part III), having completed observations of 49/140 galaxies in the R.A. range between 0-2 hours and 10-20 hours. Upon completion of this work, we will do a statistical analysis of the entire population, including H I measurements in the literature (Martin et al. 1991; van Driel et al. 2001).

One property that can be examined is the H I to H₂ mass ratio in each galaxy, by comparing the H I flux with CO flux. The very weak trend in our sample between H I mass and IR luminosity is consistent with the current understanding (Wong and Blitz 2002) that H I must be converted into molecular gas prior to star formation. Molecular gas mass should correlate better with star formation and hence IR luminosity. Comparing H I to H₂ mass ratios will constrain this conversion process and possibly shed light on the proper CO-H₂ ratio for the more extreme interstellar medium environments of ULIRGs. We compared our sample and Part

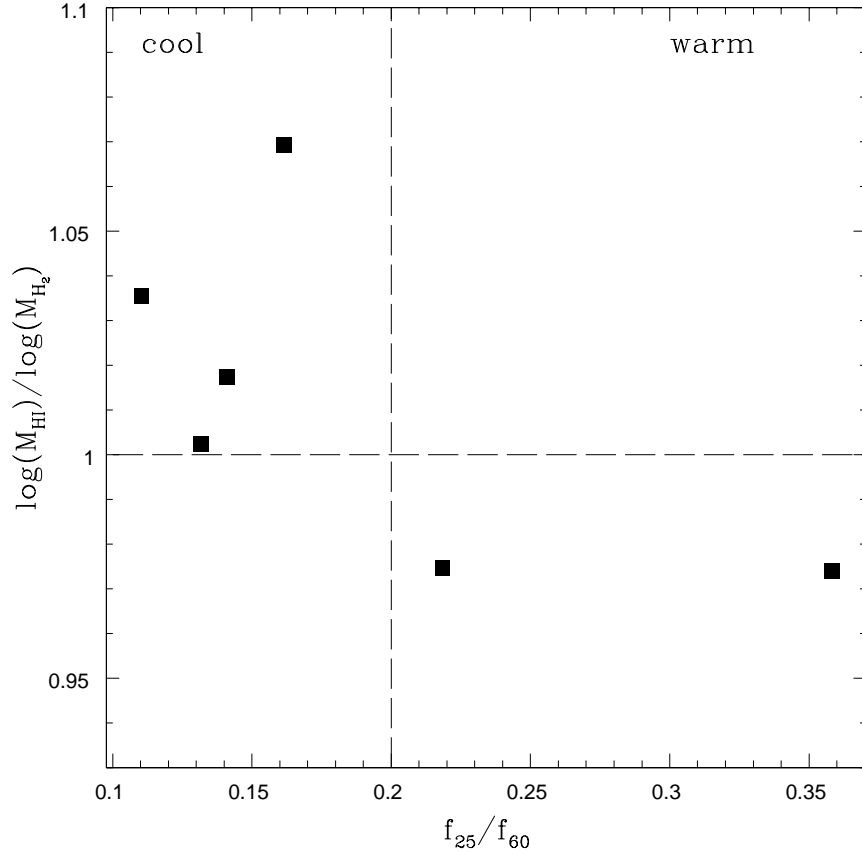


Figure 3.9: H I mass/H₂ mass vs. f_{25}/f_{60} for six galaxies in the Part I right ascension range. $M(\text{H}_2)$ was calculated from CO(1-0) measurements in these galaxies by Gracia Carpio et al. (2010 in prep.). We compute the ratio of H I mass derived from H I emission measurements with the f_{25}/f_{60} ratio. This figure indicates that cool systems have more atomic gas, while warm systems have more molecular gas.

I with CO(1-0) measurements by Gracia Carpio et al. (2010, in prep.). We found six galaxies in Part I with CO(1-0) measurements, and none in our sample. We computed the mass ratio of H I to H₂ and compared with a variety of observed and derived parameters. We found no correlation with redshift, infrared luminosity or far infrared luminosity. However, comparing the mass ratio with the f_{25}/f_{60} does show a trend. Figure 3.9 indicates that cool systems have more atomic gas, while warm systems have more molecular gas. No global conclusions should be drawn

from such small number statistics, but this hint of a trend warrants further analysis with a larger sample.

We also plan to conduct follow up observations of interesting objects, including the galaxies with OH emission and absorption in Part I of this survey and hopefully new detections yet to be made. We plan to investigate galaxies with H I absorption, imaging spatial gas distribution with the Expanded Very Large Array (EVLA).

Chapter 4

Sub-Arcsecond Molecular Gas Imaging and Phase Correction

4.1 Abstract

We use a paired antenna calibration system (PACS) for atmospheric phase correction at the Combined Array for Research in Millimeter-Wave Astronomy (CARMA) in its two longest, sub-arcsecond resolution baseline configurations. We present the results and analysis of a systematic study of several hundred test observations taken routinely during the 2009-2010 winter observing season. In this experiment, we pair the eight 3.5-m antennas from the Sunyaev-Zeldovich Array (SZA) with CARMA 6.1-m and 10.4-m antennas on baselines ranging from a few hundred meters to ~ 2 km. In these tests, the paired calibration antennas observe quasar pairs in order to quantify the usefulness of this phase correction method under different conditions. The angular separation between the atmospheric calibrator and target source is the most important factor: we find phase correction is successful for angular separations less than six degrees. Corrections are less successful if the atmospheric calibrator is

intrinsically weak or at low elevation. We find correlations, although less significant, with measured weather indicators (τ_{225} , atmospheric delay, diurnal variations and cloud cover). We conclude by applying this atmospheric calibration technique to observations of the luminous infrared galaxy Arp 193.

4.2 Introduction

4.2.1 The Problem

Many problems in astrophysics, such as the study of molecular gas emission in distant galaxies, require attaining sub-arcsecond angular resolution. This resolution corresponds to the diffraction limit of a millimeter-wave interferometer with baselines of a kilometer or longer. Realizing the diffraction limit in these long baselines happens rarely because it requires a very stable atmosphere (Carilli and Holdaway 1999). Variability of the index of refraction in the troposphere introduces variable time delays that, in effect, change the position of the source, analogous to optical “seeing” (Coulman and Vernin 1991; Masson 1994). The result of this positional jitter is that flux from the source is smeared across large scales in the resulting map. Under these conditions, the measured flux of a source is reduced by the coherence factor, $e^{-\sigma_\phi^2/2}$, where σ_ϕ is the atmospheric phase error (Thompson et al. 2001). Fluctuations in the refractive index are associated with changes in the water vapor content (wet terms) or in the air density and temperature (dry terms) in the troposphere over each antenna (Lay 1997a,b).

With improved receiver temperatures and growing interest in observations at the highest resolution, the importance of correcting for atmospheric phase fluctuations has increased. The troposphere is a limiting factor in the sensitivity and dynamic range unless a method of phase correction is used. As described by

Beasley and Conway (1995) and Bremer (2002), phase correction is applicable for interferometers, whether linked or non-linked (including the space interferometry networks where at least one antenna is ground-based). See Carilli and Holdaway (1999), Carilli et al. (1999), and references therein for a comprehensive review of the troposphere's effect on millimeter astronomy. Methods of atmospheric phase correction include indirect determination of phase errors from measurement of water vapor content in the atmosphere via emission lines or continuum power, and direct methods to measure phase errors including self-calibration, fast-switching, dual-beam, and paired antenna calibration. Each method has its advantages and limitations, which we briefly summarize.

Indirect Determination of Phase Errors: Water Vapor Radiometry and Total Power

The water vapor content in the atmosphere is a large contributing factor to the pathlength variations in the troposphere. The water content can be measured by either observing a strong atmospheric emission line (water vapor radiometry - WVR) or the continuum emission of water (total power). WVR makes use of strong atmospheric water emission lines at 183 GHz or 22 GHz. WVR at 183 GHz has been demonstrated to work over short periods of time on Mauna Kea at an elevation of approximately 4000 meters, with the first operating radiometer built at the JCMT-CSO interferometer (Wiedner et al. 2001), and was chosen for the high elevation (5000 meter) Atacama Large Millimeter Array (ALMA). However, the 183 GHz emission line is so strong it can saturate if the precipitable water vapor column exceeds 3 mm, limiting its usefulness at moderate or low elevation sites. The weaker 22 GHz water line is not saturated and has been tested at several observatories: the Owens Valley Radio Observatory (OVRO) millimeter array at an elevation of

1200 meters (Woody et al. 2000), the Plateau de Bure Interferometer (PdBI) at an elevation of 2550 meters (Bremer et al. 1996) and the Australia Telescope Compact Array (ATCA) at an elevation of 237 meters (Sault et al. 2007). The OVRO system was demonstrated to effectively correct phases for 3 mm observations in good weather, although the system did not improve observations during typical observing conditions or at higher frequency, likely because of its hardware limitations (e.g. room temperature amplifiers).

At frequencies away from these water lines, emission is optically thin and observations of the brightness temperature allow a direct determination of the column density of water vapor (Wright 1995). Groups have used the continuum emission of water for atmospheric calibration at the former Berkeley-Illinois-Maryland-Association (BIMA) millimeter array (Zivanovic 1992; Zivanovic et al. 1995), the Institut de Radioastronomie Millimétrique (IRAM) 30 m telescope (Bremer 2002; Bremer et al. 1996), and the submillimeter array (SMA) interferometer (Battat et al. 2004). Total power measurements frequently use the primary antenna receivers, which are more sensitive than separate dedicated antenna receivers often used for WVR. Uncertainties in systematics of the measurement and the contribution of atmospheric components such as liquid water droplets or ice crystals in clouds are hard to model or fit with precision.

The indirect method suffers from some limitations. They only measure the wet component, which usually dominates, but is not the sole contributor to variable delay. A major disadvantage is their reliance on an atmospheric model. Finally, we note that radiometers must be able to measure the water vapor to high precision in order to accurately compute the additional variable delay. The result is an atmospheric correction system that works very well under some conditions, but is not consistent.

Direct Monitoring of Phase Errors

Alternatives to techniques which only measure the wet component directly monitor phase errors using a point source near the target, analogous to natural guide adaptive optics in optical astronomy. Instead of a natural guide star, we use a bright compact radio source, most often a quasar, to track the phase fluctuations. Ideally, the angular separation between the calibrator and source is small enough to sample the same region of the troposphere. Self-calibration, fast-switching, dual-beam and paired antenna phase correction each utilize this concept for phase correction, differing in implementation. We briefly discuss each:

(1) Self-calibration. This requires a bright, compact source in the field of view and is not broadly useful for imaging of weaker sources. If source conditions are suitable for self-calibration, it can be applied in conjunction with other methods (Cornwell and Wilkinson 1981, 1984; Schwab 1980).

(2) Fast-Switching. Shortening the normal source-calibrator cycle times can improve phase correction, but there is a trade off between time loss and improvement made when slew time is of order a minute or longer. This has motivated the development of more efficient alternatives. Fast-switching will be implemented at ALMA (see Holdaway 1992, for details) and has been tested at Nobeyama (Morita et al. 2000). In this method, science antennas are equipped with specialized drives which allow slewing of up to several degrees in a matter of seconds instead of minutes. High sensitivity receivers are a major advantage because the science antenna itself is used, allowing use of weaker calibrators. However, the atmospheric correction is not simultaneous to the science observation, which remains a major drawback. Furthermore, this technique requires construction of new antennas.

(3) Dual-beams. In the dual-beam setup, two steerable receivers located in the focal plane simultaneously observe sources with angular separation ranging from

0.3 to 2.2 degrees (Kawaguchi et al. 2000). The first experiment was performed by Honma et al. (2003), observing two masers at 22 and 43 GHz. This system has the advantage of a high sensitivity receiver and a stable antenna that does not need to oscillate between the target and calibrator. One disadvantage is the maximum angular separation of the beams based on the off-axis design, which may be too confining for science projects where the closest bright calibrators are farther away. The primary disadvantage to this method is that it also requires specially built and designed antennas and is not an option for pre-existing arrays.

(4) Paired Antenna Methods. This technique allows simultaneous phase correction and can be implemented without specialized antenna designs, assuming extra antennas are available or can be “borrowed” from the primary science array. This is the method discussed in detail in this paper. We stress that the most important limitations we find for paired antenna calibration will also affect fast switching and dual-beam calibration.

4.2.2 Description of Paired Antenna Phase Correction

The paired antenna method for atmospheric phase correction is illustrated in Figure 4.1. In addition to the standard geometrical delay, τ_g , atmospheric cells with varying indices of refraction n insert an additional unknown time-varying delay into the system, $\Delta\tau$, for antennas separated by a distance, B . We position the paired antenna close to the primary antenna so at the height of the turbulent layer of thickness, Δh , the path through the atmosphere is essentially the same and the unknown delay can be determined. The atmospheric calibrator (red) is chosen with small enough angular separation, θ , to probe the characteristic scale size of the turbulence. The height of the turbulent layer can vary seasonally and diurnally, depending on geographic location. The thickness has been found to be of order a few hundred meters

or thinner in most cases (Grubišić et al. 2008). The *paired* antennas continuously monitor the atmospheric calibrator during science observations, so there is no loss of observing time and temporal variations of $\Delta\tau$ are well tracked.

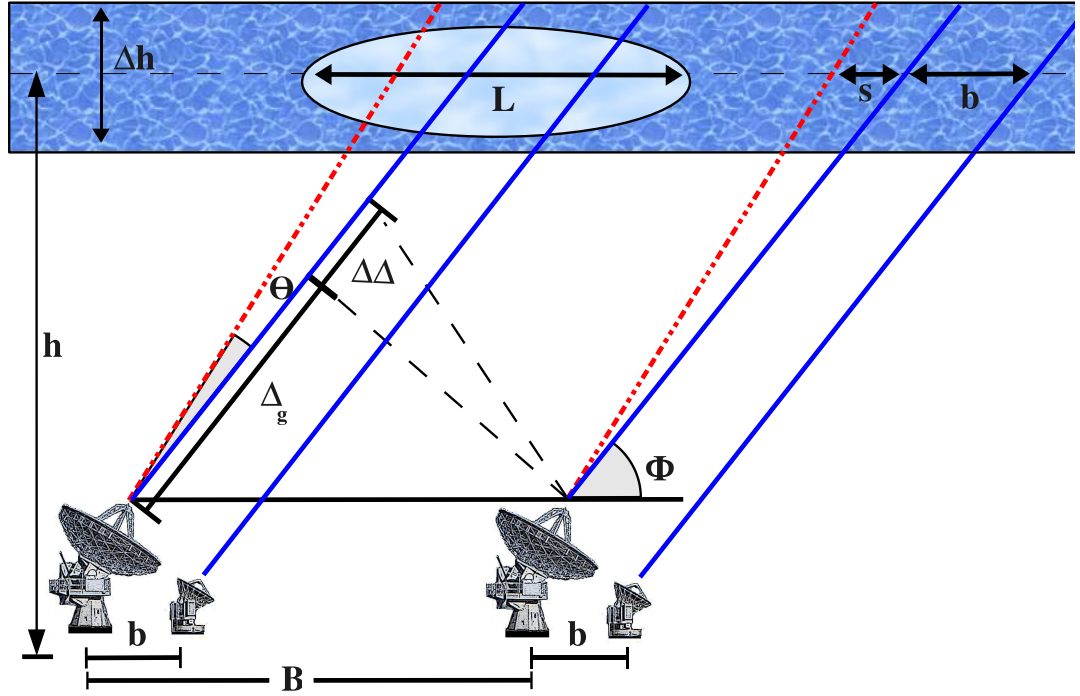


Figure 4.1: Atmospheric phase correction using paired antennas. In addition to the standard geometrical delay, τ_g , water vapor fluctuations in the troposphere insert an additional unknown delay, $\Delta\tau$. To determine this delay, we locate a smaller paired antenna close to the primary antenna so the path through the turbulent layer will be essentially the same. The turbulent layer has a characteristic height, h , a thickness, Δh , and can be conceptualized to have an average index of refraction, n within cells of characteristic size, L . The paired antenna constantly monitors an atmospheric calibrator (solid blue) with angular separation, θ , from the source (dashed red). For a successful C-PACS correction, the corresponding linear distance in the troposphere, s , should be of order or smaller than the scale size of the turbulent cell (analogous to the size of an isoplanatic patch in adaptive optics).

Paired antenna correction has been tested at Nobeyama (NMA) by Asaki et al.

(1996, 1998). They observed a quasar and a communications satellite simultaneously, using a regular science antenna for phase fluctuation monitoring (see Figure 1 in Asaki et al. 1996). CARMA PACS system (C-PACS) is unique in implementing this paired antenna phase correction using auxiliary telescopes instead of pilfering antennas from the science array. Separate, smaller, antennas preserve all science antennas for use on the science target, so that there is no reduction in sensitivity or imaging capabilities. In addition, separate calibration antennas can be placed close to the science antenna, and can observe at lower frequency, which is advantageous as most QSOs are brighter at lower frequencies. The CARMA C-PACS experiment has eight paired baselines, for a total of 28 baselines of varying length and orientation. This is the largest paired antenna experiment to-date. A recent overview of CARMA’s Paired Antenna Correction System (C-PACS) can be found in Pérez et al. (2010).

The paper is organized in the following manner: In §4.3 we describe our experiment setup. Data reduction procedures are discussed in §4.4. We present the results of our phase correction experiment in §4.5, with further discussion and analysis in §4.6. We give an example of how C-PACS improves imaging of a scientific source in §4.7, examining the ultraluminous galaxy, Arp 193. Conclusions and recommendations are given in §4.8.

4.3 Experiment Setup

In this section, we describe the specific implementation of the paired antenna calibration at CARMA (C-PACS), our experimental design and data reduction procedure.

We implement this phase correction method during two winter observing seasons of CARMA’s two longest baseline configurations, establishing a large number of ob-

servations with varying angular separations between our target and calibrators (as suggested for further work by Asaki et al. 1998). Our results are relevant to both the paired antenna and the fast-switching methods of phase correction. The primary goal of our paper is to demonstrate how the paired antenna method improves observations, reducing atmospheric decorrelation. We explore the effectiveness of C-PACS, specifically examining how improvement depends on angular separation, θ , calibrator elevation, ϕ , atmospheric calibrator brightness, S , and measured weather indicators.

In the two longest baseline configurations at CARMA (A and B), we paired eight 3.5-m antennas from the Sunyaev-Zeldovich Array (SZA) with CARMA 6.1-m and 10.4-m antennas on the longest baselines (see Figure 4.2 for a graphical overview of the configurations). We hereafter refer to the 6.1-m and 10.4-m antennas as the “science” array and the paired 3.5-m antennas as the “calibration” array. Infrastructure to support the calibration array was constructed so paired antenna pads would be as close as possible to the science antenna while minimizing shadowing and utilizing previous infrastructure constraints, such as roads and conduits for fibers. The distance between the paired calibration antenna and the science antenna ranges from 20 to 25 meters. Each array has its own local oscillator and correlator. The science array operates in the 3 mm band (85-140 GHz) or in the 1 mm band (215-260 GHz). The C-PACS calibration antennas operate at a frequency of 31 GHz, single sideband with fixed tuning and a bandwidth of 8 GHz (26-36 GHz, Muchovej et al. 2007).

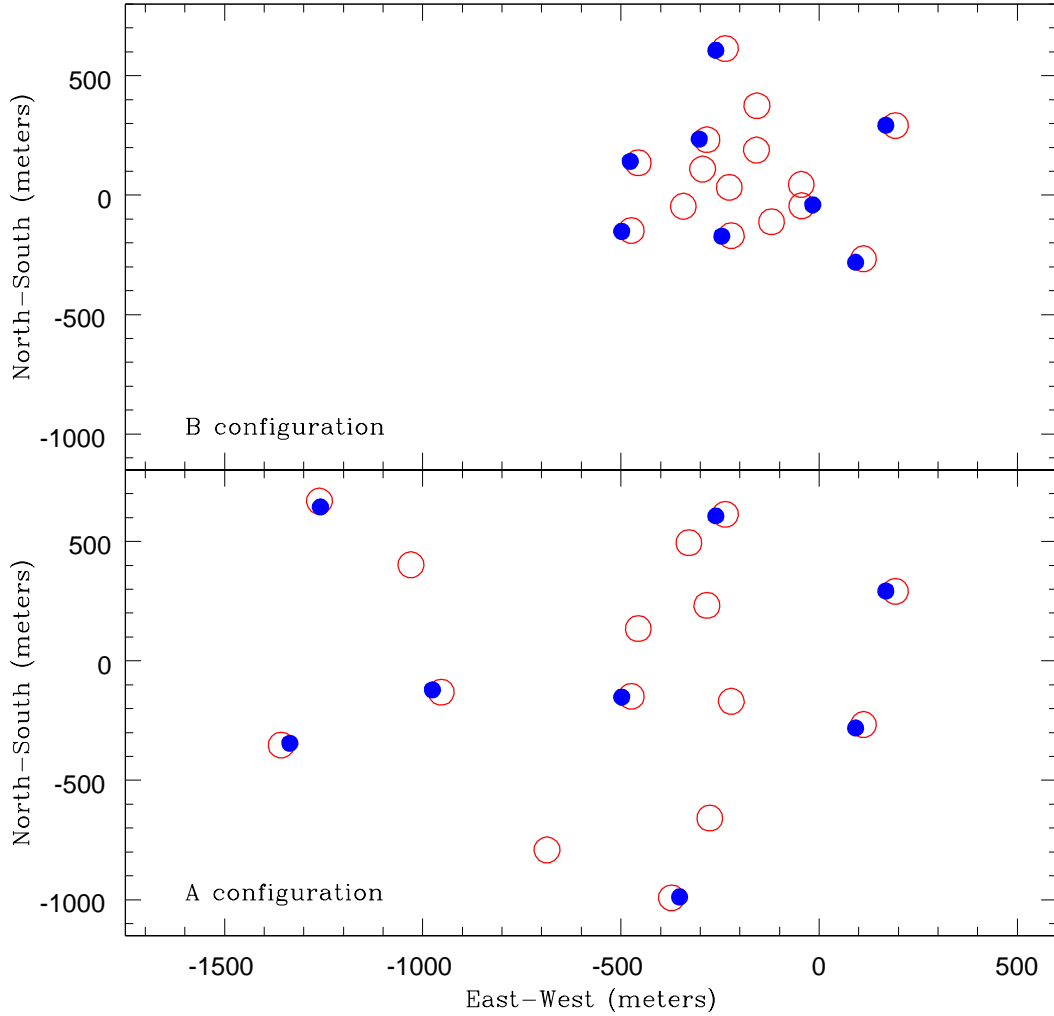


Figure 4.2: 2009/2010 A & B antenna configurations. The primary science antennas (6.1- & 10.4-m antennas) are denoted with red circles and the 3.5-m paired antennas by smaller filled blue circles. The symbols are centered on the antennas position (not to scale). Paired antennas are positioned ~ 20 -25 m from the science antenna, usually to the west, but not always. We examined and did not find the paired antenna orientation to affect our results. Baseline separations are 89 - 946 meters (B configuration) and 150 - 1883 meters (A configuration).

In order to test how well C-PACS works in a variety of conditions, we designed an experiment to be run several times weekly in between science tracks. These short test observations (MINIPACS) are comprised of pairs of quasars with a range of angular separation observed by the science and calibration arrays. The duration of each MINIPACS experiment is between five and 45 minutes, depending on the number of quasar pairs observed. The MINIPACS observations always begin by observing the same bright quasar for 5-10 minutes with both the science and calibration array. The science antennas continue to observe this bright quasar, a proxy with known structure for the “science target”, while the calibration antennas move to observe other quasars with similar properties to potential atmospheric calibrators in a science observation. The 24 quasar pairs range in angular separation from 0.48 degrees to 12.16 degrees (see Table 4.1 for QSO properties). The calibration antennas observe each quasar for approximately five minutes and then move to another atmospheric calibrator. Each MINIPACS experiment includes between two and six pairs of quasars.

We setup the respective correlators and tuned the antennas in the same manner for every observation; the rest frequencies were 99.7 GHz for the science array and 30.938 GHz for the calibration array (hereafter, we refer to these frequencies as 100 GHz and 31 GHz). In total, we obtained 152 MINIPACS tracks in A and B configurations during the winter season¹ 2009-2010. These were taken at different times each day and the final sample spans a broad range of observational parameters. During normal science tracks, the science and calibration arrays simultaneously observe the same calibrators (e.g. bandpass, flux, and phase). Science tracks provide significant “zero separation” data which we incorporated into our analysis.

¹There are seasonal variations in the mean water vapor content in the troposphere (Bean et al. 1966), with the lowest content occurring during the wintertime.

Table 4.1. Observed QSOs

Source	Alias	R.A. (J2000)	Dec (J2000)	S _{95GHz}	S _{30GHz}
J0303+472	...	03:03:35.2	+47:16:16.3	0.72	0.81
J0310+382	...	03:10:49.9	+38:14:53.8	0.48	1.60
J0313+413	...	03:13:02.0	+41:20:01.2	0.73	0.75
J0319+415	3C84	03:19:48.2	+41:30:42.1	3.92	13.0
J0336+323	...	03:36:52.0	+32:19:48.6	1.64	2.8
J0349+461	...	03:49:18.7	+46:09:59.7	0.30	0.56
J0414+343	...	04:14:37.3	+34:18:51.2	0.25	0.71
J0418+380	3C111	04:18:21.3	+38:01:35.8	1.96	5.8
J0423+418	...	04:23:56.0	+41:50:02.7	0.93	1.7
J0432+416	3C119	04:32:36.5	+41:38:28.4	0.34	1.2
J0920+446	...	09:20:58.5	+44:41:54.0	1.14	1.9
J0927+390	...	09:27:03.0	+39:02:20.9	3.28	7.2
J0948+406	...	09:48:55.3	+40:39:44.6	0.52	0.91
J1150-003	...	11:50:43.9	-00:23:54.2	0.20	0.70
J1222+042	...	12:22:22.5	+04:13:15.8	0.71	1.1
J1224+035	...	12:24:52.4	+03:30:50.3	0.30	0.31
J1229+020	3C273	12:29:06.7	+02:03:08.6	7.05	25.0
J1239+075	...	12:39:24.6	+07:30:17.2	0.57	0.73
J1256-057	3C279	12:56:11.2	-05:47:21.5	14.46	17.0
J1613+342	...	16:13:41.1	+34:12:47.9	2.60	4.3
J1625+415	...	16:25:57.7	+41:34:40.6	...	0.41
J1635+381	...	16:35:15.5	+38:08:04.5	3.44	3.5
J1637+472	...	16:37:45.1	+47:17:33.8	0.45	0.62
J1640+397	...	16:40:29.6	+39:46:46.0	0.50	1.0
J1642+398	3C345	16:42:58.8	+39:48:37.0	3.74	5.5

Table 4.1 (cont'd)

Source	Alias	R.A. (J2000)	Dec (J2000)	S _{95GHz}	S _{30GHz}
J1653+397	...	16:53:52.2	+39:45:36.6	0.69	1.0
J2203+174	...	22:03:26.9	+17:25:48.2	1.26	1.3
J2253+161	3C454.3	22:53:57.7	+16:08:53.6	14.72	12.0

4.4 Data Reduction

In this section we describe the data reduction procedure and algorithms specifically developed for the C-PACS correction. We performed the majority of data reduction in the standard way developed for CARMA observations using the Multichannel Image Reconstruction, Image Analysis and Display (MIRIAD) software package (Sault et al. 1995). After applying the standard interferometric calibrations (flagging, line-length, bandpass), we performed a long timescale self-calibration of the continuum data to remove instrumental phase offsets.

Instead of using standard 30 second integrations, we used 4 second integrations. Fast variations in phase are thought to be due primarily to atmospheric variations. The antenna phase gains we determine on four second timescales are a good representation of the delay variations $\Delta\tau$ introduced by the atmosphere. For the science data, we also performed the standard calibrations including bandpass calibration using a bright astronomical source.

Phase variations from the calibration antenna are applied to the science antenna using a specially written MIRIAD task, GPBUDDY. Conceptually, the phases from the calibration antenna are simply scaled and added to the antenna gain phases for

the science antenna at each time, interpolated if there is an offset in the four-second time stamps. Because the receivers in the calibration antennas operate at 31 GHz and the science observations occur at 100 GHz or 225 GHz, the atmospheric phases need to be scaled before applying them to the science antennas. The atmosphere is nondispersive between these frequencies, so once determined, the delay can be directly applied. As delay does not change with observing frequency in between 30 GHz and ~ 200 GHz, there is a linear scaling factor between the phases. Thus, the science array phase fluctuations are ~ 3 times that of the atmospheric array phase measured at 31 GHz for 3 mm observations and ~ 7 times that of the atmospheric array phase for 1 mm observations. In practice, we calculate the scaling factor for each CARMA channel separately, instead of using an average frequency value for a single LO setting.

After the application of the C-PACS correction, we remove slow residual instrumental drifts on time scales of 15 minutes. For comparison of the corrected CARMA data with non-corrected data, we reduce the CARMA data in the standard way, performing flagging, bandpass calibration, linelength correction and removing slow phase variations. In order to quickly process large amounts of data and to repeat data reduction with different parameters, we developed a pipeline process which we refer to as DRPACS. The details of this pipeline process will be made available in a CARMA Memo (Teuben, in prep.) The pipeline allows for data selection, data reduction, post processing, and bookkeeping.

4.5 Results

In this section, we report on the results of our MINIPACS observations. We give an example of the correction in §4.5.1. We discuss systematic effects (angular separation between the atmospheric calibrator and target source, intrinsic brightness of the atmospheric calibrator, and elevation during observations) in §4.5.2. We discuss environmental influences (atmospheric delay fluctuations, opacity, cloud cover and diurnal effects) in §4.5.3.

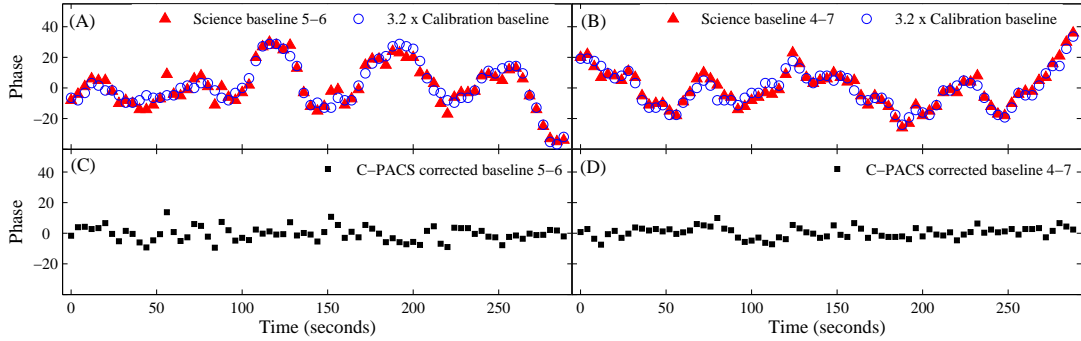


Figure 4.3: Example of C-PACS correction during A configuration (January 17, 2010). The top panels (A, B) show the measured phases during a five minute observation of 3C84 for baselines 5–6 (1678 m) and 4–7 (1034 m). The phases for the paired antennas are scaled by the ratio of the observing rest frequencies (99.7 GHz & 30.9 GHz) because the atmosphere is nondispersive. The bottom panels (C, D) show the residual phase after C-PACS correction. For CARMA baseline 5-6, the RMS phase decreases from 14.5° (A - red triangles) to 4.6° (C) after the C-PACS correction. For CARMA baseline 4-7, the RMS phase decreases from 12.4° (B) to 3.5° (D). This corresponds to an improvement in coherence from 96.9% to 99.7% and from 97.7% to 99.8% for baselines 5-6 and 4-7, respectively.

4.5.1 Successful C-PACS Correction

We begin by showing an example of the C-PACS correction in Figure 4.3. A five minute observation of the quasar 3C84 was taken during A configuration on January 17, 2010. Both the science array (6.1- and 10.4-m antennas) and the paired antenna array (3.5-m antennas) observed the same source ($\theta = 0^\circ$). We performed the data reduction described in §4.4. The resulting gains are plotted in Figure 4.3 (phase vs. time) for two of the 28 paired baselines. Figure 4.3a shows the visibility phase for baseline 5–6 (1678 m) and Figure 4.3b shows the visibility phase for baseline 4–7 (1034 m). The calibration antenna phases are scaled by a factor of 3.2, the ratio of the observing rest frequencies (99.7 GHz and 30.9 GHz). The atmosphere is nondispersive at these frequencies and indeed we find the predicted scaling factor to be an appropriate choice (see discussion in §3). The bottom panels, Figures 4.3c and 4.3d, show the residual phase variation after C-PACS correction. Significant improvement is evident. For science array baseline 5-6, the RMS phase decreases from 14.5° to 4.6° after the C-PACS correction, corresponding to an improvement in coherence from 96.9% to 99.7%. For science array baseline 4-7, the RMS phase decreases from 12.4° to 3.5° . The other 26 baselines show similar improvement.

As described in §4.3, our experiment consists of 152 MINIPACS tracks, each with several 5-10 minute observations of different quasar pairs. We consider each of the 28 baselines in every individual quasar pair observation as an individual trial. With 152 MINIPACS tracks, 3-7 quasar pair observations per track, and 28 baselines, our sample includes over 15,000 trials. For each trial, we compute the RMS phase scatter in degrees before and after C-PACS correction, calculate the corresponding coherence and compare the relative change in coherence as described for the example trials in Figure 4.3. We remove trials from our total sample in cases where we have

evidence that the entire observation or track was corrupted for some reason (for example, based on a system failure such as a problem in the correlator). The zero angular separation observations serve as our control sample and we remove trials from consideration when we fail to get a successful C-PACS correction for the zero angular separation trials that take place at the beginning of every track.

Failure Modes

In this section, we discuss how often C-PACS correction fails to improve coherence at zero angular separation and explore the reasons for failure.

We considered ~ 3000 MINIPACS trials where the science array and atmospheric array were observing the same source. C-PACS improves coherence 88% of the time (2616/2981 trial). Trials were removed from the sample for known technical problems with the array, such as wrong antenna pointing constants.

For zero angular separation data, we find that coherence improves from 0.5 to 0.8 for sources less than 45° , and from 0.65 to 0.85 for sources observed at elevations greater than 45° . We also find that the average improvement in coherence is 0.26 for baselines longer than 500 m, but only 0.1 for baselines shorter than 500 m. With elevation and baseline length in consideration, we find that C-PACS improves coherence 92% of the time for baselines longer than 500 m and 74% of the time for baselines shorter than 500 m.

The best way to predict if C-PACS will work during a science track is to analyze the zero angular separation data. If the C-PACS correction works for the zero angular separation data, it should also improve coherence during the observations. For this reason, science observations are taken on short time scales (of order a few minutes), and bracketed with zero separation phase/atmospheric calibrator observations.

4.5.2 Systematic Effects

In this section, we consider how angular separation, atmospheric calibrator flux and elevation affect the C-PACS correction. Observers choose phase calibrators that are point sources, as bright and close as possible to the science target. For successful C-PACS correction, the atmospheric calibrator must be close enough to the science target that the calibration antenna effectively samples the same atmospheric path, so that measured delays can be directly transferred to the science antenna. As suggested by Asaki et al. (1998), our experiment includes observations of quasar pairs with many different angular separations.

Figure 4.4 shows for each of these quasar pairs the expected coherence if there is no atmospheric decorrelation, indicated by a horizontal line which scales with the fluxes of the quasar pairs and the system temperature. For all observations, the “science target” is a bright quasar. The atmospheric calibrator flux varies from 0.3 Jy to over 15 Jy. The expected coherence is computed by measuring the magnitude and scatter of the amplitude for each quasar and adding the noise in quadrature from both the science and calibration antennas. The expected coherence is lower for quasar pairs with a weaker atmospheric calibrator, but in most cases the expected theoretical coherence is greater than 95%. This computation does not take into account noise added to the system by the fact that the atmospheric correction is not perfect and the antennas are looking through slightly different pieces of the atmosphere. We cannot expect the C-PACS correction to exceed this fundamental limit.

We compute the average coherence before and after C-PACS correction for trials with different angular separation. The average coherence for the science data alone is denoted with a triangle and the average coherence after C-PACS correction with

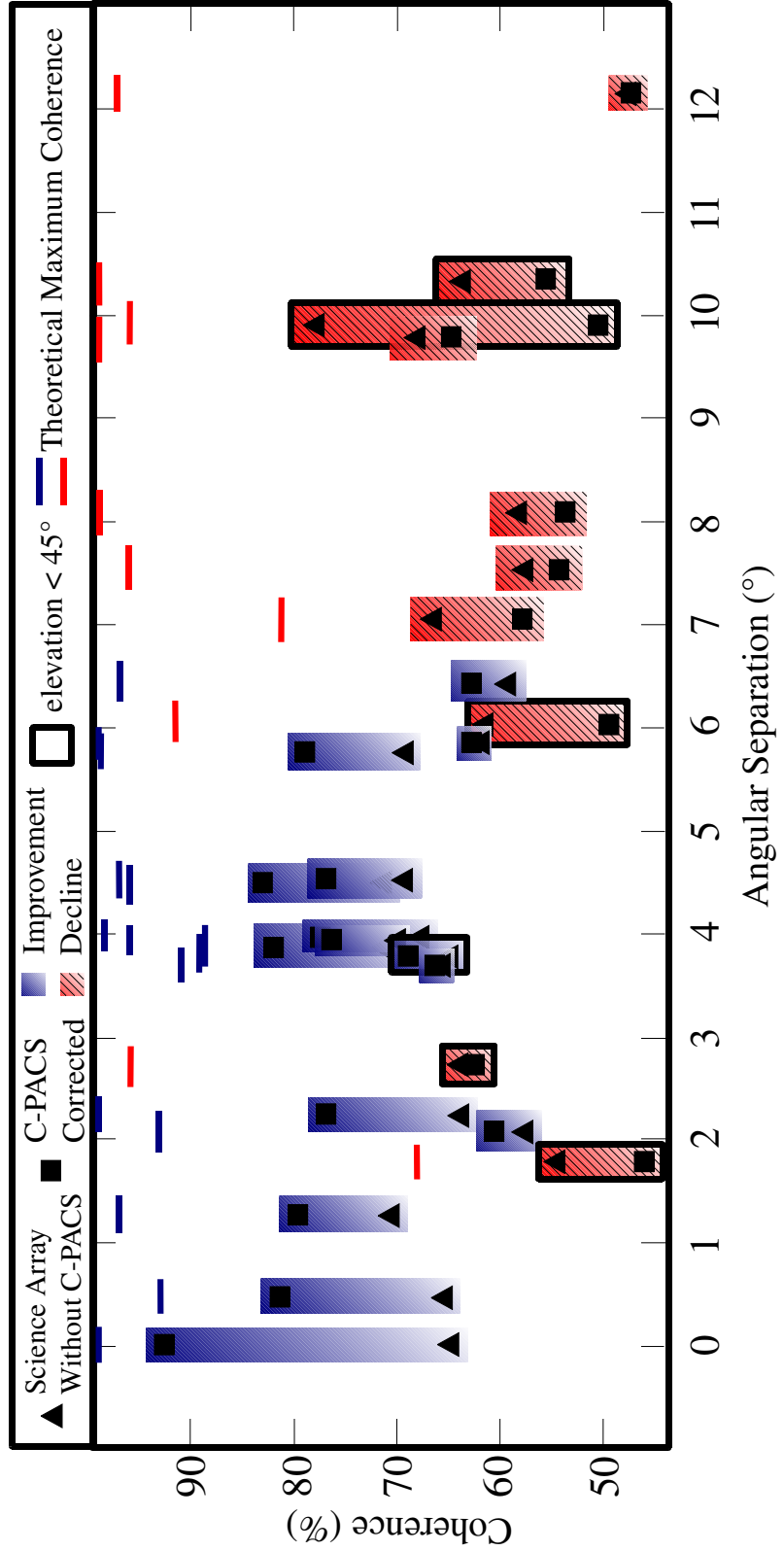


Figure 4.4: Average change in coherence as a function of angular separation. An improvement in coherence after C-PACS₁₂ correction (solid blue) is shown for all quasar pairs with an angular separation less than six degrees, save those sources with a mean elevation less than 45 degrees (outlined in black). For angular separation greater than six degrees, the C-PACS correction systematically fails and

a square. For those angular separations where there is an improvement in coherence, we have shaded the region of improvement in solid blue. For those angular separations where the coherence gets worse with C-PACS correction, the region is hatched and colored red. Figure 4.4 shows that for quasar pairs with an angular separation of less than six degrees, the average C-PACS correction is overwhelmingly successful, with a typical improvement in coherence greater than 10%.

There are two exceptions to this rule, where low signal-to-noise in the atmospheric calibration most certainly plays a role. Figure 4.4 shows that the phase coherence for two of the 16 quasar pairs with angular separation less than six degrees are degraded by C-PACS correction. For both of these, the average calibrator elevation is less than 45° . The figure shows that these quasar pairs are two of the six pairs (outlined in black) with low average elevations. The quasar pair at 1.80° separation (3C273 and J1224+035) contains the weakest atmospheric calibrator, J1224+035, measured to be ~ 0.3 Jy at 31 GHz. The only other angular separation less than six degrees not showing an improvement with C-PACS is the quasar pair separated by 2.74° (3C273 and J1222+042). The atmospheric calibrator (J1222+042) is brighter in this case (0.97 Jy), but still on the weaker side. In some individual trials, we get closer to the expected theoretical coherence. But in many cases, the atmosphere is not tracked perfectly, so the final coherence is less than the theoretical expectation based on the noise. The typical average coherence of our observations pre-PACS is $\sim 60\%$. For the pairs with an angular separation of less than six degrees, the average coherence improves to 80%. We see this reflected in images as an increase of peak brightness by about 15% and a tightening of the apparent size of the quasar image by a few percent.

In Figure 4.5, we investigate the dependence of improvement in coherence due to C-PACS correction on angular separation, quasar flux, and elevation in more

detail. We only consider trials with an elevation greater than 45° , and divide our sample into trials with angular separation $\theta \geq 6^\circ$ and $\theta < 6^\circ$ (Figure 4.5a). The change in coherence, ΔC , is positive for a successful C-PACS correction. For the ~ 6000 trials with $\theta < 6^\circ$, 81% show improvement, with a median $\Delta C = 0.14$. For the ~ 2000 trials with an angular separation greater than six degrees, only 40% show improvement. In other words, for large angular separations, one is more likely to degrade observations by applying the C-PACS correction than to improve them.

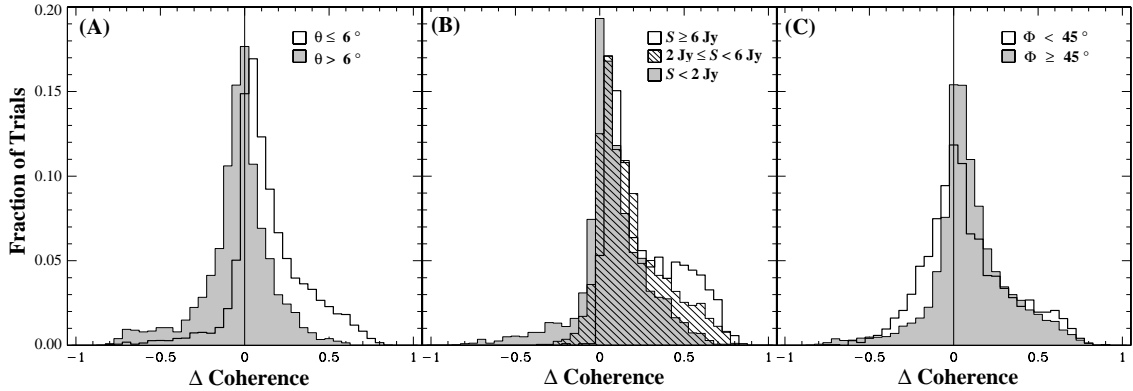


Figure 4.5: Change in coherence ($\Delta \text{Coh} = \text{PACS corrected} - \text{CARMA only}$) for basic calibrator parameters. Coherence is computed for every baseline in each track separately, as shown in Figure 4.3. (A) Distribution as a function of angular separation, θ , between the calibrator and the source: 81% of trials show improvement ($\Delta \text{Coh} > 0$) for $\theta < 6^\circ$, with median improvement in coherence of 0.14. In contrast, only 40% of trials show improvement for $\theta > 6^\circ$: coherence is more likely to be reduced with the C-PACS correction than improved. (B) Distribution as a function of calibrator flux. C-PACS correction fails more often for weaker calibrators ($S < 2 \text{ Jy}$). (C) Distribution as a function of calibrator elevation. We find correction is more successful for elevation $\Phi > 45^\circ$ with 71% of trials showing improvement compared to only 59% for $\Phi < 45^\circ$. (For (B) and (C) we only examine trials for which $\theta < 6^\circ$).

To evaluate the importance of the calibrator brightness (Figure 4.5b), we consider trials with elevation, Φ , greater than 45° and angular separation, $\theta < 6^\circ$. We bin our sample into three flux categories: bright ($S \geq 6 \text{ Jy}$), medium ($2 \text{ Jy} \leq S < 6 \text{ Jy}$), and weak ($S < 2 \text{ Jy}$). Figure 4.5b shows that we systematically improve trials for the brightest calibrators, with over 99% showing some improvement. The

median improvement in coherence is 0.18, translating to an expected amplitude brightening of almost 20%. For the medium strength calibrators, the median improvement is almost as good, at 0.16, with over 88% showing improvement. The median improvement drops to 0.11, with 71% of the trials showing improvement for the weaker calibrators. We note that the C-PACS correction is successful more often than it fails, but as expected, brighter calibrators produce better results more consistently.

In Figure 4.5c we show the effect of calibrator elevation, Φ (as defined in Figure 4.1), on the distribution of change in coherence. We include trials at all angular separations except the weak, low elevation quasar pair at 1.80° . The figure shows that C-PACS correction is more likely to fail at lower elevation: 41% of the trials with $\Phi < 45^\circ$ get worse with the C-PACS correction compared to 29% for trials with $\Phi > 45^\circ$. If we exclude trials with $\theta > 6^\circ$, we find a similar discrepancy with 81% of the trials with $\Phi > 45^\circ$ showing improvement, compared to 73% of trials at low elevation. Eliminating the large angular separation trials, we also see the low elevation source distribution become bimodal. For trials where the coherence improves, it does so dramatically compared to the high elevation sources, with the median improvement in coherence being 0.23 compared to 0.14 for the high elevation sources. However, for the trials where C-PACS is unsuccessful, it is also by a larger margin. These variations are most likely explained by atmospheric effects, which we address in the next section.

4.5.3 Environmental Influences

There are a large number of parameters that influence the conditions in the turbulent layer of the troposphere. CARMA has dedicated weather station equipment to measure and record air temperature, precipitable water vapor, relative humidity, atmospheric pressure, wind speed and direction, opacity at 225 GHz, and atmospheric delay fluctuations. We compute the median value of these weather variables for each trial and search for possible correlations with the change in coherence after the C-PACS correction. For the majority of the weather variables we find no predictive correlations. We single out four variables in this section: atmospheric delay fluctuations, opacity, cloud cover and diurnal variations. For all analysis, we only consider trials with angular separation less than six degrees, elevation greater than 45 degrees and exclude the weakest atmospheric phase calibrators (see previous section). These are trials where we would usually expect the correction to succeed.

The first variable we consider is atmospheric delay fluctuations. This delay ($c\Delta\tau$, where $\Delta\tau$ is defined in Figure 4.1) is measured at CARMA with a dedicated phase monitor system comprised of two small (18'') commercial antennas, forming a single 100-m baseline. The antenna receivers are tuned to a frequency of ~ 12.5 GHz, as emitted by a geosynchronous communications satellite. Our ability to apply a successful C-PACS correction is not adversely affected when atmospheric delay fluctuations are large. Coherence is high for pre-PACS data in the best weather ($c\Delta\tau < 150\mu\text{m}$), with only small improvement possible after applying the C-PACS correction. We divide our sample into trials with large fluctuations ($c\Delta\tau > 250\mu\text{m}$), trials with average observing conditions ($150\mu\text{m} < c\Delta\tau < 250\mu\text{m}$), and trials with the most stable atmosphere ($c\Delta\tau < 150\mu\text{m}$). The distributions for change in coherence are shown in Figure 4.6a. The C-PACS correction is successful in

improving data in poor weather ($c\Delta\tau > 250 \mu\text{m}$): 83% of the trials show some improvement in coherence, with a median improvement of 0.27. In the very best weather, the histogram peaks at zero because the coherence is high (close to 100%) without any correction needed: 81% of trials show improvement in coherence, but the median improvement is more than a factor of three smaller than in the best weather. In practice, phase monitor atmospheric fluctuations larger than $200 \mu\text{m}$ are poor conditions for observations in the high resolution A and B configurations. Our results show that with a phase correction system like C-PACS, this weather is perfectly usable.

We remind the reader that this study uses a C-PACS correction calculated with four-second integrations. We consider in more detail how short the integration times must be to achieve a useful C-PACS correction in §4.6.2. The more rapid the atmospheric variation, the more important it is to have fast integration times. We have found that 10-15 seconds would have been sufficient in most of our trials to still attain successful improvement of coherence with phase correction allowing use of weaker calibrators and thereby increasing the likelihood of finding a nearby C-PACS calibrator. There is a definite tradeoff between longer integration times on more common weaker atmospheric calibrators, and shorter integration times on brighter sources to monitor rapidly varying atmospheric conditions.

Next, we consider atmospheric zenith opacity (τ). Zenith opacity is measured by a dedicated tipper, operating at 225 GHz. We have confirmed the accuracy of the tipper measurement with sky dips using the science antennas (White & Zauderer 2008). We bin the data into trials with $\tau > 0.2$ and $\tau \leq 0.2$. Figure 4.6b shows that the C-PACS correction works better when τ is low: C-PACS improves coherence 91% of the time for $\tau < 0.2$, compared with 81% for $\tau > 0.2$. There is anecdotal evidence that atmospheric delay and opacity are inversely related, such that low

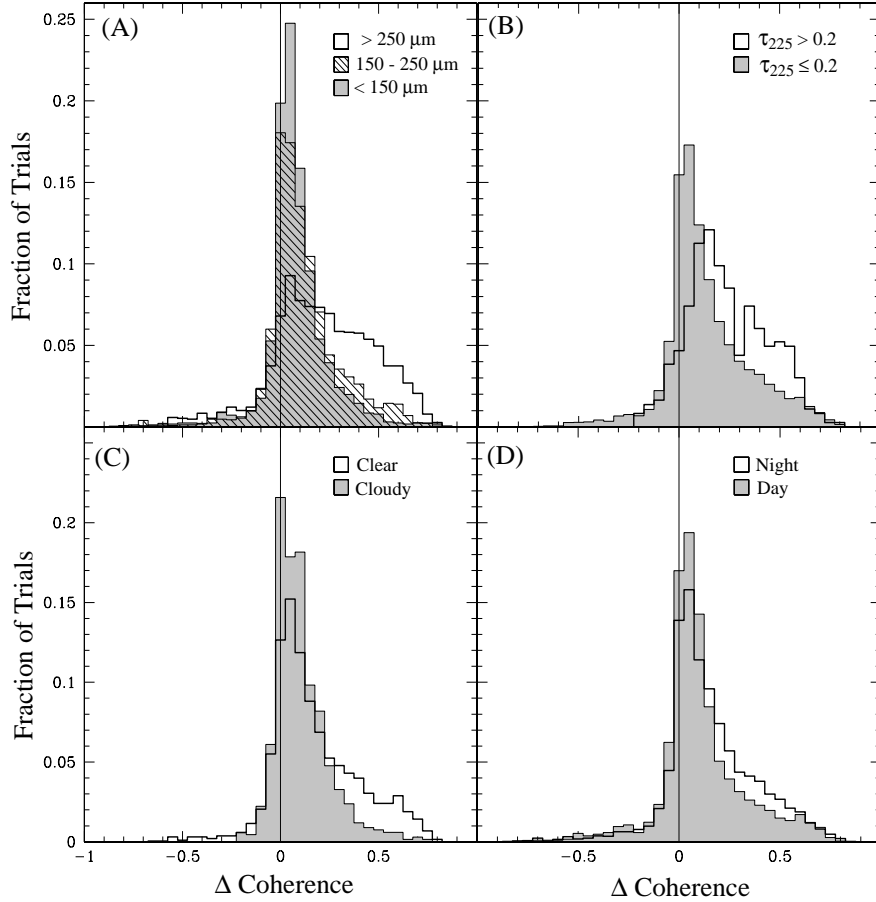


Figure 4.6: Change in coherence after C-PACS correction for atmospheric parameters. For all four parameters that we examine here, we only include trials with angular separation $< 6^\circ$ and elevation $> 45^\circ$ (see Figure 2). (A) Atmospheric delay. We find that the C-PACS correction improves coherence in weather conditions with large atmospheric delays ($c\Delta\tau > 250\mu\text{m}$). Coherence tends to be high in the best weather ($c\Delta\tau < 150\mu\text{m}$), with only small improvement possible with C-PACS correction. (B) Atmospheric opacity. We find that the C-PACS correction does not work as well in weather conditions with high opacity: C-PACS improves coherence 91% of the time for $\tau < 0.2$, compared with 81% for $\tau > 0.2$. (C) Presence of clouds. A successful C-PACS correction is made during a period of time with cloudy conditions. Other phase correction schemes have found the presence of clouds to be a challenge (e.g. water vapor radiometry). (D) Diurnal variations. We find that coherence at night is better to begin with, so the daytime data show a larger improvement in coherence. There is no major difference in the distributions, suggesting that major characteristics of the turbulent layer, such as height and thickness, do not significantly change diurnally.

opacities only accompany large atmospheric delay fluctuations and vice versa. If this were true, the association of successful C-PACS corrections with low opacity and large delay fluctuations would be a consequence of this correlation. We examine the measured opacities and delay fluctuations for each trial and find no evidence for such inverse relation. In Figure 4.7, we plot the median value for atmospheric delay as a function of opacity for each MINIPACS observation: regardless of the value of τ , the atmospheric delay varies widely.

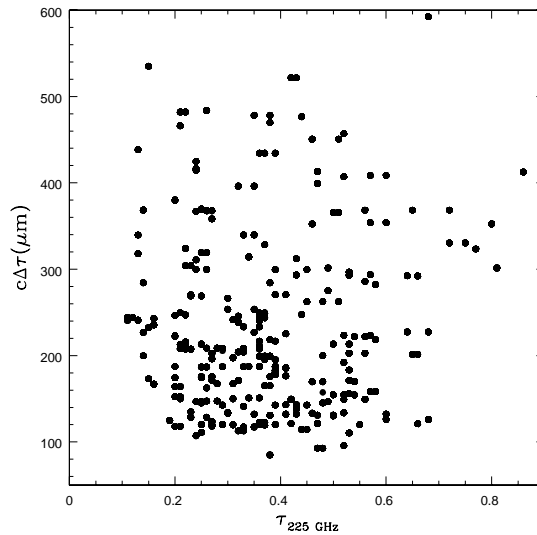


Figure 4.7: Atmospheric opacity versus delay. A successful C-PACS correction can be made regardless of atmospheric delay, $c\Delta\tau(\mu\text{m})$, but preferentially for low opacity (see Figure 4.6). There is no correlation between these weather variables.

The third environmental variable we consider is presence of clouds. Numerous previous studies have concluded that other phase correction schemes do not work reliably in the presence of clouds. Since this work has typically used water vapor radiometry, this is generally attributed to liquid and frozen water (Battat et al. 2004). We do not have equipment to assess cloud coverage at Cedar Flat, but we have obtained weather data from the Western Regional Climate Center Desert Research Institute (DRI) station at the Bishop airport, less than 20 miles from

the CARMA observatory. DRI sky observations were taken hourly and include a qualitative rating of the cloud cover (clear, few, scattered, broken, and overcast). While we do not expect that there is a minute-by-minute correlation between the cloud coverage in Bishop and Cedar Flat, cloudy periods do tend to encompass large portions of the region. Analyzing the weather data from the DRI Bishop airport station as a function of time shows that there are often several day intervals in which it is either completely clear or cloudy in Bishop and therefore, presumably also at the CARMA observatory. We examine the distribution in coherence improvement during these long extended periods of clear skies in Bishop, compared with tracks taken during periods of extended cloudy weather in Bishop (see Figure 4.6c). In the case where there is a high probability of no clouds at the observatory site, over 83% of the trials show improvement in coherence. In the case where there is a high probability of it being cloudy at the observatory, 79% of the trials show improvement in coherence. We note that the median improvement is $\Delta C=0.16$ for trials taken during the cloudy period and $\Delta C=0.14$ for trials in the clear period. Thus, Figure 4.6c shows that, contrary to other phase correction techniques, C-PACS works at least as well in cloudy weather as in clear weather. This is due to the fact that C-PACS relies on directly measuring the atmospheric phase, and is not inferring it from measurements of the water vapor obtained from total power of spectroscopy, which may be affected by liquid water and ice crystals.

The final environmental variable considered is time of day. To consider diurnal effects, we divide our sample in two by solar elevation, considering daytime to include the time one hour prior to sunrise and after sunset when the effects of solar heating of the atmosphere are largest. The distributions of change in coherence are shown in Figure 4.6d. We find that while coherence at night is intrinsically better, daytime data show a somewhat larger improvement in coherence using C-PACS. We note that

there is no major difference in the distributions, which we interpret as evidence that major characteristics of the turbulent layer (height, thickness, scale size of turbulent cells, outer scale length, wind direction and speed) do not show significant diurnal effects at Cedar Flat.

The CARMA observatory is situated in the Inyo-White Mountains, at an elevation of 2200 meters. The region has been recently studied extensively by meteorologists in a dedicated campaign to understand the physics behind rotor events on the lee side of the Sierras. Their campaign included hundreds of coordinated measurements, and has led to a more comprehensive understanding of the area (Grubisic et al. 2008). Meteorologists have noted a strong persistent easterly wind coming over the Sierra Mountain range, and have confirmed a strong diurnal pattern of wind in the north/south direction in the Owens Valley. This complicated multi-directional wind pattern might explain the occasional failure of phase correction on the Owens Valley floor, as Lay (1997b) described there to be evidence that there is more than one component of turbulence present at a given time. The CARMA observatory is elevated above and East of the Owens Valley floor, which seems to have eliminated the strong diurnal north-south component. The majority of water vapor is carried in turbulent cells over the Sierras at an elevation of ~ 4 km, which is consistent with observations indicating that the turbulent layer is found 1-2 km above the CARMA observatory. This result is obtained by beam crossing experiments performed at the observatory (Woody & Pérez, private communication).

In the next section, we further consider what the results of our observations tell us physically about the atmospheric structure.

4.6 Analysis

In this section, we consider various atmospheric phase interpolation and weighting schemes to determine if C-PACS could be extended to nonpaired antennas (§4.6.1). Next, we consider the effect of integration time on our results, specifically looking to answer how fast atmospheric variations occur on average (§4.6.2). Finally, we discuss the predictions of turbulence theory and compute the root phase structure function for all baselines (§4.6.3). In each case, we discuss what our findings mean for the physical parameters of the troposphere and the implications for atmospheric correction.

4.6.1 Interpolation

We have demonstrated thus far that the C-PACS correction is successful if the atmospheric calibrator is chosen to be bright, close to the “science target” and at a sufficiently high elevation. Only 28 of the 105 science array baselines have paired antennas, however, generally on the longest baselines. Maps made including the baselines involving unpaired antennas contain atmospheric phase errors, and therefore improvements due to C-PACS are significantly diluted. This problem is especially acute for science targets with significant extended emission, requiring the full sensitivity afforded by imaging with all 105 baselines.

To mitigate this problem of phase correction “dilution,” we explore how well we can determine atmospheric phase correction by interpolating the phase solutions of nearby antennas. We have written, implemented and tested a variety of interpolation methods in the MIRIAD program, GPBUDDY: power law, Gaussian, nearest neighbor and top hat. For each interpolation method, we consider the physical distance between antennas as well as the projected uv distance. The power law method

weights the phase for a given antenna by a factor of $R^{-\gamma}$, where R is the separation between the science antenna and the calibration antenna and γ is the weighting parameter. The Gaussian method applies a weighted average on given projected distance. The top hat method equally weights all calibration antenna phases within a given radius and computes the average for the nonpaired science antenna. The nearest neighbor algorithm simply uses the phase of the nearest paired calibration antenna, allowing the user to specify a maximum allowed distance. Beyond this separation, the science antenna retains its own non-corrected gain value.

We tested all of the interpolation methods on just one MINIPACS observation. We found that a successful interpolated C-PACS improvement can be made for non-paired antennas in this one example and the benefit of the correction is maximized using the power law interpolation method with $\gamma=3.5$ (the improvement was similar for indices ranging from 2-4). We used the power law interpolation method and a weighting parameter of 3.5 to compute interpolated corrections for a subset of MINIPACS trials chosen to be successful for C-PACS correction of paired-paired antennas, and for which $\theta > 6^\circ$, $\Phi > 45^\circ$, and $S_{Jy} > 2$. We compute the improvement in coherence for all baselines, and then divide the sample by baseline type: two paired antennas (paired-paired), baselines with one paired antenna and one nonpaired (paired-nonpaired), and baselines where neither antenna has a dedicated calibration antenna (nonpaired-nonpaired).

Figure 4.8 shows the improvement in coherence for the paired-paired baselines, compared to baselines with phases interpolated for one or both science antennas. We further divide our sample into baselines shorter and longer than 500 meters in Figure 4.8a and 4.8b, respectively. For the long baselines ($B > 500$ m), 92.3% of the paired-paired baselines show an improvement, with a median ΔC of 0.10. This success rate reflects our choice of the best trials for this test. For long baselines with

one nonpaired antenna, 71.4% show an improvement in coherence (median ΔC of 0.06). For long baselines where neither antenna had a paired calibration antenna, the interpolated C-PACS correction resulted in a success rate of 61.7% (median ΔC of 0.05). For short baselines ($B < 500$ m), the interpolated C-PACS correction did not work. The paired-paired baselines have a success rate of 74.4% (median ΔC of .05), nonpaired-paired baselines have a success rate of 53.7% (median ΔC of 0.01), and the nonpaired-nonpaired baselines have a success rate less than half (49.8%, median $\Delta C < 0.01$).

This experiment suggests that simple atmospheric phase correction interpolation fails to improve the coherence of nonpaired antennas to a significant degree, although it may be of some help for the longest baselines. We think that the failure of our interpolation attempt is partially due to the very sparse sampling of the atmospheric phase screen (i.e., too few calibration antennas). It may be possible to also increase the success rate of interpolation by incorporating more physical information about the atmosphere at the time of the observations.

4.6.2 Time Scale for Phase Variations

All MINIPACS observations were taken with short integration times of four seconds. To test how short the integration time needs to be in order to recover the same level of improvement, we did a series of tests on a sample track where there was excellent improvement in coherence with 4 second integrations. We averaged the raw data before processing on 8, 12, 16, 20, and 30 second time intervals. We then computed the coherence before and after C-PACS phase correction. We find that we obtain the same results with 8-12 second integrations, but that averaging over longer periods of time results in a lesser improvement in coherence, and in some cases, a degradation. We expect these results to vary based on weather conditions and the strength of

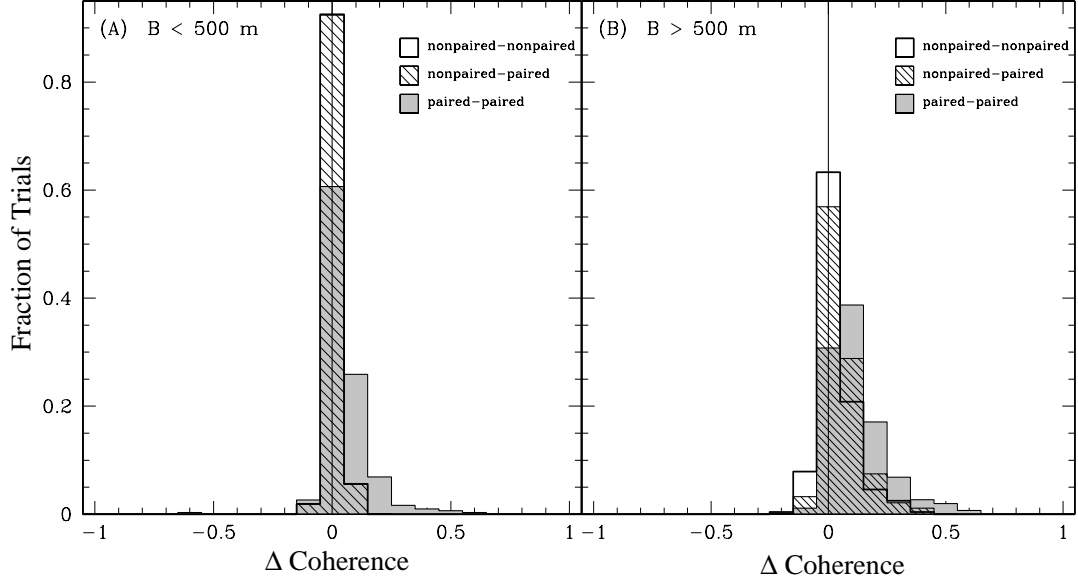


Figure 4.8: Improvement in coherence for interpolated baselines. For antennas in the science array without a paired antenna, we compute the atmospheric correction by interpolating using a power law. We weight the relative contribution of gain solutions from antennas in the calibration array by $r^{-3.5}$. (A) Improvement in coherence for baselines shorter than 500 meters. (B) Baselines longer than 500 meters.

the calibrator as the integration time must be long enough to result in a strong detection of the calibrator (good signal-to-noise). A followup investigation should be pursued as the time scale over which we can average and achieve improvement in coherence gives information about the small-scale structure of the turbulent cells in the troposphere. We are able to determine the thickness and outer size scale of the turbulent layer by computing the structure function (next section), and we can determine the magnitude of the small scale turbulence based on the integration time required to maximize coherence improvement with C-PACS phase correction.

4.6.3 Structure Function of the Atmosphere

The turbulence in the troposphere follows Kolmogorov theory (see sections §3 and §4 in Carilli and Holdaway 1999). Fluctuations measured by the spatial structure function, \mathcal{D} , correlate with changes in phase measured between two antennas separated by distance, B :

$$\mathcal{D}_\Phi(B) \equiv \langle \Phi(x+B) - \Phi(x) \rangle^2, \quad (4.1)$$

where $\Phi(x)$ is the phase measured at one antenna, and $\Phi(x+B)$ is the phase measured at the other antenna in the baseline pair under consideration, B meters away. For a single baseline, the ensemble average of temporal phase fluctuations are assumed to be equivalent to spatial fluctuations, and the measured rms phase variations correspond to the square root of \mathcal{D} . We then expect the observed behavior to follow the form

$$\sigma_\Phi(B) = \beta \times B^\alpha, \quad (4.2)$$

where β is a scaling factor and σ_Φ is the standard deviation of phase scatter measured on a baseline for which a slow instrumental correction has been applied and atmospheric variations remain. As Carilli et al. (1999) discuss, the scaling factor β is the ratio $\frac{K}{\lambda_{mm}}$ for millimeter interferometers, where K is a scaling factor dependent upon the weather and λ is the observing wavelength, expressed in millimeters. At excellent site locations, K has been found to have a typical value of ~ 100 . It is reported that under good weather conditions $K = 300$ at the VLA (Sramek 1990).

There are three scale length regimes to consider in the problem. Antenna baseline lengths can be longer than the thickness of the turbulent layer (thin screen, Kolmogorov turbulence theory predicts $\alpha=1/3$), shorter than the thickness of the turbulent layer (thick screen, Kolmogorov turbulence theory predicts $\alpha=5/6$), or the baseline length might be so long as to exceed the outer size scale of the turbulence.

In this last regime, increasing the baseline length further will not increase the phase scatter, and $\alpha = 0.0$. It has been found in previous studies that in the transition region between thick screen and the thin screen 2-D approximation, the power-law index has an intermediate value.

We calculate the root phase structure function for MINIPACS experiments, using all 105 science baselines during A and B configuration. We plot the mean and standard deviation of the phase scatter for each baseline separation as a function of baseline separation in log-log space in Figure 4.9,

$$\log(\sigma_\Phi) = \log\left(\frac{K}{\lambda}\right) + \alpha \log(B), \quad (4.3)$$

to easily compute the multiplicative scaling factor and power-law index from a linear least-squares regression. The expected Kolmogorov power law indices of 5/6 and 1/3 for the thick and thin regimes are overlaid. The transition between these slopes suggest that the thickness of the turbulent layer over Cedar Flat is approximately 150 m. For the MINIPACS data, there is a turnover to a flat slope at a baseline length of 1 km. Each track was only 5-10 minutes in length, however, corresponding to a tropospheric crossing distance of a few kilometers assuming a 10 m/s wind. This suggests that the MINIPACS observations are too short to sample scale lengths longer than a few km, and the observed flattening is artificial. When we include a longer track (6 hours), we no longer see this clear turnover and the points continue to follow the slope of 1/3 suggesting that the outer scale length at Cedar Flat is larger than 2 km. We find that $\beta \approx 1.7$, hence $K \approx 156$ at $\lambda = 3.2$ mm. This value of K suggests that Cedar Flat is at an excellent location, lying between the VLA ($K=300$) and ALMA ($K=100$) sites. We also computed the root phase structure function for the calibration antennas, and found the power-law index and scaling factor to be in good agreement with the science array for a given track suggesting that the calibration antennas “see” the same overall tropospheric structure as the

science antennas.

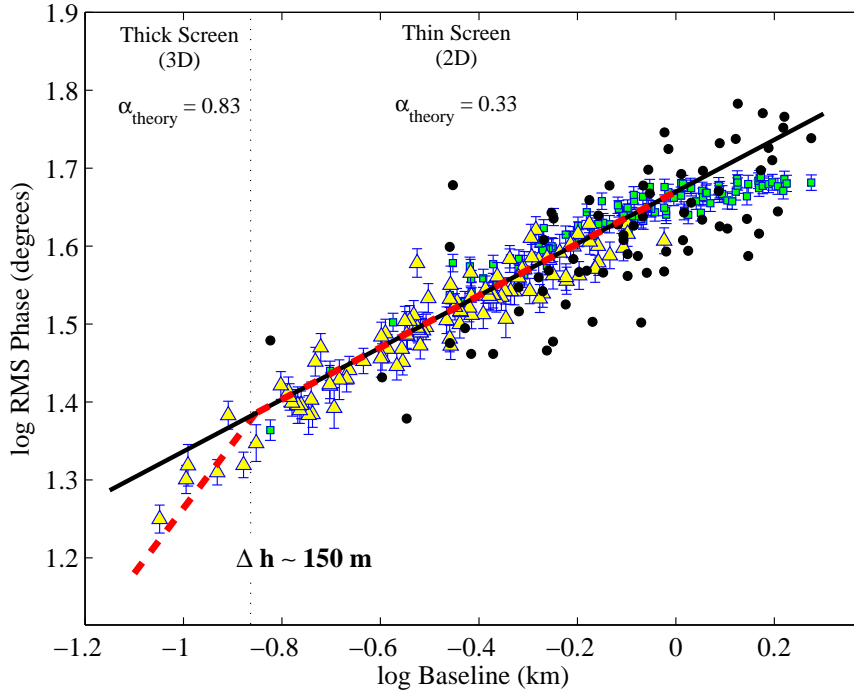


Figure 4.9: Root phase structure function. The mean and standard deviation for all trials at each baseline separation are plotted for MINIPACS A (green squares) and B (yellow triangles) observations. The expected Kolmogorov power law indices of $5/6$ and $1/3$ for the thick and thin regimes, respectively, are overlaid as slopes in this log-log plot (dashed red line). The transition between these slopes suggest that the thickness of the turbulent layer is ~ 150 m. According to the MINIPACS data, the outer scale of turbulence should be at ~ 1 km, where the slope flattens. However, each MINIPACS trial was only 5-10 minutes in length, corresponding to a tropospheric crossing distance of order a few kilometers. In fact, we find no evidence for the outer scale to be smaller than 2 km upon considering a five hour observation of the phase calibrator 1310+323 during science observations of Arp 193 on February 16, 2010. The figure shows for the longest baselines that the theoretical slope of $1/3$ is consistent with the data (solid black line).

4.7 Science Application - Arp 193

We chose to study Arp 193 because it is the best test case for C-PACS observations among nearby ultraluminous and luminous infrared galaxies (U/LIRGs). It is a good target source because we have a priori knowledge of its structure from past detailed studies, we can map it at a factor of two higher resolution with CARMA than previously achieved, and it has a bright nearby quasar suitable for phase and C-PACS atmospheric calibration. Arp 193 has been studied extensively in the past at multiple wavelengths, but there are no millimeter radio observations matching the sub-arcsecond scale of the H I absorption study by Clemens and Alexander (2004) or optical Hubble Space Telescope NICMOS images by Scoville et al. (2000).

Our purpose is twofold: (1) to confirm the C-PACS calibration method for high resolution imaging of an extended source, and (2) to image $^{12}\text{CO}(2-1)$ in Arp 193 at sub-arcsecond scale resolution and to present a brief analysis of the molecular gas distribution and dynamics. We defer a more detailed analysis of the implications of our observations for a future paper. In this section, we present a brief overview of the motivation to study molecular line emission in U/LIRGs and summarize relevant scientific studies of Arp 193. Then, we discuss details of the observations and data reduction. Finally, we present our results in two parts. In the first section of results, we discuss the success and shortcomings of the C-PACS phase calibration. In the second results section, we analyze the molecular gas distribution and dynamics.

4.7.1 Motivation: IR Galaxies and Arp 193

U/LIRGs emit the majority of their energy at infrared wavelengths from dust heated by either prolific star formation and/or the presence of an active galactic nucleus. The only identifying criterion is the infrared luminosity: $L_{\text{IR}} > 10^{11} L_{\odot}$ for LIRGs and $L_{\text{IR}} > 10^{12} L_{\odot}$ for ULIRGs. There is substantial evidence that a large number of U/LIRGs are merging or interacting galaxies, inferred from the disturbed morphologies, resolved double nuclei, and tidal tails extending beyond the nuclear region. See Wilson et al. (2008) and references therein for an overview.

Arp 193 is a LIRG with a far-infrared luminosity of $4 \times 10^{11} L_{\odot}$. With two clearly visible and long tidal arms, it was included in Halton Arp's Atlas of Peculiar Galaxies (1966). It is now understood that the narrow filaments or spikes emanating from the nuclear region are tidal arms, evidence of a merger of two galaxies. The IRAS colors ($f_{25}/f_{60} < 0.2$) are indicative of cool dust (Condon and Broderick 1991), suggesting starburst as the luminosity source, rather than a central AGN. Arp 193 was categorized as a LINER² by Veilleux et al. (1999). The observed properties in LINER galaxies could arise from either low luminosity AGNs or starbursts. Until recently, in the case of Arp 193, the energy source was thought to be entirely from a starburst. X-ray observations may indicate the presence of an AGN (Teng 2010).

Downes and Solomon (1998, hereafter, DS98) observed Arp 193 at 112.6 GHz ($1.6'' \times 0.9''$) and 225.3 GHz ($0.6'' \times 0.4''$) between 1996 and 1998. DS98 find the CO position-velocity diagram provides good evidence for a rotating molecular ring with a central gap. They also identified the inner nuclear region to host an extreme starburst, similar to Arp 220 and Mrk 273. These regions are relatively small (~ 100 pc), contain a large amount of mass ($10^9 M_{\odot}$) and emit upwards of $10^{11} L_{\odot}$. DS98

²Low-ionization nuclear emission-line region (see Heckman 1980).

conclude that the extreme starburst powers the FIR luminosity.

Scoville et al. (2000) observed Arp 193 in the near-infrared with the Hubble Space Telescope NICMOS camera along with eight other LIRGs and 15 other ULIRGS. Their sample included both warm and cool systems (based on $f_{25\mu\text{m}}/f_{60\mu\text{m}}$) and different types of systems including starbursts, QSOs, Seyferts and LINERs. The star clusters in Arp 193 are highly luminous and hence thought to be young, likely formed as a result of galactic interactions which are clearly evident from the disturbed morphology of the galaxy. In Arp 193, the near-IR (NIR) colors are consistent with reddened starlight and a few magnitudes of visual extinction. Scoville et al. describe the NIR morphology of Arp 193 as a disk with a dusty spiral. Based on radio profile fits, they find an inner disk radius (R_{inner}) of 100 pc, and an outer disk radius (R_{outer}) of 3800 pc for Arp 193. They fit various models to the data, and find the best fit is an $r^{1/4}$ law (previously recognized by Standford and Bushouse 1991), which suggests Arp 193 will eventually become a spiral with a massive central bulge or possibly even a giant elliptical galaxy.

[/citet2004MNRAS.350...66C](#) mapped the distribution of neutral hydrogen gas in Arp 193 using the VLA and MERLIN. Their high resolution neutral hydrogen maps have a restored clean beam of $0.45'' \times 0.45''$. They compare the distribution of neutral hydrogen gas with molecular gas (CO from DS98) and near-IR HST NICMOS data. They find that the ISM is increasingly enriched with H_2 towards the center of Arp 193. Comparing the velocity distribution of the H I with molecular gas, [/citeauthor2004MNRAS.350...66C](#) note variations may arise from both spatial distribution and dynamical differences. CARMA gives us the ability to improve upon the molecular gas maps, achieving an angular resolution in CARMA's A configuration that matches the HST NICMOS observations and exceeds the H I MERLIN observations, enabling detailed comparison of the nuclear region of Arp 193.

Table 4.2. Science Observations of Arp 193

Date	Configuration	Int. time (h)	Frequency (GHz)
3 FEB 2007	C (30-350 m)	1.1	226
14 DEC 2009	B (0.1-1 km)	4.42	226
16 FEB 2010	A* (0.25-2 km)	5.8	226

Note. — *Paired Antenna Observations

4.7.2 Observations and Data Reduction

We have observed the molecular transition $^{12}\text{CO}(2-1)$ in the nuclear region of Arp 193 in CARMA's A, B and C configuration. We summarize the observing parameters in Table 4.2. For all observations, we used either 3C 273 or 0854+201 as our bandpass and flux calibrator, bootstrapping the flux from regular planet measurements to a precision of $\sim 20\%$. For the C configuration observations, we used 3C 273 as the phase calibrator, and 1415+133 as a test source. We used a 14 minute cycle time, spending 10 minutes integrating on source, and 2 minutes on each of the phase and test calibrators. For our later B and A configuration observations, we used 1310+323 as the phase calibrator (2.8° from Arp 193) and 3C286 as test calibrator (4.8° from 1310+323). We shortened our cycle time to 5 minutes, spending 3 minutes on source, and one minute on each of the phase and test calibrators. For A configuration C-PACS observations, 1310+323 also served as the atmospheric calibrator.

All observations were performed at 1 mm, with the observing rest frequency set to 225.0483 GHz to center the $^{12}\text{CO}(2-1)$ line in the lower sideband, as Arp 193 has a redshift of $z=0.02333$. At the time of our observations, the CARMA correlator had

six windows which could be configured to widths of 512, 64, 32 or 8 MHz. We used the wideband correlator setup to accommodate the full width of the line velocity in one window. This resulted in a velocity resolution of 41.6 km s^{-1} per channel and an overall coverage of -291 to 290 km s^{-1} in the lower sideband. In A configuration, the atmospheric calibrator, 1310+323, was observed by the calibration array at 31 GHz, as described in §4.3. Data reduction was performed using the MIRIAD software package to apply standard interferometric calibrations. C-PACS phase correction applied to the A configuration data was performed as described in §4.3. We used a power law scaling with an exponent of 3.5 to interpolate the phase correction for non-paired antennas. All maps give relative offset in arcseconds from the positional center ($\alpha = 13:20:35.3$ and $\delta = 34:08:22.0$).

4.7.3 Results: Application of C-PACS

Analysis of the phase and test calibrator data gives us confidence that the C-PACS phase correction will result in an improved map of Arp 193. For our A configuration observations, we applied the C-PACS correction from observations of 1310+323 at 31 GHz by the calibrator array to a test point source observed by the primary array. The test source, 3C286, has an angular separation of 4.8° from the 1310+323. The mean coherence improved from 46% to 50% with C-PACS. At shorter baselines, the improvement is marginal, but is more significant at the longest baselines. Applying the C-PACS phase correction from observations of 1310+323 by the calibrator array to the science array observations of 1310+323 at five minute intervals throughout the track resulted in significant improvement. Figure 4.10 shows the change in coherence for the phase calibrator, 1310+323. The mean coherence without C-PACS applied is 74% and improves to 90% with C-PACS. Improvement increases with increasing baseline separation and is striking for baselines longer than 1 km. As Arp 193

is situated much closer to the atmospheric calibrator than our test point source (2.8° instead of 4.8°), we expect the improvement in our science data to exceed the improvement we observe in the test point source, but not to be quite as good as the improvement for 1310+323.

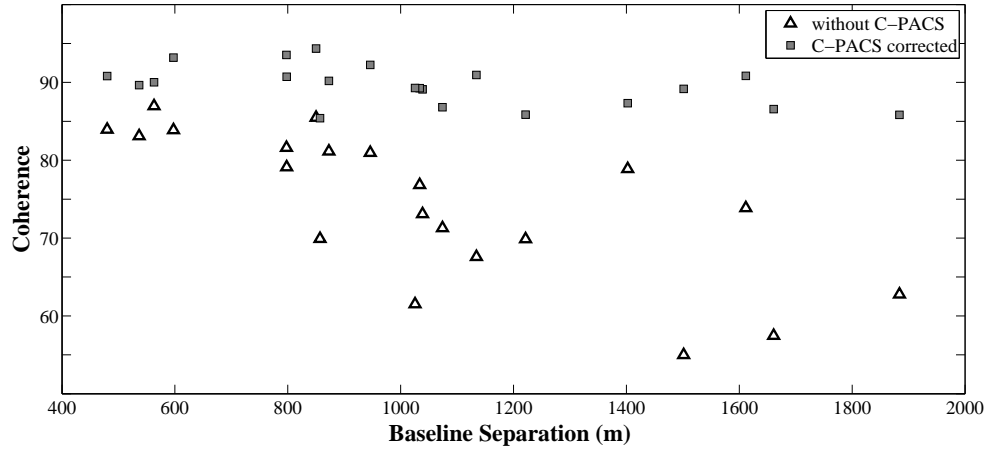


Figure 4.10: Improvement in coherence for phase calibrator, 1310+323, during 1 mm Arp 193 science track. The mean coherence without C-PACS applied is 74% and improves to 90% with C-PACS. There is more improvement with increasing baseline separation. We applied the C-PACS correction to a test point source, 3C 286, at an angular separation of 4.8° from the atmospheric calibrator. Coherence improved from 46% to 50% with C-PACS.

4.7.4 Results: Arp 193

In this section, we present our $^{12}\text{CO}(2-1)$ maps of Arp 193. We clearly resolved “clumps” of emission spatially and dynamically. We present measurements of these resolved clumps (luminosity, mass, column density) and compare the implied molecular gas mass with the dynamical mass derived from the rotation curve we fit to our data. For consistency, we adopt the same cosmology as DS98: $H_{\odot} = 75 \text{ km s}^{-1} \text{ Mpc}^{-1}$. At the redshift of Arp 193 ($z=0.0233$), $1'' = 436 \text{ pc}$.

CO Maps

We image Arp 193 using only the A configuration data to attain the highest angular resolution. Improvement in coherence for our science target, Arp 193, with application of C-PACS is demonstrated in Figure 4.11. $^{12}\text{CO}(2-1)$ emission is averaged over three channels (125 km s^{-1}) and images are presented for data reduced without C-PACS (top panels) and with C-PACS phase correction (bottom panels). Contours are plotted at 1.5, 3, 4.5 and 6 σ , where $\sigma = 5.3 \text{ mJy bm}^{-1}$. The center velocity of each is shown in the bottom right (km s^{-1}). The angular resolution is $0.18'' \times 0.12''$ or $\sim 64 \text{ pc}$ (beam in lower left).

In Figure 4.12, we present the integrated intensity map of Arp 193 using A, B and C configuration observations. For this map, we used robust weighting, and cleaned using a mask from C configuration observations to define the clean region. The angular resolution in this map from the combined observations is $0.23'' \times 0.16''$ or $\sim 84 \text{ pc}$ (beam shown in lower left). Contours are at 95%, 85%, 65%, 45% and 25% of the peak intensity (350 mJy). Contours correspond to levels of 30, 27, 21, 14 and 1 σ , where the rms noise in the map is 11 mJy beam^{-1} .

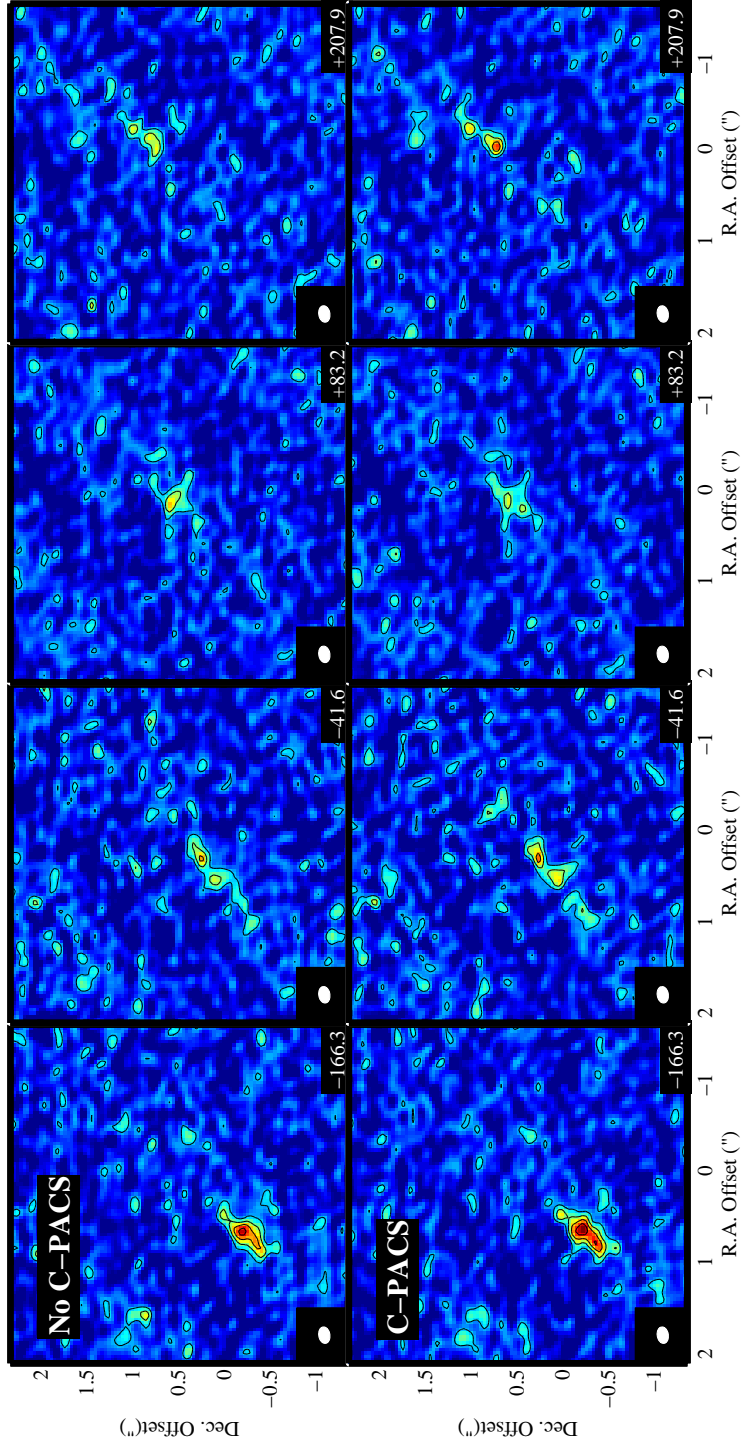


Figure 4.11: Improvement in coherence for science target, Arp 193, with application of C-PACS. $^{12}\text{CO}(2-1)$ emission in 125 km s^{-1} width channels is shown for data reduced without C-PACS (top panels) and with C-PACS phase correction (bottom panels). Contours are plotted at $1.5, 3, 4.5$ and 6σ . The center velocity of each is shown in the bottom right (km s^{-1}). Beam (lower left) is $0.18'' \times 0.12''$ or $\sim 64 \text{ pc}$.

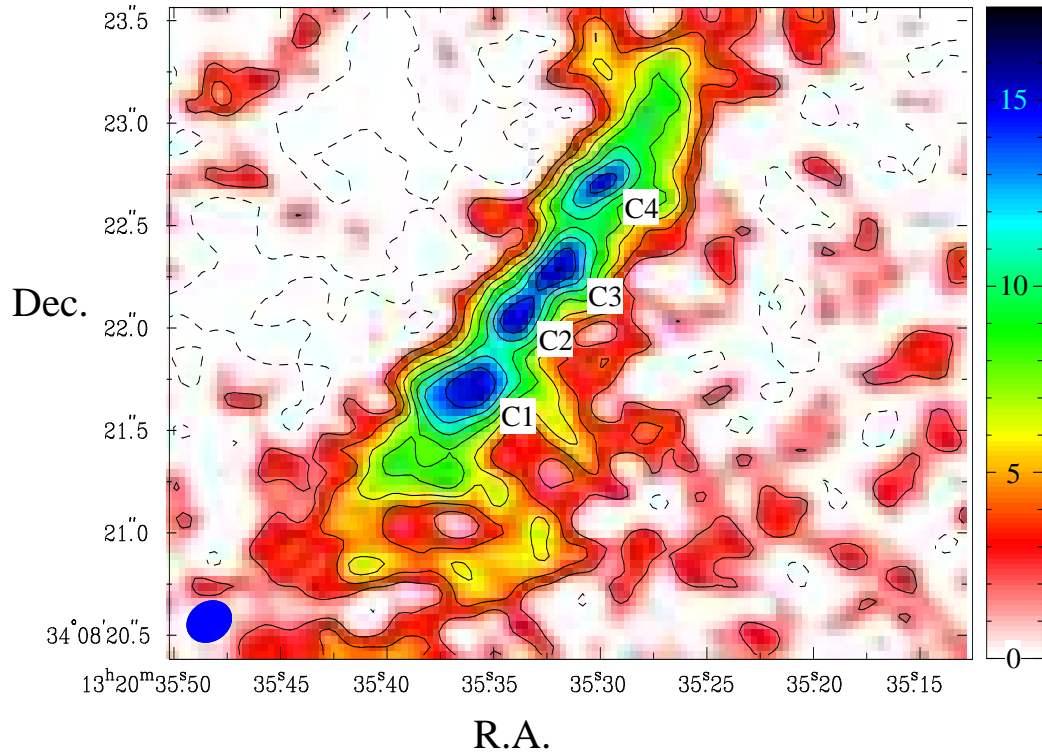


Figure 4.12: Integrated intensity map of Arp 193, using observations from A, B and C configuration. Contours are at levels of -2, 2, 4, 6, 8, 10, 12, 14 and 16 $\text{Jy beam}^{-1} \text{ km s}^{-1}$ and the colorbar scale has the same units. The RMS noise in the map is $1.6 \text{ Jy beam}^{-1} \text{ km s}^{-1}$. The beam size is $0.26'' \times 0.19''$, shown in the lower left.

Dynamics

We summarize the dynamical information from our maps and compare with results by DS98 and by Clemens and Alexander (2004). Arp 193 is thought to be a rotating disk or ring, inclined by 50° (DS98). We examined velocities along various position angle slices through our best quality A+B+C configuration maps and find consistent results with DS98. The position angle is about 140° (E of N) and the center of rotation is coincident with Clump C3 (see Figure 4.12). The coordinates of the dynamical center are approximately $\alpha=13:20:35.318$ and $\delta=34:08:22.35$.

We present $^{12}\text{CO}(2-1)$ position-velocity diagrams for two slices, as shown in Fig. 4.13. The longer slice, A, shows a flat rotation curve out to an angular distance from the center of the disk of $\sim 2''$, corresponding to 872 pc. There is more extended emission in the SE corner. We present the position-velocity diagram along slice B to zoom in on the central region. To determine the precise velocities at each position angle, we use a broader strip along the position angle instead of a single slice. We step along in the disk parallel to the disk major axis, fitting a gaussian to determine the peak velocity at that position. This rotation curve is presented in Fig. 4.14. The error bars were computed using a Monte Carlo method: we randomly varied the intensity values based on the RMS noise in the map and then re-fit gaussians along each position. We use this rotation curve to derive the dynamical mass of the system and compare with the total molecular mass (see next section and Table 4.12).

The following plots are the result of an initial comparison of our CO maps with H I absorption maps (Clemens and Alexander 2004, H I data cubes obtained and used for comparison with permission of the author). Contours of peak absorption in H I are overlaid on the integrated intensity map (from Fig. 4.12). Fig. 4.15a has several H I contours, while Fig. 4.15b only has the peak absorption contours, in

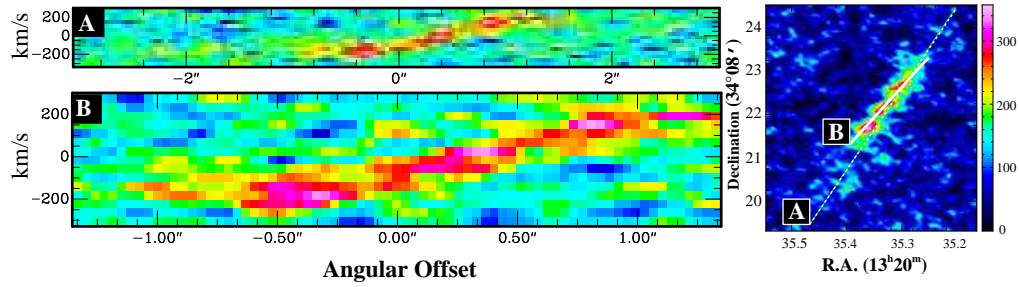


Figure 4.13: (Left) Arp 193 position velocity-maps along slices indicated in right panel. Slice A is offset from the peak CO emission in the nuclear region in order to highlight the hint of extended emission at a velocity of -200 km s^{-1} in the SE corner of the map. Slice B is zoomed in to show velocity details in the peak emission region of the rotating disk.

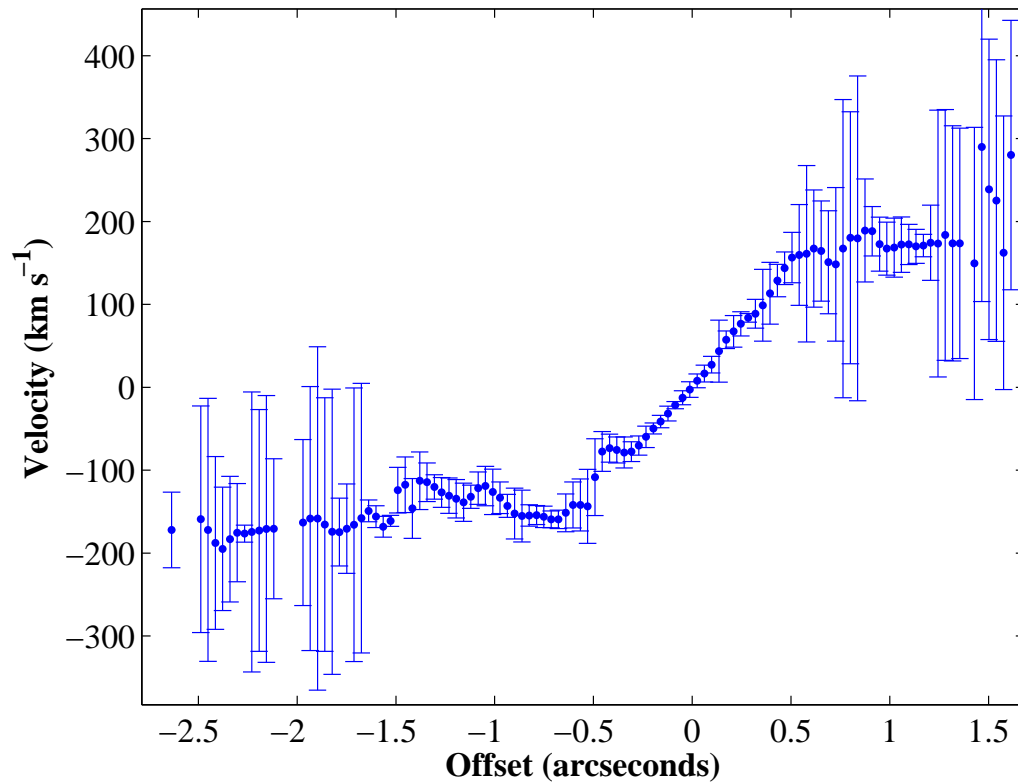


Figure 4.14: Rotation curve at same position angle as slice B (see Fig. 4.13). Our slice is broader to incorporate the full width of the signal and improve signal-to-noise. The velocity at each point along the slice was determined with a gaussian fit. The error bars are $\pm 1\sigma$. The points in this figure oversample the true resolution of $\sim 0.2''$, equivalent to about four points.

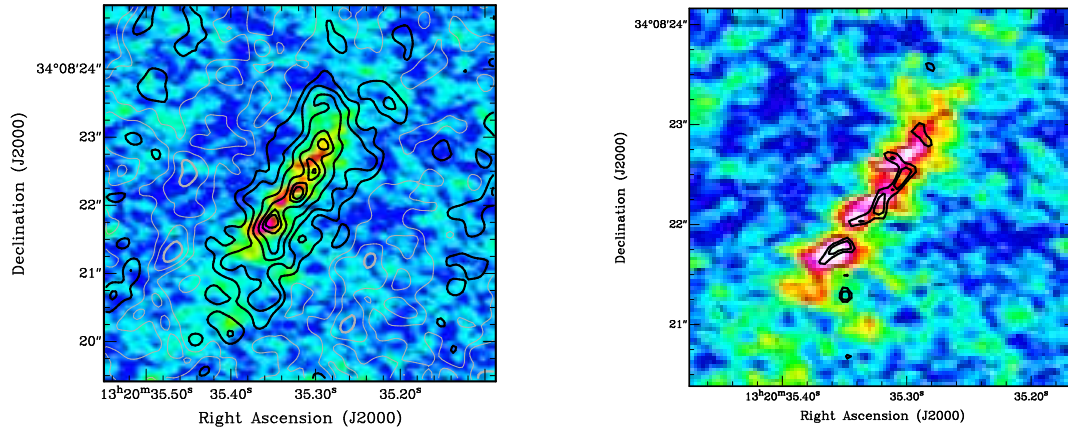


Figure 4.15: $^{12}\text{CO}(2-1)$ and H I data (Clemens and Alexander 2004) for Arp 193. The CO line emission (color scale) is the same as described in Fig. 4.12. (Left) H I convolved to an angular resolution of $0.6''$. The H I absorption contours are at levels of 95, 85, 65, 45, and 25% of the peak H I absorption of -0.89 in the SE disk. (Right) For the H I absorption, only two contours of peak absorption are shown, at levels of 85 and 90%, in order to highlight differences in distribution between H I absorption and CO emission. In the SE disk, the peak H I absorption curves around the point with peak CO emission. A slight offset is seen in the two central peaks, and in the NW corner, the peak H I emission is most clearly offset from the CO emission.

order to highlight the spatial differences. The peak H I absorption is always offset from the peak CO emission. The difficulty in interpreting absorption measurements is that lack of H I absorption could mean either a lack of absorbing H I gas or not enough background continuum emission. In addition to spatial differences, there are dynamic differences between the H I and CO gas. We show the position-velocity diagrams for each in Figure 4.16. Our results are consistent with the analysis by Clemens and Alexander (2004): the H I velocities do not rise quite as steeply as the molecular gas velocities.

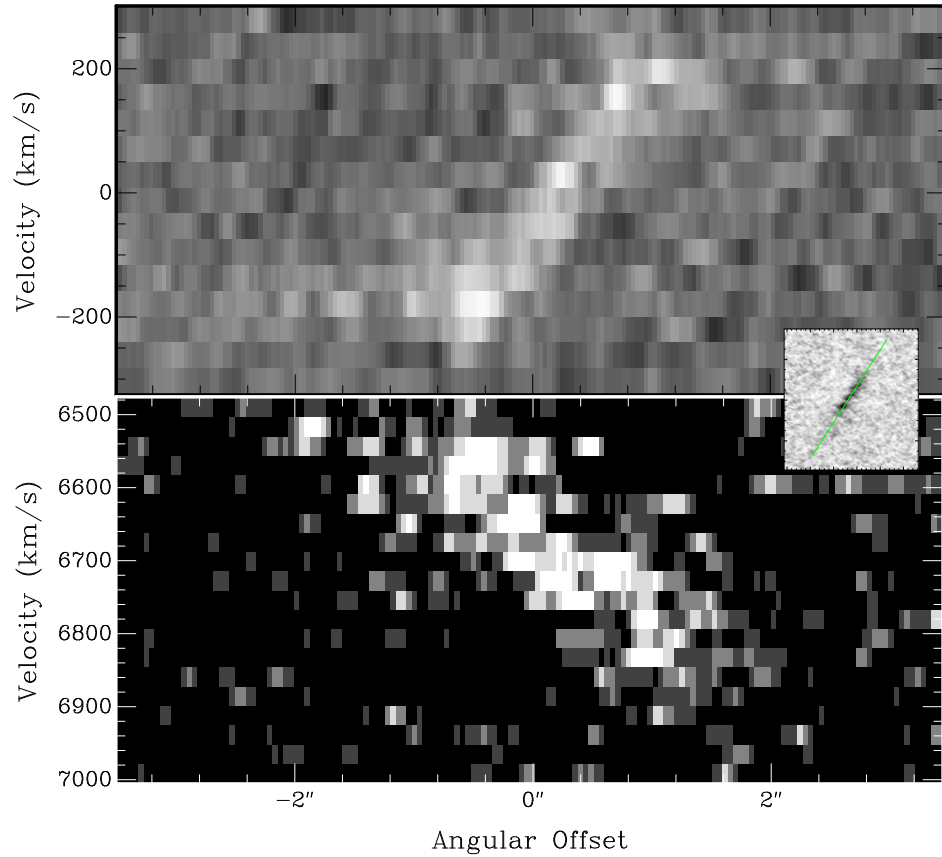


Figure 4.16: Position-velocity comparison for CO emission (top) and H I absorption (bottom) taken along the same slice (shown in inset). Clemens and Alexander (2004) note the source to have a systemic velocity of 6840 km s^{-1} , which results in a $\sim 100 \text{ km s}^{-1}$ offset between the H I and CO gas. The extent of the rotating disk before the turnover radius is consistent for both maps, extending between $-0.2''$ and $1.3''$. In this range, ΔV is $\sim 350 \text{ km s}^{-1}$ for the CO and more narrow for the H I by $\sim 100 \text{ km s}^{-1}$.

Molecular Gas Mass

To compute the CO line luminosity, we use the following equation from (Solomon et al. 1997):

$$L'_{\text{CO}} = 3.25 \times 10^7 S_{\text{CO}} \Delta V \nu_{\text{obs}}^{-2} D_L^2 (1+z)^{-3} \quad (4.4)$$

$S_{\text{CO}}\Delta V$ is the integrated line intensity in units of Jy km s⁻¹ (see Column 6 in Table 4.3). D_L is the luminosity distance in Mpc (100.3 Mpc for Arp 193 assuming $H_0=71$ km s⁻¹ Mpc⁻¹ and $\Omega_M=0.27$), and ν is the observed line frequency in GHz. We find that 36% of the CO luminosity comes from the inner 200 pc (see Table 4.12).

We compute the H₂ mass using the CO line luminosity (L'_{CO}) and the same α_{CO} conversion factor² determined by DS98 for ULIRGs: $\alpha_{\text{CO}} = 0.8 M_{\odot} L_{\odot}^{-1}$. The conversion factor they determine varies between 0.3 and 1.0 for other luminous and ultraluminous infrared galaxies.

We compare the dynamical mass, which should trace the total enclosed mass of the system, with the molecular gas mass. We find that out to a radius of 750 pc, $M_{\text{H}_2} = 1.4 \times 10^9 M_{\odot}$, $M_{\text{Dyn}} = 7.5 \times 10^9 M_{\odot}$, and the ratio is 0.19. This value is consistent with the ratio reported by DS out to 740 pc, of 0.19. Error estimates for each mass calculation could easily be 10-20% based on propagation of error from the noise in the map, uncertainties in the distance to the source, uncertainties in the geometry of the rotating ring or disk (e.g. inclination) and uncertainties in our absolute flux calibration. However, all of these errors are easily eclipsed by our uncertainty in the X_{CO} factor. Regardless of the absolute magnitude of the dynamical or gas mass, our main result is to confirm the increasing percentage of total mass comprised by molecular gas towards the center of the rotating disk. As our beam is ~ 85 pc, we

²The conversion factor between CO and H₂ can be expressed in terms of the ratio of H₂ mass to CO luminosity (α_{CO}) or the ratio of H₂ column density to CO intensity (X_{CO}).

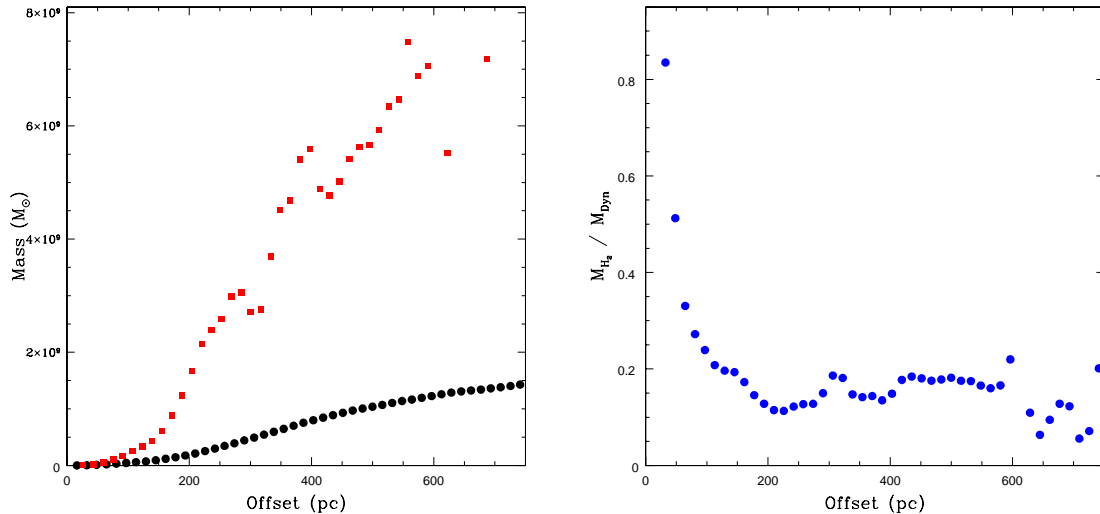


Figure 4.17: Comparison of dynamical mass and molecular gas mass. The absolute masses are shown on the left and the ratio on the right. We compute the dynamical mass from the derived rotation curve (see Figure 4.15), assuming a rotating disk, inclined by 50° (Red squares). The gas mass is calculated from the CO line luminosity summed over increasing radial annuli (black dots). Our beam size is ~ 85 pc (roughly four points in these plots). The step rise in the inner tens of parsecs is probably not physical, but due to beam smearing.

are not able to resolve the innermost region of the disk. See Figure 4.17.

We then compute column densities of H_2 for each of the clumps, and an average for the 5σ and 3σ regions. We obtain very high column densities, greater than 10^{25} cm^{-2} towards Clump 2 and Clump 3. Georgantopoulos et al. (2010) discuss the use of sub-millimeter observations of molecular gas as tracers of AGN because column densities as high as we observe towards Arp 193 absorb even hard X-rays, resulting in a Compton-thick source. Column densities of 10^{24} cm^{-2} absorb X-rays with energies up to 20 keV, and with column densities greater than 10^{25} cm^{-2} , almost all X-rays are absorbed. Teng (2010, Table 4.2) summarizes X-ray properties of U/LIRGs and reports that Arp 193 (aka. UGC 08387) had 285 total X-ray counts detected ($70 \pm_{8.35}^{9.41}$ in the “hard” 2–8 keV band and 215 ± 14.66 in the “soft” 0.5–2 keV band). It is likely that a significant amount of X-ray emission is being attenuated

in these regions of high column density. A large amount of soft X-ray emission is observed perpendicular to the position angle of the disk, emanating approximately from the dynamical center near Clump 3 (see Fig. 4.1 Teng 2010). A hard X-ray nucleus is identified by Teng, indicative of an AGN based on its X-ray color. The relative contributions of the extreme starburst and this potential AGN to the total observed IR luminosity remain open questions.

We compute the ratio of H I and H₂ column densities, using the high resolution H I absorption measurements by Clemens and Alexander (2004). If a foreground screen geometry is assumed, they calculate the H I column density to fall between $1.7\text{--}5.5 \times 10^{22} (T_s/100 \text{ K}) \text{ cm}^{-2}$. Assuming a well-mixed geometry, the column density range would be between 3.9 and $13 \times 10^{22} (T_s/100 \text{ K}) \text{ cm}^{-2}$. Comparing their values to the H₂ column densities we calculated for the regions with peak CO emission (Clumps 1-4) and a more extended region (see Table 4.3), we find $N(\text{H I})/N(\text{H}_2) \sim .001 - .03$. This range of values is consistent with the column densities ratios determined by Clemens and Alexander using the CO data from DS98.

Table 4.3. Molecular Gas in Arp 193

Clump Label	R.A.	Dec.	Area	Area	$S_{\text{CO}} \Delta V$	H_2 Mass	Column Density
	[13:20]	[34:08]	[pc ²]	[10 ⁴⁰ cm ²]	[Jy km s ⁻¹]	[10 ⁸ M _⊙]	[10 ²⁴ cm ⁻²]
(1)	(2)	(3)	(4)	(5)	(6)	(7)	(8)
C1	35.36	21.7	1810	1.7	58.5	2.8	9.8
C2	35.34	22.1	490	0.47	26.7	1.3	16.4
C3	35.32	22.3	1110	1.1	46.1	2.2	12.3
C4	35.30	22.7	1390	1.3	20.5	1.0	4.4
$\sum_{5\sigma}$			4800	4.6	152	7.3	9.5
$\sum_{3\sigma}$			25200	24.0	417	20.0	5.0

Note. — The four clumps identified were separated by requiring emission at the 5σ level. $\sum_{5\sigma}$ is the sum of these four clumps. To include more extended emission, $\sum_{3\sigma}$ includes all emission at the 3σ level. See Fig. 4.12.

4.8 Conclusions

The paired antenna method for phase correction has been implemented at CARMA during the high resolution A and B configurations (2008-2010). Eight paired, atmospheric calibration antennas monitor bright quasars to correct atmospheric phase variations on time scales of ~ 5 -10 seconds. Analysis of the near daily test observations of quasars and of our science observations of Arp 193 confirm the viability of C-PACS.

We conclude that the angular separation between the atmospheric calibrator and target is the single most important factor in determining whether a C-PACS calibration is successful. Our data show improvement in target coherence if the atmospheric calibrator is six degrees or closer to the target source. This angular separation limit might be relaxed in extremely good weather or with better site conditions. The other two most important factors are atmospheric calibrator strength and elevation. For the sensitivity of our atmospheric array receivers, we achieve improvements in coherence from C-PACS correction for atmospheric calibrators with fluxes ≥ 1 Jy, with substantially better performance above 2 Jy. The angular separation of atmospheric calibrators to science targets and this flux limitation is a serious constraint in choosing science targets. More sensitive receivers will increase the number of valid calibrators, and hence available science targets. We find the C-PACS correction does not work as well at low elevations ($< 45^\circ$), which can be explained by the fact that at low elevations there is a larger physical separation in the troposphere between calibrator and target for a given angular separation.

These results are directly applicable to fast switching arrays (ALMA) and to dual beam systems (VERA). We point out that in reality since the scale height of the turbulent layer is about 2 km, the linear separation between beams at this

height is much larger than the separation of the antennas (20–25 m), especially as θ increases. For example, for $\theta=2^\circ$, the linear separation on the sky when observing a source at an elevation of 45° increases from about 50 meters to over 200 meters as the turbulent scale height, h , increases from 1 to 4 km. Hence, only in the case of very nearby atmospheric calibrators does the linear separation on the sky effectively equal the pair spacing. For small θ , considering the spread of the respective beams of our science and paired antennas (sizes of $\sim 1'$ and $\sim 10'$), the same part of the troposphere is probed. For larger θ , the correction depends on the scale size of the turbulence. Our findings are applicable to other calibration methods (e.g. dual-beam system or fast-switching which essentially reduce b_{pair} to 0 meters) because at the height of the turbulent layer, considering the beam spread of each antenna, a distance of ~ 20 -25 meters is negligible compared to the linear separation added as the angular separation to the atmospheric calibrator, θ , increases.

Calibrators at a farther angular separation could be used if the wind direction could be determined. We found a hint of evidence in a handful of tracks that there might be a time delay if the turbulence is indeed a “frozen” structure blowing at a constant velocity, resulting in a simple time offset. However, upon further analysis, we were not able to confirm this. And in many cases, the source and paired antennas seem to track phases that are not in sync in any way. This could be due to a multi-level weather pattern in the troposphere. For example, there is a prevailing easterly wind over the Sierras, but there is also a known diurnal pattern of north-south flow in the Owens Valley to the West of the observatory. As there is another deep valley towards the east (Deep Springs), it is possible that there are patterns of wind velocity at a lower level than the ~ 4 km easterly Sierra wind.

The C-PACS system works well under a wide range of atmospheric conditions. The data shows better corrections when opacity is low ($\tau_{225} < 0.2$), but the inverse

is true for rapid atmospheric fluctuations (change in delay) where a larger C-PACS correction is made for less stable atmospheric conditions. We also examined diurnal variations and periods of time with substantial cloud cover and found C-PACS correction to yield an increased improvement in coherence for daytime observations and periods of time with cloud cover. Daytime observations are associated with increased turbulence in the troposphere due to thermal heating, so this improvement matches our expectation of increased improvement for periods of time with more rapid atmospheric fluctuations. The presence of clouds does not hinder a positive correction. We plan to also study the time scales for atmospheric variations to determine how short the integration times are required to be for successful C-PACS corrections. We anticipate that the time scale will depend on the weather conditions.

As we only had eight paired atmospheric calibration antennas, we examined methods to determine the appropriate phase for non-paired primary antennas. Among interpolation methods, we found a positive improvement made for non-paired antennas when using interpolated phases from the paired antennas. However, the improvement is not as good as that obtained by the antennas with a paired antenna. The best improvement was found interpolating with a power law with an exponent of 3.5.

Expanding C-PACS to include paired antennas for each science antenna would be useful. We have found that correction is not particularly good for baselines shorter than 300 meters. Without a full correction for all antennas, it is difficult to map sources with resolved emission. We imaged the luminous infrared galaxy, Arp 193, in A configuration to achieve a resolution of $0.18'' \times 0.12''$. We find that a lot of the source is resolved out if we only use the eight paired antennas, and have to fold in $\sim 75\%$ of baseline data that has only marginal improvement in coherence from interpolation.

Our analysis of Arp 193 shows agreement with the CO maps and interpretation by DS98. Out to a radius of 750 pc, we calculate a dynamical mass of $7.4 \times 10^9 M_{\odot}$ and infer a molecular gas mass of $\sim 1.4 \times 10^9 M_{\odot}$. The ratio of molecular gas mass rises steeply towards the center of the disk, with well over 50% of the total mass in the form of molecular gas within the inner 100 pc. The ratios we compute of atomic to molecular gas are consistent with the results presented by Clemens and Alexander (2004), with a very small fraction of H I in the inner region ($< 1\%$), increasing at greater distance from the central region. The computed column densities for two clumps in the inmost region of the rotating disk/ring are $> 10^{25} \text{ cm}^{-2}$.

Chapter 5

Concluding Remarks

5.1 Summary

We have aimed to better understand (1) why luminous infrared galaxies exist and have such prolific IR emission, (2) what physical properties are different from and in common with other types of galaxies, and (3) how much variation exists within this population.

In Chapter 2, we derived the spatial cluster-galaxy correlation amplitude, B_{gc} , for 76 $z < 0.3$ ULIRGs from the 1-Jy sample and compared our results with those in the literature for $z < 0.05$ AGNs, $z \approx 0.2$ QSOs, and $0.3 \lesssim z \lesssim 1$ QSOs. We found that local ULIRGs live in environments similar on average to that of field galaxies, with only a few exceptions. The infrared luminosity, optical spectral type, and IRAS 25-to-60 μm flux ratios of ULIRGs show no dependence with environment, nor does the environment vary over the redshift range covered by our sample (mostly $0.1 < z < 0.22$). We compared the B_{gc} distribution of local ULIRGs with those of local Seyferts, local QSOs, and intermediate- z QSOs. Overall, the results of this study suggest that ULIRGs can be a phase in the lives of all types of AGNs and QSOs, but not all moderate-luminosity QSOs have necessarily gone through a ULIRG phase.

In Chapter 3, we presented spectroscopic observations with Arecibo of 77 IR luminous galaxies from the IRAS-NVSS 2 Jy sample in the range $2^h < \text{R.A.} < 10^h$, the second part of a three-part survey. We detected H I in emission or absorption in 61 galaxies, with 52 being new detections. Six sources had pure absorption and one source had both emission and absorption. We did not detect HCN, HCO⁺, OH main or OH satellite lines, primarily due to RFI. We computed H I mass for galaxies with emission and found H I mass increases with IR luminosity. For galaxies with absorption, we computed the optical depth and H I column density. Optical depths ranged from 0.07 to 0.5, and column densities ranged from 7.0 to $67.0 \times 10^{18} \text{ cm}^{-2} \text{ K}^{-1}$. 25% of the galaxies in our sample with $L_{\text{IR}} \geq 10^{11.5} L_{\odot}$ have absorption, while less than 10% have absorption features in less-luminous galaxies in our sample.

In Chapter 4, we presented a study of the paired antenna method for phase correction at CARMA in order to achieve high resolution imaging of the nuclear region of the LIRG Arp 193. Analysis of the near daily test observations of quasars and of our science observations of Arp 193 confirm the viability of C-PACS. We concluded that angular separation between the atmospheric calibrator and target ($\leq 6^{\circ}$) is the single most important factor, but calibrator flux and elevation also have an effect. Improvement in coherence with C-PACS correction is not negatively affected by cloud cover, rapid atmospheric fluctuations, or diurnal effects. We do observe better improvements when opacity (τ_{225}) is low (< 0.2).

We imaged Arp 193 in ¹²CO(2-1) using the C-PACS method in CARMA's A configuration and achieved an angular resolution of $0.18'' \times 0.12''$ ($\sim 64 \text{ pc}^2$), a factor two higher than previous observations. Combining observations from A, B and C configurations, we calculated the total molecular gas mass contained within the inner disk to be $7.3 \times 10^8 M_{\odot}$. We compared the molecular gas mass with the dynamical mass and found the ratio to be $\sim 20\%$ at a radius of 750 pc. We computed

the molecular gas column densities and found the innermost nuclear region to contain regions $> 10^{25} \text{ cm}^{-2}$. Our results are consistent with analysis in the literature.

5.2 Future Work

Looking towards the future, we describe a few projects we plan to continue:

- Complete analysis of galaxies with H I absorption and spectral line non-detections for galaxies in Part II of the 2 Jy IRAS-NVSS sample of U/LIRGs ($2^h < \text{R.A.} < 10^h$). Publish results in a data paper to make measurements available to the community.
- Complete the third and final portion of the 2 Jy IRAS-NVSS sample ($0^h < \text{R.A.} < 2^h$ and $10^h < \text{R.A.} < 20^h$), combining all of our observational data with measurements in the literature for a full statistical analysis. Possibly enlarge the sample size by expanding the observable sky to a larger declination range using a steerable telescope, such as the Green Bank Telescope. Follow up study and imaging of interesting objects with the EVLA. This sample will include those galaxies with OH emission or absorption, H I absorption, and any galaxies in which we detect HCN, HCO⁺ or OH satellite lines. Observe more galaxies from our sample in CO to investigate the correlation between H I and H₂ gas mass.
- Conduct a more thorough analysis of the molecular gas emission in Arp 193, using our final improved maps from the C-PACS atmospheric correction.

Appendix A

Single–Dish Aperture Efficiency Measurements at CARMA

A.1 Abstract

We describe the process by which single dish aperture efficiency measurements are carried out for the antennas of the CARMA array. The basis for the measurements is explained and the practical details are described. Related topics such as the approximations used at CARMA to calculate atmospheric opacity from weather data, the analysis of sky dips to actually measure atmospheric opacity, the model for lunar brightness temperature and effective primary beam sizes are also discussed.

A.2 Introduction

The *aperture efficiency* of an antenna is simply the ratio of the effective collecting area (in terms of collected power that gets into the receiver feed horn) to the physical collecting area. An ideal antenna would have 100% efficiency. However, numerous factors can absorb the incident radiation or scatter it out of the beam path, e.g.,

- blockage of the dish surface by the subreflector and the support legs;
- gaps between the individual panels that typically make up the reflecting surface of millimeter dishes, and poor reflection from the heads of the screws used to mount the panels;
- deviation of the dish shape from a parabola such that the incident radiation is not all collected at the focus (spillover, taper). This property often changes with dish elevation as the orientation of gravitational forces relative to the support structure changes and the dish deforms;
- imperfect illumination of the subreflector and then the feed horn by the aperture. In order to reduce spillover the illumination pattern is often deliberately tapered at the edge of the aperture. This and any unintentional imperfections in the illumination pattern will reduce aperture efficiency;
- diffraction at the edge of the subreflector;
- incorrect focus position (either lateral or axial) for the subreflector; and
- imperfect reflection due to roughness on the dish surface (referred to as “Ruze loss”).

A thorough description of the elements that control aperture efficiency for reflecting antennas is given by Baars (2003). All these effects can each contribute losses of several percent in efficiency, and since they combine in series (i.e., geometrically), they can add up to tens of percent loss in efficiency compared to an ideal antenna. Lugten (1995) discusses the efficiency of the BIMA 6.1m antennas: estimates of the above effects lead to a theoretical estimate of 75% for the main beam aperture efficiency, and measurements at Hat Creek were consistent with this result. This is regarded as good for a millimeter-wavelength telescope.

There are several ways to measure the aperture efficiency. Here we discuss the use of single-dish total power measurements (a separate memo discusses interferometric measurements at CARMA). The discussion is written from a non-expert’s point of view, based on a number of sources, including the basic paper on calibration by Ulich and Haas (1976), the NRAO 12m telescope manual (Folkers 2004), the HIFI/Herschel calibration document (Kramer 2005), ALMA calibration documents (Mangum 2002; Moreno and Guilloteau 2002), and Dave Woody’s CARMA calibration memo (Woody 2006).

A.3 Single-Dish Aperture Efficiency Measurements: Theory

The aperture efficiency of a dish may be determined from measurements of the power in the receiver when illuminated by three different targets: blank sky, a bright planet, and an ambient-temperature load. A source such as a planet or a maser typically only fills a small fraction of the telescope beam, and thus is appropriate to measure the “main-beam” aperture efficiency ϵ relevant to interferometer observations.

We will discuss single-dish power measurements along the lines of the framework used in the CARMA memo on T_{sys} calculation (Woody 2006). First consider the contributions to the receiver power when the telescope points at blank sky. The power measured at the receiver is the product of a gain G (e.g., in units of dB per Kelvin) with the following temperature contributions:

- The intrinsic thermal noise of the receiver, T_{rec} .
- The thermal emission of the optically thin atmosphere above the telescope: we represent the atmosphere by a single temperature T_{atm} and an opacity τ

(which, for a given telescope elevation El , is the zenith opacity τ_0 times the “air mass” $1/\sin(El)$), so that the atmospheric contribution is $T_{atm}(1 - e^{-\tau})$.

- Above the atmosphere, the sky is filled by the cosmic microwave background (CMB). This must pass through the atmosphere and hence is attenuated by a factor $e^{-\tau}$ when it reaches the telescope.
- The subreflector support legs and any illumination into the feed from optical paths that do not reflect from the dish, such as beyond the edges of the dish (“rear spillover”) or the edge of the subreflector (“forward spillover”), contribute to the measured power.

Although we use temperatures in the formulae presented here, in each case the relevant value to use is the Rayleigh–Jeans curve equivalent contribution, $J(\nu, T) = (h\nu/k_B)/(\exp(h\nu/k_B T) - 1)$. For example, the temperature of the CMB is 2.73 K, but the temperature we need at millimeter wavelengths, T_{CMB} , is the Rayleigh–Jeans curve equivalent $J(\nu, 2.73) \approx 1$ K at 3 mm wavelength. In the 3 mm window $J(T) \approx T - 2$ is quite a good approximation above a few K, and $J(T) \approx T - 5$ in the 1.3 mm window, so the difference between T and $J(T)$ is negligible except for the CMB.

The expression for the power measured on the sky is thus

$$P_{sky} = G\{T_{rec} + (1 - e^{-\tau})\eta T_{atm} + (1 - \eta)T_{spill} + e^{-\tau}\eta T_{CMB}\} \quad (\text{A.1})$$

Here η is a “coupling efficiency” that is distinct from the aperture efficiency appropriate to compact cosmic radio sources that we seek to measure. The distinction between different forms of efficiency can be very confusing: Mangum (2002) lists no less than 7 separate types of “telescope efficiency” in his Appendix D. Here η is the

efficiency appropriate for the coupling of a source that completely fills the forward hemisphere of the dish with a uniform temperature. In this situation the receiver is effectively enclosed in a black body cavity at the corresponding temperature, and the focussing properties of the aperture have little effect on the temperature seen by the receiver. The only decrements to this efficiency are the small effects of rear spillover, blockage and ohmic losses. The 12m Telescope Manual (Folkers 2004) calls η the “warm spillover efficiency”, Serabyn et al. (1998) refer to it as the “coupling efficiency” and Plambeck (2000) describes it as the “spillover efficiency”. This efficiency is typically close to unity.

It is common in calibration documents to use the same base symbol η , suitably subscripted, to refer to all forms of telescope efficiency. While experts have no difficulty in keeping track of the seven distinct forms of η , the use of a single symbol tends to cause confusion for the non-expert. To minimize confusion here, we will use different symbols. In this document η will always and only refer to the “spillover” or “coupling” efficiency described above.

Since the CMB and the sky contribution both in effect fill the forward hemisphere of the dish, they are both modified by η . The receiver noise, on the other hand, is intrinsic and thus not affected by the coupling efficiency. T_{spill} is the effective temperature of the rear spillover and blockage effects, whose contribution to the measured power is proportional to $(1 - \eta)$ since it enters the feed through the portion of the aperture that is not illuminated by the forward hemisphere. In most discussions of calibration (e.g., Folkers 2004; Kutner and Ulich 1981) T_{spill} is set equal to the ambient temperature since most of the contributions (ground, subreflector support, etc.) are at that temperature.

As part of the calibration procedure millimeter telescopes generally use a “load” of known temperature that can be placed in the beam path, either inside the cabin

(6.1-m dishes) or outside in the ambient air (10.4-m dishes), and the power measured on the load is compared with the corresponding power measurement on the sky. The power measured on the ambient load is

$$P_{load} = G\{T_{rec} + T_{load}\} \quad (\text{A.2})$$

where T_{load} is the (Rayleigh–Jeans equivalent of the) physical temperature of the load. The use of these power measurements to determine the telescope calibration is reprised in §A.7.1. For clarity, in our discussion we will ignore the distinction between the receiver sidebands: in general G and τ may be different in the upper and lower sidebands and we have separate equations for both. However, the algebra is much clearer if we ignore this distinction for the exposition.

For the aperture efficiency measurements we use (A.1), (A.2) and the power measured while pointing at a suitable planet:

$$P_{src} = G\{T_{rec} + (1 - e^{-\tau})\eta T_{atm} + (1 - \eta) T_{spill} + e^{-\tau}(\epsilon T_{src} + \eta T_{CMB})\} \quad (\text{A.3})$$

where T_{src} is the temperature contribution of the target planet diluted over the entire area of the beam, discussed further in the next section. The contribution of the planet is explicitly modified by the telescope “main-beam” aperture efficiency ϵ as well as the atmospheric opacity. We explicitly assume in (A.3) that the planet does not fill the primary beam and that the CMB still contributes to the power measured: if this is not the case then one sets $T_{CMB} = 0$ in (A.3).

For convenience, we now define an effective sky temperature contribution seen by the telescope,

$$T_{sky} = (1 - e^{-\tau})\eta T_{atm} + (1 - \eta) T_{spill} + e^{-\tau}\eta T_{CMB} \quad (\text{A.4})$$

so that, by analogy with (A.2), we may write (A.1) as $P_{sky} = G\{T_{rec} + T_{sky}\}$. We use the common “Y” notation for ratios of the power measurements, e.g.,

$$Y_{load} = \frac{P_{load}}{P_{sky}} \quad (\text{A.5})$$

We have not yet determined the receiver temperature, but from the ratio $Y_{load} = P_{load}/P_{sky}$ (eqns. 1, 2) we find

$$T_{rec} = \frac{T_{load} - Y_{load} T_{sky}}{Y_{load} - 1} \quad (\text{A.6})$$

Substituting this expression into (A.1) and (A.3), with $Y_{src} = P_{src}/P_{sky}$, we derive the following expression for the aperture efficiency:

$$\epsilon = \frac{Y_{src} - 1}{Y_{load} - 1} \frac{T_{load} - T_{sky}}{e^{-\tau} T_{src}} = \frac{P_{src} - P_{sky}}{P_{load} - P_{sky}} \frac{T_{load} - T_{sky}}{T_{src}} e^{\tau} \quad (\text{A.7})$$

This expression can be simply interpreted as the ratio of the power contributed by the source, $P_{src} - P_{sky}$, to the power expected from multiplying the telescope gain $G = (P_{load} - P_{sky})/(T_{load} - T_{sky})$ by the source temperature contribution T_{src} , corrected for atmospheric absorption of the source with the factor e^{τ} . The aperture efficiency (A.7) may be evaluated using the 3 power measurements in (A.1)-(A.3) together with T_{src} , T_{load} and a value for T_{sky} calculated from measured values of air temperature, pressure and humidity (obtained by the CARMA weather station and available in the monitor data stream) as follows:

- The atmospheric opacity in the 1 mm band is provided by the tipper. No tipper is available at CARMA for the 3 mm band: τ is generally calculated from the expression presented in a note by Dave Woody (summarized in §A.7.2 below). The expression contains a slowly-varying term proportional to the water vapor density, and a pressure- and temperature-dependent approximation to the 119

GHz O₂ line. The value of τ calculated in this way is used in the 3 mm T_{sys} calculation at CARMA. τ at 3 mm can also be measured with a sky dip (see §A.7.3). At the Cedar Flat site at 2000 m altitude, the zenith opacity τ_0 is typically of order 0.03–0.10 in the 3 mm window but 0.2–0.8 in the 1 mm window.

- If $T_{outdoor}$ is the outdoor air temperature near the ground, the effective temperature of the atmosphere at the height of the main atmospheric absorption contribution, T_{atm} , is taken to be $0.94T_{outdoor}$.
- We set $\eta = 0.975$. The value of T_{spill} is not well determined but is not critical here since it only appears multiplied by $1 - \eta$: we use the standard assumption that $T_{spill} = T_{outdoor}$.
- T_{load} is set equal to $T_{outdoor}$ for the OVRO antennas where the absorbing load is outside the electronics cabin, but potentially different for the BIMA antennas where the cal wheel is inside the temperature-controlled cabin, i.e.,

$$T_{load} = \begin{cases} T_{outdoor} & \text{for 10.4-m dishes} \\ T_{cabin} & \text{for 6.1-m dishes} \end{cases} \quad (\text{A.8})$$

A.4 Planet Temperature Contributions

When the target is an extended source such as a planet, we can calculate its temperature contribution T_{src} by diluting the planet disk temperature using the ratio of the area (in solid angle) of the source to the area of the main beam. When the source is a point source, we convert its flux to a diluted temperature. At the present time, planets are invariably modelled as an elliptical disk of constant brightness temperature for calibration purposes, and we will assume circular disks for our discussion.

For small sources we thus have

$$T_{src} = \begin{cases} T_{planet} \frac{\Omega_{planet}}{\Omega_A} & \Omega_{planet} \ll \Omega_A \\ \frac{c^2}{2k_B f^2} \frac{S}{1.133 \theta_{FWHM}^2} & \text{point source of flux } S \end{cases} \quad (\text{A.9})$$

where Ω_{planet} is the solid angle occupied by the planet ($\pi \theta_{planet}^2/4$, where θ_{planet} is the angular diameter of the planet) and Ω_A is the solid angle for a perfect antenna with an aperture of area $\pi D^2/4$. f is the observing frequency, k_B is the Boltzmann constant and c is the speed of light. Let θ_{FWHM} be the ideal full-width-at-half-maximum of the primary beam of the telescope. For the aperture efficiency measurements the appropriate beam size corresponding to a perfect uniformly and fully illuminated aperture is $\theta_{FWHM} = \lambda/D$, as follows:

$$\theta_{FWHM} = \begin{cases} 59.5'' (100/f_{GHz}) & \text{for the 10.4m dishes} \\ 101.4'' (100/f_{GHz}) & \text{for the 6.1m dishes} \end{cases} \quad (\text{A.10})$$

In the case that θ_{planet} is a significant fraction of θ_{FWHM} , we also have to take into account the telescope primary beam response (e.g., Stutzman and Ko 1974). This is modelled by a Gaussian of the form $e^{-\theta^2/2\sigma^2}$ with $\theta_{FWHM} = 2\sqrt{2 \ln 2} \sigma$. The effective area of such a Gaussian beam pattern is $\pi \theta_{FWHM}^2/4 \ln 2 = 1.133 \theta_{FWHM}^2$. Convolution of the Gaussian beam with the planetary disk produces the result that

$$T_{src} = T_{planet} \left(1 - e^{-\ln 2 \frac{\theta_{planet}^2}{\theta_{FWHM}^2}}\right) \quad (\text{A.11})$$

Similarly, in the case of a point source, the equivalent sky temperature (/refappeq9) averaged over the area of the beam can be expressed numerically as

$$T_{src} = 1.22 \times 10^6 \frac{S_{Jy}}{f_{GHz}^2 \theta_{FWHM}^2} \quad (\text{A.12})$$

with S_{Jy} the source flux in Janskys, f_{GHz} the frequency in GHz and θ_{FWHM} measured in arcseconds.

Note that in practice the illumination pattern of the antennas is generally tapered at the edges of the dish in order to reduce spillover, and this increases the effective beam size relative to the “ideal” value used here for aperture efficiency calculations. For interest, §A.7.4 presents measurements of the effective beam size of the CARMA dishes.

Table A.1: Single-dish aperture efficiency measurements on Jupiter at 95 GHz

Date/Array	C1	C2	C3	C4	C5	C6	C7	C8	C9	C10	C11	C12	C13	C14	C15
080501/C	0.50	0.47	0.53	0.47	0.46	0.49	0.59	0.53	0.51	0.59	0.48	0.55	0.53	0.42	0.40
080531/C	0.45	0.42	0.46	0.44	0.39	0.42	0.52	0.58	0.57	0.61	0.52	0.51	0.52	0.51	0.57
080601/C	0.50	0.48	0.53	0.49	0.46	0.50	0.57	0.61	0.57	0.65	0.57	0.58	0.58	0.55	0.57
080802/D	0.53	0.51	0.55	0.52	0.48	0.53	0.61	0.59	0.57	0.62	0.59	0.57	0.62	0.58	0.62
080925/E	0.50	0.55	0.55	0.49	0.46	0.52	0.48	0.61	0.52	0.51	0.64	0.59	0.64	0.61	0.46
081002/E	0.47	0.53	0.47	0.49	0.45	0.50	0.49	0.43	0.57	0.36	0.36	0.56	0.08	0.51	0.48
081019/C	0.50	0.53	0.53	0.49	0.46	0.50	0.60	0.60	0.56	0.63	0.61	0.59	0.65	0.58	0.59
081023/C	0.50	0.56		0.50	0.47	0.52	0.63	0.59	0.63	0.68	0.67	0.64	0.65	0.63	0.64
081029/C	0.52	0.56	0.55	0.52	0.50	0.53	0.60	0.61	0.59	0.64	0.62	0.56	0.65	0.61	0.61
081105/C	0.48	0.54	0.54	0.50	0.48	0.50	0.60	0.61	0.61	0.66	0.65	0.61	0.64	0.62	0.66
081113/C	0.45	0.53	0.51	0.46	0.44	0.47	0.56	0.59	0.60	0.64	0.61	0.56	0.63	0.60	0.63
081205/B	0.51	0.54	0.50	0.50	0.49	0.52	0.62	0.61	0.61	0.66	0.66	0.54	0.65	0.62	0.60
081210/B	0.51	0.53	0.52	0.52	0.48	0.53	0.63		0.64	0.67	0.66		0.65	0.61	0.70
081217/B	0.48	0.53	0.49		0.45	0.48	0.64	0.63	0.63		0.71	0.54	0.65	0.61	0.65
090112/A	0.46	0.49	0.49	0.48	0.46	0.50	0.63	0.60	0.62	0.64	0.66	0.68	0.62	0.60	0.64
090114/A	0.46	0.51	0.51	0.51	0.48	0.53	0.60	0.59	0.59	0.61	0.26	0.58	0.61	0.59	0.63
090128/A		0.50	0.51	0.50	0.44	0.48		0.59	0.48	0.57		0.60	0.61	0.53	0.58
090204/A		0.47	0.50	0.49	0.48	0.51	0.47			0.57	0.56	0.59	0.58	0.55	0.60
090218/D	0.48	0.51	0.50	0.54	0.50	0.53	0.59	0.59	0.58	0.60	0.60	0.59		0.57	0.59
090304/D		0.55	0.53	0.49		0.47	0.63	0.42			0.65	0.60	0.64	0.53	0.62
090318/D	0.51	0.55	0.52	0.52	0.51	0.54	0.59	0.54		0.60		0.60	0.62	0.54	
100212/A	0.52	0.48	0.47	0.54	0.44	0.47	0.64	0.57	0.63	0.63	0.60	0.56	0.65	0.52	0.61
Median	0.48	0.53	0.51	0.49	0.46	0.50	0.60	0.59	0.57	0.61	0.60	0.59	0.62	0.58	0.61

A.5 Measurements on Jupiter

Data sufficient to carry out the calculation in (/refappeq7) are acquired (as of June 2008) using the script **ApertureEfficiencySD.py**. This script is described in more detail in §A.7.5. The power measurements are the Psys values corresponding to each of the 500 MHz spectral bands at the inputs to the CARMA correlator; front-end power measurements in the receiver, with potentially wider bandwidths, were not found to be as stable as the Psys data for this purpose.

Between 2008 May and 2010 February, a significant number of datasets have been acquired using Jupiter (generally the brightest available planet) as the target. During this period the CARMA system could produce 3 separate spectral windows each with 500 MHz bandwidth in each sideband (upper and lower). The power measurements are not sideband-separated. On each date 3 separate measurements were obtained, simultaneously in each of the three spectral windows. Elevations were generally low (below 25°) due to the low declination of Jupiter. For a given

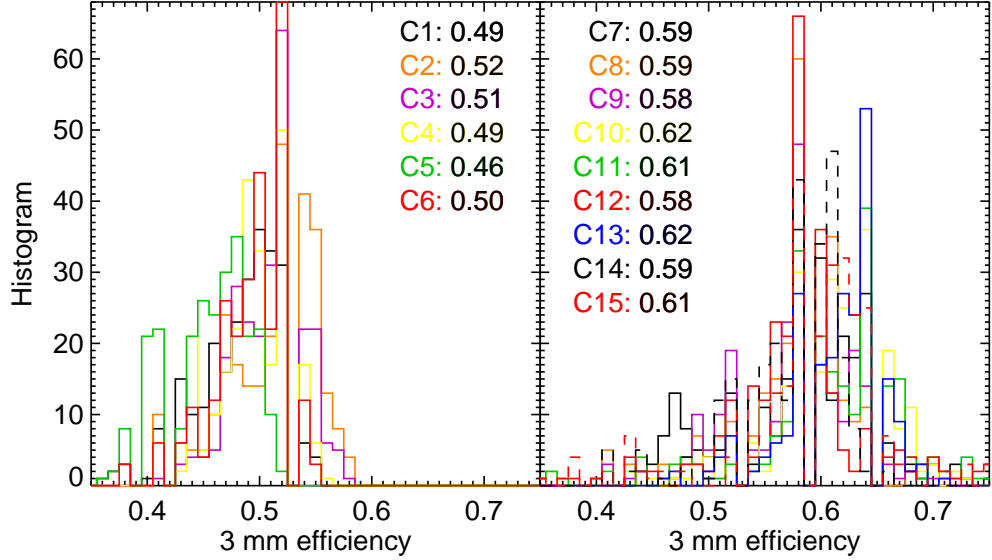


Figure A.1: Histograms of the single-dish aperture efficiency measurements at 3 mm using Jupiter as the reference source. The 10.4-m antennas are shown in the left panel and the 6.1-m antennas in the right. Different colors are used for different antennas, as labelled: the labels also report the median efficiencies over all the data for each antenna.

measurement, the 3 spectral windows on a given antenna agreed typically to within 1%. Median efficiencies for each date, calculated using (`/refappeq7`), are shown in Table A.1. The final row of this table shows the median of the values in the table for each antenna. A histogram of all of the 3 mm measurements in each band for each antenna is shown in Figure A.1.

The calculations assume a brightness temperature of 179 K for Jupiter at 95 GHz, and diameters (41" – 45") obtained from the planetary ephemeris. In these measurements, the 10.4-m antennas generally have efficiencies at 3 mm that are close to 50%, while the 6.1-m dishes are all close to 60%. Generally all antennas of a given type have similar efficiencies, although C5 does seem to be significantly worse than the other 10.4-m dishes. Note also that the 10.4-m antennas show a fairly sharp upper cutoff in the distribution of measured efficiencies, whereas the 6.1-m values seem to show a larger spread.

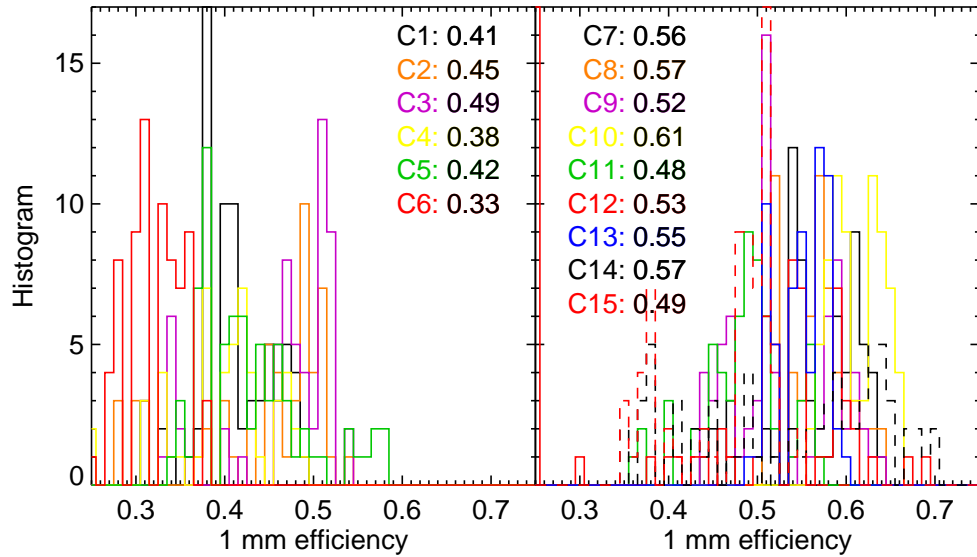


Figure A.2: Histograms of the single-dish aperture efficiency measurements at 1 mm using Jupiter as the reference source. The 10 m antennas are shown in the left panel and the 6.1-m antennas in the right. Different colors are used for different antennas, as labelled: the labels also report the median efficiencies over all the data for each antenna.

The results of measurements at 1 mm on Jupiter are shown in Table A.2 and plotted in Figure A.2. In both tables anomalies on individual antennas may be found: such anomalies seldom represent true aperture efficiencies, but result from other factors (poor tuning, etc.), and a number of measurements, as are available at 3 mm, are needed in order to recognize clear trends. At present we do not have enough 1 mm measurements to draw strong conclusions. C6 appears consistently to be lower (around 33%) than the other 10.4-m dishes, and C11 and C15, at least during this period, were worse than the other 6.1-m dishes. The 10.4-m dishes are significantly less efficient than at 3 mm, as expected, but the variation from one measurement to the next is larger at 1 mm than at 3 mm and this may explain why, e.g., C10 appears to have the same aperture efficiency at 1 mm as at 3 mm.

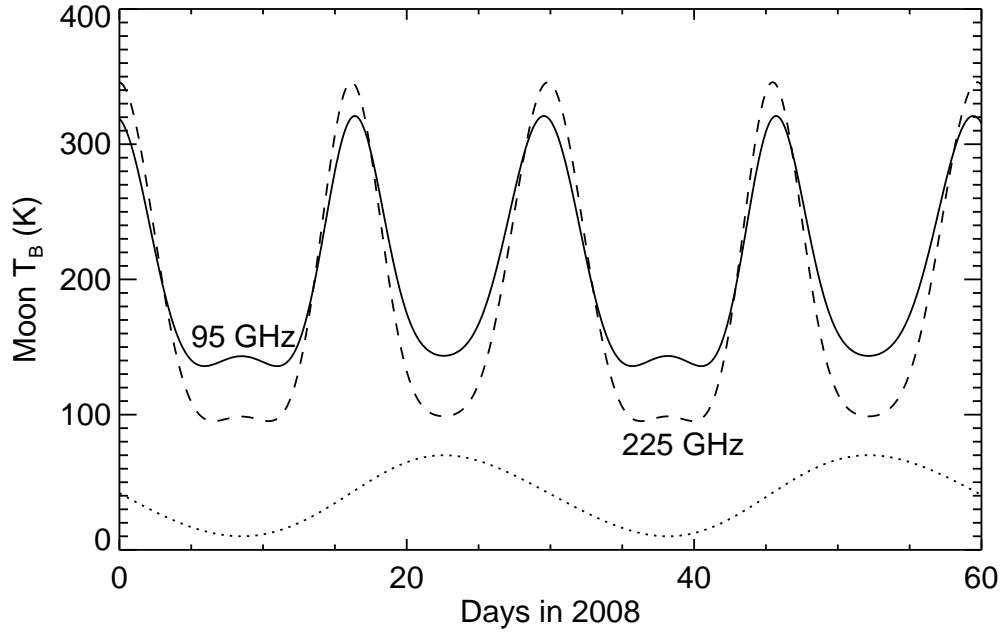


Figure A.3: Plot of the apparent brightness temperature of the center of the Moon as a function of date in 2008 at 3 mm (solid line) and 1 mm (dashed line) wavelengths. The data are calculated using the formula from Mangum (1993), based on the study by Linsky (1973). The phase of the Moon is plotted as a dotted line at the bottom of the panel: minima in this curve correspond to new moon.

Table A.2: Single-dish aperture efficiency measurements at 1 mm

Date/Array	C1	C2	C3	C4	C5	C6	C7	C8	C9	C10	C11	C12	C13	C14	C15
080501/C	0.41	0.14	0.52	0.23	0.39	0.29	0.54	0.53	0.46	0.59	0.50	0.54	0.39	0.49	
081023/C	0.39	0.48		0.33	0.40	0.30	0.59	0.57	0.58	0.62	0.55	0.57	0.57	0.64	0.50
081030/C	0.48	0.50	0.49	0.41	0.46	0.35	0.47	0.57	0.58	0.64	0.46	0.53	0.55	0.63	0.38
081205/B	0.38	0.45	0.47	0.38	0.44	0.32	0.61	0.62	0.61	0.65	0.50	0.59	0.57	0.63	0.53
081210/B	0.33	0.30	0.34	0.21	0.37	0.34	0.56		0.53	0.61		0.51	0.55	0.49	0.38
090311/D	0.46	0.40	0.53	0.47	0.56	0.34	0.63	0.57	0.52	0.58	0.45	0.54		0.57	0.50
090318/D	0.41	0.40	0.43	0.49	0.58	0.44	0.50	0.46		0.48		0.61	0.63	0.39	
090422/C	0.41	0.51	0.48	0.42	0.46	0.36		0.56	0.50	0.60	0.40	0.55	0.51	0.55	0.47
090513/D	0.37	0.53	0.49	0.39	0.53	0.40	0.44	0.42	0.42	0.56	0.36	0.63	0.56	0.53	0.46

A.6 Filled–Aperture Measurements on the Moon

The Moon is the brightest object available for calibration at millimeter wavelengths because it fills the telescope beam with a source of temperature 100–300 K. However, it also has several drawbacks: its effective temperature varies with position across the disk, and varies dramatically with lunar phase due to solar heating and the time delay required as heat propagates from the lunar surface downwards through the subsurface layers into which millimeter wavelengths penetrate (see Figure 1; Linsky 1973; Mangum 1993; Sandor and Clancy 1995). Another important difference is that because the Moon is so large it fills not only the primary beam, but also any beam sidelobes out to some considerable distance. This is in contrast to observing a smaller object, which occupies only a fraction of the primary beam. Measurements of the power on the Moon are therefore sensitive to the entire forward gain of the dish, rather than just the (smaller) forward gain of the main lobe of the primary beam that is the relevant quantity for aperture efficiency measurements for an interferometer observing a compact source. In the literature the telescope efficiency measured on the Moon, which we will refer to as ϵ_f , is described as the “forward scattering” efficiency, while the measurement of the efficiency of the main lobe of the primary beam is referred to as the “main beam” efficiency.

In this case the power measured when the telescopes point at the Moon can be represented by the following expression:

$$P_{moon} = G\{T_{rec} + (1 - e^{-\tau})\eta T_{atm} + (1 - \eta) T_{spill} + e^{-\tau}\epsilon_f T_{moon}\} \quad (\text{A.13})$$

The only significant difference from (A.3) is that the Moon always blocks the CMB entirely, so the CMB no longer contributes to the power on source. Now setting $Y_{Moon} = P_{Moon}/P_{sky}$ and using (A.1), (A.2) and (/refappeq13), after some algebra

we find

$$\epsilon_f = \frac{Y_{Moon} - 1}{Y_{load} - 1} \frac{T_{load} - T_{sky}}{e^{-\tau} T_{Moon}} + \eta \frac{T_{CMB}}{T_{Moon}} \quad (\text{A.14})$$

As noted earlier, T_{Moon} is problematic due to its rapid variation in time as direct solar heating moves progressively across the visible disk of the Moon, but at new Moon the disk-center brightness temperature is relatively stable for a few days at minimum values of order 140 K at 95 GHz and 95 K at 225 GHz (see Figure 1). Thus the best time to use the Moon for telescope efficiency measurements is around new Moon.

Table A.3 shows the results of single-dish measurements of the Moon on 2008 April 10 (central disk brightness temperature of 222 K from Mangum 1993), April 17 (183 K) and July 31 (close to new moon, 141 K) at 97 GHz. As the table convincingly demonstrates, the absolute values of the efficiencies (frequently in excess of 100%) are not reliable. The variation from one dataset to the next presumably reflects the limitations of the model used for the Moon disk-center brightness temperature. The main feature of these measurements is that all telescopes with good data show very similar efficiencies, with the 6.1-m antennas only slightly better (on average) than the 10.4-m antennas. The similarity across all antennas presumably reflects the fact that the Moon fills all the forward-scattering sidelobes, and any imperfections in main-beam patterns are compensated by the filled sidelobes.

Table A.3: Single-dish Forward-scattering Efficiency Measurements on the Moon

Date/Array	C1	C2	C3	C4	C5	C6	C7	C8	C9	C10	C11	C12	C13	C14	C15
080410/C	0.61	0.62	0.61		0.60	0.63	0.68	0.63	0.65	0.68	0.67	0.67	0.65	0.63	
080417/C	1.21	1.23	1.19	1.24	1.15			1.22	1.21	1.28	1.24	1.24	1.22	1.23	1.22
080731/D	1.02	1.02	1.00	1.05	0.97	1.03	1.07	1.04	1.04	1.11	1.08	1.08	1.07	1.08	1.07

A.7 Aperture Efficiency Memo Appendices

A.7.1 Telescope Calibration

As described in CARMA Memo 33 (Woody 2006), we use power measurements on the sky and on an ambient load to determine the telescope system temperature and thus the calibration factors needed to convert the correlator output into calibrated visibilities. At millimeter wavelengths the atmosphere can be a significant issue that needs to be addressed by calibration. A common technique, used by CARMA and previously by BIMA, is to calculate an equivalent temperature of a load *above* the atmosphere that would produce the same power level in the receiver as the ambient load placed in the optical path. This temperature is called T_{cal} , and this method is known as the T_{cal} method. (Note that at some telescopes both hot and cold loads are available, which gives an additional measurement for calibration, but the discussion here only applies to the single-load system appropriate to CARMA.) Recall that the power measured on the sky is, from (A.1),

$$P_{sky} = G\{T_{rec} + (1 - e^{-\tau})\eta T_{atm} + (1 - \eta)T_{spill} + e^{-\tau}\eta T_{CMB}\}$$

while the power measured on the ambient load is given by (A.2),

$$P_{load} = G\{T_{rec} + T_{load}\}$$

where, as before, at CARMA T_{load} is the outside air temperature for the 10.4m dishes and the cabin temperature for the 6.1m dishes. We now define T_{cal} to be the temperature of a load placed above the atmosphere that produces the same power measurement in the receiver as the ambient load, i.e., we combine (A.1) and (A.2) and set

$$P_{load} = G\{T_{rec} + T_{load}\} = G\{T_{rec} + (1 - e^{-\tau})\eta T_{atm} + (1 - \eta)T_{spill} + e^{-\tau}\eta T_{cal}\} \quad (\text{A.15})$$

Thus we find that

$$T_{cal} = \frac{T_{load} - (1 - e^{-\tau})\eta T_{atm} - (1 - \eta)T_{spill}}{e^{-\tau}\eta} \quad (\text{A.16})$$

The contribution of spillover is often ignored, since it is multiplied by the small number $(1 - \eta)$. Note that in (/refappeq15) we have assumed that the T_{cal} load fills the beam and blocks the CMB; if instead we assume that the T_{cal} load is physically small, then T_{cal} in (/refappeq15) is replaced by $T_{cal} + T_{CMB}$ and we do the same thing in (/refappeq16).

We can now write out an expression for the *system temperature*, defined as the temperature of a load that doubles the output receiver power compared to its value with no load. The system temperature is the critical quantity used to convert the correlation coefficients measured by an interferometer's correlator into visibilities correctly calibrated in Janskys. With $Y_{load} = P_{load}/P_{sky}$ the system temperature becomes (Woody 2006)

$$T_{sys} = \frac{T_{cal}}{Y_{load} - 1} \quad (\text{A.17})$$

This expression gives the system temperature above the atmosphere since it uses T_{cal} . Optionally, the numerator may be $T_{cal} - T_{CMB}$ if the CMB is always in the beam (not the case when observing the Moon), but since T_{CMB} is of order 1 K and hence is always much less than T_{cal} , we can ignore this subtlety here.

A.7.2 Opacities from Weather Data

When the 3 mm opacity at CARMA is not measured with a sky dip but must instead be calculated from weather data (since there appears to be no simple relationship between the 3 mm opacity and the opacity at 225 GHz measured by the tipper), we use a simple approximation to the continuum opacity from Waters (1976) together with a model for the 119 GHz oxygen line due to Dave Woody (described in an 1989 note, and in Andy Beard’s note on CARMA flux and T_{sys} calibration):

$$\tau_0 = 0.039 + 0.0090 \rho_V + \frac{3.57 (P/876)^2 (300/T)^{2.5}}{(f_{GHz} - 118.75)^2 + 1.4 (P/876) (300/T)^{0.5}} \quad (\text{A.18})$$

Here P is the pressure in millibars, T is the temperature in Kelvin, f_{GHz} is the frequency in GHz and ρ_V is the “surface absolute humidity” in g m^{-3} . ρ_V is derived from the measured humidity H (as a decimal fraction) as follows: the saturated water vapor pressure for a given temperature T is

$$P_{H_2O_{sat}} = 6.11 \left(\frac{T}{273}\right)^{-5.3} e^{25.2 \frac{T-273}{T}} \quad (\text{A.19})$$

Then the partial vapor pressure is just $P_{H_2O} = H P_{H_2O_{sat}}$ and $\rho_V = 217 P_{H_2O}/T$, i.e.,

$$\rho_V = 1325 H \left(\frac{T}{273}\right)^{-6.3} e^{25.2 \frac{T-273}{T}} \quad (\text{A.20})$$

Note that τ_0 is the zenith opacity, i.e. looking straight upwards (90° elevation). At any other elevation El the opacity is proportional to the air mass appropriate to that line of sight:

$$\tau = \tau_0 \sec(El) \quad (\text{A.21})$$

In the 1 mm band, the τ_0 measurement reported by the tipper should be used when available. Initially the tipper was controlled by a laptop independent of the rest of the CARMA control system and the tipper data were not available in the monitor data stream. The tipper measurements were however to be found on the plots used at CARMA to assess the viability of 1 mm observations, and they are stored in the directory `/array/rt/TipperData`. The monitor-stream variable is “Opacity-Monitor.tau225”, but at the time of writing (2009 February) this variable is zeroed out. Instead the monitor data stream reports the zenith value τ_{225} derived for 225 GHz from the precipitable water vapor measurement according to the following approximation:

$$\tau_{225} \approx 0.06 \text{ precip}_{mm} + 0.005 \quad (\text{A.22})$$

where precip_{mm} is the precipitable water column in millimeters reported by the weather station. Comparison of this formula with the tipper data suggests that it is correct to within about 20%. This is the value used in (`/refappeq16`) to calculate the system temperature.

A.7.3 Sky Dips

In order to measure the zenith opacity τ_0 in practice, one can carry out a “sky dip”: the power on the sky, P_{sky} , is measured at a number of different elevations, El . By (A.1),

$$P_{sky}(El) = G\{T_{rec} + \eta T_{atm} + (1 - \eta) T_{spill} - \eta (T_{atm} - T_{CMB}) e^{-\tau_0 \sec(El)}\} \quad (\text{A.23})$$

Assuming that we have also measured the power on the ambient load given by (A.2), we may fit the measured Y-factor P_{load}/P_{sky} as a function of air mass $AM =$

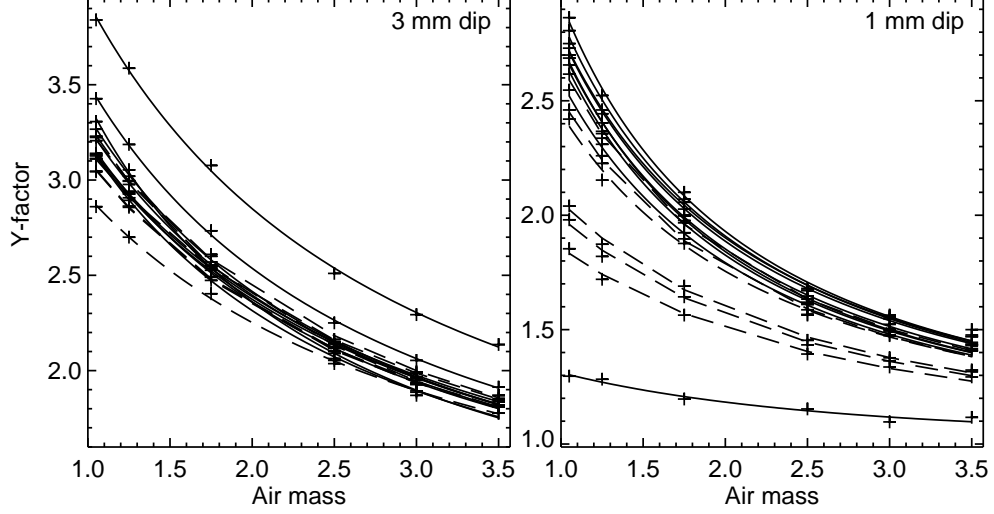


Figure A.4: Plot of the “Y-factor” (ratio of ambient-load power to sky power) versus air mass for measurements at 3 mm (113 GHz, left panel) and 1 mm (222 GHz, right panel) for each of the 15 CARMA antennas. The measured values (averaged over the three observing bands) at each of 6 different air mass values are plotted with cross symbols, and the best-fit shape of (/refappeq25) is shown by a line (dashed for the 10.4m antennas, solid for the 6.1m antennas).

$1/\sin(El)$ and the receiver temperature ratio $R = T_{rec}/T_{atm}$ and determine both τ_0 and T_{rec} :

$$Y(AM) = \frac{P_{load}}{P_{sky}(AM)} = \frac{R + T_{load}/T_{atm}}{R + \eta(1 - e^{-\tau_0 AM}) + (1 - \eta)T_{spill}/T_{atm} + \eta e^{-\tau_0 AM} T_{CMB}/T_{atm}} \quad (\text{A.24})$$

As noted earlier, the relevant efficiency η that appears in this expression is not the main-beam efficiency that is the principal subject of this memo, but rather the spillover or coupling efficiency. η is taken to be close to unity in the dip analysis: at the Arizona 12m telescope $\eta = 1$ is used, while at CARMA we set $\eta = 0.975$.

The standard single-load calibration approach available at CARMA does not generally provide enough data to determine unambiguously all the variables (τ_0 , T_{rec} , η , T_{spill}) in this equation.¹ In practice the assumption that T_{spill} does not

¹James Lamb uses an additional liquid nitrogen load for spillover measurements on the CARMA

depend on elevation is not correct: the dish elevation influences how much of the spillover is warm ground and how much is cold sky, so adopting a constant value for T_{spill} is not strictly appropriate. However, in practice T_{spill} appears only in the denominator multiplied by a small number, and usually does not make a large contribution to the measured power, so the assumption of constant T_{spill} does not significantly bias the results.

In the limit that $\tau_0 AM \ll 1$ and ignoring T_{CMB}/T_{atm} , $(1 - \eta) \ll 1$, we can write

$$Y(AM) = \frac{R + T_{load}/T_{atm}}{R + \tau_0 AM} \quad (\text{A.25})$$

A plot of Y versus AM should therefore show a simple hyperbolic shape. The necessary data are acquired at CARMA using the script **dip1.py**. We fit equation (/refappeq24) for τ_0 and T_{rec} for each antenna separately with the assumptions described above ($\eta = 0.975$, $T_{spill} = T_{outdoor}$) using an IDL routine that carries out a Levenberg-Marquardt least-squares minimization of (/refappeq24) (the routine optionally allows T_{spill} to be included in the fit, or allows τ_0 to be held fixed). An example of such data (acquired on 2008 June 15 at 113.2 GHz and 222.0 GHz) and the corresponding fits is shown in Figure A.4, with the results of the fits given in Table A.4. Each antenna can be well fit by the functional form (/refappeq24) and the resulting values of τ_0 agree surprisingly well between the 15 antennas even though the shapes of the curves, and the corresponding T_{rec} values, vary considerably (C13 is clearly an outlier at 1 mm, with an anomalously poor T_{rec}).

The weather data predict opacities (as described in §A.7.2) of order 0.18 at 3 mm (where the two sidebands were at 111 and 115 GHz, so they saw very different opac-

dishes, but this presently is a two-person operation that is carried out one telescope at a time and requires taking the dish out of the array.

Table A.4: Sky-dip measurements of opacity and receiver temperature on 2008 June 15

Antenna	3 mm τ_0	1 mm τ_0	3 mm T_{rec}	1 mm T_{rec}
C1	0.19	0.37	85	64
C2	0.19	0.37	71	165
C3	0.19	0.37	64	43
C4	0.21	0.38	57	115
C5	0.18	0.38	72	54
C6	0.19	0.38	72	129
C7	0.19	0.37	56	35
C8	0.15	0.35	49	34
C9	0.20	0.36	63	38
C10	0.20	0.35	60	41
C11	0.19	0.38	68	36
C12	0.21	0.36	59	29
C13	0.19	0.52	54	498
C14	0.19	0.37	67	47
C15	0.23	0.37	45	39

ities) and 0.3-0.4 at 225 GHz during the data acquisition, while the 230 GHz tipper reported a zenith opacity in the range 0.32 to 0.35, in quite good agreement with our 1 mm dip value. Figure A.5 shows a comparison of measured sky-dip opacities with the values derived from the weather data as described in the previous section for a number of measurements in 2008/2009. While the 1 mm formula appears to work quite well, there is a clear problem with the 3 mm formula (refappeq18): it predicts very little variation in opacity at frequencies below 110 GHz where the oxygen line has no significant contribution. Opacities at 100 GHz are almost always predicted to be around 0.05 from the weather data, being dominated by the constant 0.04 term in (refappeq18), while the 3mm dip measurements show much more variation in reality. From (refappeq16), the system temperature measurement at low opacities is proportional to $1 + \tau$, so, e.g., use of the value $\tau = 0.05$ in calculating T_{sys} when

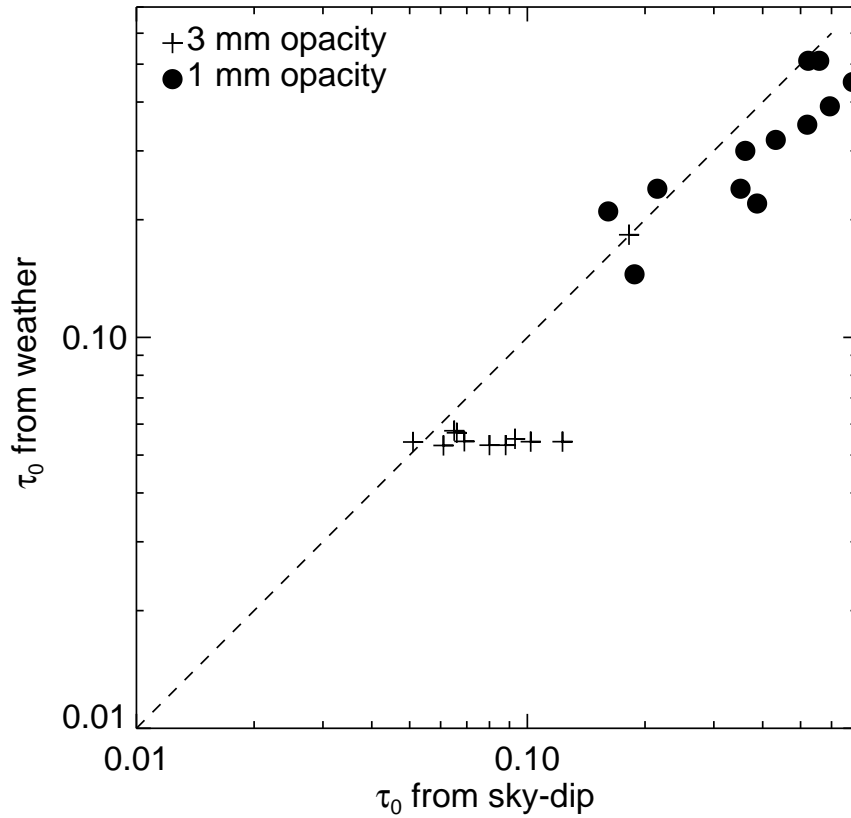


Figure A.5: A comparison of measurements of zenith opacity from sky dips with the corresponding values predicted from the weather data using equations (/refappeq18) and (/refappeq22) at 3 mm (plus symbols) and 1 mm (dot symbols), respectively.

the true value should be $\tau = 0.10$ results in a 5% underestimate of T_{sys} .

To fit dip data at CARMA, follow the instructions in the file *tau_dip_instructions.txt*, alternatively, there is a one-step IDL routine as follows, e.g.,

```
cd /array/rt/Dips
idl
IDL> fit_dip,'2008may31.dip1_tsys.dat',/output
```

Since the data for each fit (each of 3 bands on each of 15 antennas) is independent, consistency between antennas indicates a good result. We generally find this to be the case with CARMA dip data.

A.7.4 Primary Beam Sizes

As discussed by Baars (2003), the actual size of an antenna primary beam depends on the way in which the dish surface illuminates the subreflector and then the feed horn. In practice it is usually easier to think about this in reverse order with the feed horn as a radiator that illuminates the subreflector and in turn the dish surface. The illumination pattern (which in theory is a Bessel function for a uniform circular aperture, not a Gaussian function) can be controlled by the design of the feed horn and subreflector, and is often tapered at the edges of the dish in order to reduce spillover effects at the edge of the primary beam, with the effect that the full dish aperture is not being used and the primary beam size is slightly larger than the canonical value for uniform illumination of the dish (no tapering), $\theta_{FWHM} = \lambda/D$, where λ is the wavelength and D the dish diameter (Baars 2003, finds $1.02 \lambda/D$ in practice for uniform illumination out to the edge of the dish). For a typical Gaussian taper with an 11 dB reduction in sensitivity at the edge of the illumination pattern compared to the center of the dish, $\theta_{FWHM} = 1.22 \lambda/D$ (which also happens to be the angular size of the first null in the Bessel function pattern of a uniformly illuminated dish). Most real dishes lie somewhere between these two limits, e.g., Lugten (1995) reports that $\theta_{FWHM} = 1.14 \lambda/D$ for the antenna power pattern in his analysis of the performance of the $D = 6.1\text{m}$ BIMA antennas. For the CARMA dishes, different illumination patterns give the beam sizes (at 100 GHz) reported in Table 5.

As part of the radio pointing procedure at CARMA, Gaussian fits are made to the widths of the primary beams in order to exclude bad data, so the radio pointing data contain a large number of actual fits of the amplitude (not the power) FWHM. Note that in practice a Gaussian is not always a good representation of the beam

Table A.5: Theoretical CARMA antenna primary beam sizes (FWHM) at 100 GHz

	10.4m dishes	6.1m dishes
λ/D	59.5"	101.4"
1.14 λ/D	67.8"	115.6"
1.22 λ/D	72.6"	123.8"

pattern (Corder and Wright 2006; Wright and Corder 2008). We have gone through recent data and using close to 500 “good” measurements per antenna, we find that the mean primary beam sizes (geometric mean of azimuth and elevation axis widths, converted to the power FWHM assuming that it is the amplitude FWHM divided by $\sqrt{2}$) at 100 GHz are as shown in Table A.6. The results in this table correspond to 1.10 λ/D for the 10.4m dishes and 1.07 λ/D for the 6.1m dishes.

Table A.6: Measured CARMA antenna primary beam sizes (FWHM) at 100 GHz

Antenna	Median (")	Mean (")	St. dev. (")
1	65.5	65.7	± 2.4
2	65.0	65.4	± 2.5
3	63.4	63.7	± 2.4
4	66.7	67.1	± 2.7
5	65.2	65.4	± 1.7
6	66.6	66.8	± 2.2
7	106.6	106.8	± 3.0
8	107.9	108.3	± 3.6
9	109.1	109.5	± 3.2
10	108.9	109.3	± 2.9
11	110.0	110.7	± 3.8
12	108.9	109.0	± 3.2
13	108.5	108.8	± 3.0
14	108.4	108.7	± 3.4
15	108.5	108.7	± 3.6

A.7.5 The ApertureEfficiencySD Script

In this appendix we describe the script for acquiring single-dish aperture efficiency data (as of July 2008). The script is invoked as follows: in sac (the python subarray controller), type, e.g.,

```
import ApertureEfficiencySD as SD
SD.CalculateApertureEff(planet='jupiter', tuning_frequency='3mm', \
    pointing_source='1924-292')
or
SD.CalculateApertureEff(planet='moon', tuning_frequency='3mm', \
    performPointing=False, myoffset=20.)
```

The keywords should be fairly self-explanatory: reference pointing is not necessary on the Moon since it is so large. The offset on the Moon (in arcminutes) is for the sky power measurement: it needs to be large enough to move off the planet (defaults to 5').

The script carries out the following actions:

- Tunes to “3 mm” (IF at 95 GHz) or “1 mm” (IF at 223.0 GHz).
- Carries out reference pointing (if requested; highly desirable for any source except the Moon). Generally a nearby quasar should be used, since pointing on large planets is not reliable.
- Reads the weather data necessary for the load temperatures and to calculate atmospheric opacity (Drive.Weather.ambientTemp at each active 10.4-m antenna, BimaSpecific.CalPlate.tempAmb at each active 6.1-m antenna, Weather.Tau225, PhaseMonitor.skyRMS, Weather.DewPointSensor.humidity,

Weather.pressure, Weather.waterDensity, Weather.precipWater) from the monitor stream.

- The physical parameters of the planet (brightness temperature, size), which are extracted from the planetary ephemeris and loaded into the monitor data when the source name is set, are read (Control.Subarray*n*.planetTemperature, Control.Subarray*n*.planetMajorAxis, Control.Subarray*n*.planetMinorAxis) and recorded.
- If desired (checkPointing=True, not the default) carries out an interferometer measurement on the planet in a cross pattern to check that the pointing is good (generally not needed).
- Offsets in azimuth from the planet, then the ambient load is placed into the beam path and the power on the load is measured. Each time the power is measured, the following is done: the elevation is recorded, T_{sys} is determined for each antenna and band (monitor point SlPipeline.Input*n*.Band*m*.Tsys.Dsb), the P_{sys} power values at the inputs to the correlator (Sldc.Band*m*.Input*n*.psys) are recorded, and for comparison the front-end power levels (*n*.AntennaIfContainer.AntennaIF.ifOutTotalPower), which sample a wider bandwidth but are less stable than the P_{sys} powers and hence are not used for the final analysis, may be recorded. Each of these measurements may be sampled up to 20 times, but tests indicate that a single P_{sys} power measurement is sufficiently repeatable.
- The load is removed from the beam path and the power P_{sky} is measured in the sky position.
- The antennas are moved back to the source, the ambient load is placed in the

beam path and the power is measured.

- The load is removed from the beam path and the power P_{src} is measured on the source.
- This cycle is repeated 3 times.
- A sky dip is carried out at the observing frequency to measure the sky opacity (unless skyDip=False).

The output data files are written to the directory /array/rt/apertureEff/singleDish. There are then two paths for the final calculation of aperture efficiency: a python script, and an IDL routine. The python analysis routine SingleDishEfficiency.py is the result of the conversion by Brian Prager of an Excel spreadsheet of Ashley Zauderer and can be invoked as follows, e.g.

```
cd /array/rt/apertureEff/singleDish
Preprocess_Data.csh 3mmfreq2008mmdd.SD.planet.dat
cd 3mmfreq2008mmdd.planet
../SingleDishEfficiency.py A=43.81 Tau225=.436 \
    In=output.txt TPlanet=179 IntTime=.5 BandWid=1.5 \
    Date=06-01-2008 Tout=282.75 Elevat=30.2 Phase=372 \
    Freq=97.15 Tau=.09 Planet=Jupiter Full=0 \
    Out=Efficiencies.dat Stat=Stats.dat
```

Presently, the planet data and atmospheric data have to be supplied as keywords. A future version will avoid this requirement. To use the IDL version, in the same directory run the routine **sd_to_eff** with the data file name as an argument:

```
cd /array/rt/apertureEff/singleDish
```

```
idl
IDL> sd_to_eff, '3mmfreq2008aug02.SD.jupiter.dat', /output
IDL> exit
```

With the `/output` option the results are written to a file in the Results subdirectory; optionally, the zenith opacity measured by the sky dip can be used in place of the weather value by supplying it as a keyword (`tau=...`).

Appendix B

Antenna Shadowing in E array

B.1 Abstract

We simulated CARMA E-array configuration¹ observations with sources between declinations of -30 and 85 degrees to determine the extent of shadowing in this most compact configuration. The percentage of shadowed visibilities for various hour angle ranges at each source declination is presented. We find that shadowing only becomes significant for a standard four-hour track, centered on transit, for sources below a declination of 0 degrees. The shadowing ramps up for larger hour angles, especially for lower declination sources. The percentage of shadowed visibilities we obtained uses the full antenna diameters, when in practice, one might be able to get better performance from the actual system by including visibility data where the antenna dish was only slightly shadowed at the edge of the dish. We suggest the use of MIRIAD task, `csflag`, to flag shadowed antennas. However, users should be aware that shadowing does not seem to have a detrimental effect on the data, as unflagged shadowed data have not shown a drop in amplitude or scattering in phase

¹E is the most compact CARMA configuration, with baseline lengths varying between 8 and 66 meters.

coherence, as might have been expected. Shadowing is not a serious concern in the less compact configurations: A, B, C and D, although users may still want to run `csflag` to see the extent of shadowing themselves and to compare their maps with and without this data.

B.2 Simulating E Array Data: Model Parameters

CARMA memorandum 20 (Helfer 2004) describes how the E array configuration was designed to optimize desired parameters and minimize shadowing. The shadowing was described to be significant for sources with a declination of -30 degrees, with as many as 69–77% of visibilities shadowed, but not as problematic for sources with a declination of 0 degrees. We have considered a much finer grid of source declinations and hour angles in order to guide the choice of target sources in E array by observers, and the optimal hour angle range for scheduling.

This memorandum should also serve as a guide for observers to be aware of at what declinations they should know that their data includes shadowed data. Users should use `CSFLAG` to flag these data and compare their data with and without the flagged visibilities.

We used the MIRIAD task, `uvgen`, to generate the simulated visibility data. We used the 2007 E array position file, an observatory latitude of 37.3 and declinations ranging from -30 to 85, in steps of 5 degrees. At each declination, we considered 6 hour angle ranges: -1,1; -2,2; -3,3; -4,4; -5,5; and -6,6.

B.3 Shadowing Math

A right handed Cartesian coordinate system (X, Y, Z) is normally used to designate the positions of the antennae in the array (see *e.g.* Thompson et al. 2001, section 4.2). In these coordinates X and Y are parallel to the earth’s equator, X points to the (local) meridian, Y towards the east, and Z measured towards the north pole. In MIRIAD you can find these in the `antpos` UV-variable, measured in nano-seconds. Note that antenna position files in MIRIAD (*e.g.* `$MIRCAT/carma.E.ant`) are often in a local (topocentric) coordinate system and using MIRIAD’s `uvgen` program need to be converted to a geocentric system. See the description of its `baseunit=` and `ant=` keywords.

For given hour angle (H) and declination (δ) of a source being tracked during an observation, the (u, v, w) coordinates are computed as followed (see Thompson et al. 2001, eq. 4.15):

$$u = X \sin H + Y \cos H \tag{B.1}$$

$$v = (X \cos H + Y \sin H) \sin \delta + Z \cos \delta \tag{B.2}$$

$$w = -(X \cos H + Y \sin H) \cos \delta + Z \sin \delta \tag{B.3}$$

For any antenna pair (i, j) we then compute if the difference vector $(u_i, v_i) - (u_j, v_j)$ is within a distance of $(D_i + D_j)/2$ to cause shadowing. The computation has to be done twice, depending on the sign of $w_i - w_j$ (*e.g.* considering which antenna shadows and which is being shadowed).

A standard UV selection in MIRIAD is available to select shadowed visibilities, *e.g.* `select=shadow(10)` would select visibilities that are shadowed within 10 m. For OVRO=10m and BIMA=6m it was found that for mapping programs a BIMA-OVRO baseline corresponds fairly closely to an 8m “dish”. You will thus find

that such baselines are labeled with telescope type CARMA. However, the current MIRIAD visibility data format does not know about individual antenna sizes, which causes inaccuracies in the shadowing computations. Hence the `csflag` program that knows about the peculiar CARMA array with its 10.4-m and 6.1-m dishes.

CAVEAT: The algorithm silently assumes that all antennae are in the array pointing at the same object and are always present.

B.4 Flagged Visibilities

To determine the amount of shadowing, we used the new MIRIAD task `csflag` (see the CARMA MIRIAD Cookbook, Teuben 2007). This task includes the ability to determine shadowing with a heterogenous array, and takes into account both differing antenna diameters and differing antenna heights. The antenna diameters were conservatively entered to be the actual full diameter of each antenna type (10.4 m and 6.1 m). In reality, these values may be able to be pushed a bit smaller, leading to a slight decrease in visibilities flagged because there is some small and insignificant portion of the dish shadowed. The determination of the optimal antenna diameter values to use will require observational tests.

B.5 Results and Example Script

We present the results of our simulation in Figure 1.

The following combination of MIRIAD commands create a simulation of a point source observed in E array, at an RA of 0, declination of -20 , over an hour angle range of $-2,2$. The `baseunit` conversion factor is for the purpose of changing the antenna position file into the correct units for `uvgen`. Then, the output from `csflag` will be the total number of records in the visibility file, and the number of visibilities

where shadowing occurs.

```
% uvgen source=$MIRCAT/point.source ant=$MIRCAT/carma_E.ant baseunit=-3.33564 \  
telescop=carma corr=0 radec=0,-20 harange=-2,2 ellim=20 lat=37.3 out=EarrayPoint.mir  
...  
4200 records written to file: EarrayPoint.mir  
  
% csflag vis=EarrayPoint.mir carma=true \  
antdiam=10.4,10.4,10.4,10.4,10.4,10.4,6.1,6.1,6.1,6.1,6.1,6.1,6.1,6.1,6.1  
...  
Processed 4200 records, flagged 1795 0/H/C: 10 936 849
```

See Table 2 for the specific E antenna configuration file we used for our simulation.

CARMA users can modify this example to create predictions of shadowing tailored to their specific observations, using the correct antenna configuration file, and their source specifics. `csflag` can be run with defaults, shadowing all visibilities where there was any shadowing, or it can be run with a smaller antenna diameter size, to only flag those visibilities where a large fraction of the dish was shadowed by another.

Table B.1. Flagged Visibilities as a Function of Declination

A - Dec	B - HA	C - Elevation	D - Flagged Records	E - Total Records	F - Shadowing
-30	1	21	1381	2100	66
-30	2	17	3100	4200	74
-30	3	11	5077	6405	80
-25	1	26	991	2100	47
-25	2	22	2414	4200	57
-25	3	15	4168	6405	65
-20	1	31	802	2100	38
-20	2	26	1795	4200	43
-20	3	19	3369	6405	53
-20	4	10	5171	8505	61
-15	1	36	409	2100	19
-15	2	31	831	4200	20
-15	3	23	2015	6405	31
-15	4	13	3636	8505	43
-10	1	41	126	2100	6
-10	2	35	385	4200	9
-10	3	27	1304	6405	20
-10	4	17	2866	8505	34
-5	1	45	0	2100	0
-5	2	39	28	4200	1
-5	3	30	765	6405	12
-5	4	20	2093	8505	25
0	1	50	0	2100	0
0	2	44	0	4200	0
0	3	34	426	6405	7
0	4	23	1609	8505	19
5	1	55	0	2100	0
5	2	48	0	4200	0
5	3	38	277	6405	4
5	4	27	1067	8505	13
5	5	15	2592	10605	24

Table B.1 (cont'd)

A - Dec	B - HA	C - Elevation	D - Flagged Records	E - Total Records	F - Shadowing
10	1	60	0	2100	0
10	2	52	0	4200	0
10	3	41	140	6405	2
10	4	30	702	8505	8
10	5	18	2134	10605	20
15	1	64	0	2100	0
15	2	55	0	4200	0
15	3	44	42	6405	1
15	4	33	526	8505	6
15	5	21	1779	10605	17
20	1	68	0	2100	0
20	2	59	0	4200	0
20	3	47	0	6405	0
20	4	36	271	8505	3
20	5	24	1423	10605	13
25	1	72	0	2100	0
25	2	62	0	4200	0
25	3	50	0	6405	0
25	4	38	152	8505	2
25	5	26	930	10605	9
25	6	15	2517	12705	20
30	1	76	0	2100	0
30	2	64	0	4200	0
30	3	52	0	6405	0
30	4	40	98	8505	1
30	5	29	718	10605	7
30	6	18	2143	12705	17

Table B.1 (cont'd)

A - Dec	B - HA	C - Elevation	D - Flagged Records	E - Total Records	F - Shadowing
35	1	78	0	2100	0
35	2	66	0	4200	0
35	3	54	0	6405	0
35	4	42	84	8505	1
35	5	31	640	10605	6
35	6	20	1990	12705	16
40	1	78	0	2100	0
40	2	67	0	4200	0
40	3	55	0	6405	0
40	4	44	70	8505	1
40	5	33	553	10605	5
40	6	23	1794	12705	14
45	1	76	0	2100	0
45	2	66	0	4200	0
45	3	56	0	6405	0
45	4	45	56	8505	1
45	5	35	459	10605	4
45	6	25	1567	12705	12
50	1	73	0	2100	0
50	2	65	0	4200	0
50	3	56	0	6405	0
50	4	46	14	8505	0
50	5	37	329	10605	3
50	6	28	1211	12705	10
55	1	70	0	2100	0
55	2	63	0	4200	0
55	3	55	0	6405	0
55	4	46	0	8505	0
55	5	38	223	10605	2
55	6	30	955	12705	8

Table B.1 (cont'd)

A - Dec	B - HA	C - Elevation	D - Flagged Records	E - Total Records	F - Shadowing
60	1	65	0	2100	0
60	2	60	0	4200	0
60	3	54	0	6405	0
60	4	46	0	8505	0
60	5	39	84	10605	1
60	6	32	666	12705	5
65	1	61	0	2100	0
65	2	57	0	4200	0
65	3	52	0	6405	0
65	4	46	0	8505	0
65	5	40	14	10605	0
65	6	33	390	12705	3
70	1	56	0	2100	0
70	2	54	0	4200	0
70	3	50	0	6405	0
70	4	45	0	8505	0
70	5	40	28	10605	0
70	6	35	168	12705	1
75	1	52	0	2100	0
75	2	50	0	4200	0
75	3	47	0	6405	0
75	4	43	0	8505	0
75	5	40	112	10605	1
75	6	36	252	12705	2
80	1	47	0	2100	0
80	2	46	0	4200	0
80	3	44	0	6405	0
80	4	42	98	8505	1
80	5	39	238	10605	2
80	6	37	502	12705	4

Table B.1 (cont'd)

A - Dec	B - HA	C - Elevation	D - Flagged Records	E - Total Records	F - Shadowing
85	1	42	280	2100	13
85	2	42	560	4200	13
85	3	41	854	6405	13
85	4	40	1134	8505	13
85	5	38	1414	10605	13
85	6	37	1824	12705	14

^aSource Declination. RA=0

^bHour angle range: -p1,p1

^cElevation of source at maximum hour angle in range

^dNumber of flagged visibilities. CSFLAG output

^eTotal number of visibilities in simulated data

^fThe percentage of flagged visibilities based on shadowing, using full antenna diameters

Table B.2. E Array Configuration File

north	east	zenith	station	ant
-16.880	-2.270	0.000	49/70	10m
25.170	24.000	0.000	71	10m
33.420	6.800	0.000	72	10m
36.070	-18.600	0.000	73	10m
15.730	-29.230	0.000	74	10m
-22.370	12.620	0.000	75	10m
10.500	-0.850	0.000	61	6m
13.230	8.580	0.000	62	6m
3.050	-7.750	0.000	63	6m
4.460	7.150	0.000	64	6m
0.000	0.000	0.000	32/47/65	6m
3.620	19.700	0.000	66	6m
-0.370	-20.020	0.000	48/67	6m
-7.310	-11.540	0.000	46/68	6m
-9.060	12.000	0.000	69	6m

^aTopocentric coordinates in meters

^bbaseunit=-3.33564 to convert to equatorial system measured in nanoseconds

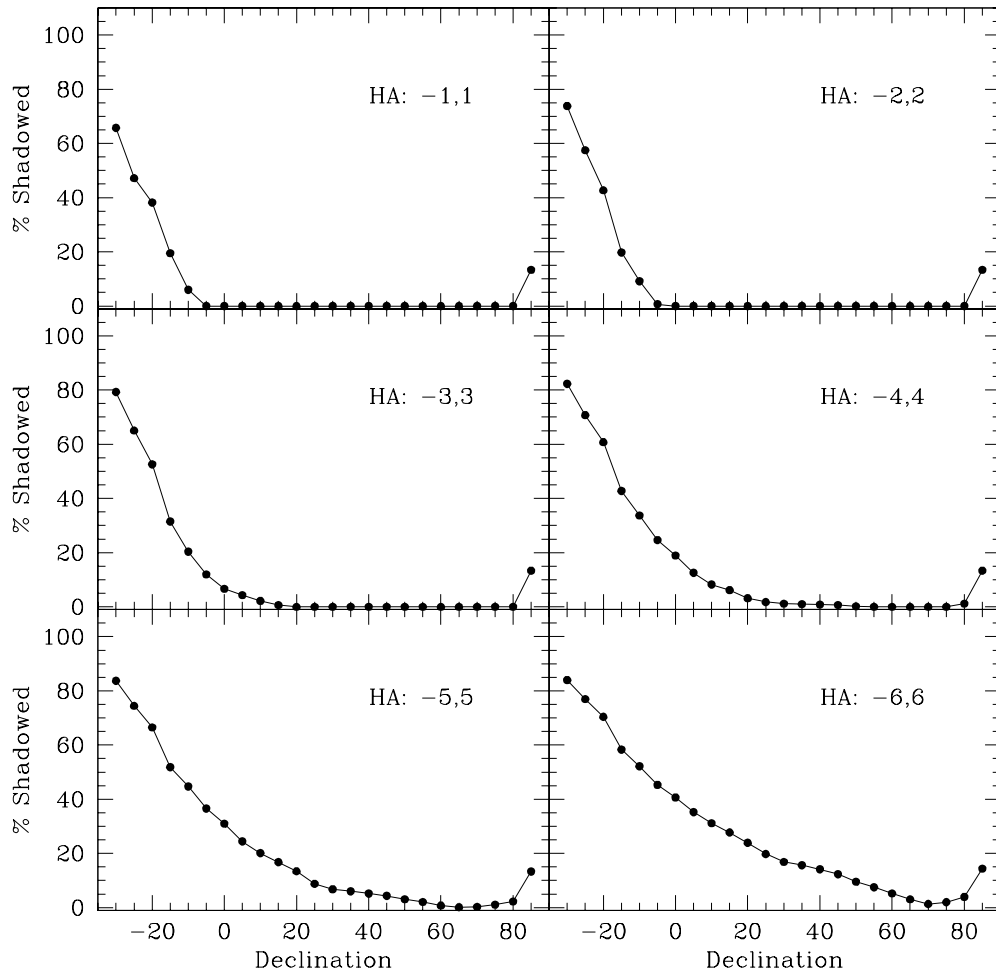


Figure B.1: Percentage of flagged visibilities due to shadowing by hour angle range and declination.

Appendix C

SDSS Follow up to Environmental Study of ULIRGs

C.1 Summary of Work

To followup on the suggestion of an anonymous referee of Zauderer et al. (2007), we have cross-matched the Kim and Sanders (1998) IRAS 1-Jy sample of 118 ULIRGs with Sloan Digital Sky Survey (SDSS) data and found 29 matching objects with photometric and spectroscopic data (see Figure C.2). Following the methodology of Yoon et al. (2008), we located all objects in the field with spectroscopic information and identified galaxies within a small redshift range of our ULIRG of interest. Unfortunately, Yoon's method had been finely tuned to match the depth of the SDSS survey, much more shallow than our R-band images. Reliable density calculation results could be obtained for objects with $z \leq 0.1$, but all of the galaxies in our sample are at $0.1 < z \leq 0.2$. We did an initial calculation of the density, using only SDSS spectroscopic information and found very low densities for all ULIRGs in our sample. While this spectro-photometric method needs fine-tuning to properly

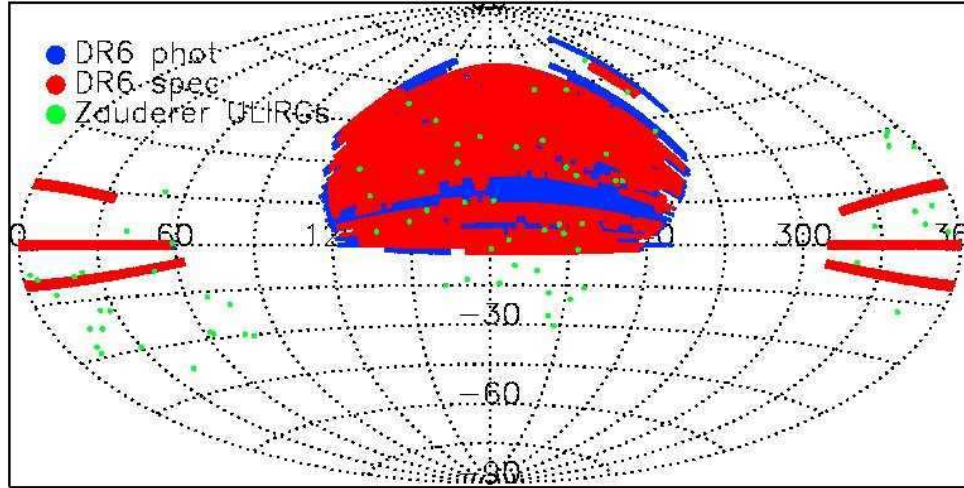


Figure C.1: Sky coverage by the Sloan Digital Sky Survey (SDSS) data release six (DR6) in photometry and spectroscopy (blue and red, respectively). The objects from the 1-Jy sample by Zauderer et al. (2007) are shown with green dots. For this followup work, we consider the 29 ULIRGs which overlap with both SDSS datasets. Figure courtesy of J. H. Yoon.

extrapolate the redshift range to values typical of the ULIRGs in our sample, our findings are consistent with the conclusions of Zauderer et al. (2007)¹.

¹Recent papers confirming our results using the SDSS include Ellison et al. (2010) and Hwang et al. (2010).

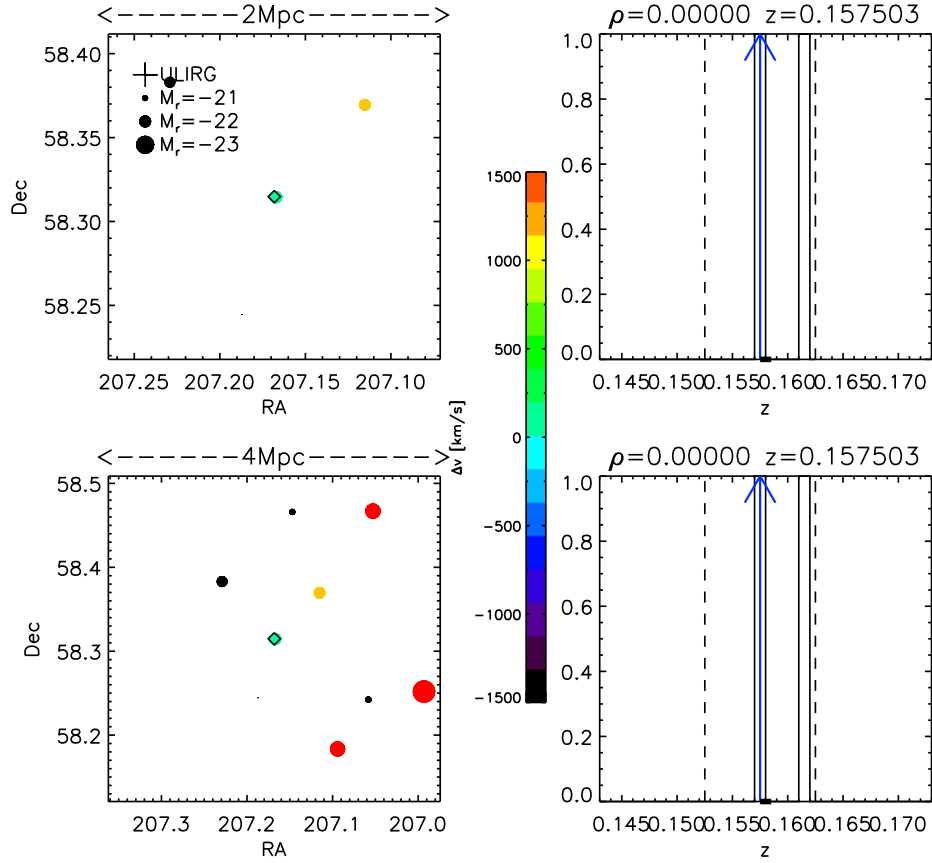


Figure C.2: Spectro-photometric results for IRAS 13469+5833. Zauderer et al. (2007) found this ULIRG to be in a very sparse field ($B_{gc} = -134 \pm 128$), and these figures showing the ULIRG to reside in an environment with no other galaxies ($\rho=0.00$) are consistent. The galaxies are colored by their redshift, and only those blue/green in color would be within the specified distance of 2 Mpc (top plots) or 4 Mpc (bottom plots). This result is typical of the 29 ULIRGs in the cross-matched sample. Figure courtesy of J. H. Yoon.

Glossary

AGN	Active Galactic Nucleus, 2
C-PACS	CARMA's Paired Antenna Calibration System, 19
CARMA	Combined Array for Research in Millimeter Astronomy, 13
HI	21 cm Neutral Hydrogen Line, 12
HST	Hubble Space Telescope, 2
HyLIRG	Hyperluminous Infrared Galaxy, 2
IC	Index Catalog, 6
IR	Infrared, 2
IRAS	Infrared Astronomical Satellite, 17
ISM	Interstellar Medium, 19
LIRG	Luminous Infrared Galaxy, 2

NAIC	National Astronomy and Ionosphere Center, 13
NED	NASA/IPAC Extragalactic Database, 2
NGC	New General Catalog, 6
NSF	National Science Foundation, 13
PACS	Paired Antenna Calibration System, 19
U/LIRG	Luminous and/or Ultraluminous Infrared Galaxy, 2
ULIRG	Ultraluminous Infrared Galaxy, 2
VLBI	Very Long Baseline Interferometry, 13

Bibliography

- Abell, G. O. (1958). The Distribution of Rich Clusters of Galaxies. *ApJS*, 3:211–+.
- Ahmad, A. and Cohen, L. (1974). Dynamical Friction in Gravitational Systems. *ApJ*, 188:469–472.
- Ahmed, F. (1979). Dynamical friction in colliding galaxies. *Ap&SS*, 60:493–503.
- Andersen, V. and Owen, F. N. (1994). A comparison of the richness of clusters and groups of galaxies. *AJ*, 108:361–367.
- Asaki, Y., Saito, M., Kawabe, R., Morita, K., and Sasao, T. (1996). Phase compensation experiments with the paired antennas method. *Radio Science*, 31:1615–1626.
- Asaki, Y., Shibata, K. M., Kawabe, R., Roh, D., Saito, M., Morita, K., and Sasao, T. (1998). Phase compensation experiments with the paired antennas method 2. Millimeter-wave fringe correction using centimeter-wave reference. *Radio Science*, 33:1297–1318.
- Baan, W. A. (1989). Infrared properties of OH galaxies. *ApJ*, 338:804–811.
- Baan, W. A., van Gorkom, J. H., Schmelz, J. T., and Mirabel, I. F. (1987). The peculiar galaxy IC 4553. II - VLA observations of the neutral hydrogen. *ApJ*, 313:102–111.
- Baars, J. W. M. (2003). *ALMA Memo 456: Characteristics of a reflector antenna*. NRAO/ESO.

- Barnes, J. E. (2004). Shock-induced star formation in a model of the Mice. *MNRAS*, 350:798–808.
- Barnes, J. E. and Hernquist, L. (1992). Dynamics of interacting galaxies. *ARA&A*, 30:705–742.
- Barnes, J. E. and Hernquist, L. E. (1991). Fueling starburst galaxies with gas-rich mergers. *ApJ*, 370:L65–L68.
- Barr, J. M., Bremer, M. N., Baker, J. C., and Lehnert, M. D. (2003). The cluster environments of radio-loud quasars at $0.6 < z < 1.1$. *MNRAS*, 346:229–250.
- Battat, J. B., Blundell, R., Moran, J. M., and Paine, S. (2004). Atmospheric Phase Correction Using Total Power Radiometry at the Submillimeter Array. *ApJ*, 616:L71–L74.
- Beasley, A. J. and Conway, J. E. (1995). VLBI Phase-Referencing. In J. A. Zensus, P. J. Diamond, & P. J. Napier, editor, *Very Long Baseline Interferometry and the VLBA*, volume 82 of *Astronomical Society of the Pacific Conference Series*, pages 328–+.
- Blain, A. W., Chapman, S. C., Smail, I., and Ivison, R. (2004). Clustering of Submillimeter-selected Galaxies. *ApJ*, 611:725–731.
- Bremer, M. (2002). Atmospheric Phase Correction for Connected-Element Interferometry and for VLBI. In J. Vernin, Z. Benkhaldoun, & C. Muñoz-Tuñón, editor, *Astronomical Site Evaluation in the Visible and Radio Range*, volume 266 of *Astronomical Society of the Pacific Conference Series*, pages 238–+.
- Bremer, M., Guilloteau, S., and Lucas, R. (1996). Atmospheric Phase Correction Based on Sky Emission in the 210-248 GHz Band. In P. A. Shaver, editor, *Science with Large Millimetre Arrays*, pages 371–+.
- Carilli, C. L., Carlstrom, J. E., and Holdaway, M. A. (1999). Millimeter Interferometry. In G. B. Taylor, C. L. Carilli, & R. A. Perley, editor, *Synthesis Imaging in*

- Radio Astronomy II*, volume 180 of *Astronomical Society of the Pacific Conference Series*, pages 565–+.
- Carilli, C. L. and Holdaway, M. A. (1999). Tropospheric phase calibration in millimeter interferometry. *Radio Science*, 34:817–840.
- Chandrasekhar, S. (1943). Dynamical Friction. I. General Considerations: the Coefficient of Dynamical Friction. *ApJ*, 97:255–+.
- Chapman, S. C., Blain, A. W., Smail, I., and Ivison, R. J. (2005). A Redshift Survey of the Submillimeter Galaxy Population. *ApJ*, 622:772–796.
- Clemens, M. S. and Alexander, P. (2004). A high-resolution study of the interstellar medium in the luminous IRAS galaxy Arp 193. *MNRAS*, 350:66–76.
- Condon, J. J. (1992). Radio emission from normal galaxies. *ARA&A*, 30:575–611.
- Condon, J. J., Cotton, W. D., Greisen, E. W., Yin, Q. F., Perley, R. A., Taylor, G. B., and Broderick, J. J. (1998). The NRAO VLA Sky Survey. *AJ*, 115:1693–1716.
- Corder, S. and Wright, M. C. H. (2006). Carma holography. *CARMA Memo 36*.
- Cornwell, T. J. and Wilkinson, P. N. (1981). A new method for making maps with unstable radio interferometers. *MNRAS*, 196:1067–1086.
- Cornwell, T. J. and Wilkinson, P. N. (1984). Selfcalibration. In J. A. Roberts, editor, *Indirect Imaging. Measurement and Processing for Indirect Imaging*, pages 207–+.
- Coulman, C. E. and Vernin, J. (1991). Significance of anisotropy and the outer scale of turbulence for optical and radio seeing. *Appl. Opt.*, 30:118–126.
- Croom, S. M., Boyle, B. J., Shanks, T., Smith, R. J., Miller, L., Outram, P. J., Loaring, N. S., Hoyle, F., and da Ângela, J. (2005). The 2dF QSO Redshift Survey - XIV. Structure and evolution from the two-point correlation function. *MNRAS*, 356:415–438.
- Darling, J. and Giovanelli, R. (2000). A Search for OH Megamasers at $Z \gt 0.1$. I.

- Preliminary Results. *AJ*, 119:3003–3014.
- Darling, J. and Giovanelli, R. (2001). A Search for OH Megamasers at $Z \geq 0.1$. II. Further Results. *AJ*, 121:1278–1293.
- Darling, J. and Giovanelli, R. (2002). A Search for OH Megamasers at $z \geq 0.1$. III. The Complete Survey. *AJ*, 124:100–126.
- Dasyra, K. M., Tacconi, L. J., Davies, R. I., Genzel, R., Lutz, D., Naab, T., Burkert, A., Veilleux, S., and Sanders, D. B. (2006a). Dynamical Properties of Ultraluminous Infrared Galaxies. I. Mass Ratio Conditions for ULIRG Activity in Interacting Pairs. *ApJ*, 638:745–758.
- Dasyra, K. M., Tacconi, L. J., Davies, R. I., Genzel, R., Lutz, D., Peterson, B. M., Veilleux, S., Baker, A. J., Schweitzer, M., and Sturm, E. (2007). Host Dynamics and Origin of Palomar-Green QSOs. *ApJ*, 657:102–115.
- Dasyra, K. M., Tacconi, L. J., Davies, R. I., Naab, T., Genzel, R., Lutz, D., Sturm, E., Baker, A. J., Veilleux, S., Sanders, D. B., and Burkert, A. (2006b). Dynamical Properties of Ultraluminous Infrared Galaxies. II. Traces of Dynamical Evolution and End Products of Local Ultraluminous Mergers. *ApJ*, 651:835–852.
- Davis, M. and Peebles, P. J. E. (1983). A survey of galaxy redshifts. V - The two-point position and velocity correlations. *ApJ*, 267:465–482.
- De Robertis, M. M., Hayhoe, K., and Yee, H. K. C. (1998a). A CCD Study of the Environment of Seyfert Galaxies. I. The Survey. *ApJS*, 115:163–+.
- De Robertis, M. M., Yee, H. K. C., and Hayhoe, K. (1998b). A CCD Study of the Environment of Seyfert Galaxies. II. Testing the Interaction Hypothesis. *ApJ*, 496:93–+.
- Dinh-V-Trung, Lo, K. Y., Kim, D., Gao, Y., and Gruendl, R. A. (2001). Nature of Widely Separated Ultraluminous Infrared Galaxies. *ApJ*, 556:141–149.
- Downes, D. and Solomon, P. M. (1998). Rotating Nuclear Rings and Extreme

- Starbursts in Ultraluminous Galaxies. *ApJ*, 507:615–654.
- Dreyer, J. L. E. (1888). A New General Catalogue of Nebulae and Clusters of Stars, being the Catalogue of the late Sir John F.W. Herschel, Bart., revised, corrected, and enlarged. *MmRAS*, 49:1–237.
- Dreyer, J. L. E. (1908). Index Catalogue of Nebulae and Clusters of Stars, containing objects found in the years 1895 to 1907; with Notes and Corrections to the New General Catalogue and to the Index Catalogue for 1888-94. *MmRAS*, 59:105–198.
- Dunlop, J. S., McLure, R. J., Kucula, M. J., Baum, S. A., O’Dea, C. P., and Hughes, D. H. (2003). Quasars, their host galaxies and their central black holes. *MNRAS*, 340:1095–1135.
- Dyson, J. E. and Williams, D. A. (1997). *The physics of the interstellar medium*.
- Ellingson, E., Yee, H. K. C., and Green, R. F. (1991). Quasars and active galactic nuclei in rich environments. II - The evolution of radio-loud quasars. *ApJ*, 371:49–59.
- Ellison, S. L., Patton, D. R., Simard, L., McConnachie, A. W., Baldry, I. K., and Mendel, J. T. (2010). Galaxy pairs in the Sloan Digital Sky Survey - II. The effect of environment on interactions. *MNRAS*, 407:1514–1528.
- Ewen, H. I. and Purcell, E. M. (1951). Observation of a Line in the Galactic Radio Spectrum: Radiation from Galactic Hydrogen at 1,420 Mc./sec. *Nature*, 168:356–+.
- Falco, E. E., Kurtz, M. J., Geller, M. J., Huchra, J. P., Peters, J., Berlind, P., Mink, D. J., Tokarz, S. P., and Elwell, B. (1999). The Updated Zwicky Catalog (UZC). *PASP*, 111:438–452.
- Farrah, D., Geach, J., Fox, M., Serjeant, S., Oliver, S., Verma, A., Kaviani, A., and Rowan-Robinson, M. (2004). The environments of hyperluminous infrared galaxies at $0.44 < z < 1.55$. *MNRAS*, 349:518–526.

- Farrah, D., Lonsdale, C. J., Borys, C., Fang, F., Waddington, I., Oliver, S., Rowan-Robinson, M., Babbedge, T., Shupe, D., Polletta, M., Smith, H. E., and Surace, J. (2006). The Spatial Clustering of Ultraluminous Infrared Galaxies over 1.5 lt z lt 3. *ApJ*, 641:L17–L20.
- Fernandez, M. X., Momjian, E., Salter, C. J., and Ghosh, T. (2010). A Radio Spectral Line Study of the 2 Jy IRAS-NVSS Sample. I. *AJ*, 139:2066–2082.
- Folkers, T. W. (2004). *Users Manual for the ARO 12m Millimeter-Wave Telescope*. Arizona Radio Observatory, Tucson.
- Freedman, W. L. and Madore, B. F. (2010). The Hubble Constant. *ARA&A*, 48:673–710.
- Genzel, R., Lutz, D., Sturm, E., Egami, E., Kunze, D., Moorwood, A. F. M., Rigopoulou, D., Spoon, H. W. W., Sternberg, A., Tacconi-Garman, L. E., Tacconi, L., and Thatte, N. (1998). What Powers Ultraluminous IRAS Galaxies? *ApJ*, 498:579–+.
- Genzel, R., Tacconi, L. J., Rigopoulou, D., Lutz, D., and Tecza, M. (2001). Ultraluminous Infrared Mergers: Elliptical Galaxies in Formation? *ApJ*, 563:527–545.
- Georgantopoulos, I., Rovilos, E., Akylas, A., and Xilouris, E. (2010). Molecular lines as tracers of Compton-thick AGN? *A&A*, 520:L4+.
- Ghosh, T. and Salter, C. (2002). Arecibo Spectral Baselines in the Presence of Continuum Emission. In S. Stanimirovic, D. Altschuler, P. Goldsmith, & C. Salter, editor, *Single-Dish Radio Astronomy: Techniques and Applications*, volume 278 of *Astronomical Society of the Pacific Conference Series*, pages 521–524.
- Gladders, M. D. and Yee, H. K. C. (2005). The Red-Sequence Cluster Survey. I. The Survey and Cluster Catalogs for Patches RCS 0926+37 and RCS 1327+29. *ApJS*, 157:1–29.
- Groth, E. J. and Peebles, P. J. E. (1977). Statistical analysis of catalogs of extra-

- galactic objects. VII - Two- and three-point correlation functions for the high-resolution Shane-Wirtanen catalog of galaxies. *ApJ*, 217:385–405.
- Grubišić, V., Doyle, J. D., Kuettner, J., Dirks, R., Cohn, S. A., Pan, L. L., Mobbs, S., Smith, R. B., Whiteman, C. D., Czyzyk, S., Vosper, S., Weissmann, M., Haimov, S., De Wekker, S. F. J., and Chow, F. K. (2008). The Terrain-Induced Rotor Experiment A Field Campaign Overview Including Observational Highlights. *Bull. Amer. Metero. Soc.*, 89:1513–1533.
- Heckman, T. M. (1980). An optical and radio survey of the nuclei of bright galaxies - Activity in normal galactic nuclei. *A&A*, 87:152–164.
- Helfer, T. T. (2004). Memo 20: CARMA Configurations for Cedar Flat. *CARMA Technical Memoranda Series*.
- Helou, G., Soifer, B. T., and Rowan-Robinson, M. (1985). Thermal infrared and nonthermal radio - Remarkable correlation in disks of galaxies. *ApJ*, 298:L7–L11.
- Herschel, F. W. (1858). pages 649, plate VI. London: Longman, Brown, Green, Longmans, and Roberts.
- Hill, G. J. and Lilly, S. J. (1991). A change in the cluster environments of radio galaxies with cosmic epoch. *ApJ*, 367:1–18.
- Holdaway, M. A. (1992). Estimation of atmospheric phase stability from sky brightness temperature fluctuations at millimeter wavelengths. In A. Kohnle & W. B. Miller, editor, *Society of Photo-Optical Instrumentation Engineers (SPIE) Conference Series*, volume 1688 of *Society of Photo-Optical Instrumentation Engineers (SPIE) Conference Series*, pages 625–636.
- Honma, M., Fujii, T., Hirota, T., Horiai, K., Iwadate, K., Jike, T., Kameya, O., Kamohara, R., Kan-Ya, Y., Kawaguchi, N., Kobayashi, H., Kuji, S., Kurayama, T., Manabe, S., Miyaji, T., Nakashima, K., Omodaka, T., Oyama, T., Sakai, S., Sakakibara, S., Sato, K., Sasao, T., Shibata, K. M., Shimizu, R., Suda, H.,

- Tamura, Y., Ujihara, H., and Yoshimura, A. (2003). First Fringe Detection with VERA’s Dual-Beam System and Its Phase-Referencing Capability. *PASJ*, 55:L57–L60.
- Hopkins, P. F. and Quataert, E. (2010). How do massive black holes get their gas? *MNRAS*, 407:1529–1564.
- Hubble, E. (1936). Effects of Red Shifts on the Distribution of Nebulae. *ApJ*, 84:517–+.
- Hubble, E. P. (1922). A general study of diffuse galactic nebulae. *ApJ*, 56:162–199.
- Hubble, E. P. (1926). Extragalactic nebulae. *ApJ*, 64:321–369.
- Hubble, E. P. (1927). The classification of spiral nebulae. *The Observatory*, 50:276–281.
- Hughes, D. H., Serjeant, S., Dunlop, J., Rowan-Robinson, M., Blain, A., Mann, R. G., Ivison, R., Peacock, J., Efstathiou, A., Gear, W., Oliver, S., Lawrence, A., Longair, M., Goldschmidt, P., and Jenness, T. (1998). High-redshift star formation in the Hubble Deep Field revealed by a submillimetre-wavelength survey. *Nature*, 394:241–247.
- Hwang, H. S., Elbaz, D., Lee, J. C., Jeong, W., Park, C., Lee, M. G., and Lee, H. M. (2010). Environmental Dependence of Local Luminous Infrared Galaxies. *ArXiv e-prints*.
- Jansky, K. G. (1933). Radio Waves from Outside the Solar System. *Nature*, 132:66–+.
- Kandalian, R. A. (1996). Megamaser galaxies. *Astrophysics*, 39:237–244.
- Kauffmann, G., White, S. D. M., Heckman, T. M., Ménard, B., Brinchmann, J., Charlot, S., Tremonti, C., and Brinkmann, J. (2004). The environmental dependence of the relations between stellar mass, structure, star formation and nuclear activity in galaxies. *MNRAS*, 353:713–731.

- Kavanagh, T. C. and Tung, D. H. H. (1965). Arecibo Radar-Radio Telescope—Design and Construction. *Journal of the Construction Division: ASCE*, 91:69–98.
- Kawaguchi, N., Sasao, T., and Manabe, S. (2000). Dual-beam VLBI techniques for precision astrometry of the VERA project. In H. R. Butcher, editor, *Society of Photo-Optical Instrumentation Engineers (SPIE) Conference Series*, volume 4015 of *Society of Photo-Optical Instrumentation Engineers (SPIE) Conference Series*, pages 544–551.
- Keel, W. C. (1996). Rotation Curves and Velocity Measures for Spiral Galaxies in Pairs. *ApJS*, 106:27–+.
- Kim, D. and Sanders, D. B. (1998). The IRAS 1 Jy Survey of Ultraluminous Infrared Galaxies. I. The Sample and Luminosity Function. *ApJS*, 119:41–58.
- Kim, D., Veilleux, S., and Sanders, D. B. (1998). The IRAS 1 Jy Sample of Ultraluminous Infrared Galaxies. II. Optical Spectroscopy. *ApJ*, 508:627–647.
- Kim, D., Veilleux, S., and Sanders, D. B. (2002). Optical and Near-Infrared Imaging of the IRAS 1 Jy Sample of Ultraluminous Infrared Galaxies. I. The Atlas. *ApJS*, 143:277–314.
- Kramer, C. (2005). *Spatial response framework document of the HIFI/Herschel Calibration Group*. KOSMA/Uni. Köln.
- Kron, R. G. (1980). Photometry of a complete sample of faint galaxies. *ApJS*, 43:305–325.
- Kutner, M. L. and Ulich, B. L. (1981). Recommendations for calibration of millimeter-wavelength spectral line data. *Astrophys. J.*, 250:341–348.
- Lay, O. P. (1997a). Phase calibration and water vapor radiometry for millimeter-wave arrays. *A&AS*, 122:547–557.
- Lay, O. P. (1997b). The temporal power spectrum of atmospheric fluctuations due to water vapor. *A&AS*, 122:535–545.

- Leavitt, H. S. and Pickering, E. C. (1912). Periods of 25 Variable Stars in the Small Magellanic Cloud. *Harvard College Observatory Circular*, 173:1–3.
- Lecar, M. (1975). Dynamical Friction in the Coma Cluster. In A. Hayli, editor, *Dynamics of the Solar Systems*, volume 69 of *IAU Symposium*, pages 161–+.
- Linsky, J. L. (1973). The Moon as a Proposed Radiometric Standard for Microwave and Infrared Observations of Extended Sources. *Astrophys. J. Supp.*, 25:163.
- Longair, M. S. and Seldner, M. (1979). The clustering of galaxies about extragalactic radio sources. *MNRAS*, 189:433–453.
- Lonsdale, C. J., Farrah, D., and Smith, H. E. (2006). *Ultraluminous Infrared Galaxies*, pages 285–+. Springer Verlag.
- Lu, N. Y., Dow, M. W., Houck, J. R., Salpeter, E. E., and Lewis, B. M. (1990). Identifying galaxies in the zone of avoidance. *ApJ*, 357:388–407.
- Lu, N. Y. and Freudling, W. (1995). Large-Scale Structures in the Zone of Avoidance: The Galactic Anticenter Region. *ApJ*, 449:527–+.
- Lugten, J. B. (1995). *BIMA Memo 39: Optical Design and Performance of the BIMA Interferometer*.
- Lutz, D., Spoon, H. W. W., Rigopoulou, D., Moorwood, A. F. M., and Genzel, R. (1998). The Nature and Evolution of Ultraluminous Infrared Galaxies: A Mid-Infrared Spectroscopic Survey. *ApJ*, 505:L103–L107.
- Lutz, D., Veilleux, S., and Genzel, R. (1999). Mid-Infrared and Optical Spectroscopy of Ultraluminous Infrared Galaxies: A Comparison. *ApJ*, 517:L13–L17.
- Mahdavi, A. and Geller, M. J. (2004). A Redshift Survey of Nearby Galaxy Groups: The Shape of the Mass Density Profile. *ApJ*, 607:202–219.
- Mangum, J. (2002). *ALMA Memo 434: Load calibration at millimeter and submillimeter wavelengths*. NRAO/ESO.
- Mangum, J. G. (1993). Main-beam efficiency measurements of the Caltech Submil-

- limeter Observatory. *Publ. Astron. Soc. Pacific*, 105:117–122.
- Martin, C. L. (2005). Mapping Large-Scale Gaseous Outflows in Ultraluminous Galaxies with Keck II ESI Spectra: Variations in Outflow Velocity with Galactic Mass. *ApJ*, 621:227–245.
- Martin, J. M., Bottinelli, L., Gouguenheim, L., and Dennefeld, M. (1991). An 18-cm OH and 21-cm H I survey of luminous far-infrared galaxies. II - H I properties. *A&A*, 245:393–417.
- Masson, C. R. (1994). Atmospheric Effects and Calibrations. In M. Ishiguro & J. Welch, editor, *IAU Colloq. 140: Astronomy with Millimeter and Submillimeter Wave Interferometry*, volume 59 of *Astronomical Society of the Pacific Conference Series*, pages 87–+.
- McLure, R. J. and Dunlop, J. S. (2001). The cluster environments of powerful radio-loud and radio-quiet active galactic nuclei. *MNRAS*, 321:515–524.
- Mihos, J. C. and Hernquist, L. (1994). Ultraluminous starbursts in major mergers. *ApJ*, 431:L9–L12.
- Mihos, J. C. and Hernquist, L. (1996). Gasdynamics and Starbursts in Major Mergers. *ApJ*, 464:641–+.
- Miller, C. J., Nichol, R. C., Gómez, P. L., Hopkins, A. M., and Bernardi, M. (2003). The Environment of Active Galactic Nuclei in the Sloan Digital Sky Survey. *ApJ*, 597:142–156.
- Mirabel, I. F. (1982). Neutral hydrogen in bright galaxies with strong radio sources. *ApJ*, 260:75–80.
- Mirabel, I. F. and Sanders, D. B. (1988). 21 centimeter survey of luminous infrared galaxies. *ApJ*, 335:104–121.
- Momjian, E., Romney, J. D., Carilli, C. L., and Troland, T. H. (2003). Sensitive VLBI Continuum and H I Absorption Observations of NGC 7674: First Scientific

- Observations with the Combined Array VLBA, VLA, and Arecibo. *ApJ*, 597:809–822.
- Moreno, R. and Guilloteau, S. (2002). *ALMA Memo 372: An amplitude calibration strategy for ALMA*. NRAO/ESO.
- Morita, K., Handa, K., Asaki, Y., Kitamura, Y., Yokogawa, S., Saito, M., Wilner, D. W., and Ho, P. T. P. (2000). Fast Switching Experiments with the Nobeyama Millimeter Array. In J. G. Mangum & S. J. E. Radford, editor, *Imaging at Radio through Submillimeter Wavelengths*, volume 217 of *Astronomical Society of the Pacific Conference Series*, pages 340–+.
- Muchovej, S., Mroczkowski, T., Carlstrom, J. E., Cartwright, J., Greer, C., Hennesy, R., Loh, M., Pryke, C., Reddall, B., Runyan, M., Sharp, M., Hawkins, D., Lamb, J. W., Woody, D., Joy, M., Leitch, E. M., and Miller, A. D. (2007). Observations of High-Redshift X-Ray Selected Clusters with the Sunyaev-Zel’dovich Array. *ApJ*, 663:708–716.
- Muller, C. A. and Oort, J. H. (1951). Observation of a Line in the Galactic Radio Spectrum: The Interstellar Hydrogen Line at 1,420 Mc./sec., and an Estimate of Galactic Rotation. *Nature*, 168:357–358.
- Murphy, Jr., T. W., Soifer, B. T., Matthews, K., Armus, L., and Kiger, J. R. (2001). K-Band Spectroscopy of Ultraluminous Infrared Galaxies: The 2 JY Sample. *AJ*, 121:97–127.
- Nature Editor (1875). Another Monster Refractor. *Nature*, page 517.
- Nature Editor (1876). The New Observatory at Vienna. *Nature*, pages 192–193.
- Neugebauer, G., Becklin, E., and Hyland, A. R. (1971). Infrared Sources of Radiation. *ARA&A*, 9:67–+.
- Paturel, G., Petit, C., Prugniel, P., Theureau, G., Rousseau, J., Brouty, M., Dubois, P., and Cambr esy, L. (2003). HYPERLEDA. I. Identification and designation of

- galaxies. *A&A*, 412:45–55.
- Pérez, L. M., Lamb, J. W., Woody, D. P., Carpenter, J. M., Zauderer, B. A., Isella, A., Bock, D. C., Bolatto, A. D., Carlstrom, J., Culverhouse, T. L., Joy, M., Kwon, W., Leitch, E. M., Marrone, D. P., Muchovej, S. J., Plambeck, R. L., Scott, S. L., Teuben, P. J., and Wright, M. C. H. (2010). Atmospheric Phase Correction using CARMA-PACS: High Angular Resolution Observations of the FU-Orionis star PP 13S*. *ArXiv e-prints*.
- Plambeck, R. L. (2000). Receiver amplitude calibration for ALMA. *ALMA Memo Series*, 321.
- Rieke, G. H. and Lebofsky, M. J. (1979). Infrared emission of extragalactic sources. *ARA&A*, 17:477–511.
- Rigopoulou, D., Spoon, H. W. W., Genzel, R., Lutz, D., Moorwood, A. F. M., and Tran, Q. D. (1999). A Large Mid-Infrared Spectroscopic and Near-Infrared Imaging Survey of Ultraluminous Infrared Galaxies: Their Nature and Evolution. *AJ*, 118:2625–2645.
- Roberts, M. S. (1975). *Radio Observations of Neutral Hydrogen in Galaxies*, pages 309–+. the University of Chicago Press.
- Rohlfs, K. (1986). *Tools of radio astronomy*. Springer-Verlag.
- Rupke, D. S., Veilleux, S., and Sanders, D. B. (2002). Keck Absorption-Line Spectroscopy of Galactic Winds in Ultraluminous Infrared Galaxies. *ApJ*, 570:588–609.
- Rupke, D. S., Veilleux, S., and Sanders, D. B. (2005a). Outflows in Active Galactic Nucleus/Starburst-Composite Ultraluminous Infrared Galaxies1,. *ApJ*, 632:751–780.
- Rupke, D. S., Veilleux, S., and Sanders, D. B. (2005b). Outflows in Infrared-Luminous Starbursts at $z \leq 0.5$. II. Analysis and Discussion. *ApJS*, 160:115–148.
- Sanders, D. B. and Mirabel, I. F. (1996). Luminous Infrared Galaxies. *ARA&A*,

34:749–+.

- Sanders, D. B., Soifer, B. T., Elias, J. H., Madore, B. F., Matthews, K., Neugebauer, G., and Scoville, N. Z. (1988). Ultraluminous infrared galaxies and the origin of quasars. *ApJ*, 325:74–91.
- Sandor, B. J. and Clancy, R. T. (1995). Microwave observations and modeling of a lunar eclipse. *Icarus*, 115:387–398.
- Sault, R. J., Carrad, G. J., Hall, P. J., and Crofts, J. (2007). Radio path length correction using water vapour radiometry. *ArXiv Astrophysics e-prints*.
- Schmidt, M. and Green, R. F. (1983). Quasar evolution derived from the Palomar bright quasar survey and other complete quasar surveys. *ApJ*, 269:352–374.
- Schwab, F. R. (1980). Adaptive calibration of radio interferometer data. In W. T. Rhodes, editor, *Society of Photo-Optical Instrumentation Engineers (SPIE) Conference Series*, volume 231 of *Society of Photo-Optical Instrumentation Engineers (SPIE) Conference Series*, pages 18–25.
- Scott, E. L., Shane, C. D., and Swanson, M. D. (1954). Comparison of the Synthetic and Actual Distribution of Galaxies on a Photographic Plate. *ApJ*, 119:91–+.
- Scoville, N. Z., Evans, A. S., Thompson, R., Rieke, M., Hines, D. C., Low, F. J., Dinshaw, N., Surace, J. A., and Armus, L. (2000). NICMOS Imaging of Infrared-Luminous Galaxies. *AJ*, 119:991–1061.
- Seldner, M. and Peebles, P. J. E. (1978). Statistical analysis of catalogs of extragalactic objects. X - Clustering of 4C radio sources. *ApJ*, 225:7–20.
- Serabyn, E., Weisstein, E. W., Lis, D. C., and Pardo, J. R. (1998). Submillimeter Fourier-transform spectrometer measurements of atmospheric opacity above Mauna Kea. *Applied Optics*, 37:2185–2198.
- Serber, W., Bahcall, N., Ménard, B., and Richards, G. (2006). The Small-Scale Environment of Quasars. *ApJ*, 643:68–74.

- Smail, I., Ivison, R. J., and Blain, A. W. (1997). A Deep Sub-millimeter Survey of Lensing Clusters: A New Window on Galaxy Formation and Evolution. *ApJ*, 490:L5+.
- Söchting, I. K., Clowes, R. G., and Campusano, L. E. (2004). Relation of radio-quiet quasars to galaxy clusters at $z \leq 0.3$. *MNRAS*, 347:1241–1254.
- Soifer, B. T. and Neugebauer, G. (1991). The properties of infrared galaxies in the local universe. *AJ*, 101:354–361.
- Soifer, B. T., Neugebauer, G., Matthews, K., Egami, E., Becklin, E. E., Weinberger, A. J., Ressler, M., Werner, M. W., Evans, A. S., Scoville, N. Z., Surace, J. A., and Condon, J. J. (2000). High Resolution Mid-Infrared Imaging of Ultraluminous Infrared Galaxies. *AJ*, 119:509–523.
- Soifer, B. T., Neugebauer, G., Matthews, K., Egami, E., Weinberger, A. J., Ressler, M., Scoville, N. Z., Stolovy, S. R., Condon, J. J., and Becklin, E. E. (2001). High-Resolution Mid-Infrared Imaging of Infrared-Luminous Starburst Galaxies. *AJ*, 122:1213–1237.
- Soifer, B. T., Sanders, D. B., Madore, B. F., Neugebauer, G., Danielson, G. E., Elias, J. H., Lonsdale, C. J., and Rice, W. L. (1987). The IRAS bright galaxy sample. II - The sample and luminosity function. *ApJ*, 320:238–257.
- Solomon, P. M. and Barrett, J. W. (1991). The CO - H₂ Mass Conversion Factor. In F. Combes & F. Casoli, editor, *Dynamics of Galaxies and Their Molecular Cloud Distributions*, volume 146 of *IAU Symposium*, pages 235–+.
- Solomon, P. M., Downes, D., Radford, S. J. E., and Barrett, J. W. (1997). The Molecular Interstellar Medium in Ultraluminous Infrared Galaxies. *ApJ*, 478:144–+.
- Spitaler, R. (1887). Large Telescopes for Celestial Photography. *The American Annual of Photography and Photographic Times*, pages 76–79.

- Springob, C. M., Haynes, M. P., Giovanelli, R., and Kent, B. R. (2005). A Digital Archive of H I 21 Centimeter Line Spectra of Optically Targeted Galaxies. *ApJS*, 160:149–162.
- Strauss, M. A., Huchra, J. P., Davis, M., Yahil, A., Fisher, K. B., and Tonry, J. (1992). A redshift survey of IRAS galaxies. VII - The infrared and redshift data for the 1.936 Jansky sample. *ApJS*, 83:29–63.
- Stutzman, W. L. and Ko, H. C. (1974). On the measurement of antenna beamwidth using extraterrestrial radio sources. *IEEE Transactions on Antennas and Propagation*, 22:493–495.
- Surace, J. A. and Sanders, D. B. (1999). High-Resolution Tip/Tilt Near-Infrared Imaging of Warm Ultraluminous Infrared Galaxies. *ApJ*, 512:162–177.
- Surace, J. A., Sanders, D. B., and Evans, A. S. (2001). Optical and Near-Infrared Imaging of Infrared-Excess Palomar-Green Quasars. *AJ*, 122:2791–2809.
- Tacconi, L. J., Genzel, R., Lutz, D., Rigopoulou, D., Baker, A. J., Iserlohe, C., and Tecza, M. (2002). Ultraluminous Infrared Galaxies: QSOs in Formation? *ApJ*, 580:73–87.
- Taylor, G. B., Carilli, C. L., and Perley, R. A., editors (1999). *Synthesis Imaging in Radio Astronomy II*, volume 180 of *Astronomical Society of the Pacific Conference Series*.
- Teng, S. (2010). *From Merging Galaxies to Quasars: The Evolution of Nuclear Activity in Luminous and Ultraluminous Infrared Galaxies*. PhD thesis, University of Maryland.
- Teuben, P. J. (2007). CARMA MIRIAD Cookbook. <http://www.astro.umd.edu/~teuben/carma/carmacookbook.ps>.
- Thompson, A. R., Moran, J. M., and Swenson, Jr., G. W. (2001). *Interferometry and Synthesis in Radio Astronomy, 2nd Edition*. Wiley-VCH.

- Toomre, A. (1974). Gravitational interactions between galaxies. In J. R. Shakeshaft, editor, *The Formation and Dynamics of Galaxies*, volume 58 of *IAU Symposium*, pages 347–363.
- Tran, Q. D., Lutz, D., Genzel, R., Rigopoulou, D., Spoon, H. W. W., Sturm, E., Gerin, M., Hines, D. C., Moorwood, A. F. M., Sanders, D. B., Scoville, N., Taniguchi, Y., and Ward, M. (2001). Isocam-Cvf 5-12 Micron Spectroscopy of Ultraluminous Infrared Galaxies. *ApJ*, 552:527–543.
- Turner, B. E. (1973). Nonthermal OH Emission in Interstellar Dust Clouds. *ApJ*, 186:357–398.
- Ulich, B. L. and Haas, R. W. (1976). Absolute calibration of millimeter-wavelength spectral lines. *Astrophys. J. Supp.*, 30:247–258.
- Urban, J., Baron, P., Lautie, N., Schneider, N., Dassas, K., Ricaud, P., and De Lanoe, J. (2004). Moliere (v5): a versatile forward- and inversion model for the millimeter and sub-millimeter wavelength range. *Journal of Quantitative Spectroscopy and Radiative Transfer*, 83:529–554.
- van Driel, W., Gao, Y., and Monnier-Ragaine, D. (2001). H I line observations of luminous infrared galaxy mergers. *A&A*, 368:64–73.
- Veilleux, S., Cecil, G., and Bland-Hawthorn, J. (2005). Galactic Winds. *ARA&A*, 43:769–826.
- Veilleux, S., Kim, D., Peng, C. Y., Ho, L. C., Tacconi, L. J., Dasyra, K. M., Genzel, R., Lutz, D., and Sanders, D. B. (2006). A Deep Hubble Space Telescope H-Band Imaging Survey of Massive Gas-rich Mergers. *ApJ*, 643:707–723.
- Veilleux, S., Kim, D., and Sanders, D. B. (1999a). Optical Spectroscopy of the IRAS 1 JY Sample of Ultraluminous Infrared Galaxies. *ApJ*, 522:113–138.
- Veilleux, S., Kim, D., and Sanders, D. B. (2002). Optical and Near-Infrared Imaging of the IRAS 1 Jy Sample of Ultraluminous Infrared Galaxies. II. The Analysis.

- ApJS*, 143:315–376.
- Veilleux, S., Sanders, D. B., and Kim, D. (1997). A Near-Infrared Search for Hidden Broad-Line Regions in Ultraluminous Infrared Galaxies. *ApJ*, 484:92–+.
- Veilleux, S., Sanders, D. B., and Kim, D. (1999b). New Results from a Near-Infrared Search for Hidden Broad-Line Regions in Ultraluminous Infrared Galaxies. *ApJ*, 522:139–156.
- Verschuur, G. L. and Kellermann, K. I. (1988). *Galactic and extra-galactic radio astronomy*.
- Vorontsov-Velyaminov, B. A. (1959). Atlas and catalog of interacting galaxies. 1959, Sternberg Institute, Moscow State University. In *Atlas and catalog of interacting galaxies (1959)*, pages 0–+.
- Vorontsov-Vel’Yaminov, B. A. and Arkhipova, V. P. (1963). Morphological catalogue of galaxies. Part 3. In *Morphological catalogue of galaxies., 3 (1963)*, pages 0–+.
- Wake, D. A., Miller, C. J., Di Matteo, T., Nichol, R. C., Pope, A., Szalay, A. S., Gray, A., Schneider, D. P., and York, D. G. (2004). The Clustering of Active Galactic Nuclei in the Sloan Digital Sky Survey. *ApJ*, 610:L85–L88.
- Wasilewski, A. J. (1981). A new Seyfert galaxy with asymmetric forbidden-line profiles in an interacting system. *PASP*, 93:560–563.
- Waskett, T. J., Eales, S. A., Gear, W. K., McCracken, H. J., Lilly, S., and Brodwin, M. (2005). XMM-Newton surveys of the Canada-France Redshift Survey Fields - III. The environments of X-ray selected active galactic nuclei at $0.4 < z < 0.6$. *MNRAS*, 363:801–810.
- Waters, J. W. (1976). Absorption and emission by atmospheric gases. In Meeks, M. L., editor, *Methods of Experimental Physics and Vol. 12B*, page 142, New York. Academic Press.
- Watts, W. M. (1904). pages 75–94. New York: Longmans, Green and Co.

- Wei, L. H., Kannappan, S. J., Vogel, S. N., and Baker, A. J. (2010). Gas Mass Fractions and Star Formation in Blue-Sequence E/S0 Galaxies. *ApJ*, 708:841–861.
- Weinberg, M. D. (1985). Evolution of barred galaxies by dynamical friction. *MNRAS*, 213:451–471.
- Wiedner, M. C., Hills, R. E., Carlstrom, J. E., and Lay, O. P. (2001). Interferometric Phase Correction Using 183 GHz Water Vapor Monitors. *ApJ*, 553:1036–1041.
- Wold, M., Lacy, M., Lilje, P. B., and Serjeant, S. (2000). Clustering of galaxies around radio quasars at $0.5 < z < 0.8$. *MNRAS*, 316:267–282.
- Wold, M., Lacy, M., Lilje, P. B., and Serjeant, S. (2001). Radio-quiet quasar environments at $0.5 < z < 0.8$. *MNRAS*, 323:231–247.
- Wong, T. and Blitz, L. (2002). The Relationship between Gas Content and Star Formation in Molecule-rich Spiral Galaxies. *ApJ*, 569:157–183.
- Woody, D., Carpenter, J., and Scoville, N. (2000). Phase Correction at OVRO Using 22 GHz Water Line Monitors. In J. G. Mangum & S. J. E. Radford, editor, *Imaging at Radio through Submillimeter Wavelengths*, volume 217 of *Astronomical Society of the Pacific Conference Series*, pages 317–+.
- Woody, D. P. (2006). Tsys calculation from ambient load and sky measurements. *CARMA Memo 33*.
- Wright, M. C. (1995). *BIMA Memo 44: A Recipe for Phase Prediction from Total Power Measurements*.
- Wright, M. C. H. and Corder, S. (2008). Deconvolving primary beam patterns from mosaic and polarization images. *CARMA Memo 43*.
- Wunderlich, E. and Klein, U. (1988). A further study of the radio-far-infrared relation in galaxies. II - The ubiquity of the correlation. *A&A*, 206:47–52.

- Yee, H. K. C. (1991). A faint-galaxy photometry and image-analysis system. *PASP*, 103:396–411.
- Yee, H. K. C. and Ellingson, E. (2003). Correlations of Richness and Global Properties in Galaxy Clusters. *ApJ*, 585:215–226.
- Yee, H. K. C. and Green, R. F. (1984). An imaging survey of fields around quasars. II - The association of galaxies with quasars. *ApJ*, 280:79–90.
- Yee, H. K. C. and Green, R. F. (1987a). Surveys of fields around quasars. IV - Luminosity of galaxies at Z roughly 0.6 and preliminary evidence for the evolution of the environment of radio-loud quasars. *ApJ*, 319:28–43.
- Yee, H. K. C. and Green, R. F. (1987b). The environment of the quasar PG 1613 + 65 (Mkn 876) - A close interacting pair. *AJ*, 94:618–627.
- Yee, H. K. C., Green, R. F., and Stockman, H. S. (1986). Surveys of fields around quasars. III - Intermediate-redshift quasars: Catalog and background galaxy counts. *ApJS*, 62:681–702.
- Yee, H. K. C. and López-Cruz, O. (1999). A Quantitative Measure of the Richness of Galaxy Clusters. *AJ*, 117:1985–1994.
- Yoon, J. H., Schawinski, K., Sheen, Y., Ree, C. H., and Yi, S. K. (2008). Finding galaxy clusters with spectro-photometric density in SDSS. In M. Bureau, E. Athanassoula, & B. Barbuy, editor, *IAU Symposium*, volume 245 of *IAU Symposium*, pages 421–426.
- Yun, M. S., Reddy, N. A., and Condon, J. J. (2001). Radio Properties of Infrared-selected Galaxies in the IRAS 2 Jy Sample. *ApJ*, 554:803–822.
- Zauderer, B. A., Momjian, E., Ghosh, T., and Salter, C. (2010). Radio Spectral Line Study of the 2 Jy IRAS-NVSS Sample: Further Results. In *American Astronomical Society Meeting Abstracts*, volume 216 of *American Astronomical Society Meeting Abstracts*, pages 419.03–+.

- Zauderer, B. A., Veilleux, S., and Yee, H. K. C. (2007). The Environment of Local Ultraluminous Infrared Galaxies. *ApJ*, 659:1096–1105.
- Zivanovic, S. S. (1992). *A New Method for Improving the Interferometric Resolution by Compensating for the Atmospherically Induced Phase Shift*. PhD thesis, UNIVERSITY OF CALIFORNIA, BERKELEY.
- Zivanovic, S. S., Forster, J. R., and Welch, W. J. (1995). A new method for improving the interferometric resolution by compensating for the atmospherically induced phase shift. *Radio Science*, 30:877–884.
- Zwicky, F. (1938). On the Clustering of Nebulae. *PASP*, 50:218–220.
- Zwicky, F. (1956). Multiple Galaxies. *Ergebnisse der exakten Naturwissenschaften*, 29:344–385.
- Zwicky, F. and Kowal, C. T. (1968). "*Catalogue of Galaxies and of Clusters of Galaxies*", Volume VI.
- Zwicky, I. F. (1942). On the Clustering of Nebulae. *ApJ*, 95:555–+.